American Iron and Steel Institute
Technology Roadmap Program

680 Andersen Drive
Pittsburgh, PA 15220-2700
Phone 412.922.2772
Fax 412.922.3213
www.steel.org

Joseph R. Vehec
Director

December 13, 2001

To: Marshall C. Garr

Reference: Cooperative Agreement No. DE-FC07-97ID13554

Subject: 9707 - Strip Casting: Anticipating New Routes to Steel Sheet
Final Technical Report

In accordance with Cooperative Agreement No. DE-FC07-97ID13554, the enclosed Final Technical Report is submitted for Strip Casting: Anticipating New Routes to Steel Sheet Project.

1. Form DOE F 1430.22	Completed
2. Form DOE F 1332.15	Completed
3. Final Report	Assembled and edited (non-proprietary) By AISI-TRP on behalf of the performing Organization

Note: "Protected metals initiative data" should not be published, disseminated or disclosed without prior permission of AISI, the designated Holding Company, in accordance with the provisions of Part VI, Clause 6, Rights in Technical Data of the above referenced cooperative agreement.

Please call me if you have any questions.

Sincerely,

Joseph R. Vehec

Enclosure: Two (2) sets of Final Report

Phone: 412.922.2772 ext. 216
Fax: 412.922.3213
E-mail: AISIAP@aol.com
JRV:ghm

Cc: R. Trimberger
E. Fleischman
A. Cramb
P. Salmon Cox
I. Chan
L. Kavanagh
T. Sneeringer
T. Stackrow

DOE F 1430.22 (04-91) All other editions are obsolete (Replaces DOE F 538)	**U.S. DEPARTMENT OF ENERGY NOTICE OF ENERGY RD&D PROJECT**	OMB Control No. 1910-1400 Burden Disclosure Statement on Back

1. DOE CONTRACT OR GRANT NUMBER					**DE-FC07-97ID13554**	
✠ New contract ☐ Continuation/Revision						
2. A. Name of Performing Organization					**Carnegie Mellon University**	
B. Department or Division					**Materials Science and Engineering Department**	
C. Street Address	**5000 Forbes Avenue**					
City	**Pittsburgh**		State	**PA**	Zip	**15213**

D. Type of Performing Organization (circle only one two-letter code)	
(CU) College, university, or trade school	NP-Foundation or laboratory not operated for profit
EG-Electric or gas utility	ST-Regional, state, or local government facility
FF-Federally funded RD&D centers or laboratory operated for agency of US government	TA-Trade or professional organization
IN-Private industry	US-Federal Agency
	XX-Other

3. PRINCIPAL OR SENIOR INVESTIGATOR					
A. Last	**Cramb**	First	**Alan**	M I	**W.**
B. Phone:Commercial	**412-268-5548**	FTS			
4. DOE SPONSORING OFFICE OR DIVISION	**Idaho Operations Office**				

5. TITLE OF PROJECT AISI/DOE Technology Roadmap Program: **STRIP CASTING: ANTICIPATING NEW ROUTES TO STEEL SHEET**

6. DESCRIPTIVE SUMMARY (limit to 200 words)

Based upon a study of strip cast carbon steel samples, the following conclusions were made. Strip casting of carbon steels is technically feasible for sheet material, with thickness from slightly less than 1 mm to 3 mm, and, if economically viable, it will be first applied in carbon steel markets that do not require stringent surface quality or extensive forming. The potential of strip casting for flat products is very high as the cast strip has some very novel characteristics. Direct cast carbon strip has better surface quality, shape and profile than any other casting process currently available. The more rapidly solidified structure of direct cast strip tends to be strong with low ductility; however, with adequate thermal treatment, it is possible to develop a variety of properties from the same grade. The process is more suitable for production rates of ~ 500, 000 tons/yr. and as such will first find niche type applications. This technology is an additional technology for steel production and will be in addition to than a replacement for current casting machines.

7. RESPONDENT INFORMATION. List name and address of person filling out this form. Give telephone number and extension where person can be reached. Record the date this form was completed or updated. This information will not be published.

Last	**Vehec**	First	**Joseph**	MI	**R.**
Address	AISI – Technology Roadmap Program, 680 Andersen Drive,				
City	Pittsburgh	State	Pennsylvania	ZIP	15220
Phone	412-922-2772, Ext. 216	Date	December 15, 2001		

DOE F 1332.15 U.S. DEPARTMENT OF ENERGY OMB Control No.
(2-96) (p. 1 of 5) ANNOUNCEMENT AND DISTRIBUTION OF DEPARTMENT OF ENERGY (DOE) 1910-1400
(All other versions are SCIENTIFIC AND TECHNICAL INFORMATION (STI)
obsolete.) (When submitting form, input should be typed, not handwritten.)

PART I Information Product Identification

A. Identifiers

1. Product/Report Nos. _____

2. Award/Contract Nos. **DE-FC07-97ID13554**

3. Title **AISI/DOE Technology Roadmap Program: STRIP CASTING: ANTICIPATING NEW ROUTES TO STEEL SHEET**

(Grantees and Awardees skip to Part 1.B.)

4. Funding Office(s) _____

5. B&R Code(s) _____

6. Project ID(s) _____

7. CRADA Nos. _____

8. UC/C Category(ies) _____

9. Information Product Filename _____

B. Information Product Description

X 1. Report

a. Type _____ Quarterly _____ Semiannual _____ Annual __X__ Final _____ Topical _____ Other (Specify)_____

b. Dates covered (mm/dd/yyyy) **04/01/1998** - thru **08/31/2001**

__ 2. Conference

a. Type _____ Conference paper _____ Published proceedings _____ Other (Specify) _____

b. Conference title (No abbreviations) _____

c. Conference location (city/state/country)_____

d. Conference dates (mm/dd/yyyy) _____/_____/_____ thru _____/_____/_____

e. Conference sponsor(s)_____

__ 3. Software (Note: Additional forms are required. Follow instructions provided with this form.)

__ 4. Other (Provide complete description.)_____

C. Information Product Format

__ 1. Product not submitted to OSTI (i.e., electronic version) _____

a. Location (FTP, URL, etc.) _____

b. File format ___ SGML ___ HTML ___ Postscript ___ PDF ___ TIFFG4 ___ Other (Specify)

c. SGML bibliographic record available _____ With product _____ Separately (Specify)_____

__ 2. Product submitted to OSTI (i.e., electronic, paper, audiovisual or computer medium)

a. Number of copies

__X__ (1) Two for unclassified processing _____ (2) _____ copies for program unclassified distribution
___ (3) One for classified processing _____ (4) _____ copies for standard classified distribution
_____ (5) _____ copies for OSTI to reproduce (Complete part C.3.)
_____ (6) Other (Complete part C.3.)

b. SGML bibliographic record submitted to OSTI _____ With product _____ Separately (Specify)_____

c. Method of transmittal to OSTI

_____ (1) Electronic (e.g., FTP, E-mail) (Note: Transmit only unclassified unlimited information not subject to access limitation over open systems. Contact OSTI for further information.)

(a) File format___ SGML___ HTML ___ Postscript ___ PDF ___ TIFFG4 ___ Other (Specify) _____

_____ (2) Computer medium (e.g., magnetic tape or diskette) (Complete all. Provide a separate electronic or print abstract.)

(a) Quantity/type (Specify) _____

(b) Machine compatibility (Specify) _____

(c) Operating system (Specify)_____

(d) File format___ SGML ___ HTML ___ Postscript ___ PDF ___ TIFFG4 ___ Other (Specify)_____

_____ (3) Audiovisual Material (Complete all. Provide a separate electronic or print abstract.)

(a) Quantity/type (Specify)_____

(b) Machine compatibility (Specify) _____

(c) Sound ____ Yes ____ No (d) Color ____ Yes ____ No (e) Playing time_____

__X__ (4) Paper

__ 3. Additional instructions/explanations_____

_____

D. Contact (Person knowledgeable about the information product and its submission)

Name **Alan W. Cramb** Position **Professor** Phone **412-268-5548**
Organization **Carnegie Mellon University** Email **Cramb@cmu.edu**

PART II Information Product Announcement and Handling

(DOE/DOE Contractors complete; Grantees and Awardees complete as instructed by contracting officer)

A. Recommendations (Mark at least one)

_____ 1. Unlimited Announcement (Available to U.S. and non-U.S. public)

__X__ 2. Unlimited Announcement/U.S. Dissemination Only

___ 3. Classified (Standard announcement)

___ 4. OpenNet

a. Non-NTIS Availability (Required if not available from NTIS)

(1) Accession Number _____ (2) Document Location _____

_____

b. Field Office Acronym _____

c. Declassification date (mm/dd/yyyy) _____/_____/_____ _____ Sanitized _____ Never classified

___ 5. Special Handling (Legal basis must be noted below.)

___ a. Copyrighted material _____ All _____ Part (Specify) _____

___ b. Unclassified Controlled Nuclear Information (UCNI)

___ c. Export Control/ITAR/EAR

___ d. Temporary hold pending patent review

___ e. Translation of copyrighted material

___ f. Small Business Innovation Research (SBIR) Release date (mm/dd/yyyy) _____/_____/_____

___ g. Small Business Technology Transfer (STTR) Release date (mm/dd/yyyy) _____/_____/_____

___ h. Proprietary

___ i. Protected CRADA information Release date (mm/dd/yyyy) _____/_____/_____

___ j. Official Use Only (OUO)

___ k. Program-Directed Special Handling (Specify)_____

___ l. Other (Specify)_____

B. Releasing Official

___ 1. Patent Clearance (Mark one)

___ a. Submitted for DOE patent clearance Date submitted (mm/dd/yyyy) _____/_____/_____

___ b. DOE patent clearance has been granted

___ c. DOE patent clearance not required

___ 2. Released by Name _____ Date (mm/dd/yyyy) _____/_____/_____

Phone _____ E-mail_____

PART III Bibliographic Information

(Note: Providing the following information is optional. For information products that are to be included in the OpenNet Database, the following information will be used for the OpenNet Database records. For all information products, it will be used in announcing those products, as appropriate, to other parts of the DOE community.)

A. Personal Author/Affiliation
Prof. Alan W. Cramb and Prof. Anthony Rollett

B. Performing Organization **Carnegie Mellon University, Materials Science and Engineering Department, 5000 Forbes Avenue, Pittsburgh, PA 15213**

C. Date of Publication (mm/dd/yyyy) **08/31/2001**

D. Pages/Size **366 @ 8-1/2" x 11"**

E. Abstract

This project had two goals: (1) to determine the potential for strip casting in the steel industry and, (2) to develop the fundamental knowledge necessary to allow the role of strip casting in the modern steel industry to be understood. Based upon a study of carbon steel strip castings that were either produced for the program at British Steel or were received from a pre-commercial production machine, the following conclusions were made. Strip casting of carbon steels is technically feasible for sheet material from slightly less than 1 mm thick to 3 mm thick, and, assuming that it is economically viable, it will be first applied in carbon steel markets that do not require stringent surface quality or extensive forming. The potential of strip casting as a casting process to be developed for steel castings is very high as the cast strip has some very novel characteristics. Direct cast carbon strip has better surface quality, shape and profile than any other casting process currently available. The more rapidly solidified structure of direct cast strip tends to be strong with low ductility; however, with adequate thermal treatment, it is possible to develop a variety of properties from the same grade. The process is more amenable at this time to production tonnages per year of the order of 500, 000 tons and as such will first find niche type applications. This technology is an additional technology for steel production and will be in addition to, rather than a replacement for, current casting machines.

F. Subject Terms _____

_____

G. OpenNet Document Type _____

H. OpenNet Document Categories _____

_____

I. OpenNet Addressee _____

Report Documentation Page Information

Title and Subtitle:

AISI/DOE Technology Roadmap Program
TRP 9703: Strip Casting: Anticipating New Routes to Sheet Steel

Authors:

Alan W. Cramb
Anthony Rollett

Performing Organization

Carnegie Mellon University
Department of Materials Science and Engineering
5000 Forbes Avenue
Pittsburgh, PA 15213

Abstract

This project had two goals: (1) to determine the potential for strip casting in the steel industry and, (2) to develop the fundamental knowledge necessary to allow the role of strip casting in the modern steel industry to be understood. Based upon a study of carbon steel strip castings that were either produced for the program at British Steel or were received from a pre-commercial production machine, the following conclusions were made. Strip casting of carbon steels is technically feasible for sheet material from slightly less than 1 mm thick to 3 mm thick, and, assuming that it is economically viable, it will be first applied in carbon steel markets that do not require stringent surface quality or extensive forming. The potential of strip casting as a casting process to be developed for steel castings is very high as the cast strip has some very novel characteristics. Direct cast carbon strip has better surface quality, shape and profile than any other casting process currently available. The more rapidly solidified structure of direct cast strip tends to be strong with low ductility; however, with adequate thermal treatment, it is possible to develop a variety of properties from the same grade. The process is more amenable at this time to production tonnages per year of the order of 500, 000 tons and as such will first find niche type applications. This technology is an additional technology for steel production and will be in addition to, rather than a replacement for, current casting machines.

(RDP standard Form, Form 298)

Sponsor TBD Report No.:

AISI/DOE Technology Roadmap Program

Final Report

Strip Casting:

Anticipating New Routes to Steel Sheet

By

Alan W. Cramb

And

Anthony Rollet

August 2001

Work Performed under Cooperative Agreement
No. DE-FC07-97ID13554

Prepared for
U.S. Department of Energy

Prepared by
American Iron and Steel Institute
Technology Roadmap Program Office
Pittsburgh, PA 15220

DISCLAIMER

TABLE OF CONTENTS

LIST OF FIGURES

LIST OF TABLES

Executive Summary

This project had two goals: (1) to determine the potential for strip casting in the steel industry and, (2) to develop the fundamental knowledge necessary to allow the role of strip casting in the modern steel industry to be understood.

Strip cast low carbon steels are quite unique due to the more rapid processing conditions that occur during twin roll casting. There is a potential for castings produced by this technique to be significantly better in surface, shape, profile and internal quality than any other current casting process. This direct casting process is also the first casting process where the cast surface directly becomes the product surface and the process must produce a casting that is equivalent in geometry to a hot rolled material. This makes the process a combination of a casting and a rolling process.

As the twin roll direct casting process does not mimic the thermo-mechanical processing that a slab encounters in conventional processing, it should be of no surprise that the properties that are encountered in twin roll cast product are substantially different than that of conventionally processed material. It is however noteworthy that strip cast material is amenable to thermo-mechanical processing and combinations of heat treatment and cold reduction can lead to a wide variety in properties from a single chemistry. However, the initial results of this work suggest that the properties that can be achieved by strip casting from a given grade are not necessarily equivalent to that which can be achieved by conventional processing of the same chemistry. Significant thermal control during casting and coiling and subsequent thermo-mechanical processing will be necessary for strip cast material in order to control properties as the material properties are sensitive to thermal cycling. In addition, to allow conventional properties to be achieved in low carbon steels products, many grade chemistry adjustments will probably be necessary. This will prevent strip cast material from being transparent in the marketplace.

This work has not found any issue that is a major problem with the technology of strip casting. Strip casting of carbon steels is technically feasible for sheet material from slightly less than 1 mm thick to 3 mm thick, and, assuming that it is economically viable, it will be first applied in carbon steel markets that do not require stringent surface quality or extensive forming. The more rapidly solidified structure of direct cast strip tends to be strong with low ductility; however, with adequate thermal treatment, it is possible to develop a variety of properties from the same grade. The process is more amenable at this time to production tonnages per year of the order of 500, 000 tons and as such will first find niche type applications. This technology is an additional technology for steel production and will be in addition to than a replacement for current casting machines.

It is clear that strip casting is not at this time developed to the point that application of the technology is risk-free. There is great potential for strip casting; in fact, this work points out that the potential of strip cast material is to be better than that produced by current technologies. However, many basic questions remain unanswered and there are significant technological questions to be answered in the area of thermo-mechanical processing

AISI/DOE Technology Roadmap Program

TRP 9703: Strip Casting: Anticipating New Routes to Sheet Steel

Final Project Report

By

Paretosh Misra,
Prof. Anthony Rollett
And
Prof. Alan Cramb

August 17, 2001

1. Abstract

This project had two goals: (1) to determine the potential for strip casting in the steel industry and, (2) to develop the fundamental knowledge necessary to allow the role of strip casting in the modern steel industry to be understood. Based upon a study of carbon steel strip castings that were either produced for the program at British Steel or were received from a pre-commercial production machine, the following conclusions were made. Strip casting of carbon steels is technically feasible for sheet material from slightly less than 1 mm thick to 3 mm thick, and, assuming that it is economically viable, it will be first applied in carbon steel markets that do not require stringent surface quality or extensive forming. The potential of strip casting as a casting process to be developed for steel castings is very high as the cast strip has some very novel characteristics. Direct cast carbon strip has better surface quality, shape and profile than any other casting process currently available. The more rapidly solidified structure of direct cast strip tends to be strong with low ductility; however, with adequate thermal treatment, it is possible to develop a variety of properties from the same grade. The process is more amenable at this time to production tonnages per year of the order of 500, 000 tons and as such will first find niche type applications. This technology is an additional technology for steel production and will be in addition to than a replacement for current casting machines.

2. Introduction

The project was initiated on April 2, 1998 with the first meeting of the advisory board. The project team includes CMU, USS, LTV, Dofasco, SMS Concast, Kvaerner, AK Steel and National Steel.

The goals of the program were as follows:

- To determine the potential for strip casting in the steel industry
- To develop the fundamental knowledge necessary to allow the role of strip casting in the modern steel industry to be understood

To achieve these goals it was necessary to institute a program aimed at the determination of the post caster processing steps necessary to develop appropriate mechanical properties. This project had three major thrust areas: casting, secondary processing and characterization of processed materials. It was initially proposed that two centers of steelmaking research (the Center for Iron and Steelmaking Research at Carnegie Mellon University and The Max Planck Institute in Germany) combine with a number of North American steel companies in a three year long program. Unfortunately after a year of negotiation Max Planck dropped out of the project.

Casting was carried out in the initial stage (18 months) of the project at the British Steel Research Laboratories in Middlesborough, England. Grade selection and processing parameters were determined by both the steel industry and CMU. Secondary processing and characterization of the strip cast material was carried out at CMU and at selected steel industry labs. Casting of carbon steel grades at British Steel was pursued, to allow different process parameter ranges to be studied. Work at Carnegie Mellon was aimed at developing a fundamental understanding of the effect of heat transfer in strip casting structure development, determining strip cast structures, developing and characterizing microstructural development and determining the relationship between microstructural and mechanical property development. Various steel company laboratories performed secondary processing on the strip cast material and aided in property determination.

The objectives of the program were initially planned in three phases:

Phase 1

- To determine the operating window and types of solidification structures produced by the pilot machines and benchmark the solidification structures versus known literature values from other operating machines

Phase 2

- To strip cast various low and ultra-low carbon steels and determine their cast structure, mechanical properties and the effect of post casting processing on mechanical properties
- To determine if a modification in steel grade composition will allow variations in processed strip properties to be developed
- To test the response of strip cast commercial steel grades to varying residual element contents

Phase 3

- To optimize the post processing of strip cast material
- To determine the potential of strip casting for novel or unconventional applications based upon the information gathered during phases 1 and 2

However after the Max Planck problem and the strip casting trials at British Steel and information supplied by BHP in Australia, the program objectives were recast as follows:

- To determine the cast strip properties of carbon steels produced at British Steel and benchmark the cast strip properties versus values determined from other pre-commercial machines
- To study both aluminum and manganese silicon killed carbon steel strip cast material
- To optimize the post processing of strip cast material
- To determine the potential of strip casting for carbon steels

3. Results

Strip cast material, obtained from both commercial and pilot casters, was tested to characterize microstructure, mechanical properties, texture and quality issues like porosity, gauge and inclusions.

The technologies to produce hot strip can be divided into three broad categories on the basis of the thickness of the strip produced from the caster. They are:

Thick slab casting:

Molten metal is poured into a tundish from where it goes to a mold, solidifies and emerges from the caster as slabs of 250-300 mm thickness. The slabs are further hot rolled to achieve thickness less than 3 mm.

Thin slab casting:

Molten metal emerges from the mold as thin slabs of thickness 50-60 mm. Hot rolling is necessary to reduce the thickness to close to 3mm.

Strip Casting:

Molten metal is poured between two rolls and it comes out directly as strips of thickness less than 3 mm. Some inline hot rolling may be required to further reduce the gauge.

Continuous caster which produce thick slabs typically require 8 strands of rolls for hot reduction which have huge energy and maintenance requirements. On the other hand, in strip casting even inline hot rolling may not be required. Thus strip casting offers huge savings in capital and operating costs.

While the advantages of strip casting are obvious, there are many challenges which need to be overcome before it could be commercialized for all grades of steel. The basic idea of strip casting was conceived more than one hundred years back by none other than Sir Henry Bessemer. However it has only been in the last 20 years that the idea became a reality.

The first test of any technology promising to deliver products with thinner gauge is the issue of productivity. A simple calculation can demonstrate the casting velocities which are desirable if strip casting has to be a success.

Productivity (measured in volume cast per minute) can be calculated as follows:

Productivity (P)= Strip Thickness (m) * Strip Width (m) * Casting Speed (m/min)

For Thick Slab Casting taking typical values.

$$P_{slab} = (300*10^{-3}) * 1 * 1$$

For Strip Casting:

$$P_{strip} = (3*10^{-3}) * 1 * V_{reqd}$$

Thus strip caster needs to operate at a casting speed of 100m/min, if its productivity is to match that of a thick slab caster. High casting speeds mean that the sensible heat of the molten steel has to be removed much more quickly than in traditional casters. Owing to this, it is not surprising that heat fluxes in the range 10-15 MW/m^2 have to be sustained

by the rolls. Roll life and design must be thoroughly considered when ascertaining the economic viability of the process.

It must also be noted that solidification of the molten metal has to be complete by the time it reaches "kissing point". If any molten metal remains inside the solidified shell beyond this point then the metallostatic pressure it exerts could cause bulging of the surface.

In addition, the quality of the strip cast material must at least match the standard of hot rolled material since the aim is to eliminate hot rolling as a process.

Gauge variation, roughness, mechanical properties such as tensile strength, ductility and texture are the important material properties of interest which must be benchmarked against suitable standards

The properties and characteristics that were analyzed during the course of the project were:

1. Composition and strip dimensions (Appendix 1)
2. Microstructure and Solidification Structure (Appendix 2)
3. Mechanical Properties (Appendix 3)
4. Texture (Appendix 4)
5. Surface Oxides using Confocal Microscopy (Appendix 5)
6. Effect of Oxide Films on Heat Transfer (Appendix 6)[1]
7. Paper on Mechanical Properties (Appendix 7)

The major findings were:

- The surface quality of the pre-commercial castings was excellent with no visible defects or measurable defects.
- The pilot caster strips were not close to the quality of that from the pre-commercial caster. The lack of control in the pilot caster made the castings interesting but not of a high enough quality to truly determine the potential of strip cast material. Strip cast material must be analyzed using a caster with advanced control systems for process and chemical control in order to produce defect free castings.

[1]Appendix 6 contains the thesis work of Natthapong Phinichka. The work in chapter 6 was carried out to augment and understand the fundamental issues raised in this work. The rest of the thesis (chapter 1 to 5) was directly sponsored by the Center for Iron and Steelmaking Research. The complete thesis is supplied so that the reader can better understand the nature of the results and the experimental techniques used to measure the effects of oxide films on heat transfer behavior in casting. The work in chapter 6, although not directly funded by this project, was carried out to better understand heat transfer issues in continuous casting and to better under stand the confocal findings of Paretosh Misra in this work. It is reported here as it was supporting research to this project and is a key part in understanding the future of strip casting.

- Maganese-Silicon killed steels produce liquid inclusions which coat the mold surface and lead to an increase in heat transfer rate during casting. The coating also coats the strip at high temperatures and probably aids in the retardation of scale formation.
- The strip cast steels studied were quite dirty when judged by standard total oxygen analysis; however, the inclusion size distribution indicated that the majority of inclusions were very small (less than 5 microns in diameter) and no larger agglomerated inclusions were found.
- The cast strips analyzed in this study had a roughness in the center of the casting measured by arithmetic mean roughness (**Ra**) which varied from 2-3 μm and waviness measured by the maximum profile depth (**Pt**) which varied from 19 to 25 μm.
- After some edge trimming (5cm) the standard deviation in gauge variation across the width decreased from 40 μm to 15 μm.
- The as-cast structure is dendritic with a primary dendrite arm spacing varying from 20 to 40 μm. Some central porosity is evident. Microsegregation is minimal due to the fine solidification structure.
- The microstructure of the as-cast strip (pre-commercial) exhibited a mixture of acicular and Widmanstätten ferrite that resulted from the rapid cooling experienced by the sheet. The cooling rates, as judged from the microstructure, were comparable to those observed in welds.
- The mechanical properties of the cast strip can be varied by subsequent thermo-mechanical processing. The most surprising finding was the large variations in properties that are possible from the same chemistry through a variation of the post casting strip processing.
- Cold rolled, batch annealed sheet has promising ductility (close to 50%) and reasonably high strength (350 MPa).
- The texture of the as-cast sheet was nearly random such that it exhibited little anisotropy in mechanical properties.
- Cold rolling induces the typical texture observed for low carbon steels with mild development of γ fiber and r-values are slightly greater than 1 and are comparable to conventionally cast silicon killed steels.

4. Discussion

This project was particularly timely as during the time of the project two additional commercial ventures in strip cast were announced - Eurostrip for stainless production at Krefeld in Germany and Cast-Strip, the joint venture between Nucor and BHP at Crawfordsville Indiana. The issue of the future of strip casting from an economic viewpoint will be revealed by these venture and the one in Japan. This project started

with the premise that these venture would occur and that they would be economically successful and it was the objective of this project to study strip casting material with a view to prediction of the potential of strip casting of carbon steels.

The Effect of a Liquid Inclusion

Clearly from the limited samples studied, strip casting of manganese silicon killed steels is technically feasible at a commercial scale. This statement cannot be made at this time for fully aluminum killed steels. Even though a fully aluminum killed steel casting was attempted at British steel, the excessive reoxidation encountered in the process due to a lack of reoxidation control at the caster made it impossible to predict the true results of casting these steels. It is clear, however, that the process that makes high productivity possible in manganese silicon killed steels (formation of a liquid film that allows a liquid-solid contact rather than a solid-solid contact), will not be present in a fully aluminum-killed steel. Caster productivity during the casting of aluminum killed steels will be inherently lower than that of manganese silicon killed steel unless a surface coating technology is developed. This coating on the surface of the rolls would serve the same heat transfer purpose as the oxide film that occurs during the casting of manganese silicon killed steels. In this case, the presence of solid alumina agglomerates on the pool surface will lead to local areas of potential cast strip defects if the agglomerates reach the roll surface. In the absence of the development of an external applied liquid flux the heat transfer rate during casting of aluminum killed steels will be significantly lower, leading to the necessity of larger rolls and a larger pool depth to compensate for the decreased heat transfer rate.

However casting of fully aluminum-killed steels is probably doubtful due to clogging issues that will be even more problematic in a small section caster such as a strip caster. It is notable that all thin slab casters use calcium treated steels in order to avoid solid alumina inclusions and nozzle clogging. It is probable, based upon that experience, that an even smaller section caster (a strip caster) will also have to change the natural inclusions from a solid to a liquid form and that aluminum killed steels on a strip caster would be calcium treated. The next obvious question is will liquid calcium aluminates inclusions be self fluxing in a manner similar to manganese silicates? Although theoretically possible - there are a number of issues that indicate that this might be difficult. In manganese silicon killed steels, there is a large window of composition over which there is a liquid inclusion and the natural inclusions are plentiful due to the significantly higher mass of inclusions that occur in Mn-Si killed steels verses aluminum killed steels. In addition, the effect of oxidation on a manganese-silicon steel is to make the inclusion more fluid, whereas in Ca-Al killed steels, reoxidation makes the inclusion more solid. Thus the tolerance to reoxidation is significantly different. This will have significant implication for pool reoxidation strategies and probably lead to active gas reoxidation control (CO or hydrogen) rather than inert gas reoxidation control (Ar). As the inclusions that lead to the oxide film must come from the steel, there must be a balance between the total mass of inclusions available to coat the mold and the thickness of the coating. Cleaner steels will possibly make it more difficult to achieve this optimal coating.

One other additional benefit of using a manganese silicate based liquid inclusion is that it tends to coat the strip surface as well as the roll surface. This could lead to a reduced scaling rate at the caster for grades based upon a liquid inclusion.

Small vs. Large Roll Diameter

In strip casting developments at this time, we see two different approaches - a large diameter roll (1.2 m in diameter, for example) and a small diameter roll (0.5 m, for example). An economic issue in strip casting is productivity. This can be achieved by increasing heat transfer rate in a small diameter caster or by increasing roll diameter. Thus similar production rates can be reached by both techniques and has been demonstrated by Nippon Steel and BHP/IHI. One must realize, however, that each solution brings different technical problems. Liquid steel feeding and control of heat transfer rate are major issues in the small roll solutions while edge containment, roll and refractory costs become major issues in larger roll solutions.

Thus, at this time it is not clear if the technology applied to the strip casting of manganese silicon grades with a small diameter roll is readily applicable to steel grades employing other methods of deoxidation. This leads to a significant issue in the future of carbon steel strip casting - will the development be limited to specific grades and applications? It is clear that the first application will be in grades that are manganese - silicon killed where aluminum killing is not required. This is the lower quality end of flat products and fits the current Nucor model. Where steels can be sold by property rather than by chemistry, the technology will probably have a number of niche applications in its current status. However, it is clear from the current chemistry restrictions that the growth of the application of strip cast material will be controlled by product acceptance and testing in the marketplace as the material will not necessarily be a blind replacement for conventional steels.

It appears that significant developments are necessary to allow high productivity casting rates using solely aluminum killed steels. The status of such developments is not known at this time. These developments will either be successful and the small roll approach will become predominant or the developments will be unsuccessful and two approaches to strip casting will be necessary. The first will be the BHP/Nucor approach focussed on specific grades where manganese silicon killing yields acceptable properties. The second will be the larger diameter roll machine for aluminum killed steels. For this to be feasible the operating costs of the large roll machine will have to be comparable or less than that of current thin slab processing routes. This will be a major challenge for those operating strip casters with large roll diameters.

Strip Cast Structures[2]

The as-cast strip shows an inhomogeneous structure, with a blend of acicular ferrite, irregular polygonal ferrite and Widmanstätten ferrite morphologies, as shown in Fig. 1(a)

[2] A detailed referenced discussion of this section can be found in Appendix 7.

and (b). This is related to the high cooling rate associated with the strip casting process. Moreover, the coarse austenite grains that would have been present at the beginning of the ferrite transformation, also favor the formation of Widmanstätten ferrite because of the consequent low density of nucleation sites for transformation.

The solidification structure of the as-cast strip shows well-defined columnar grains, inclined to the sheet normal. It was not been possible to observe secondary dendrites in the sheet because of the low levels of phosphorus in this steel. The primary dendrite arm spacing was obtained directly from the optical micrograph. In addition, primary and secondary dendrite arm spacings were also calculated with the Procast^{TM} model. The initial and boundary conditions used in the model were:

At $t = 0$, $T = 1600°C$ $\quad 0 \leq x \leq 1$ mm
At $x = 0$, $q = 0$ (center line of the strip)
At $x = 1.0$ mm, $q = 12.5$ MW/m^2 (surface of the strip),

where x is the distance from the center line of the strip and q is the heat flux.

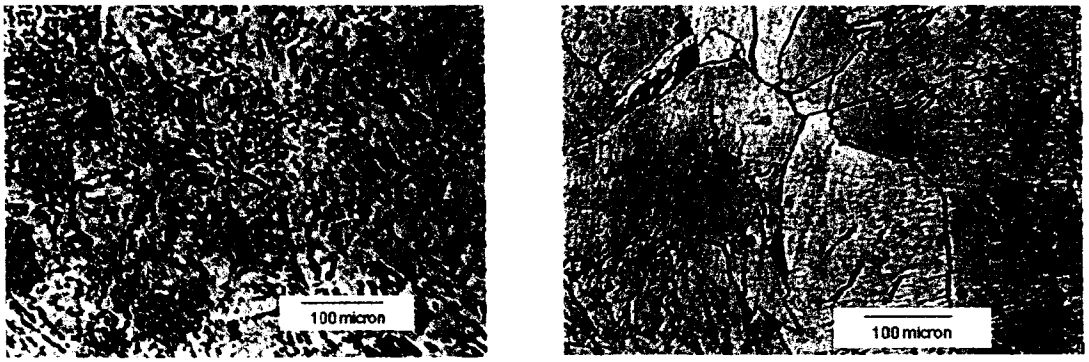

Figure 1: Microstructure of as-cast strip, 4% nital etch. (a) region showing acicular ferrite. (b) region showing irregular polygonal and Widmanstätten ferrite

The thermophysical properties of the strip were reasonably approximated with those of pure iron. In strip casting conditions, the shell thickness (x_s) is related to time (t) as:
$x_s = 2.33\ t^{0.575}$

From the above relationship, a surface heat flux value close to 12.5 MW/m^2 can be obtained using the analysis of Sha and Schwerdtfeger[3] and was used as the surface boundary condition. Both the experiment and the simulation suggest a primary dendrite arm spacing of 20-30 μm, which is 5-6 times smaller than that observed for conventional slab casting. The secondary dendrite arm spacing is predicted to be between 10 and 15 μm, and is related to the cooling rate during solidification of the sheet. The heat transfer model suggests a cooling rate in the range of 1500-2000°C/sec, which is in agreement with the cooling rates reported for strip casting of low C steel.

[3] H. Sha, and K. Schwerdtfeger: *International Journal of Heat and Mass Transfer, 1998, vol. 41, p. 3265.*

Strip castings cool considerably faster than conventional slab based processes resulting in significantly less time at temperature for scale growth. Thus there is a potential for higher yield and the ability of strip cast steels to be much less sensitive to residual levels in scrap as defect formation due to residuals (surface cracking) is a function of scale growth rate. Initial patents and reports by both BHP and Nippon steel support this fact. There is also a possibility that by atmosphere control, post casting scaling could be eliminated.

The in-line hot rolled strip shows a microstructure that is very similar to the as-cast strip. Irregular polygonal ferrite is present, as is some acicular and Widmanstätten ferrite plates. Some ferrite veining has also been observed at the prior austenite grain boundaries in the hot rolled sheet. This microstructure resembles the structures obtained in welding of low C steel sheets, because of the higher cooling rates of the welding processes. The hot rolling microstructure suggests that the temperature for rolling was high enough to result in a large austenite grain size, and the cooling rate was probably also high; both these factors promote acicular and Widmanstätten ferrite morphologies. However, changing the rolling and coiling parameters may lead to fully polygonal ferrite grain structure, with enhanced ductility, and thus needs further investigation in this direction.

By contrast, the cold rolled and batch annealed samples show a fully recrystallized polygonal ferrite structure. The initial microstructure has been completely destroyed during cold rolling and batch annealing. The grains are elongated in the rolling direction, i.e. they are pancaked (with an average aspect ratio of 2.3), which is in agreement with the results obtained by various investigators.

The orientation imaging microscopy (OIM) obtained for the as-cast strip confirms the optical characterization of a very inhomogeneous structure, with large irregular polygonal ferrite, and bands of Widmanstätten ferrite. OIM allows simultaneous study of the grain morphology (size and shape) and orientation. The average grain size obtained from OIM grain mapping is 22μm, compared to 55μm observed by optical microscopy. This significantly finer grain structure obtained from the OIM explains the enhancement of the strength properties for the as-cast strip. OIM shows the presence of low angle grain boundaries, and sub-grain structure explicitly, which are not fully revealed by chemical etching. OIM mapping of grains in a region dominated by Widmanstätten ferrite side plate indicates a particular orientation is selected within a tolerance angle of 10^0 and indicates the presence of parallel laths of ferrite with similar orientation.

Thus the strip cast structures indicate that an entirely new starting structure results from strip casting. This starting structure is quite unlike any cast structure previously used in steel processing.

Strip Cast Mechanical Properties

Mechanical properties (tensile and hardness) of the following materials were evaluated in the laboratory: (a) as-cast strip material obtained from a pre-commercial facility, (b) Strip cast and in-line hot rolled material obtained from the above source, and (c) strip cast

material cold rolled (50 to 80%) and annealed [at 660° - 827° C (1220° - 1520° F)] at the laboratory.

The engineering and true stress strain curves for the as-cast strip are shown in Fig. 2. It is interesting to note that no yield point phenomenon is observed in the as-cast sheet. The tensile properties were measured in samples machined parallel to the rolling, transverse and diagonal directions, and the average value has been reported here. The properties are nearly isotropic for the various sheets and the variation is less than 5%. The strip cast steel has slightly higher yield strength due to the high dislocation density that has been observed with Widmanstätten ferrite structure. The tensile strength is 80-100MPa higher than the conventional hot band, with almost the same ductility level. This is not surprising because the lower the transformation temperature of austenite to ferrite, the higher the strength and the lower the ductility. The same trend is valid for bainitic and martensitic transformations of austenite, which are obtained at much higher cooling rates than obtained in the cast strip, which is of the order of $10^4 - 10^5$ °C/s.

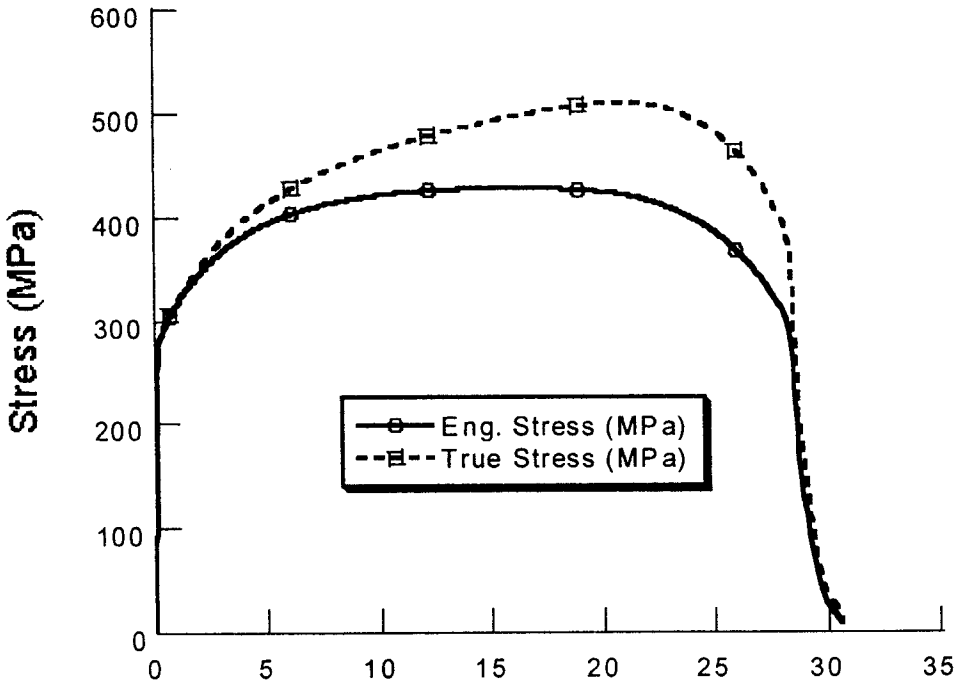

Figure 2: Engineering and true stress strain curves for as-cast sheet

The in-line hot rolled strip has similar elongations to the as-cast strip, though with slightly higher strength values. This is in agreement with the microstructures observed. The variation in strength values is related to the different volume fractions of the various morphologies of ferrite present in the material. Basically, hot rolling has not been successful in increasing the ductility of the as-cast strip under the current processing conditions. However, the directly cold rolled (70%) and batch annealed [at 720° C (1330°

F) for 30 min.] sheet shows elongations very close to 50%, with useful strength. The mechanical properties are summarized in Table 1.

Table 1: Mechanical Properties of As-cast, In-line Hot Rolled, and Cold Rolled and Annealed Steel.

Mechanical Properties	As-Cast	In-Line Hot rolled	Cold Rolled Batch, Annealed*
Yield Strength, MPa (ksi)	276 (40)	331 (48)	241.5 (35)
Ultimate Tensile Strength, MPa (ksi)	428 (62)	462 (67)	359 (52)
Elongation (%)	32	33	48
Hardness, R_B	71	77	55

* Cold rolled 70% and annealed at 721° C (1330° F) for 30 min.

The plastic strain ratio (i.e. r-value), obtained by simultaneously measuring the strain in the length and width directions, has been obtained for the various samples as shown in Table 2. The high r-values indicate resistance to thinning during a forming operation. The planar anisotropy factor (Δr), which measures the in-plane variation of the r-value, is predictive of the earing tendency of the sheet and should be minimized for deep drawing applications. A positive value of Δr denotes the tendency of earing in the rolling and transverse directions (typical of annealed material), and a negative value of Δr, a tendency in the diagonal direction (typical of rolled sheet). The plastic strain ratio is related to the amount of gamma fiber present in the sheet, i.e. <111>|| ND, and tends to be high for the Al-killed steel, because of the beneficial effects of AlN precipitation during recrystallization. In-line hot rolling decreases the r-value, but cold rolling and batch annealing increases the r-value, though at the expense of high Δr.

Table 2: Plastic Strain Ratio of as-cast, in-line hot rolled, and cold rolled batch annealed sheet

Processing Type	r-value (r_m)	Plastic Anisotropy factor (Δr)
As-Cast	0.93	0.07
In-line Hot Rolled	0.79	-0.11
Cold Rolled, Batch Annealed	1.1	0.45

The texture work was focused on cold rolled batch annealed strip cast steel, and its comparison with the conventionally cast, cold rolled batch annealed US Steel. Both the samples were 70% cold reduced before batch annealing. X-ray texture measurements were performed on both the samples. Based on these measurements, the texture was analyzed with a particular interest in the gamma fiber. The microtexture of the US Steel cold rolled batch annealed sample was measured by orientation imaging microscopy. A similar study on the strip cast cold rolled batch annealed sample is being performed. Figure 3 shows the (idealized) fiber textures for rolled and annealed steel.

The X-ray pole figure for the two samples is shown in Fig.4. It can be seen from this figure that the pole figures look very similar and both exhibit a prominent gamma fiber, <111> || ND. However, the gamma fiber analysis shows that the fiber intensity is slightly stronger for the conventionally cast US Steel sample. The important point to mention here is that, although US Steel is Al-killed (automotive grade) compared to commercial quality Si-killed strip cast steel, direct cold rolling and batch annealing of the strip cast steel results in moderately strong gamma fiber, with intensity close to the drawing quality US Steel. This is a very encouraging result and shows the potential of the strip cast sheet for demanding applications, given further development of processing methods.

The r-value of the as-cast strip (>0.9) is suggestive of the presence of some γ-fiber, which can be seen from the X-ray pole figure results. The sheet is nearly isotropic, as can be seen from the very small value of Δr. In-line hot rolling with the current process parameters decreases the r-value, which is apparent from the pole figures, and can be explained in terms of the slight increase of {111} intensity and decrease of {100} intensity as compared to the as-cast strip. The cold rolled, batch annealed sample shows significant increase in r-value and there is mild development of gamma fiber, compared to that obtained for Si-killed steels, and is highly encouraging. However, the large anisotropy factor (Δr) suggests that further investigation needs to be done in rolling and annealing schedules to get high r-value, and small Δr. Increasing the amount of cold reduction improves the development of gamma fiber, needed for deep drawing.

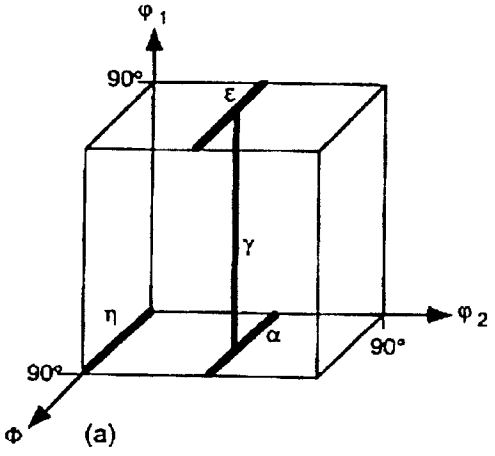

Fiber	Fiber Axis
α-fiber	<110> || RD
γ-fiber	<111> || ND
η-fiber	<001> || RD
ε-fiber	<110> || TD

Figure 3. (a) Diagram of the (idealized) fiber textures for rolled and annealed steel. (b) Table of idealized fibers with Miller indices.

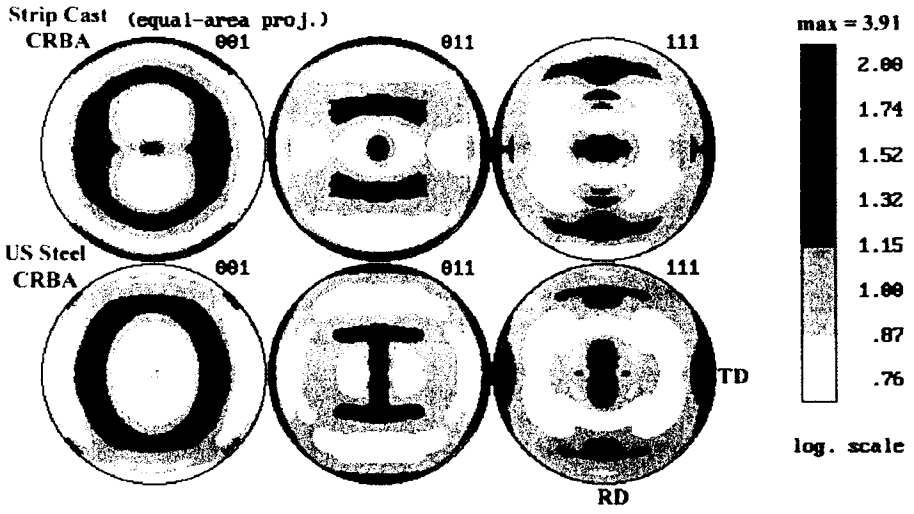

Fig. 4: X-ray pole figure for 70% cold rolled batch annealed strip cast steel and conventionally cast US Steel.

This work indicates that strip cast properties are very sensitive to the thermo-mechanical processing steps that occur after the strip is cast. Thus the achievable properties of material that is strip cast covers a very wide range within a given grade chemistry from very strong [550 MPa (70 ksi) tensile strength] with low ductility (10% total elongation) to lower strength [350 MPa (55 ksi) tensile strength] with improved ductility (50%, total elongation). This is a benefit and a problem as it will prevent strip cast material from being identical to conventionally processed material and may require strip cast grades chemistries to be altered to allow conventional properties to be produced in low carbon aluminum killed grades.

Carbon Steel Strip Cast Potential

This work suggests that:

- Strip casting is technically feasible for Mn-Si killed carbon steels. The application of current technologies to aluminum killed steels may lead to lower productivities than those of a Mn-Si killed steel in a given twin roll machine.
- The surface and internal quality of strip cast sheets has the potential to be better than any previous casting process.
- Strip cast steels are very sensitive to the details of thermo-mechanical processing. The thermo-mechanical processing cycle starts immediately after the liquid steel contacts the mold.

- A wide range of properties are possible from a given grade chemistry. Compared to conventional properties it is possible to expand the window of possible properties by strip casting.
- In order to simplify thermo-mechanical processing, grade chemistry adjustments may be necessary.
- Strip cast material will not necessarily be a blind replacement for currently produced grades.

Issues that cannot be answered at this time are:

- Economics
- Consistency of product
- Acceptance of product in the marketplace

Given the above, it is clear that strip casting is not at this time developed to the point that application of the technology is not without risk. There is great potential for strip casting but many basic questions remain unanswered and there are large technological questions to be answered in the area of thermo-mechanical processing. This work has not found any issue that is a major problem with the technology of strip casting; in fact, this work points out that the potential of strip cast material is to be better than that produced by current technologies. The process is more amenable at this time to production tonnages per year of the order of 500,000 tons and as such will first find niche type applications. This technology is an additional technology for steel production and will be in addition to rather than a replacement for current casting machines.

5. Conclusion

Strip cast low carbon steels are quite unique due to the more rapid processing conditions that occur during twin roll casting. There is a potential for castings produced by this technique to be significantly better in surface and internal quality than any other current casting process. This direct casting process is also the first casting process where the cast surface directly becomes the product surface and the process must produce a casting that is equivalent in geometry to a hot rolled material. This makes the process a combination of a casting and a rolling process.

As the twin roll direct casting process does not mimic the thermo-mechanical processing that a slab encounters in conventional processing, it should be of no surprise that the properties that are encountered in twin roll cast product are substantially different than that of conventionally processed material. It is however noteworthy that strip cast material is amenable to thermo-mechanical processing and combinations of heat treatment and cold reduction can lead to a wide variety in properties from a single chemistry. However, the initial results of this work suggest that the properties that can be

achieved by strip casting from a given grade are not necessarily equivalent to that which can be achieved by conventional processing of the same chemistry. Significant thermal control during casting and coiling and subsequent thermo-mechanical processing will be necessary for strip cast material in order to control properties as the material properties are sensitive to thermal cycling. In addition, to allow conventional properties to be achieved in low carbon steels products, many grade chemistry adjustments will probably be necessary. This will prevent strip cast material from being transparent in the marketplace.

It is clear that strip casting is not at this time developed to the point that application of the technology is risk-free. There is great potential for strip casting but many basic questions remain unanswered and there are significant technological questions to be answered in the area of thermo-mechanical processing. This work has not found any issue that is a major problem with the technology of strip casting; in fact, this work points out that the potential of strip cast material is to be better than that produced by current technologies.

Appendix 1: Composition and surface quality of the strips

1.1 Major issues in surface quality control of the strip cast steel strips

Variations in width and thickness of the strips can be used to characterize their surface quality and dimensional control. This can be benchmarked against the hot-rolled sheet standards to ascertain the quality control in strip casting. Major factors that influence the quality are melt surface stability, solidified shell-roll contact, uniformity of the heat transfer and control systems [Ref. 1.1].

Instability in the melt pool can cause longitudinal non-uniformity in the thickness of the strip. The occurrence of edge serration has also been related to surface active element content of the melt [Ref. 1.2]. Nozzle design is an important issue in controlling the pool level [Ref. 1.3]. Sophisticated feedback and feed forward systems are needed to control the thickness of the cast strip. If the pool level increases then the casting speed must accordingly be increased to decrease the shell-roll contact time [Ref. 1.1].

Surface roughness of the strips is related to the shell-roll contact. A low roughness value would indicate a better contact between the shell and the roll which in turn indicates a higher heat flux.

1.2 Composition and strip dimensions:

Pictures of some of the strip cast material that was analyzed are given in Fig. 1-1 and 1-2. Fig. 1a and 1b show the commercial strip cast material and Fig. 2a and Fig. 2b show the strips which were cast at a pilot caster at British Steel (now Corus™). It can be seen that the commercial material exhibits very good edge control. On the other hand, edge quality in material from the pilot caster is poor. Typical results have been summarized in Table 1-1.

Material	Variation in width
Commercial Caster	± 1 %
British Steel pilot strip caster	± 8 %

Table 1-1: Edge quality control in the strip cast material.

The material from the commercial strip caster was of Mn-Si killed low C (~0.045 %) chemistry. Oxygen was 90 ppm. The composition of the strip cast material from the pilot caster at Corus™ is given in Table 1-2. Note that a range in composition has been given for most of the elements to account for the discrepancies in the chemistry data received from different labs where the material was analyzed. These discrepancies could possibly be due to heavy macrosegregation in the material. In order to facilitate comparison between the properties of strip cast material and traditional hot-rolled material, samples of the latter, obtained from US Steel were also characterized. Its composition has also been given in Table 1-2.

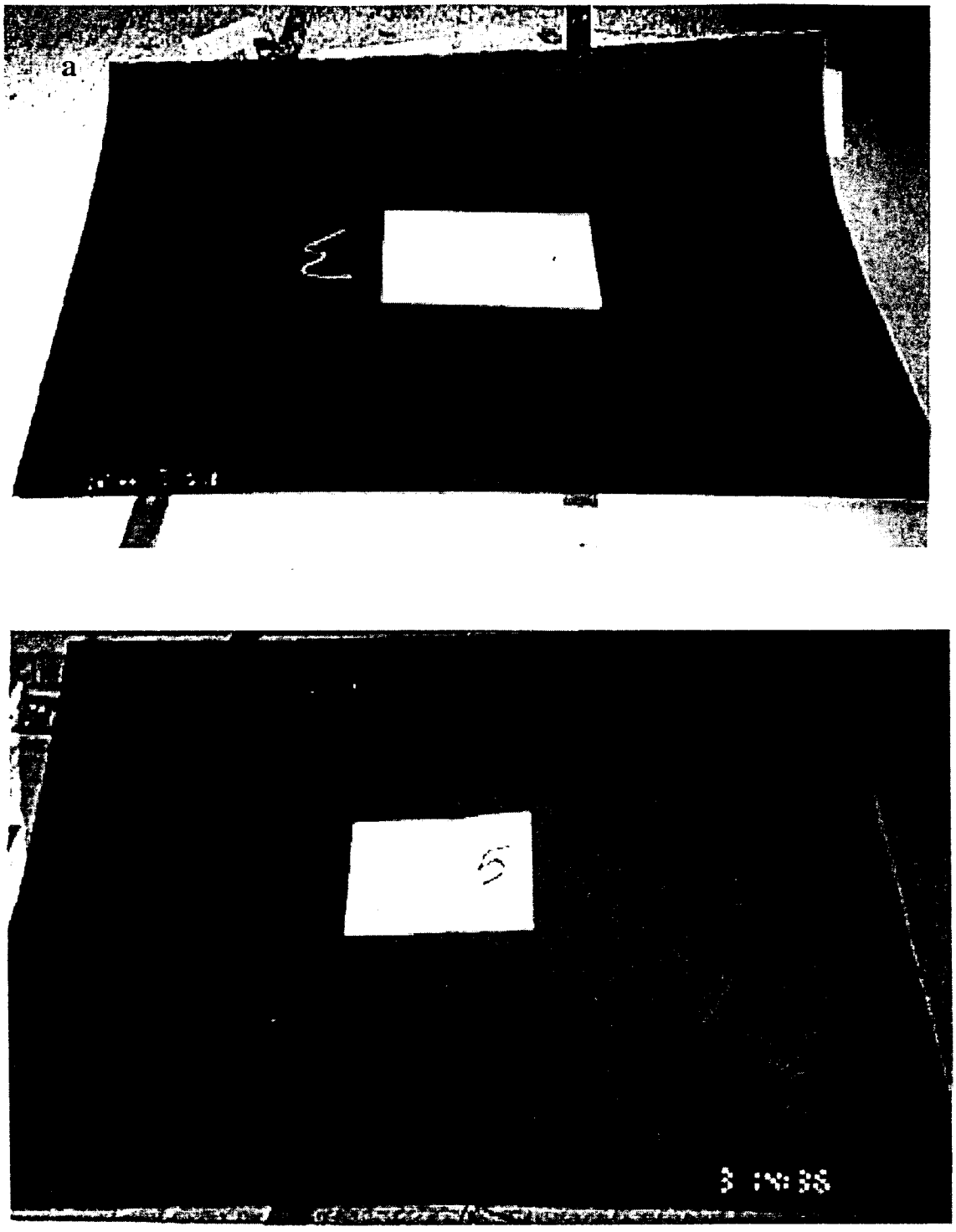

Fig. 1-1 As-cast strip cast material from the commercial caster

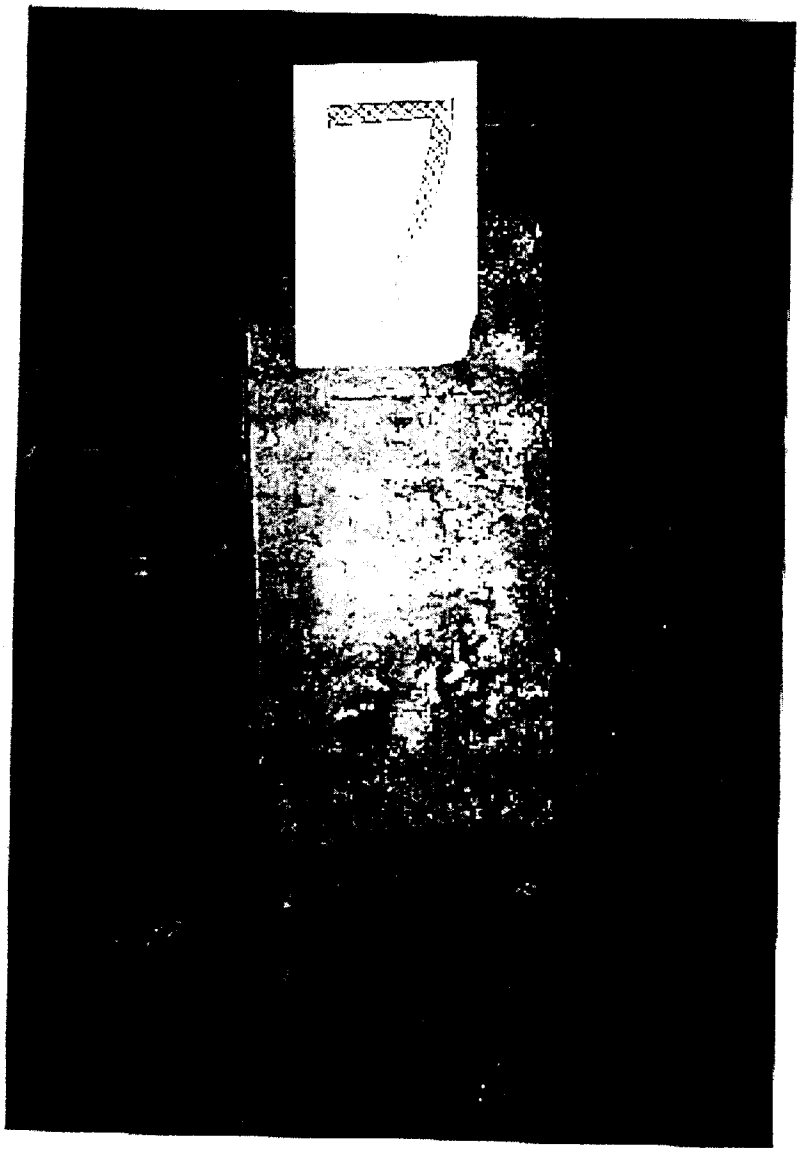

Fig. 1-2a: As-cast strip cast material from the pilot caster at British Steel

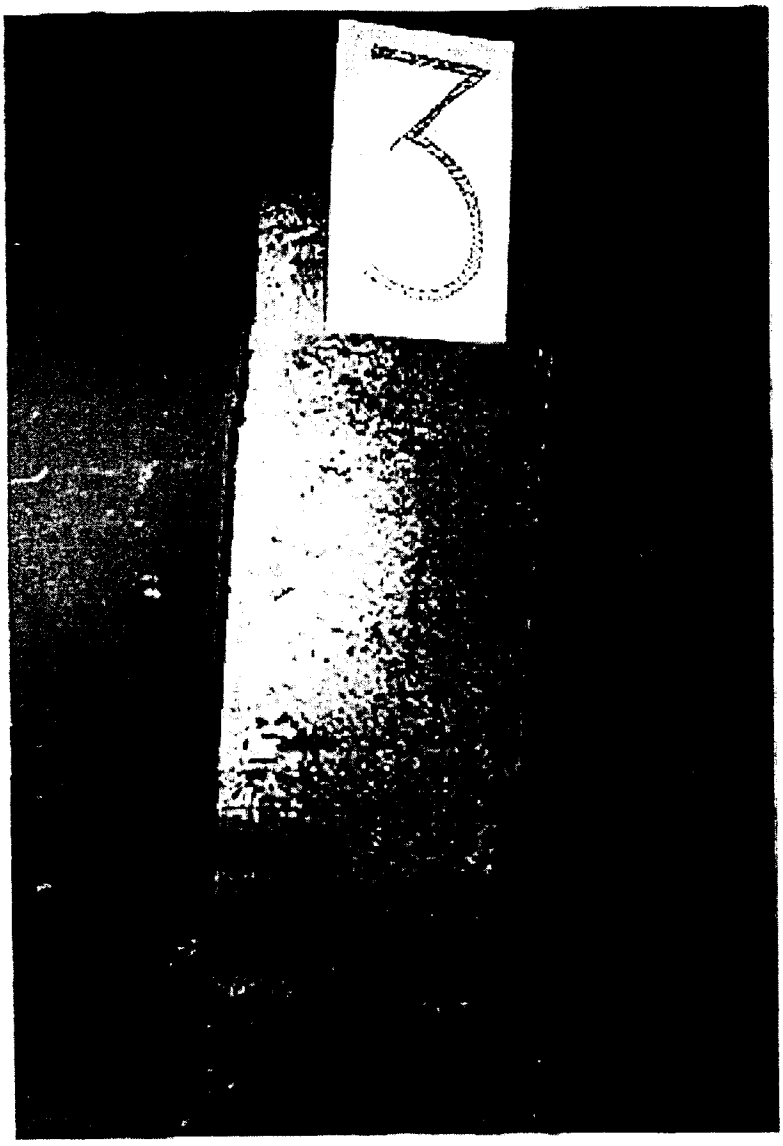

Fig. 1-2b: As-cast strip cast material from the pilot caster at British Steel

Element	Corus ™ Si-killed		Corus ™ Al-killed		US Steel Hot band
	Min	*Max*	*Min*	*Max*	
C	0.041	0.049	.042	0.049	0.040
Si	0.18	0.19	.023	0.028	0.008
Mn	0.49	0.52	0.44	0.47	0.23
P	0.014	0.021	0.012	0.014	0.012
S	0.011	0.014	0.015	0.019	0.009
Cu	0.022	0.024	0.024	0.027	0.016
N	0.0076	0.0081	0.0061	0.0071	0.0030
Total O	0.0274	0.0324	0.0169	0.0226	NA
Total Al	< 0.002		0.008	0.012	0.040

Table 1-2 Composition of material tested in wt. %

Dimensions of the strips used for tests and experiments are given in table 1-3.

Sheet ID	Width (transverse to the rolling direction)	Length (parallel to the rolling direction)	Average Thickness	Crown	Wedge
M31-2	131.5 cm	99 cm	1.973±.0364 mm	58 μm	35 μm
M31-5	131.5 cm	95 cm	1.961±0.049 mm	64 μm	48 μm
M31-6	131.5 cm	102 cm	1.961±0.038 mm	46 μm	41 μm
M31-8	131.5 cm	97 cm	1.973±0.033 mm	18 μm	28 μm
Corus ™ Al-killed*	40 cm (approx.)	150 cm (approx.)	2.31 ± 0.32 mm	300 μm	100 μm
Corus ™ Si-killed*	40 cm (approx.)	150 cm (approx.)	2.68 ± 0.39 mm	450 μm	90 μm

Table 1-3: Dimensions of the steel sheets used for experimentation

* Because of the presence of large number of surface defects and edge serrations, there was a considerable scatter in the thickness data and hence the reported values should be taken only as a guideline.

1.3 Roughness Measurement:

Strips cast sheets from the commercial caster were analyzed for roughness variation. For roughness measurement, samples were taken from various locations on the sheet. Using a HOMMEL T500 surface profile recording device, roughness was characterized by two parameters, arithmetic mean roughness (*Ra)* and maximum profile depth (*Pt)*. A brief description of these parameters is as follows:

1.3.1 Arithmetic mean roughness (*Ra*):

Ra is defined by the equation:

$$Ra = \frac{1}{l_m}\int_0^{l_m} | y | \, dx$$

Where l_m is the length over which the probe was run and y is the roughness profile with waviness filtered out.

1.3.2 Maximum Profile depth (Pt):

Pt is a measure of the waviness on the surface profile and is measured as the distance between two parallel lines which contain the unfiltered profile over the probed distance.

Figure 1-3 further illustrates the difference between the two parameters. Roughness data are given in Table 1-4.

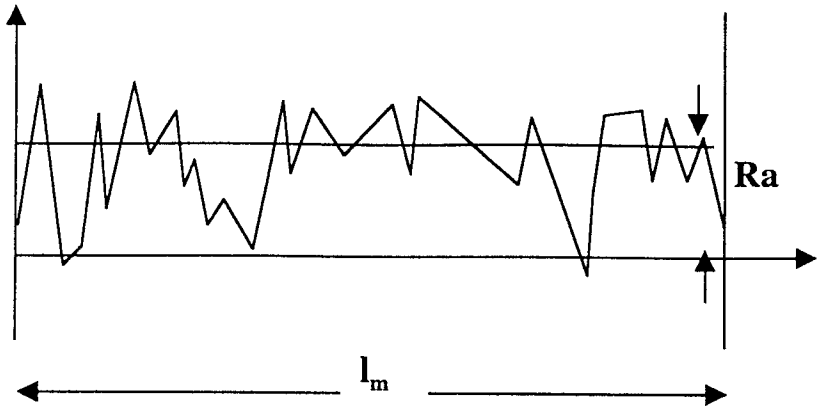

Fig 1-3(a): Filtered Profile of the surface having both waviness and roughness

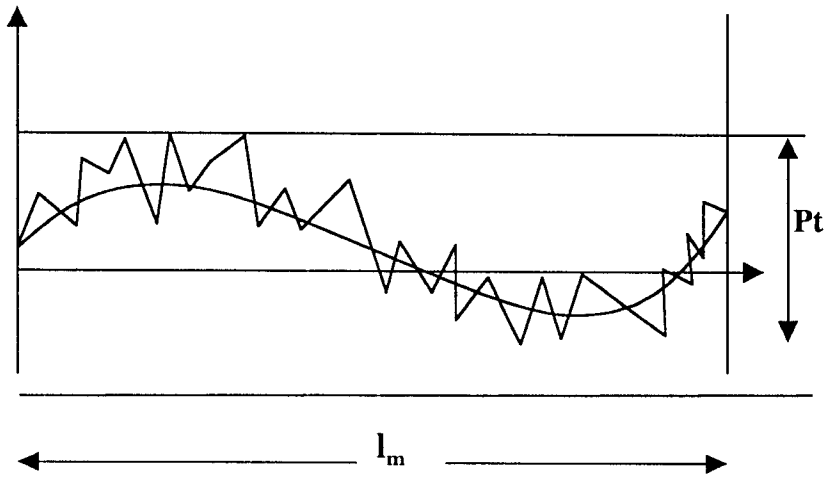

Fig 1-3(b): Unfiltered Profile of the surface with waviness filtered out

ID	Parameter	Location	1	2	3	4	5	Avg. (μm)
1	**Ra**	1st edge	3.33	3.44	4.95	4.09	3.93	**3.95**
	Pt		25.49	26.66	28.97	28.86	29.2	**27.84**
2	**Ra**	1st edge	4.03	3.55	2.81	3.71	3.85	**3.59**
	Pt		26.73	28.1	23.66	31.89	30.07	**28.09**
3	**Ra**	1st edge	3.01	2.81	1.92	3.5	3.51	**2.95**
	Pt		22.52	22.24	33.41	20.83	24.19	**24.64**
4	**Ra**	Center	2.5	3.36	2.85	2.34	2.51	**2.71**
	Pt		23.37	20.45	20.44	20.6	16.34	**20.24**
5	**Ra**	Center	3.44	3.11	2.34	1.85	3.45	**2.84**
	Pt		17.33	21.92	17.14	17.58	23.32	**19.46**
6	**Ra**	Center	3.49	3.89	4.03	2.54	3.84	**3.56**
	Pt		23.17	31.26	25.86	18.94	24.12	**24.67**
7	**Ra**	2nd edge	1.69	2.54	1.78	1.90	2.04	**1.99**
	Pt		21.65	25.65	27.65	30.23	21.20	**25.28**
8	**Ra**	2nd edge	1.96	2.18	1.77	1.98	1.7	**1.92**
	Pt		23.65	24.81	27.28	21.27	23.1	**24.02**
9	**Ra**	2nd edge	2.05	2.58	2.01	2.43	2.89	**2.39**
	Pt		30.88	32.59	38.52	36.11	35.30	**34.68**

Table 1-4: Roughness values for the material from the commercial strip caster

Surface quality was better away from the edge with Ra in the range 2-3 μm. BHP has reported values even lower than this, between 1.5-2.0 μm. Strips from hot strip mill have Ra in the range 1.0-1.5 μm. Cold rolling reduces Ra to well below 0.5 μm.

1.4 Gauge Measurement

A good indicator of a well-controlled strip casting process is a constant thickness of the strip. The gauge of the strips was measured to analyze the thickness control of the process. Thickness was measured at more than 100 points, nearly equi-spaced, along the width of the strips. Typical results have been tabulated in Table 1-5 below and plotted in Figure 1-4. It was generally observed that most of the deviation occurred near the edges. An interesting way to analyze this is to take away some data points from close to the edges and note the effect it has on the standard deviation of the thickness data of the strip. It was found that if the edges were trimmed by about 4 % of the total width, thereby reducing the yield of the process, a decrease in the standard deviation from 40 μm to 15 μm would be obtained, as shown in Figure 1-5.

Point Number	Thickness (mm)	Point Number	Thickness (mm)	Point Number	Thickness (mm)	Point Number	Thickness (mm)
1	1.75	11	1.968	21	1.956	31	1.963
2	1.877	12	1.975	22	1.96	32	1.961
3	1.945	13	1.974	23	1.962	33	1.954
4	1.945	14	1.968	24	1.963	34	1.959
5	1.96	15	1.973	25	1.971	35	1.958
6	1.95	16	1.979	26	1.969	36	1.957
7	1.95	17	1.976	27	1.966	37	1.962
8	1.955	18	1.989	28	1.963	38	1.965
9	1.957	19	1.977	29	1.971	39	1.96
10	1.976	20	1.965	30	1.962	40	1.972

Point Number	Thickness (mm)	Point Number	Thickness (mm)	Point Number	Thickness (mm)	Point Number	Thickness (mm)
41	1.971	61	1.982	81	1.95	101	1.937
42	1.957	62	1.975	82	1.957	102	1.98
43	1.967	63	1.977	83	1.949	103	1.992
44	1.961	64	1.976	84	1.955	104	1.939
45	1.972	65	1.984	85	1.948	105	1.81
46	1.959	66	1.978	86	1.941	106	1.692
47	1.971	67	1.991	87	1.934		
48	1.969	68	1.981	88	1.951		
49	1.959	69	1.978	89	1.952		
50	1.964	70	1.964	90	1.949		
51	1.97	71	1.974	91	1.934		
52	1.961	72	1.969	92	1.93		
53	1.971	72	1.968	93	1.936		
54	1.969	74	1.971	94	1.936		
55	1.967	75	1.954	95	1.931		
56	1.976	76	1.955	96	1.944		
57	1.975	77	1.952	97	1.945		
58	1.979	78	1.95	98	1.944		
59	1.987	79	1.952	99	1.932		
60	1.985	80	1.952	100	1.931		

Table 1-5: Thickness of the strips was measured at many nearly equi-spaced points along the width of the strips (normal to the rolling direction)

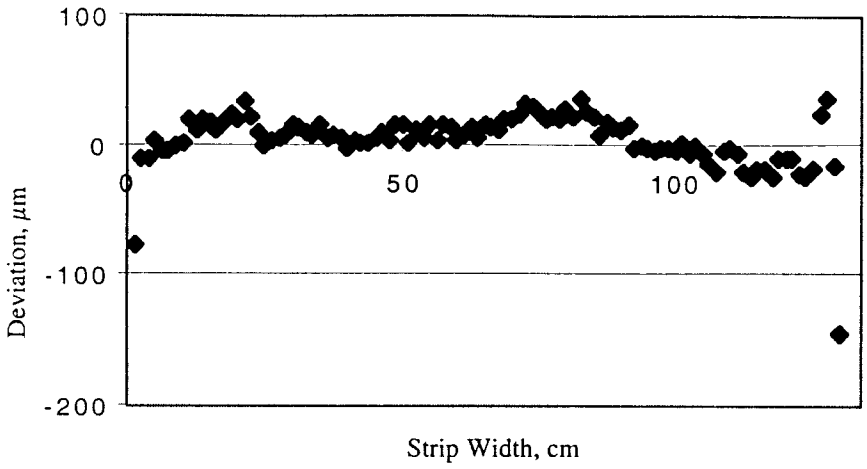

Figure 1-4: Deviation of thickness from the average thickness plotted for the whole strip width. Major deviations occur near the edges.

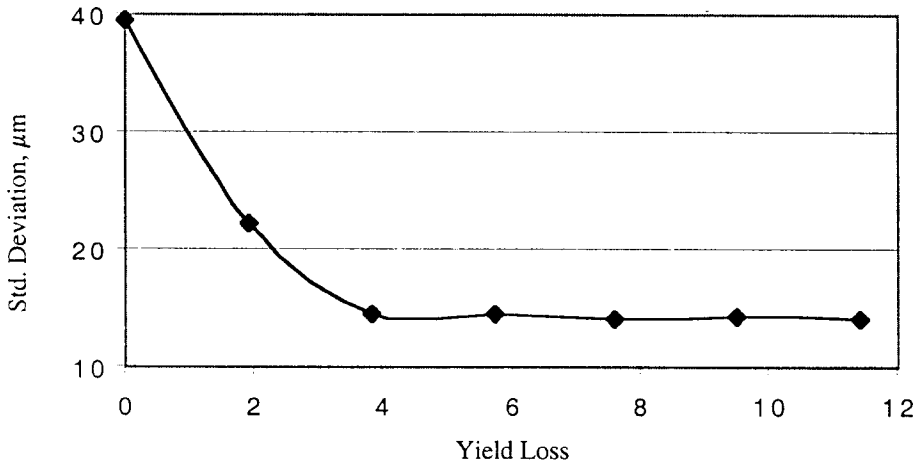

Figure 1-5: Effect of cutting of strip near the edges on the standard deviation in the thickness.

Reference:

1.1 Alan W. Cramb, *Strip Casting of Steels: Current status and fundamental aspects*, Proceedings of the international symposium on near-net-shape casting in the Minimills, Canadian Institute of Mining, Metallurgy and Petroleum, 1995, pp. 355-372.

1.2 Ali Kalkanli, John V. Wood, and Nicholas Braithwaite, *Melt Instabilities and the effect of surface tension on preventing edge serrations in melt overflow alloy strip casting*, ISIJ International, Vol. 38, 1998, no. 2, pp. 142-148. pp. 689-695.

1.3 Shigeru Miyake, Hiroshi Yamane, Massao Yukumoto and Michiharu Ozawa, *Strip quality of highly alloyed metals by twin roll casting*, ISIJ International, Vol. 31, no. 7, 1991,

Appendix 2 – Microstructure and Solidification structure

2.1 Microstructure & Solidification Structure

Strip cast material was analyzed for solidification structure. Solidification structure of an alloy gives information about the extent of segregation that occurred during solidification.

The strip cast material from both commercial and pilot casters were analyzed for microstructure by chemical etching. Transverse and longitudinal sections were cut from near the center and edge of the strips.

As-cast structure assumes greater importance for strip casting because of the absence of reheating stage which can possibly alter the as-cast structure. As the metal is solidified during strip casting, it is cooled from both sides. Columnar dendrites grow in the direction opposite to that of heat flow, *i.e.*, from the edges towards the center. These columnar dendrites may run all the way up to the center line of the strip or they may terminate before that with an equi-axed crystal zone occupying the center. The presence of equi-axed zone can actually reveal information about the control of the solidification during the casting process. As the following figure 2-1 illustrates, formation of an equi-axed crystal zone at the center indicates that solidification was not complete at the kissing point. Clearly, it indicates that rate of heat transfer was not compatible with the casting speed and strip width.

Nital was used to delineate the ferrite grain boundaries of the material. 2% Nital, i.e., 2% HNO_3 in a methanol solution, was found to be suitable for chemistry of the strips.

A hot Picral etch was used to observe the solidification structure. The composition of the etch was: 2 g picric acid, 100 ml. distilled water, 1 drop of teepal detergent and 1 drop of HCl. Etching was done at 45° C.

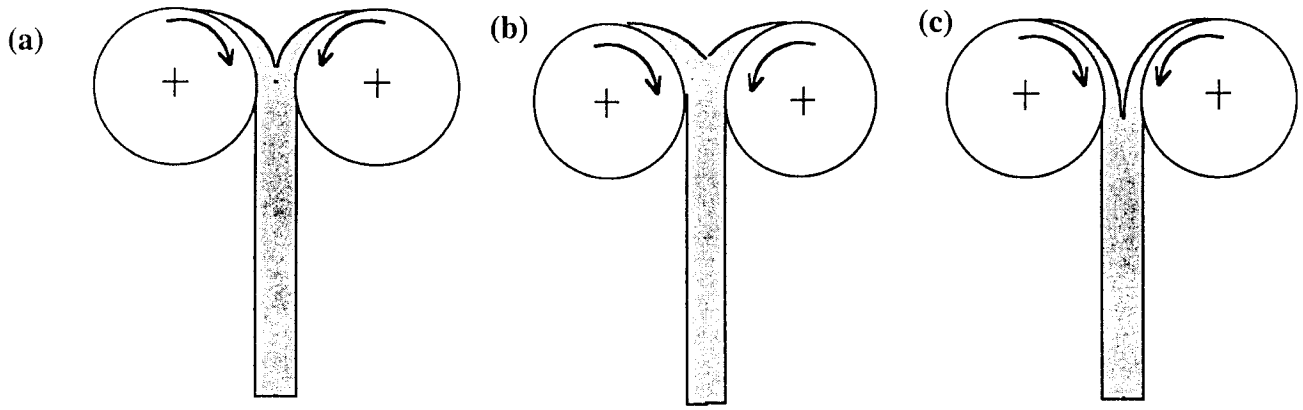

Fig. 2-1: Schematic illustration of solidification in strip casting. Solidification must be finished at the kissing point as shown in (a). If it finishes before that, as in (b), or if the liquid phase is carried beyond that as in (c) then the product will show non-uniformity.

2.2 Commercial strip cast material:

Carbide morphology was revealed using a 4% picral etch (Fig. 2-2, 2-3). Hot Picric Etch was very effective in revealing the columnar growth in these samples (Fig. 2-4, 2-5). The centerline was heavily etched, which can be associated with interdendritic liquid flow caused by the roll force. The columnar grains are inclined to the sheet normal.

The as-cast structure of strip cast material shows acicular ferrite structure along with a few polygonal ferrite grains as shown in Fig. 2-6 to 2-8. It is different from the hot strip structure which is composed of fine equiaxed ferrite. The structure was quite uniform throughout the cross section. No variation in structure was observed in longitudinal and transverse directions in the as-cast microstructure. Thus from the solidification and microstructure it can be concluded that heat transfer was well controlled.

Fig. 2-9 and 2-10 show pictures of pores in this material. Pores were found majorly at the centerline and their size was in a few microns.

2.3 British Steel material:

British Steel material had more non-uniform carbide distribution as shown in Fig. 2-11. Solidification strucuture as shown in Fig., 2-12 to 2-16 also reflects an uneven heat transfer and equiaxed sone in the center. As mentioned above, presence of equi-axed zone imply that solidification was not complete at the kissing point. The as-cast structure revealed by nital shows polygonal ferrite grains throughout the cross-section with finer grains near the edges, and coarser in the center. Si-killed steel has finer grains compared to Al-killed grade, suggesting some sort of grain refinement induced in the material (Fig. 2-17 and 2-18). A peculiar tendency of banding was observed in all the British Steel samples near the edge, which is not currently understood. British Steel material exhibits more porosity than the commercial strip cast material as shown in Fig. 2-19 and 2-20. Inclusions can also be observed in the unetched samples. Out of the two types of materials from British Steel, the inclusion and porosity distribution in Si-killed British steel sheet is more random and uniformly dispersed compared to the Al-killed grade, which shows more concentrated defects.

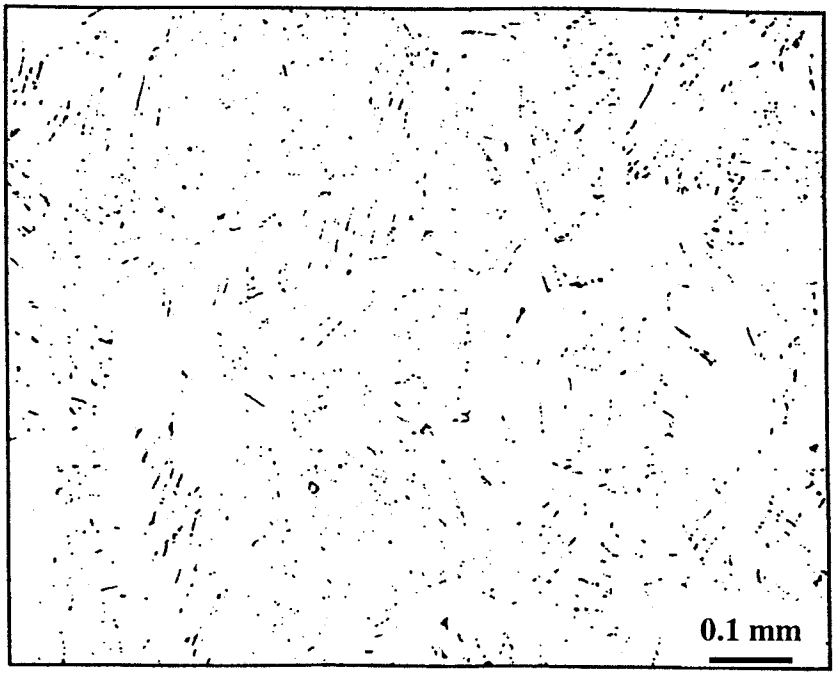

Figure 2-2: Commercial strip cast material: longitudinal section showing carbide morphology 4 % picral, 100x

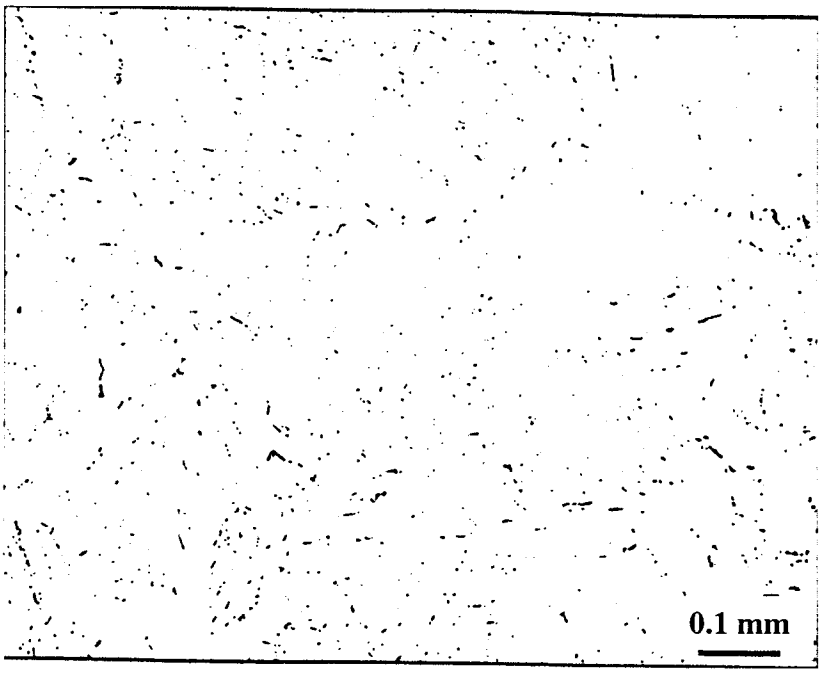

Figure 2-3: Commercial strip cast material: transverse section, carbide morphology. 4% picral 100x.

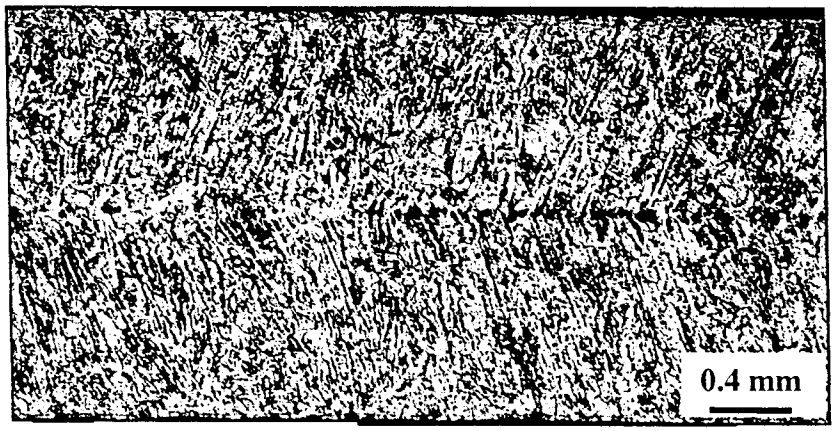

Figure 2-4: Commercial strip cast material: longitudinal section - Columnar and acicular ferrite structure, black spots in center are due to both segregation and porosity, Hot Picric etch, 25x

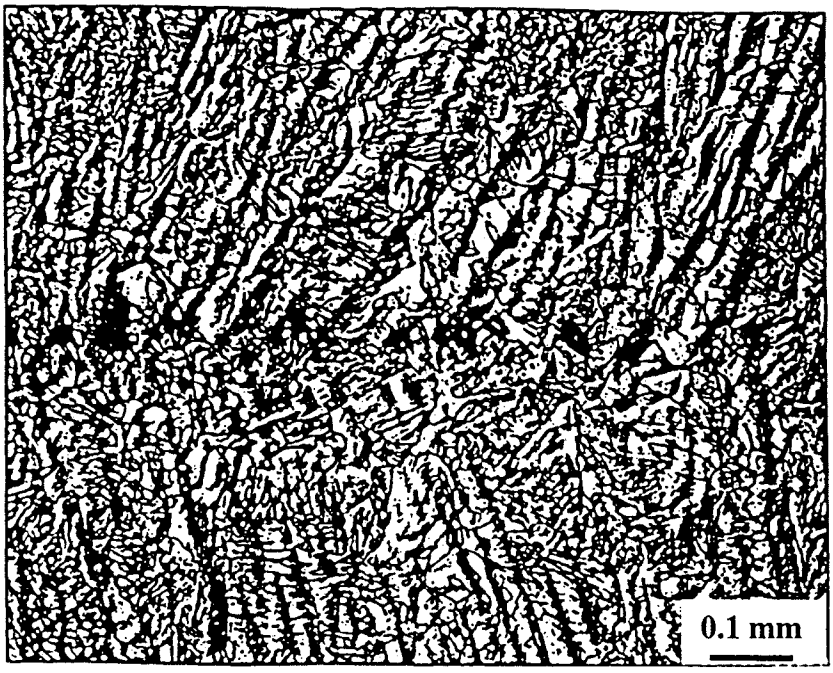

Figure 2-5: Commercial strip cast material: longitudinal section - Columnar and acicular ferrite structure, black spots in center are due to both segregation and porosity, Hot Picric etch, 100x.

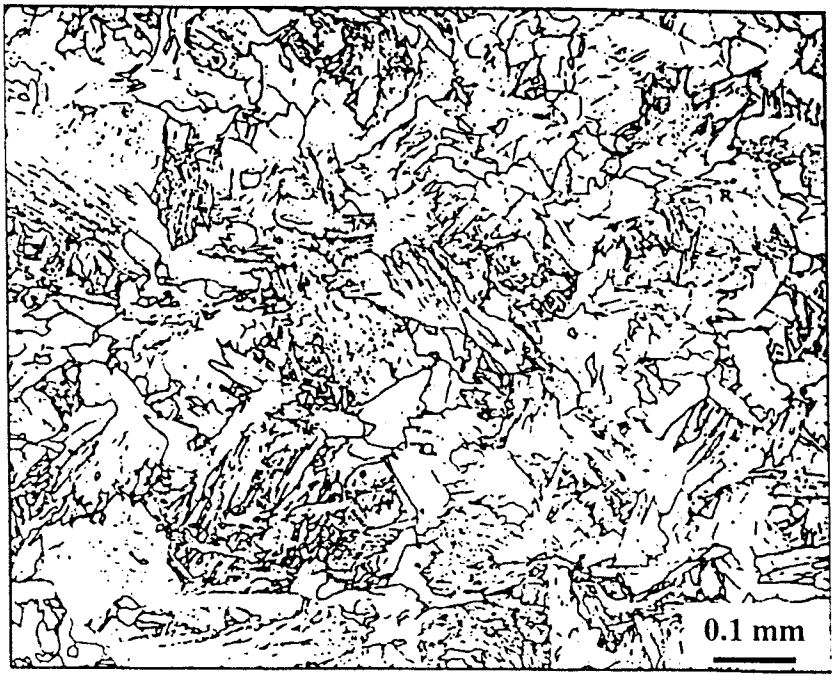

Figure 2-6: Commercial strip cast material: transverse section, acicular ferrite microstructure, 2% Nital etch, 100x

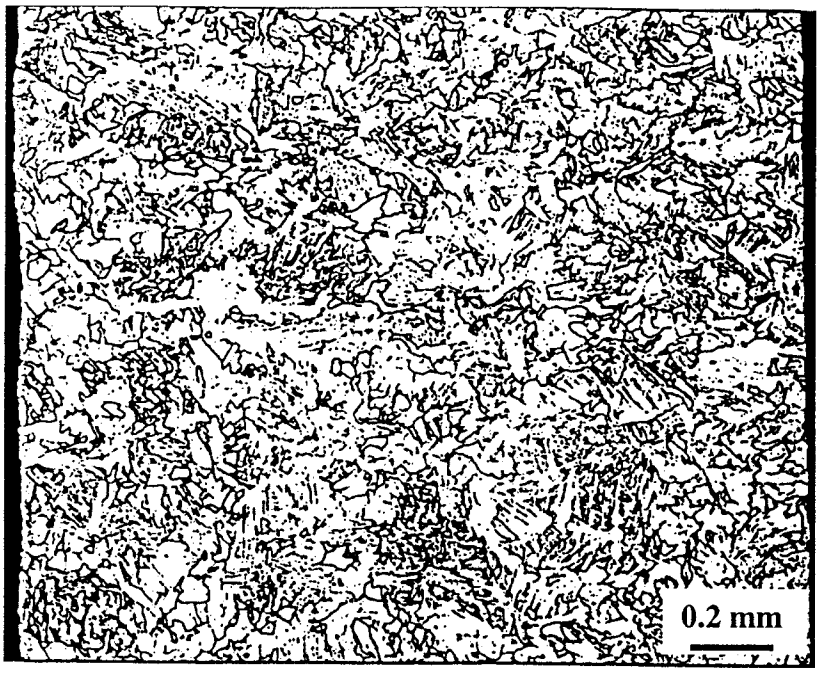

Figure 2-7: Commercial strip cast material: transverse section, acicular ferrite microstructure, 2% Nital etch, 50x

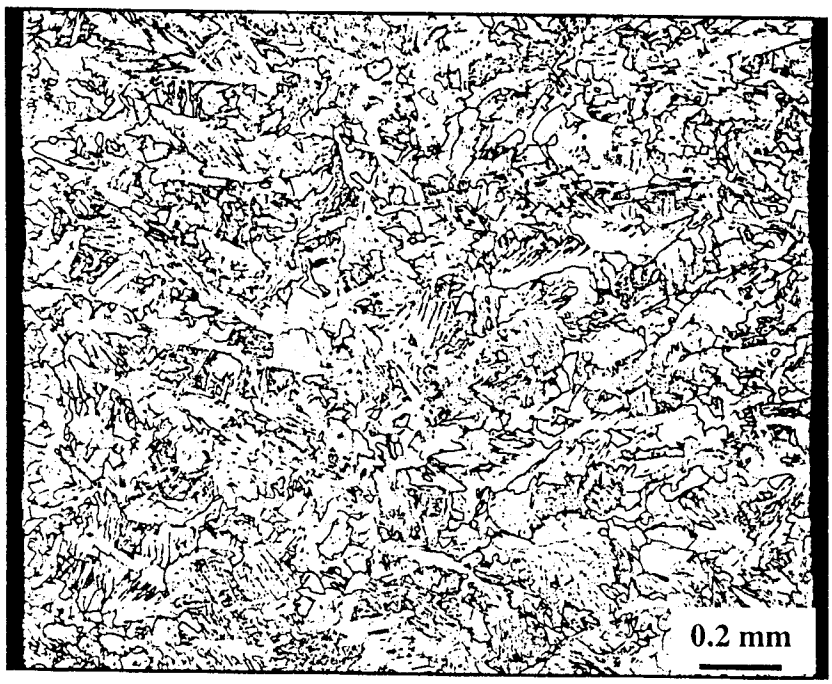

Figure 2-8: Commercial strip cast material: longitudinal section, acicular ferrite microstructure from Edge to Center to Edge. 2% Nital etch.

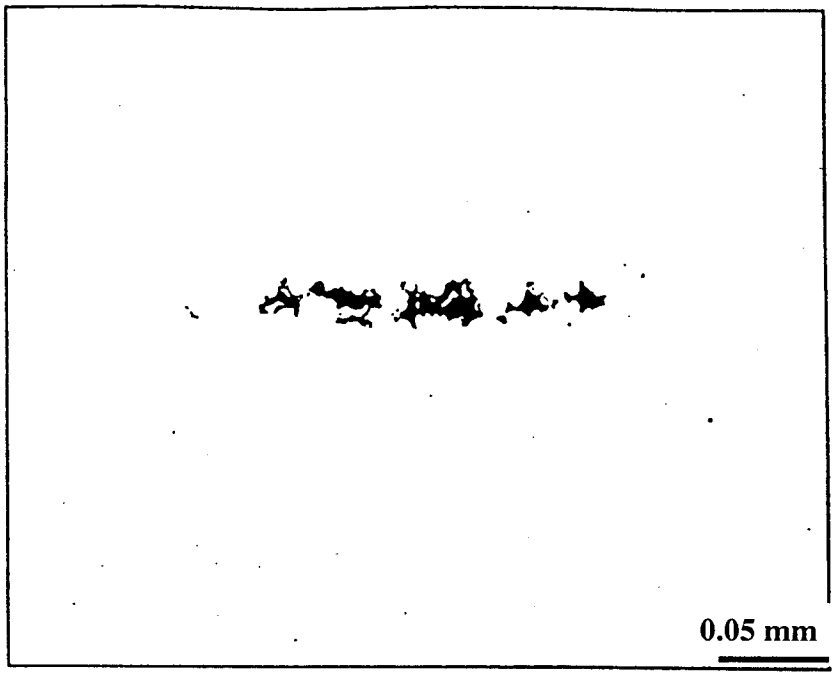

Figure 2-9: Commercial strip cast material: longitudinal section, slight porosity along the centerline, unetched 200x.

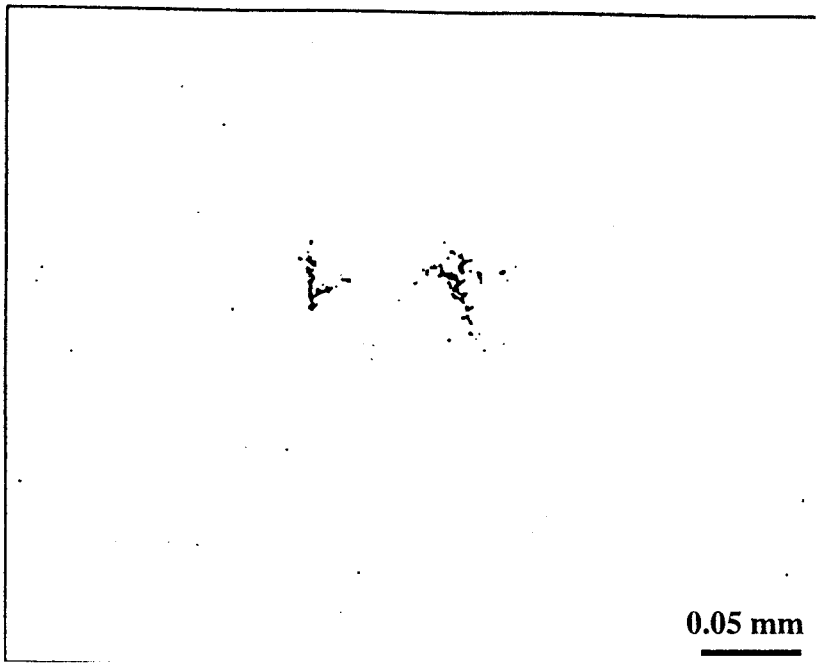

Figure 2-10: Commercial strip cast material: Transverse section, Slight Porosity along the centerline, unetched 200x.

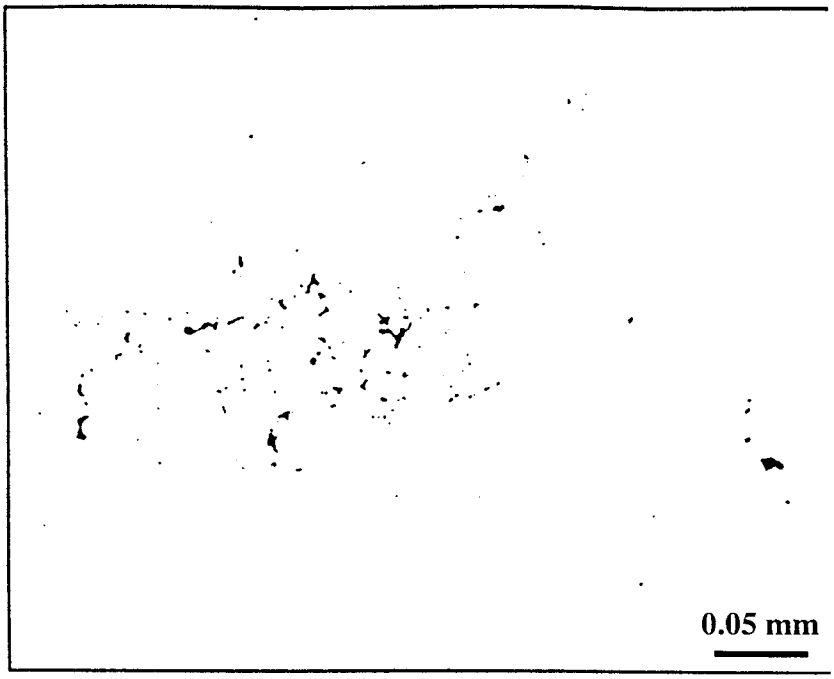

Figure 2-11 British Steel Low Carbon Steel Strip Cast Material - longitudinal section; Al-killed- Inclusions and porosity throughout the material, Unetched 200x

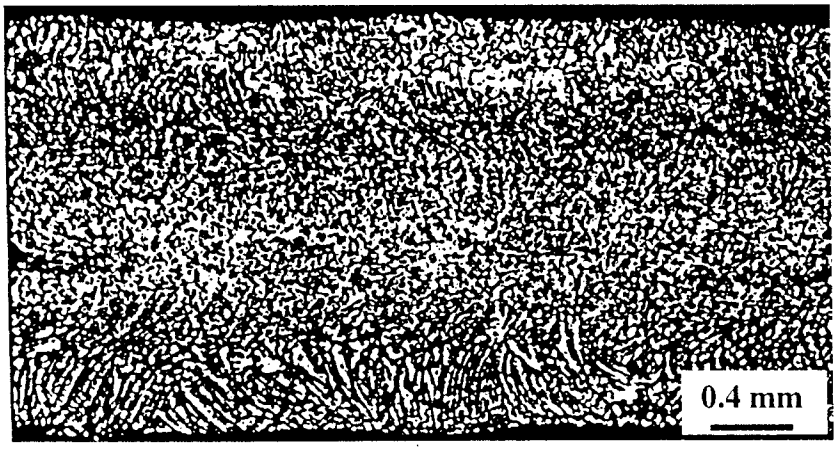

Figure 2-12: British Steel Low Carbon Steel Strip Cast Material –Longitudinal Section; Si Killed – As-Cast Solidification Structure – 25x

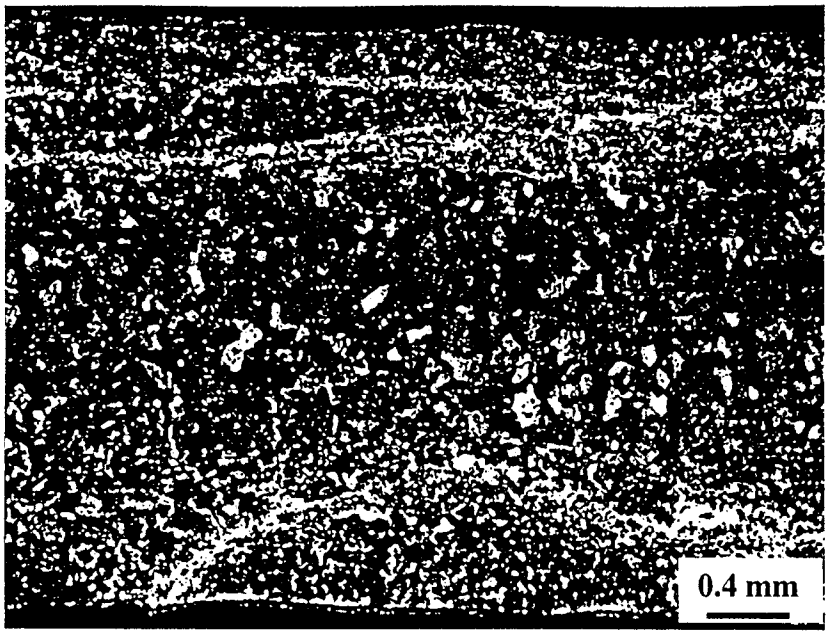

Figure 2-13: British Steel Low Carbon Steel Strip Cast Material – Transverse; Al killed- As-Cast Macro Structure – Oberhoffer's Reagent – 25x

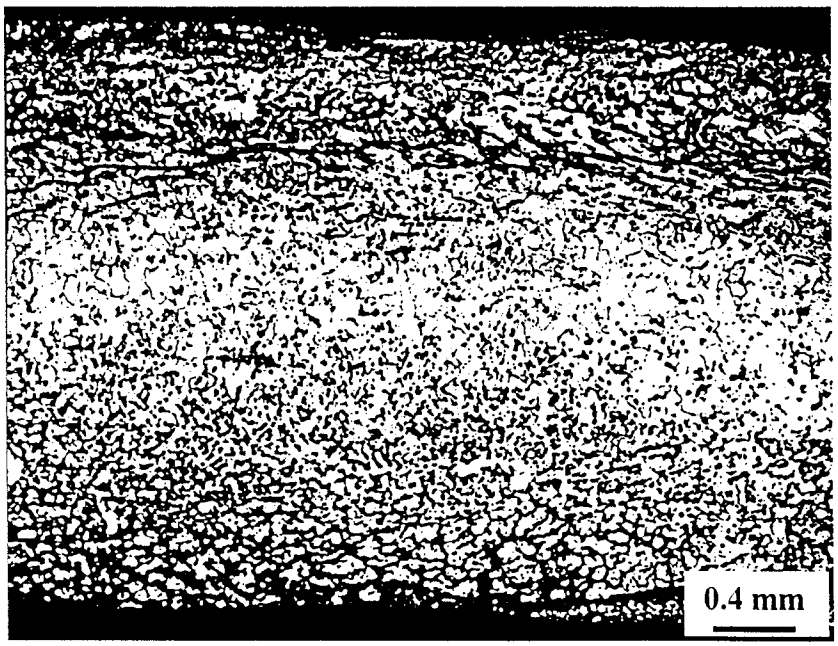

Figure 2-14: British Steel Low Carbon Steel Strip Cast Material – Longitudinal section, Al killed As-Cast Solidification Structure- Hot Picric Acid Etch- 25x

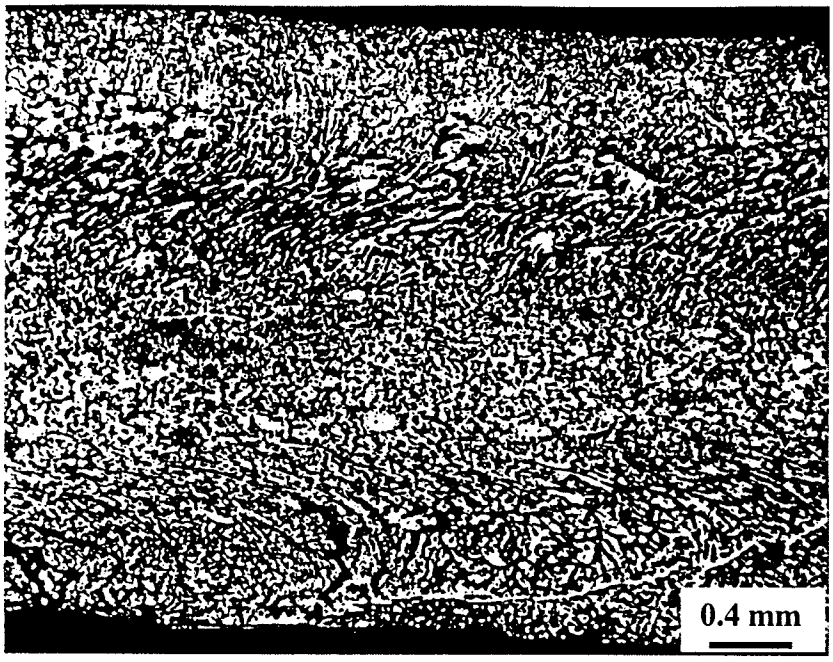

Figure 2-15: British Steel Low Carbon Steel Strip Cast Material –Longitudinal Section; Si Killed – As Cast solidification Structure – Hot Picric Acid Etch –25x

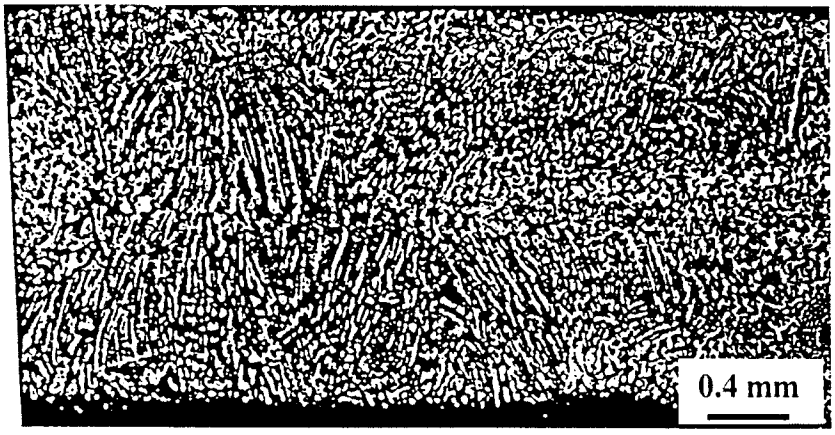

Figure 2-16: British Steel Low Carbon Steel Strip Cast Material –Transverse Section; Si Killed – As Cast Solidification Structure – Hot Picric Acid Etch – 25x

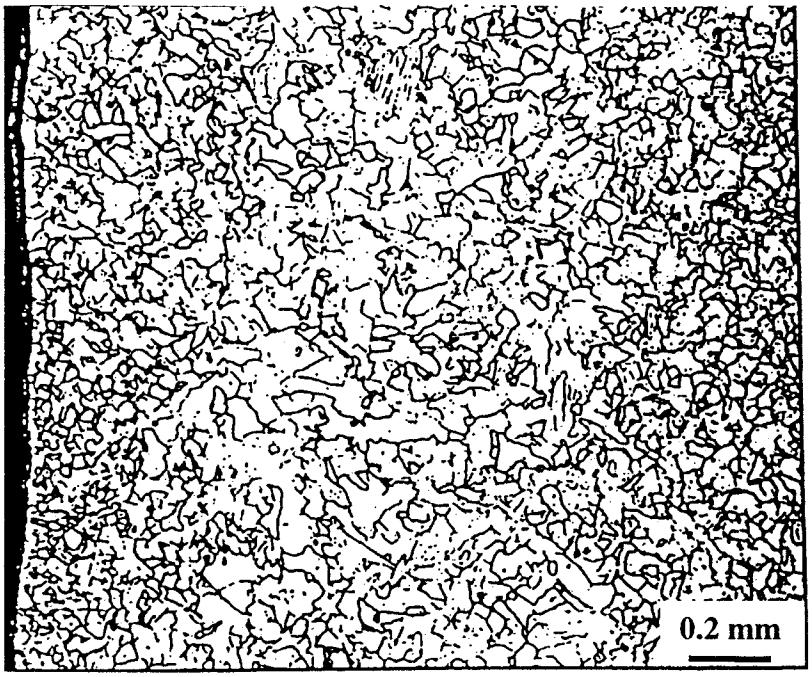

Figure 2-17: British Steel Low Carbon Steel Strip Cast Material – Longitudinal Section; Si killed – Grain Structure from Edge – Center – Edge – 2% Nital – 50x

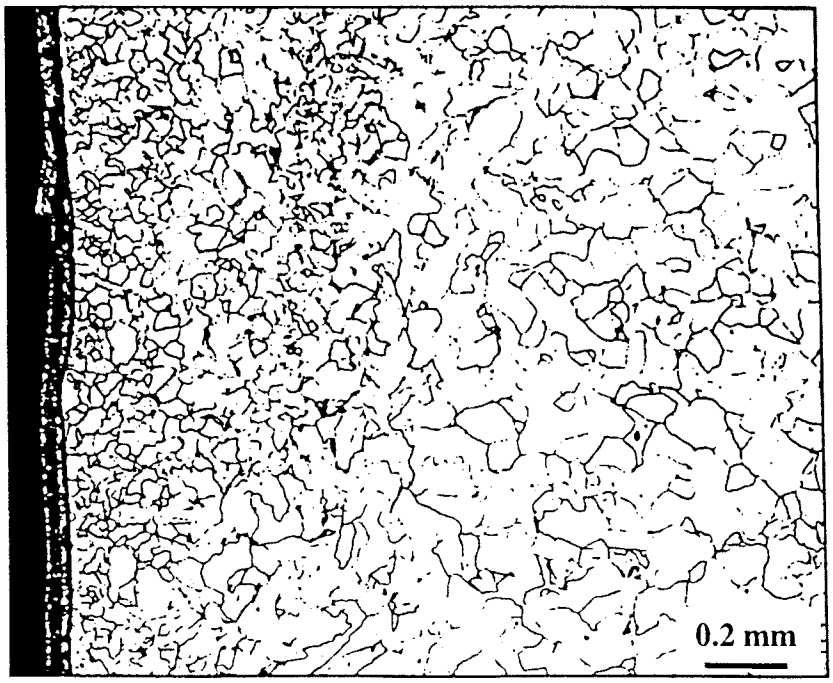

Figure 2-18: British Steel Low Carbon Steel Strip Cast Material – longitudinal section; Al killed- Grain structure from edge to Center Thickness – 2% Nital – 50x

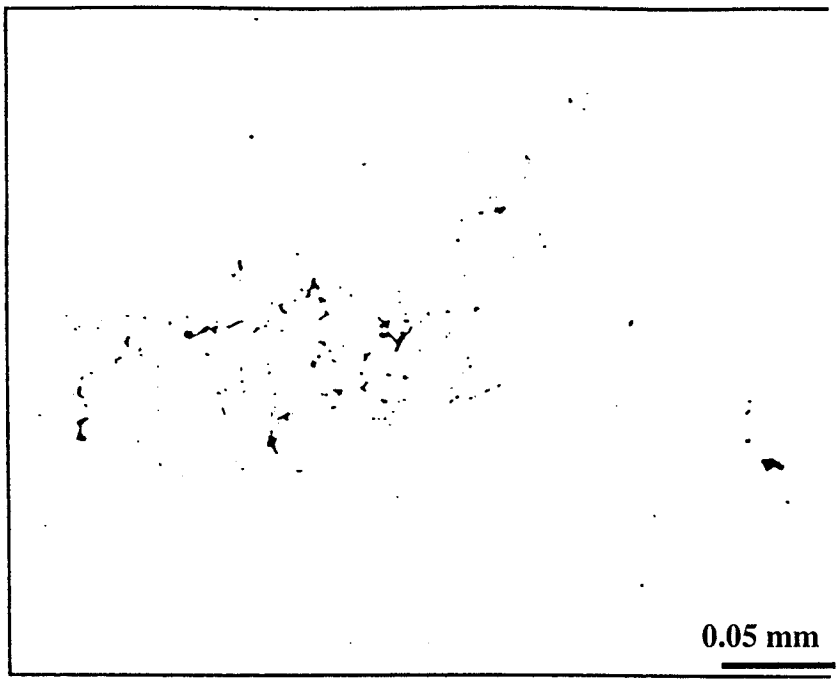

Figure 2-19: British Steel Low Carbon Steel Strip Cast Material - longitudinal section; Si-killed- Inclusions and porosity throughout the material, Unetched 200x

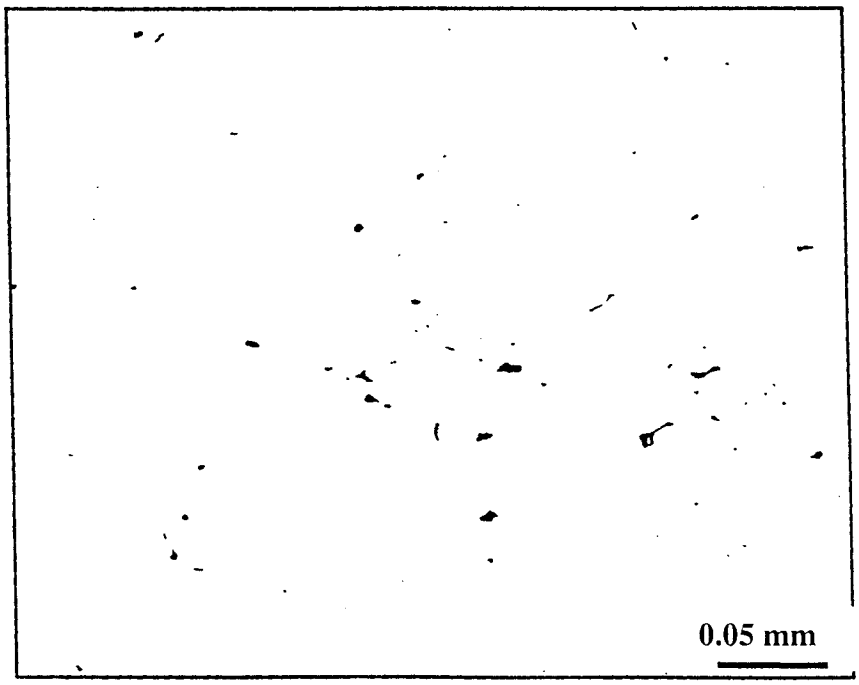

Figure 2-20: British Steel Low Carbon Steel Strip Cast Material- Longitudinal; Al Killed – Inclusions & Porosity throughout the Sample – Unetched – 200x

2.4 Inclusions and porosity

Strip cast material was analyzed for the inclusion content. First the slime method was tried where attempts were made to electrolytically dissolve the metal into a solvent and subsequently separate the inclusions by filtering the solvent. However after a few unsuccessful attempts with HCl and $FeCl_3$ solutions, this approach was aborted. The problem was in finding a solvent that would selectively dissolve the metal but not the inclusions.

Finally, scanning electron microscope (SEM) equipped with an energy dispersive system (EDX) was employed for examining inclusion content of the steel. Before examination, strip cast samples were polished on SiC polishing papers upto 1200 grit and then on 6 μm and 1 μm diamond paste. The samples were then observed under SEM. A back-scattered electron detector was employed for better contrast between the inclusion and matrix. EDX facilitated the chemical analysis of the inclusions. A typical SEM picture is given in Figure 2-23. It can be seen that while there are only a few big (>1 μm) inclusions, there is large number of small inclusions.

After SEM pictures were obtained, they were analyzed using the NIH image analyzer. There the digital image was processed to enhance the contrast between the matrix and the inclusions, thus the inclusions were identified and their sizes were determined.

Predominantly, two types of inclusions were observed in the system: (i) Mn-Si-O type (Figure 2-21) and (ii) Mn-Si-O type containing Al-O precipitates (Figure 2-22).

The inclusion size distribution of the strip cast material is given in Figures 2-24 and 2-25. Inclusion volume fraction was much higher for British Steel material as compared to the commercial material. While the percentage of area occupied by inclusions in the cross section was 0.18% for commercial material, it was 0.85% for British Steel material. Inclusions are of finer size in British Steel material compared to that from commercial caster.

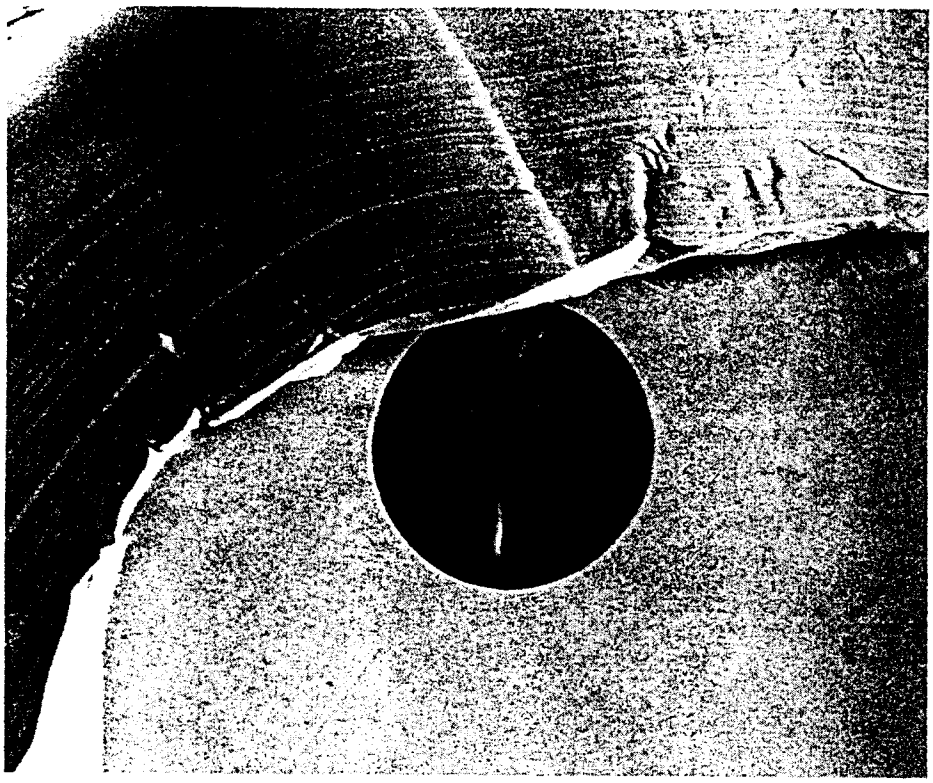

Figure 2-21: An inclusion in the Commerical strip cast material showing two phases.

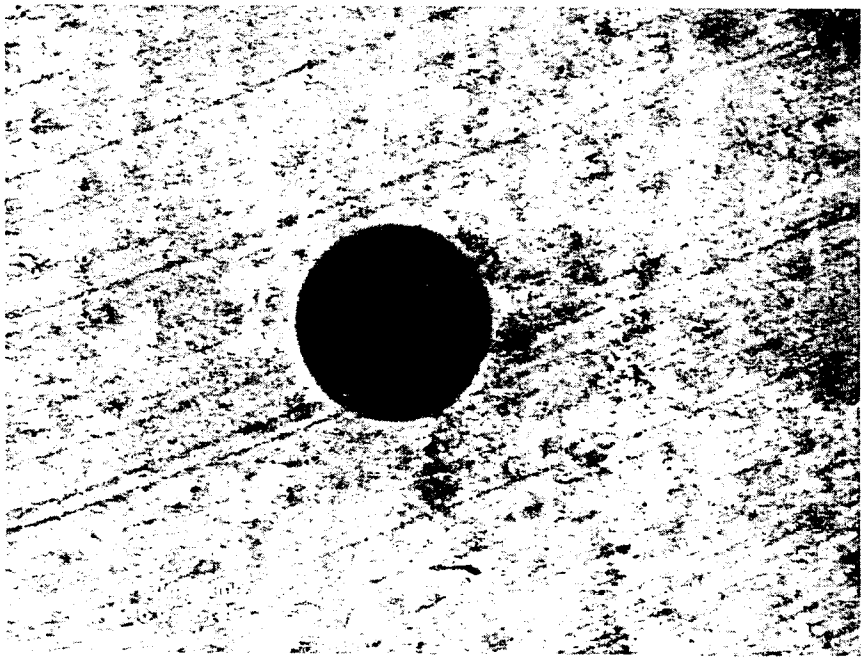

Figure 2-22: SEM picture of Mn-Si-O inclusion

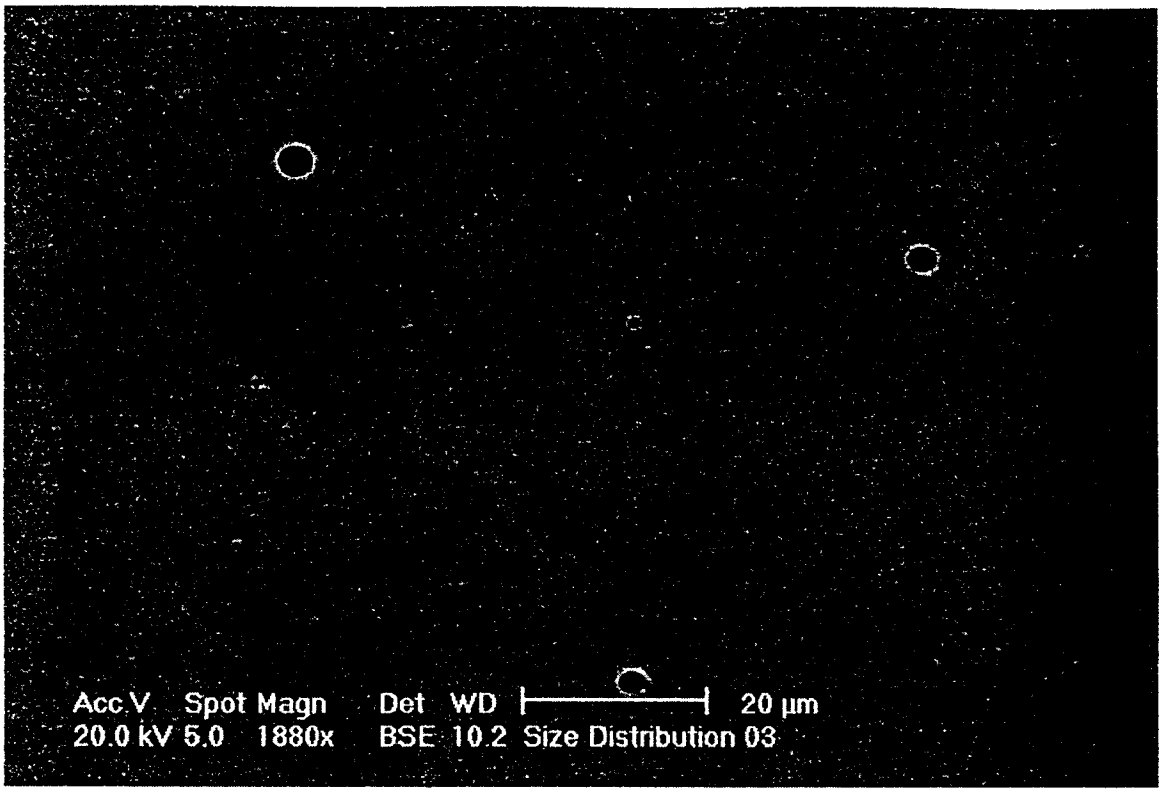

Figure 2-23: SEM picture of metal in Back Scattered Electron Mode

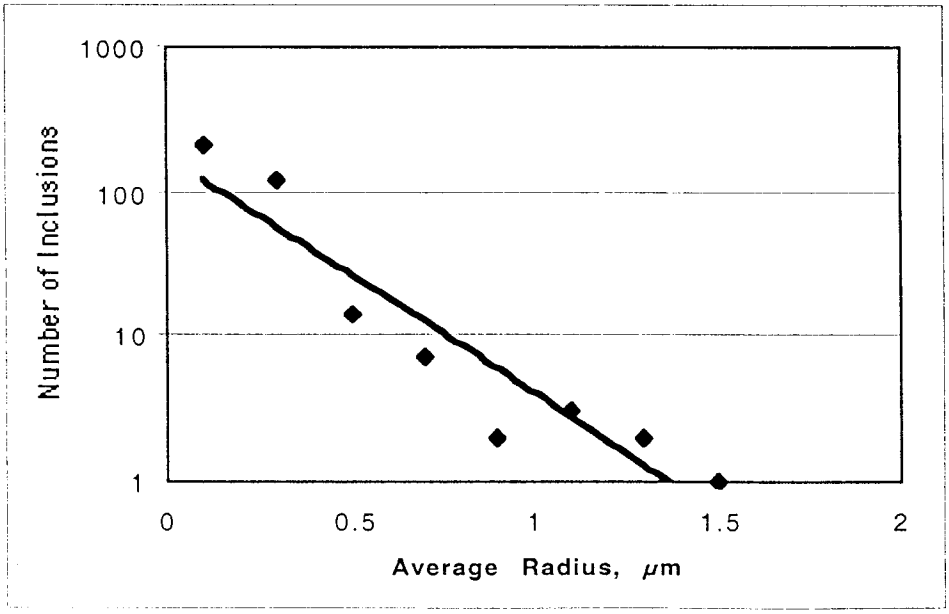

Figure 2-24: Inclusion size distribution of Commercial Strip Cast Material

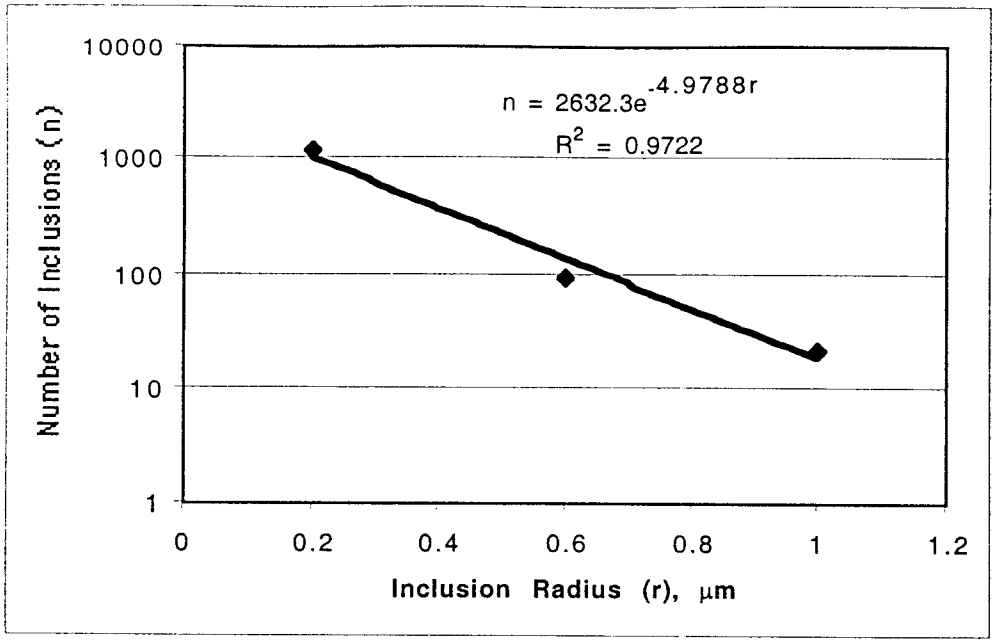

Figure 2-25: Inclusion Size Distribution of British Steel Mn-Si killed material

2.5 Determination of Secondary dendrite arm spacings:

More insight into the process control can be had by looking into the secondary dendrite arm spacing (DAS). Secondary DAS provide a good measure of cooling rate and structural refinement. Solidification structure showing secondary DAS is revealed by chemical etching due to the presence of segregating elements like phosphorus. However the strip cast materials under investigation have very low phosphorus content. Add to this is the fact that the carbon level is very low too. It results into elements getting re-segregated during δ to γ and γ to α transformation and thus the segregation caused during liquid to solid solidification, which reflects the cooling rate, becomes difficult to observe. Due to the difficulties mentioned above in measurement of secondary DAS, calculations based on solidification theory were made.

The heat transfer was modeled using PROCAST. The system was conceived as below:

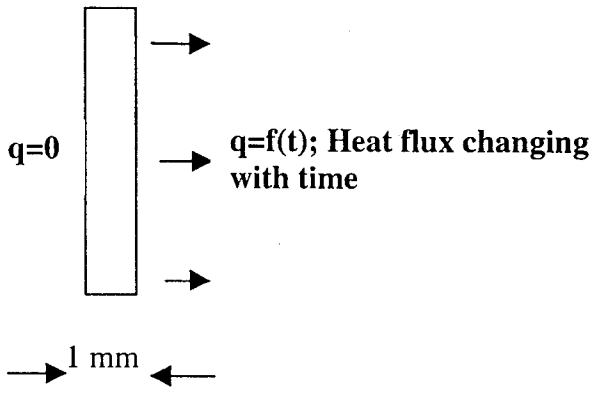

Figure 2-26: Schematic representation of the one-dimensional model of the heat transfer

Thermal Gradients and Growth Velocity calculated from the model were further used to find Seconday DAS and homogenizing time-temperature curves.

Primary DAS were calculated from the model using the following equation (Ref. 2.1),

$$\lambda_1 = (3\Delta TR/G)^{1/2} \qquad \ldots(1)$$

where,

R=tip radius,

ΔT=dendrite tip to radius temperature difference

G=Thermal Gradient

R was calculated using the equation,

$$R^2V = 4\pi^2 D\Gamma/(\Delta T_o k) \quad \ldots(2)$$

V = Growth Velocity

D = Diffusion coefficient

Γ= Gibbs-Thomson Coefficient

k = Equilibrium Distribution coefficient

ΔT_o = Liquidus Soildus Range

PROCAST provides the values of V and G and the rest of the quantities are constant. The value of V and G can be mapped on a V-G map to located the operational window of strip casting as done in Fig. 2-27. Besides, one can calculate the Primary DAS from the model. Primary DAS was also measured from hot picric etched samples. By comparing Primary DAS with those measured from the etched samples model validity can be tested. The results in Figure 2-28 show that the values obtained from the simple calculation are in good agreement with the measured values.

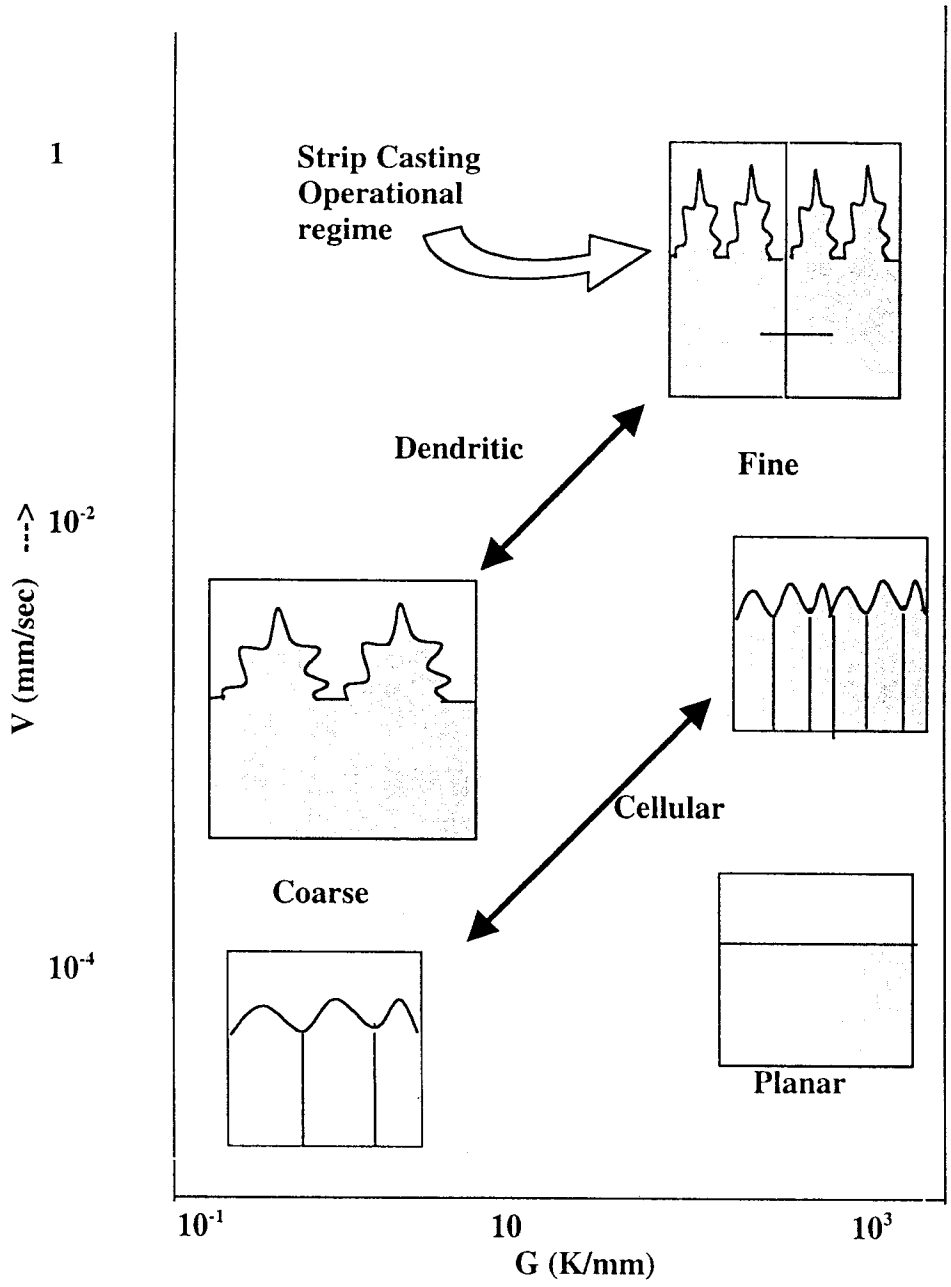

Figure 2-27: Schematic diagram illustrating the role of thermal gradient (G) and shell thickness growth rate velocity (V) on structure.

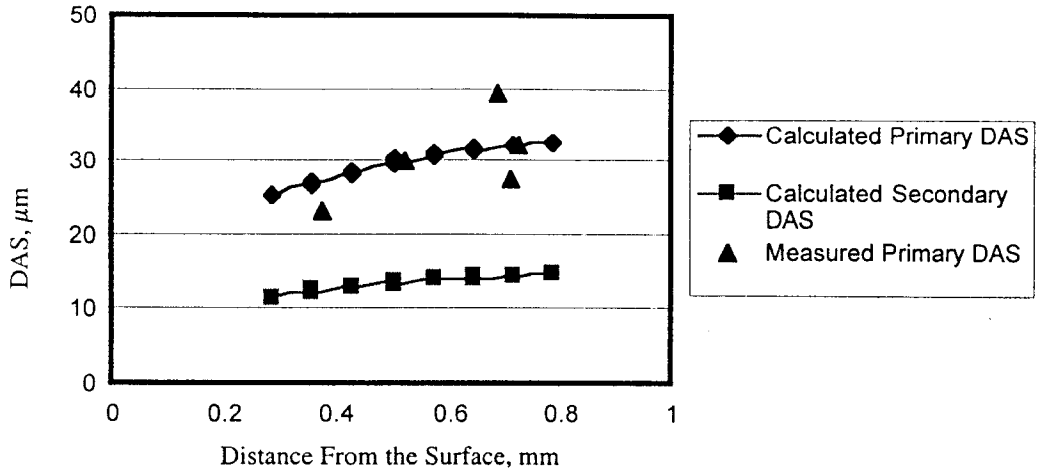

Figure 2-28: Primary and Secondary Dendrite calculated from the PROCAST model. The measured values of Primary Dendrite Spacings have also been plotted.

2.6 Linescan Analysis

Using the Linescan utility in SEM, a surface can be scanned along a line and the variation in composition of elements can be recorded. The work was undertaken to measure the primary and if possible, secondary dendrite arms spacing. Thus linescans were performed on P, S, Mn, Si and Al. Scanning was done in both longitudinal and transverse direction which are illustrated in the Figure 2-29.

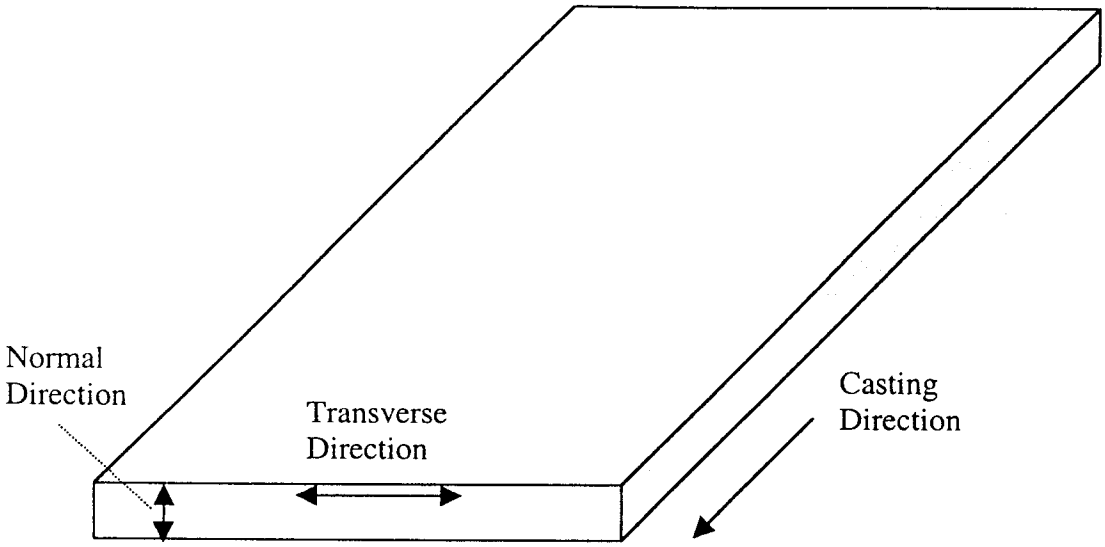

Figure 2-29: Schematic diagram showing the direction of line scans.

Because of the low levels of alloying additions, it was very difficult to see any recurring trend in their compositional variation.

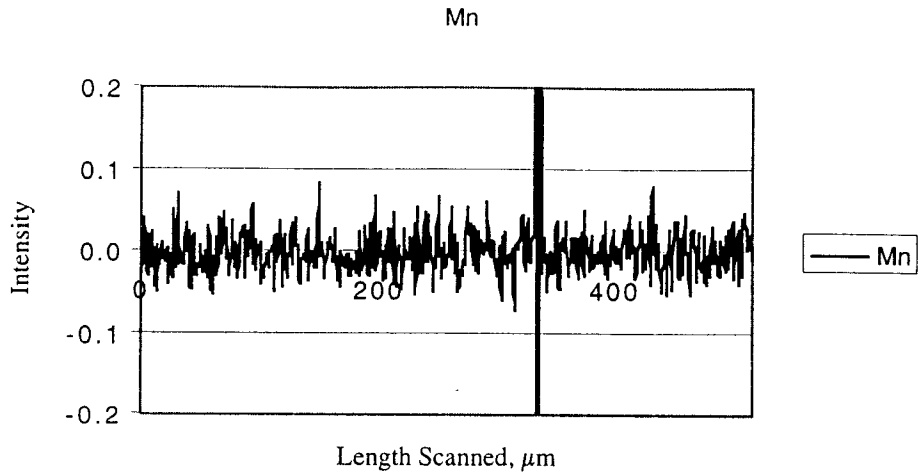

Figure 2-30: Transverse linescan to detect Mn

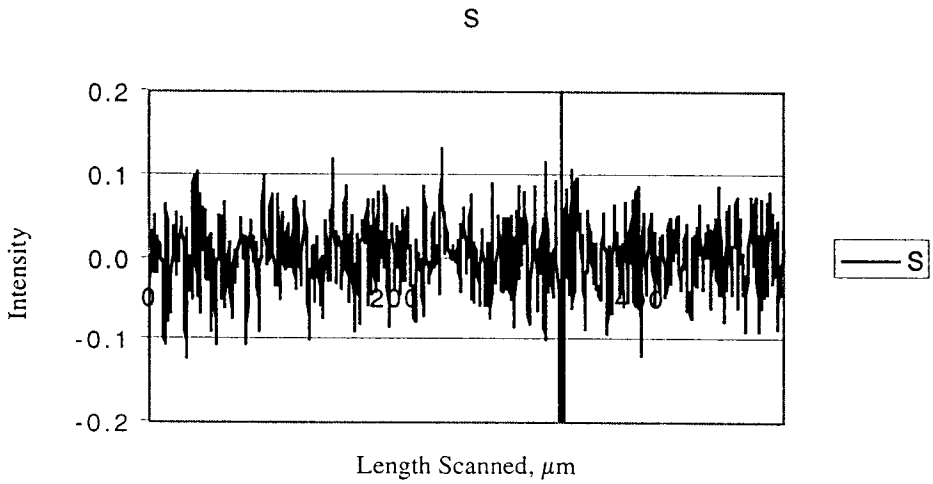

Figure 2-31: Transverse linescan to detect S

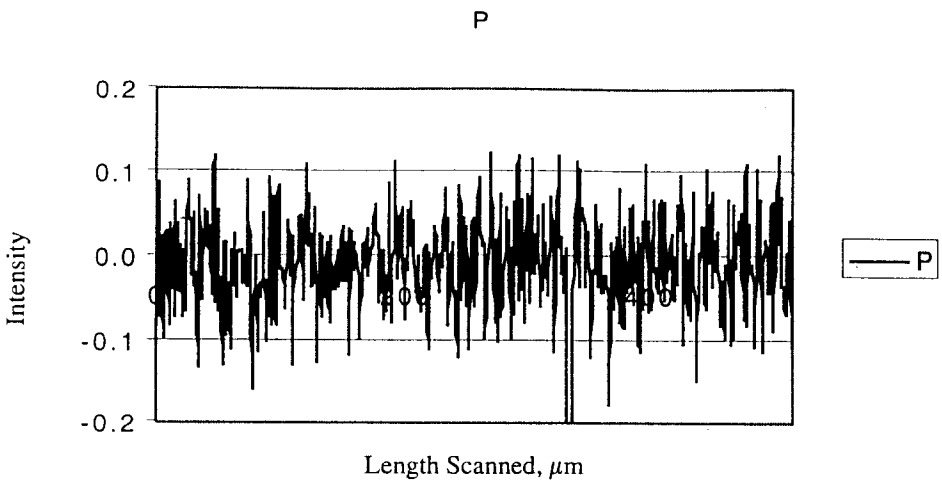

Figure 2-32: Transverse linescan to detect P.

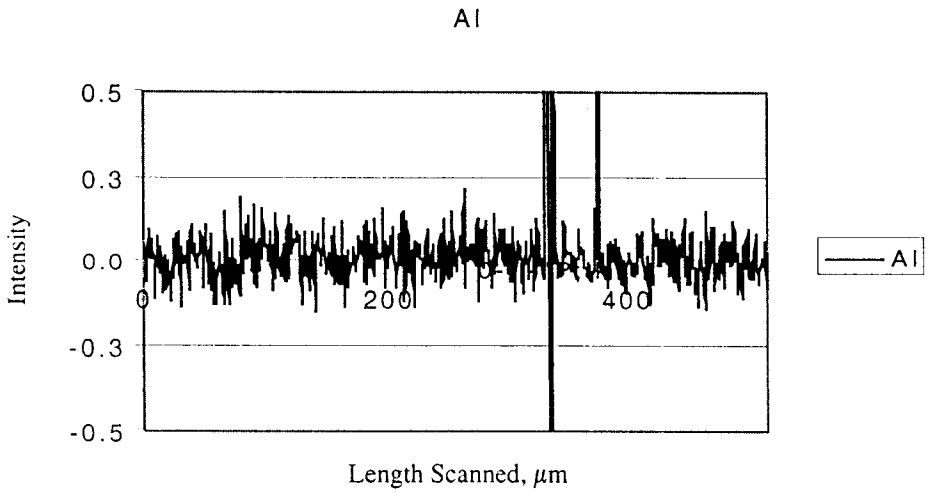

Figure 2-33: Transverse linescan to detect Al.

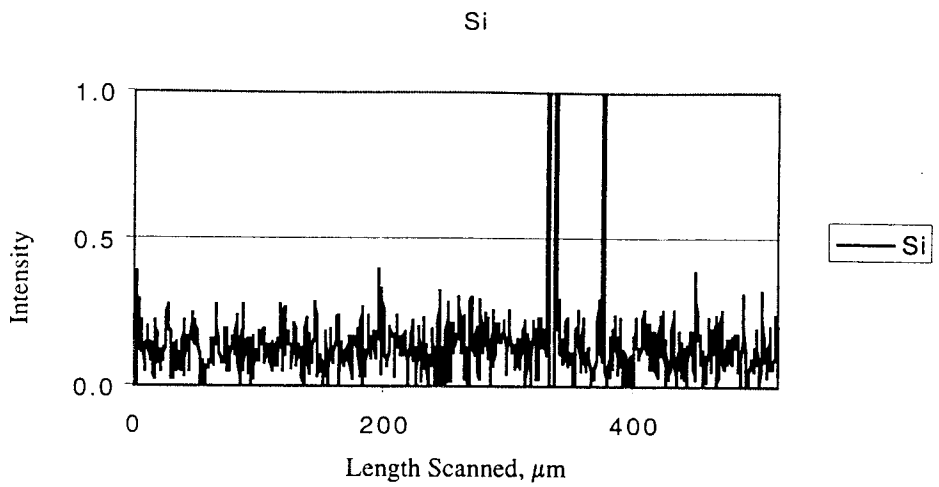

Figure 2-34: Transverse linescan to detect Si.

The correlation between the segregation of Mn, Si and Al was investigated by calculating the correlation coefficient for the Mn-Si, Si-Al and Al-Mn pairs. Al-Si pair exhibits coefficient in the 0.4-0.5 range while for Mn-Al and Si-Mn show almost no correlation. High correlation coefficient indicates that a high in Al concentration is accompanied by a high in Si and vice versa.

An examination of line scan data itself was not very helpful in measuring primary dendrite spacings so Fourier transformation of data was performed to identify t he dominating wavelengths. Fourier transformation converts the intensity-distance curves into intensity-inverse of distance curves. As the data are noisy, they were often filtered to remove small wavelengths (<2 to 4 μm) from interfering with the analysis (Fig. 2-35). The Fourier transformation of the final curves showed peaks in the neighborhood of 40-60 μm (Fig. 2-36). Again due to the low level of additions and various transformations that the material has gone through, it was difficult to pick a consistent wavelength from the different samples that were analyzed. However it is proposed that the technique may be useful for grades with higher alloying additions.

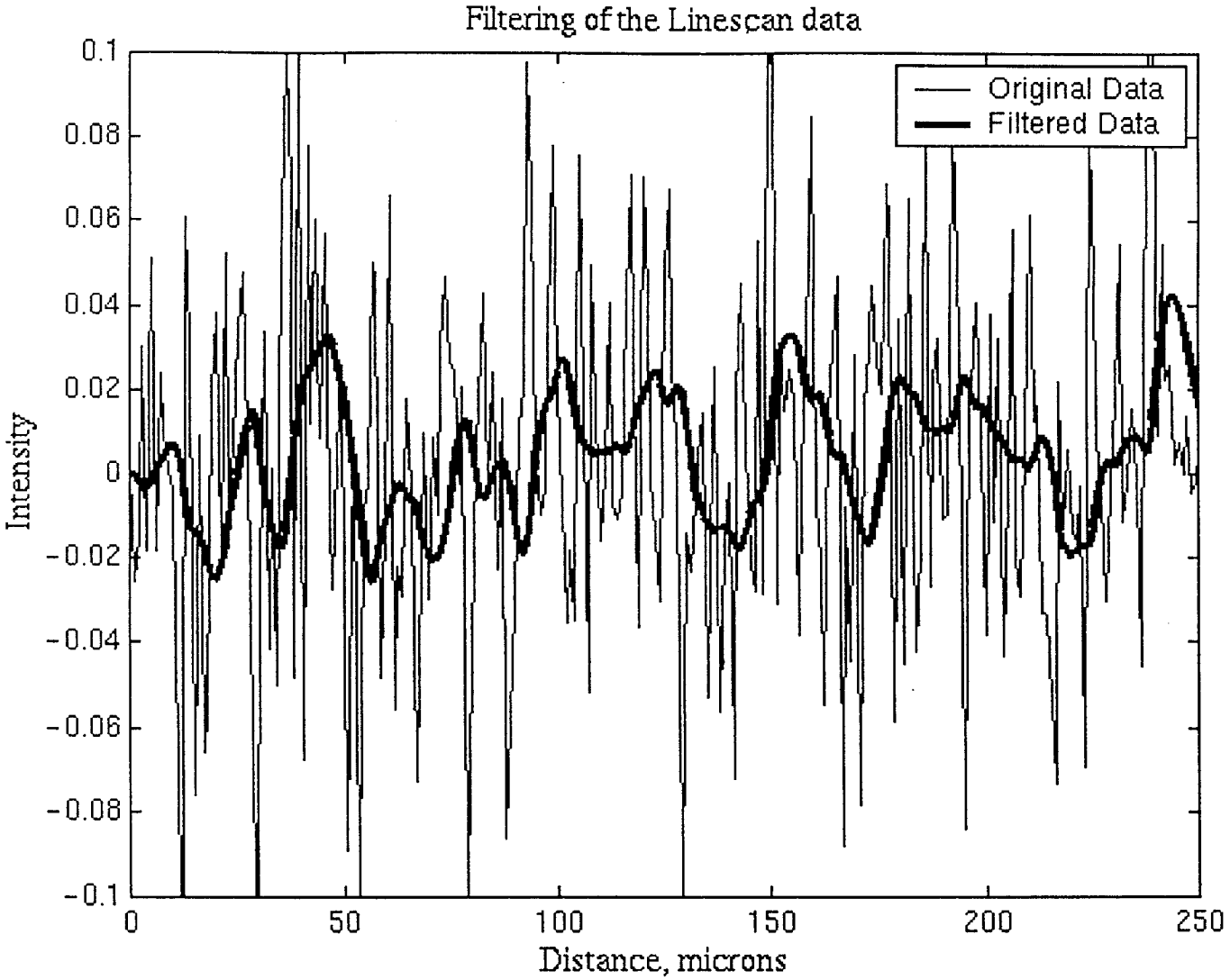

Figure 2-35: Filtering has the effect of smoothing the line scan data and thus removing the "local" variations in the composition.

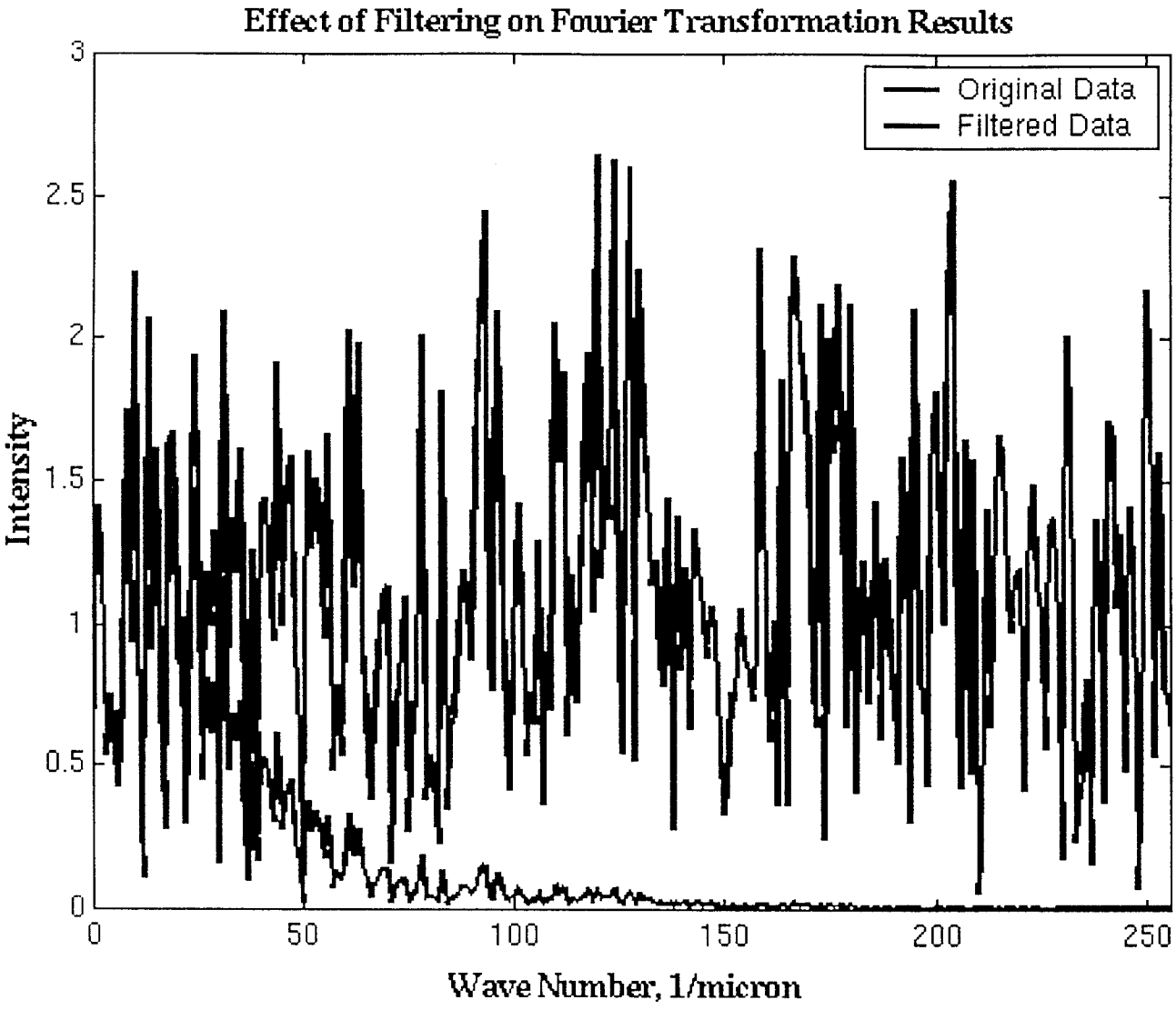

Figure 2-36: Filtering not only removes all wavelengths smaller that the cutoff (2μm here) but also the wavelengths that are created by interference of these wavelengths.

Reference:

2.1 Kurz and Fisher, Fundamentals of Solidification, Trans Tech publications 1992.

Appendix 3: Mechanical Properties:

Structure-property relationship of strip cast material has been of huge interest among the researchers [Ref. 3-1 to 3-5]. In order to ascertain the commercial viability of the product, tension tests were performed on the longitudinal and transverse sections of the as-received (AR) commercial strip cast material. Subsequently, the material was put under a variety of thermo-mechanical treatments and the effect on mechanical properties was determined.

Thermo-mechanical processing of material can be divided into three stages:

- Preprocessing
- Cold working by 50 % or 80%
- Gleeble simulated continuous annealing at temperatures between 1220°F (660°C) to 1520°F (827°C)

Three sets of starting material can be differentiated with respect to step 1. First set consisted of as-cast strip cast (AC) material itself, i.e., no preprocessing, and this had a gauge of 1.9 mm. Second set consisted of as-cast material batch-annealed in furnace for 900° C and 1/2 hour and subsequently furnace cooled (ACHT). The last set was composed of inline hot rolled material (ILHR) which had a gauge of about 1.4 mm. This was produced by sending the as-cast strip of 1.6 mm directly from mold to an in-line hot roll mill at 1050°C giving a reduction of 13%.

In addition to this, another set of samples of as-cast, as-received strips was cold-rolled by 70% and then batch annealed (BA) at 1330° F for 30 hours. Detailed results from all the tests have been presented in Table 3-1.

In Figures 3-1 to 3-6, important mechanical properties are compared for different thermo-mechanical processing routes. For 50% CW material a significant change in properties in going from 660° C annealed to 716° annealed can be seen in Fig. 3-1, 3-3 and 3-5. Tensile strength and yield strength drop by about 33% while the ductility increases by

about 45%. It appears that the annealing done at 660° C was not enough to recrystallize the material and remove the strain caused by cold working. The change in properties in going from 660° C to 716° C is less pronounced for 80% cold-worked material which can be attributed to creation of higher number of nucleation sites for recrystallized grains at higher degree of cold reduction.

Inline hot rolled material appears to undergo a local maxima of strength around 770° C. Except for the already mentioned cases of insufficient recrystallization, ductility is high for inline hot rolled material, with elongation above 25%.

Pre-annealed material (ACHT) shows an improvement in the ductility as compared to the as-cast material. This offers an opportunity to tailor the strength and ductility of the product by varying the pre-annealing temperature and time.

For 80% cold worked material, yield strength and tensile strength of the as-cast material decreases (Fig. 3-2,3-4) while the ductility increases (Fig. 3-6) with increase in annealing temperature.

Elongation values of close to 50% were obtained for batch annealed/70% cold worked material (Fig. 3-6).

A useful way to analyze the strength-ductility trade-off is to analyze the plot of strength against ductility. For example, an application might require the material to have strength higher than a critical level without going below an acceptable level of ductility. A prospective material for such an application can easily be researched based on the strength-ductility plots.

In Figure 3-7, properties of as cast strip cast material (without any post processing) have been shown. All the three types of material appear to have ductility in the same range but strips from the commercial caster appear to have higher strength.

A comparison between properties of samples that had undergone different thermo-mechanical processing, has been made in Fig. 3-8. In general, Si-killed material seems to have a higher tensile strength than Al-killed while their ductility level is nearly equivalent. This could be due to smaller grain size in Si-killed material.

Similar comparisons for material with 50% cold work have been made in Fig. 3-9 and for those with 70% and 80% cold work in Fig. 3-10. With some exceptions, mainly due to incomplete recrystallization, ductility increases in going from as-cast (AC) to in-line hot rolled (ILHR) to as-cast heat treated (ACHT) to batch annealed (BA) material. The opposite trend is observed for strength values.

Finally, properties of all the material analyzed in the project have been compared with some important types of steel in Fig. 3-11. Materials used for comparison include IF (Interstitial Free), EDD (Extra Deep Drawing), DP (Dual Phase) and HSLA (High Strength Low Alloy). Thus it can be seen that thermo-mechanical processing can cause a fairly large spectrum in the mechanical properties of the strip cast material, with 50% ductility and 350 MPa tensile strength at one end, and 15% ductilty and 550 MPa tensile strength at the other end of the spectrum.

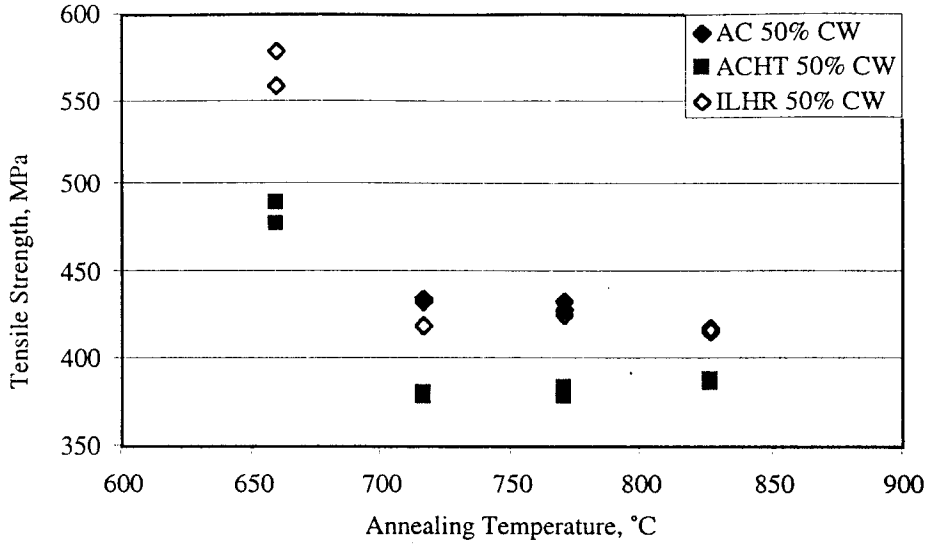

Figure 3-1: Effect of annealing temperature on tensile strength at 50% cold work.

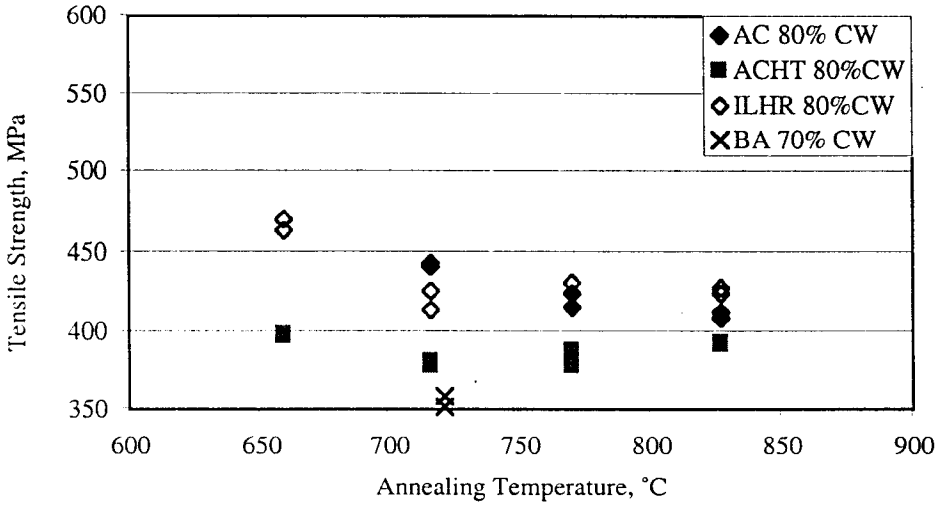

Figure 3-2: Effect of annealing temperature on tensile strength at 70% and 80% cold work.

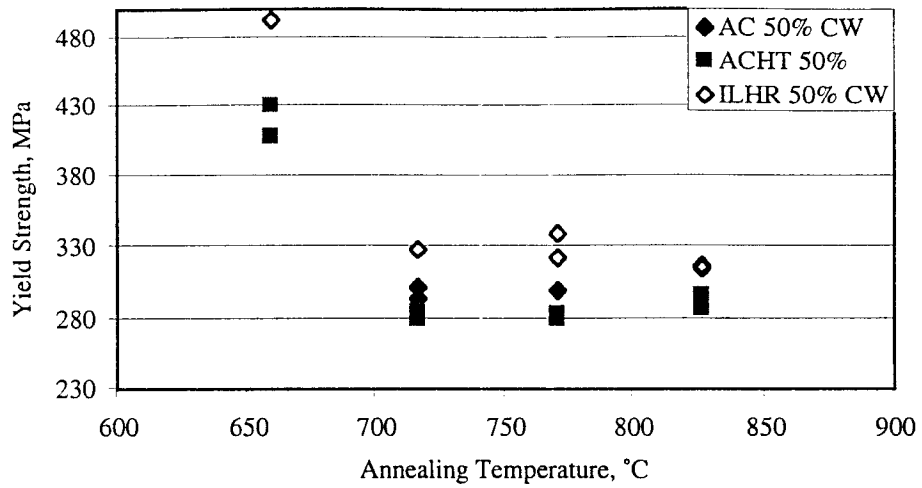

Figure 3-3: Effect of annealing temperature on yield strength at 50% cold work.

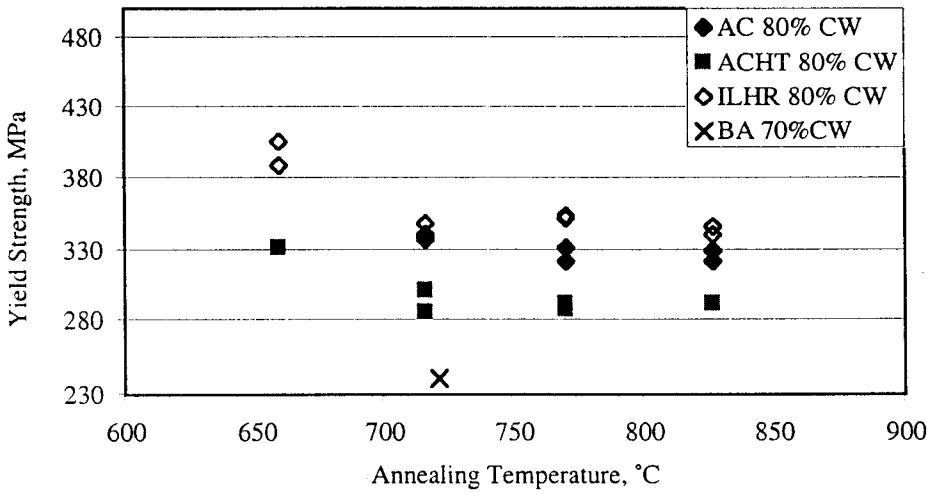

Figure 3-4: Effect of annealing temperature on yield strength at 70% and 80% cold work.

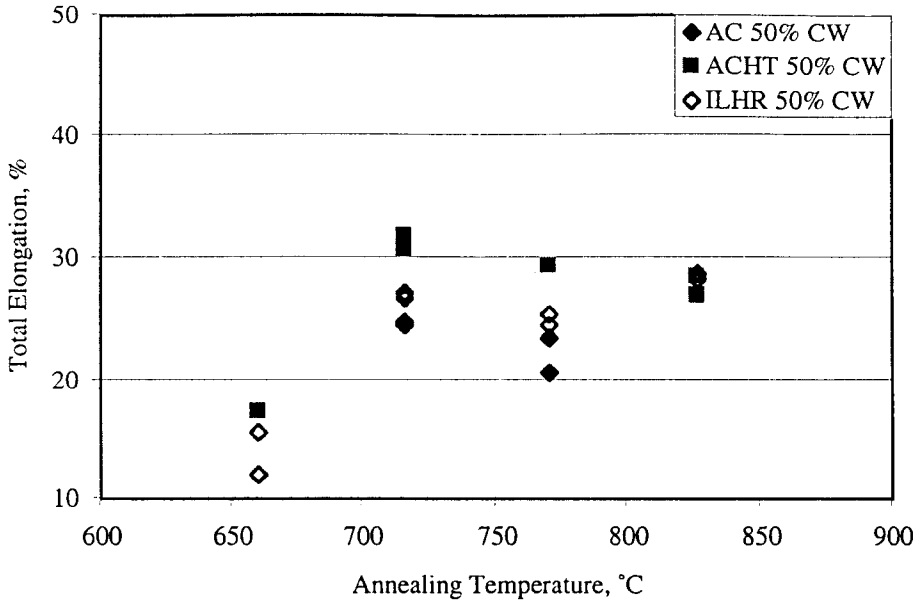

Figure 3-5: Effect of annealing temperature on total elongation at 50% cold work.

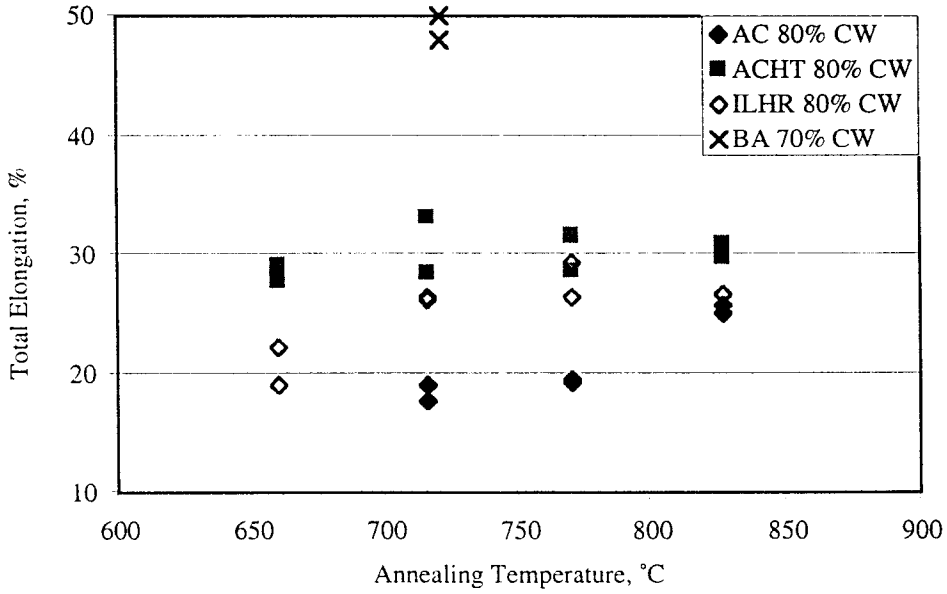

Figure 3-6: Effect of annealing temperature on total elongation at 70% and 80% cold work.

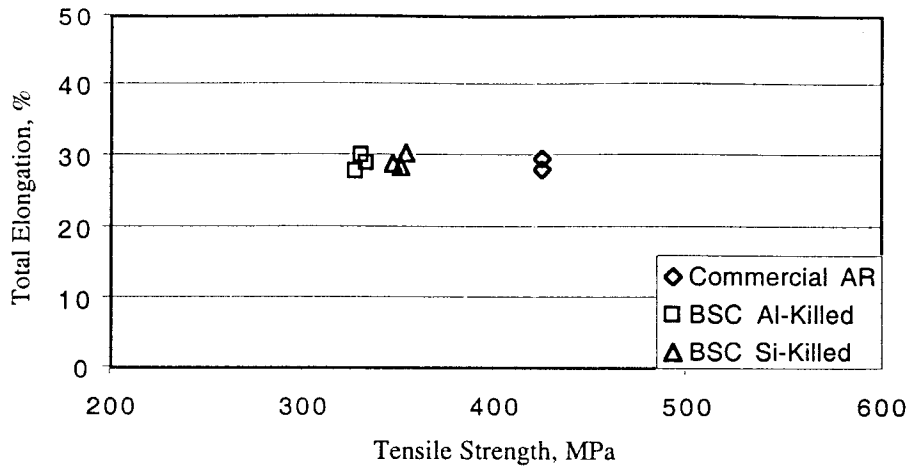

Figure 3-7: Performance of as-received (AR) commercial strip cast material compared with that from a pilot caster (BSC)

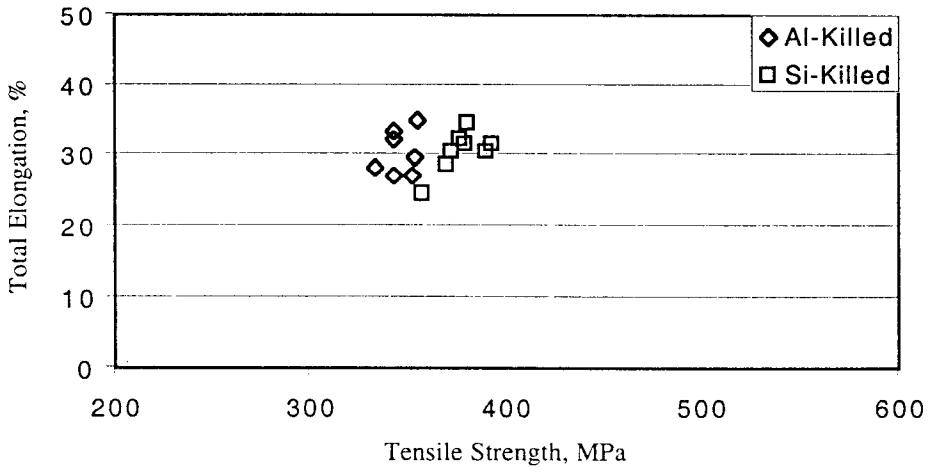

Figure 3-8: Performance of cold worked-annealed British Steel material

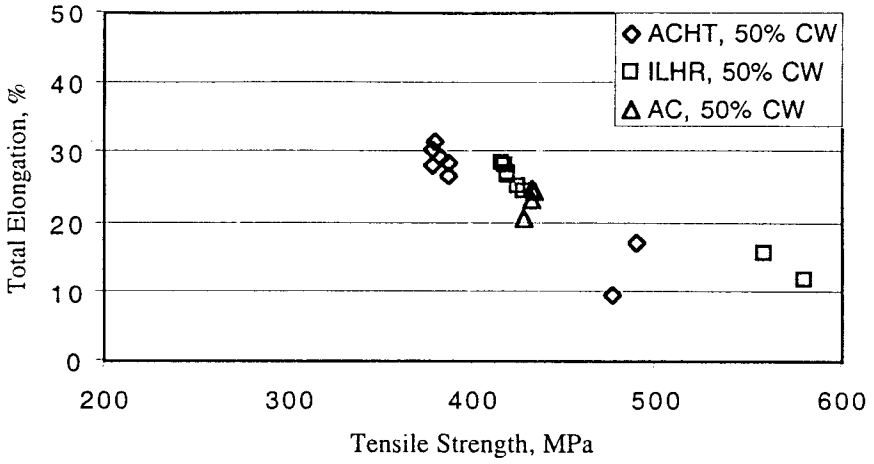

Fig. 3-9: Performance of 50% CW and annealed material

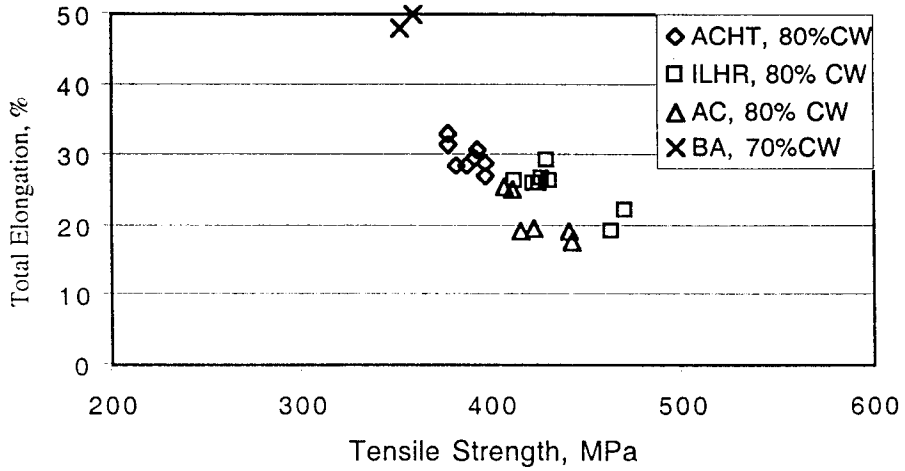

Fig. 3-10: Performance of 70% and 80% CW and annealed material

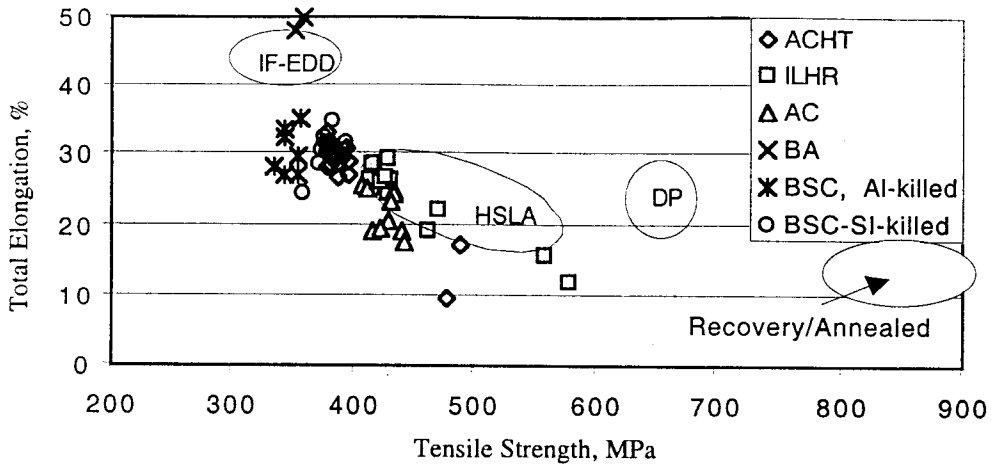

Figure 3-11: Performance of strip cast material vis-a-vis other steel grades (IF=Interstitial Free, EDD=Extra Deep Drawing, HSLA=High Strength Low Alloy, DP=Dual Phase)

Table 3-1: Mechanical properties of the material

Material	CW %	AT °C	t inch	W Inch	YS Ksi*	YPE %	TS Ksi*	UE %	TE %	N Value	K Value	Strain range for n, K	Hardness Rb
AC	As-received		0.0776	.5007	41.7	0.4	61.5	15.4	29.9	0.153	95.8	10.1-15.4	71
AC	As-received		0.0777	0.5019	41.6	0.2	61.6	16.4	28.3	0.105	95.3	10.0-16.4	70
AC	50	716	0.0387	0.4985	43.7	0.4	62.8	17.0	24.8	0.164	99.8	10.1-17.0	73
AC	50	716	0.0385	0.4986	42.7	0.4	62.9	19.1	24.6	0.163	99.6	10.1-19.1	73
AC	50	771	0.0394	0.4998	43.5	0.4	62.0	14.8	20.6	0.162	98.3	10.0-14.8	72
AC	50	771	0.0391	0.5002	43.6	Trace	62.7	15.9	23.4	0.168	100.5	10.1-15.9	72
AC	80	716	0.0156	0.5014	49.0	0.6	64.0	13.7	18.9	0.130	95.0	10.1-13.7	77
AC	80	716	0.0153	0.5020	49.4	0.7	64.2	13.5	17.6	0.132	95.7	10.1-13.5	77
AC	80	771	0.0161	0.5016	46.8	0.7	60.3	15.6	19.2	0.160	95.0	10.1-15.6	72
AC	80	771	0.0160	0.5017	48.1	0.6	61.4	13.9	19.4	0.169	98.8	10.1-13.9	72
AC	80	827	0.0172	0.4917	46.7	1.9	59.1	18.2	25.7	0.204	100.4	10.1-18.2	63
AC	80	827	0.0170	0.4937	47.8	6.2	59.7	18.5	25.1	0.205	101.7	10.0-18.5	63
ACHT	50	660	0.0396	0.5019	59.0	0.9	69.3	8.9	9.6	0.116	100.1	2.6-7.9	79
ACHT	50	660	0.0396	0.4959	62.4	0.7	71.0	12.0	17.3	0.136	10.7.3	7.1-12.0	79
ACHT	50	716	0.0395	0.4963	41.2	2.0	55.1	19.7	30.6	0.227	97.5	10.0-19.7	62
ACHT	50	716	0.0395	0.4956	40.6	4.8	55.0	22.7	31.7	0.232	97.9	10.1-20.0	62
ACHT	50	771	0.0393	0.4987	40.6	5.1	55.6	22.1	29.3	0.230	98.8	10.0-20.2	63
ACHT	50	771	0.0393	0.4967	41.0	5.7	55.0	21.6	29.4	0.230	97.8	10.0-20.2	63
ACHT	50	827	0.0397	0.4984	41.7	1.9	56.4	19.9	28.5	0.224	99.5	10.1-19.9	65
ACHT	50	827	0.0392	0.4970	42.8	1.9	56.1	19.1	26.9	0.224	99.1	10.1-19.1	65
ACHT	80	660	0.0170	0.4975	48.1	7.0	57.5	20.8	27.7	0.214	99.6	10.0-20.1	61
ACHT	80	660	0.0169	0.4944	47.9	0.9	57.6	21.6	29.1	0.208	98.6	10.0-20.2	61
ACHT	80	716	0.0163	0.4955	43.7	7.4	55.3	22.3	28.5	0.220	96.5	10.0-20.1	61
ACHT	80	716	0.0167	0.4964	41.5	7.5	54.8	24.2	33.1	0.236	97.6	10.0-20.0	61
ACHT	80	771	0.0168	0.4977	41.9	5.6	54.7	24.1	31.6	0.243	99.0	10.0-20.1	62
ACHT	80	771	0.0165	0.4954	42.2	1.8	56.3	20.7	28.7	0.221	98.2	10.0-20.0	62
ACHT	80	827	0.0167	0.4989	42.2	4.8	57.0	25.1	31.0	0.240	102.7	10.1-20.1	62
ACHT	80	827	0.0166	0.4954	42.3	6.5	56.7	20.9	29.7	0.227	100.0	10.0-20.2	62

Material	CW %	AT °C	t inch	w Inch	YS Ksi*	YPE %	TS Ksi*	UE %	TE %	N Value	K Value	Strain range for n, K	Hardness Rb
ILHR	50	660	0.0286	0.4979	71.4	2.0	80.9	11.3	15.6	0.126	119.6	7.0-11.3	88
ILHR	50	660	0.0284	0.4974	74.0	1.9	83.9	9.1	12.0	0.120	123.3	7.1-9.1	88
ILHR	50	716	0.0283	0.4991	47.7	5.6	60.8	20.7	27.2	0.204	103.6	10.1-20.0	71
ILHR	50	716	0.0278	0.4957	47.5	5.3	60.7	19.3	26.8	0.206	103.8	10.1-19.3	71
ILHR	50	771	0.0281	0.4984	46.8	4.2	61.7	19.5	25.3	0.196	103.4	10.0-19.5	72
ILHR	50	771	0.0280	0.4978	49.2	5.2	62.2	17.4	24.5	0.197	104.8	10.1-17.4	72
ILHR	50	827	0.0286	0.4988	45.7	1.8	60.6	21.9	28.3	0.206	103.4	10.0-20.0	71
ILHR	50	827	0.0282	0.4972	46.0	1.8	60.3	21.8	28.7	0.204	102.6	10.1-20.0	71
ILHR	80	660	0.0119	0.4941	58.9	5.6	68.2	17.5	22.2	0.180	111.4	10.1-17.5	71
ILHR	80	660	0.0119	0.4967	56.5	6.4	67.2	15.7	19.1	0.176	109.4	10.1-15.7	71
ILHR	80	716	0.0124	0.4932	48.9	6.2	59.9	20.7	26.4	0.209	102.6	10.0-20.1	69
ILHR	80	716	0.0120	0.4951	50.4	4.5	61.7	18.6	26.1	0.211	106.1	10.0-18.6	69
ILHR	80	771	0.0120	0.4934	51.3	1.9	62.4	21.6	29.3	0.214	107.5	10.1-20.1	68
ILHR	80	771	0.0119	0.4935	51.0	7.0	62.5	19.6	26.4	0.207	106.6	10.1-19.6	68
ILHR	80	827	0.0118	0.4931	49.4	1.8	61.4	19.4	25.8	0.212	105.8	10.1-19.4	63
ILHR	80	827	0.0115	0.4942	50.3	7.1	61.9	21.3	26.7	0.208	105.8	10.1-20.1	63
BA (l)	70	721	NA	NA	35	NA	51	28	48	NA	NA	NA	NA
BA(t)	70	721	NA	NA	35	NA	52	27	>50	NA	NA	NA	NA
ILHR(l)	50	1050	NA	NA	50	NA	67	13	-	NA	NA	NA	NA
ILHR(t)	46	1050	NA	NA	46	NA	64	18	34	NA	NA	NA	NA

(AC=As-cast strip cast material, ACHT=As-cast strip cast material heat treated at 900°C for 1/2 hour and then furnace cooled before cold working, ILHR=Inline hot rolled-material, t= tension test sample thickness, w=tension test sample width, YS=Yield Strength, YPE= Yield Point Elongation, TS= Tensile Strength, UE=Uniform Elongation, TE=Total Elongation, n=Strain-hardening Coefficient, K= Strength Coefficient. (l)=Stretched along the rolling direction, (t)=Stretched along the transverse direction)

*** 1 ksi = 6.8965 MPa**

Microstructure study of Samples

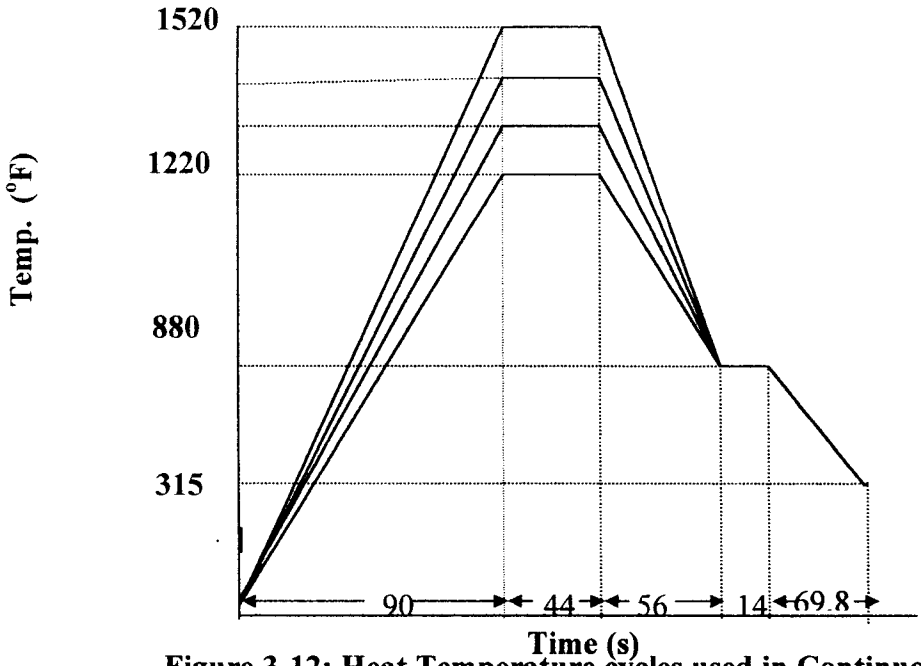

Figure 3-12: Heat Temperature cycles used in Continuous Annealing

Samples for metallography were prepared by using mechanical grinding followed by polishing with oil based diamond suspension. The microstructures were observed under the optical microscope by revealing the features with 2% Nital etchant. Average grain size for the recrystallized samples was measured by using the linear-intercept method.

OBSERVATIONS :

- **Pre-Annealed Material :**

As cast materials were annealed at a temperature of 1652°F for 0.5 hr. and were subjected to metallographic sample preparation. Fully recrystallized equiaxed grains in association

with some slightly elongated randomly oriented grains are depicted in Figure 3-13 (a) & (b). The average grain size was measured to be ~56-60 μm.

- **Continuously Annealed Materials :**

(a) As-Cast Condition :

Intercritical anneal at 1520°F

As-cast samples subjected to continuous annealing at peak temperature of 1520°F for 44s after 80 pct cold reduction showed fully recrystallized grain [Figure 3-14(a)] along with some elongated grains in the rolling direction, which is much discernible in the transverse section of the strip [Figure 3-14(b)]. The average grain size was calculated to be ~25-28 μm.

(b) Pre-Annealed Condition

Subcritical anneal at 1220°F & 1320°F

Pre-annealed material subjected to 80 pct cold work followed by a continuous annealing at a sub-critical annealing temperature of 1220°F for 44 s, showed a non-recrystallized deformed structure in the rolling direction clearly depicted in Figure 3-15 (a) & (b).

However, As the peak temperature was raised to 1320°F maintaing the same stay time for 44s, partial recrystallization was observed in the transverse section of the strip in conjunction with a deformed structure [Figure 3-15(c)], however, the longitudinal section of the sample represents sharp elongated non-recrystallized grain structure [Figure 3-15(d)].

Inter-critical anneal at 1420°F & 1520°F

At still higher peak temperature of 1420°F, fully recrystallized grain structure was observed with slightly elongated in the rolling direction [Figure 3-15(e)]. The maximum annealing temperature of 1520°F represented complete recrystallization which was manifested by equiaxed grains represented by both the longitudinal [Figure 3-15(f) & (g)] as well as the transverse section of the strip material [Figure 3-15(h)]. The average grain size was recorded to be ~23 μm , which is to be noted as smaller than the grain size of the as-cast material with the same thermo-mechanical processing condition.

(c) In-Line Hot-Rolled Condition

Sub-critical anneal at 1220°F

At the sub-critical annealing temperature of 1220°F the sample showed non-recrystallized deformed structure in both the longitudinal as well as the transverse section of the strip [Figure 3-15(a) & (b)].

Inter-critical anneal at 1520°F

At higher annealing temperature in the inter-critical region of 1520°F, again fully recrystallized grain structure was noticed [Figure 3-15 (c) & (d)]. The average recrystallized grain size for 1520°F was recorded to be ~15 μm, which is smaller than the as-cast as well as the pre-annealed materials. However, at some small regions non-crystallized deformed structure accompanying fully recrystallized equiaxed grains were also present in the longitudinal section of the material annealed at 1520°F which was absent in the case of pre-annealed material at similar condition.

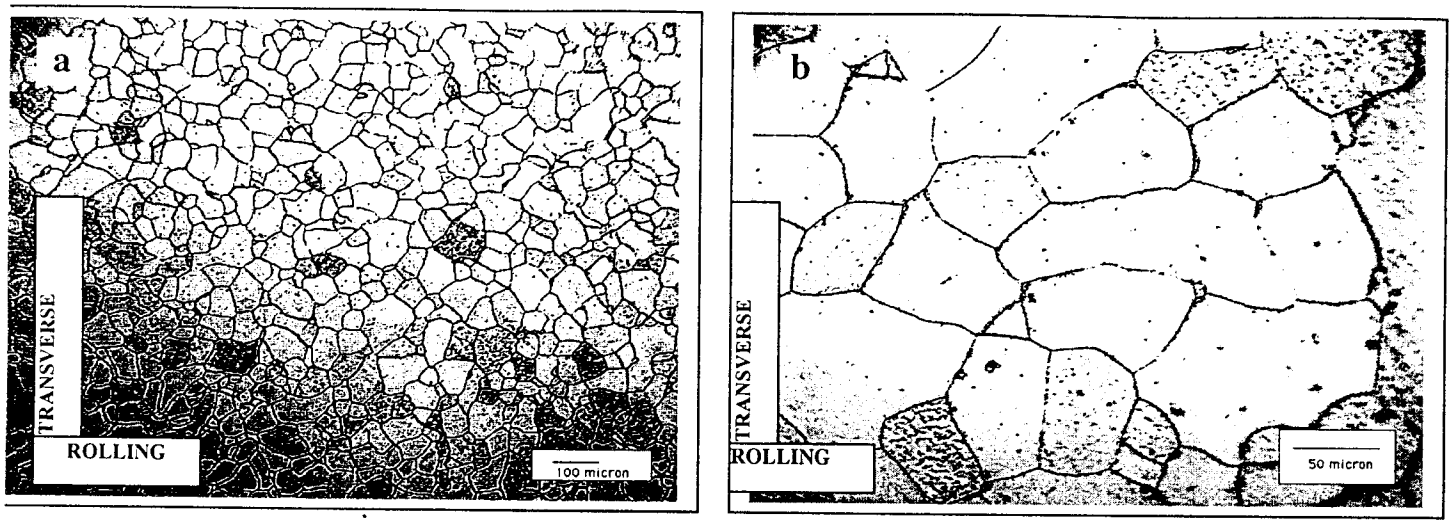

Figure 3-13--Grain structure of pre-annealed material annealed at 900°F for 30 mins.

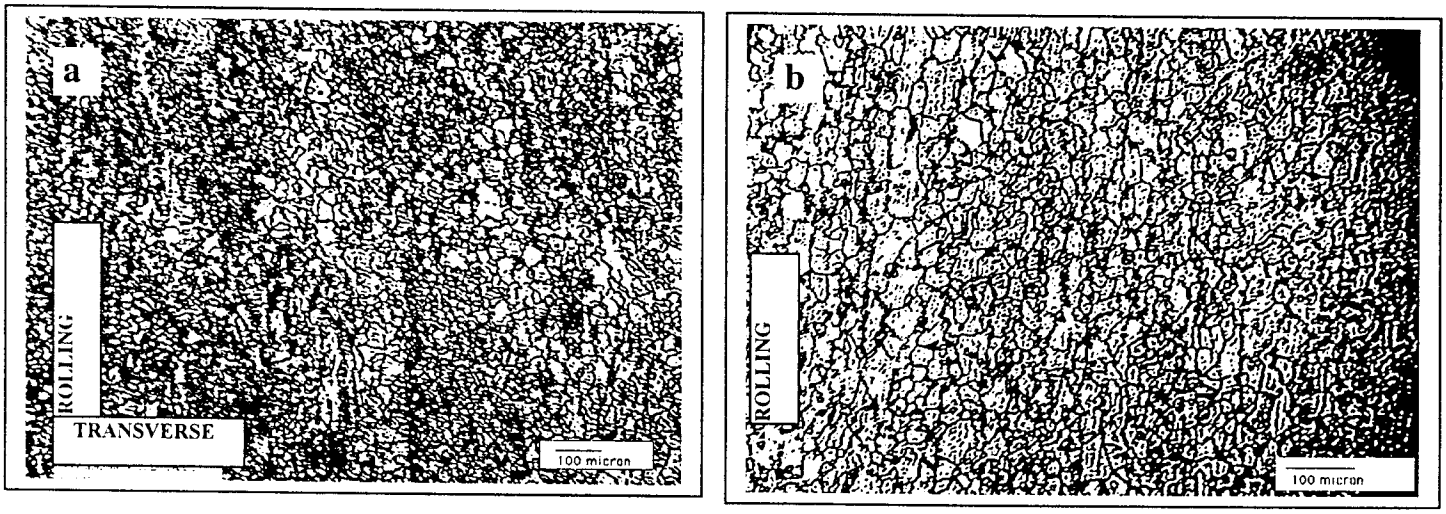

Figure 3-14: Grain structures of 80% cold-rolled strip cast steel followed by continuous inter-critical annealing at 1520°F peak temperature for 44 sec.

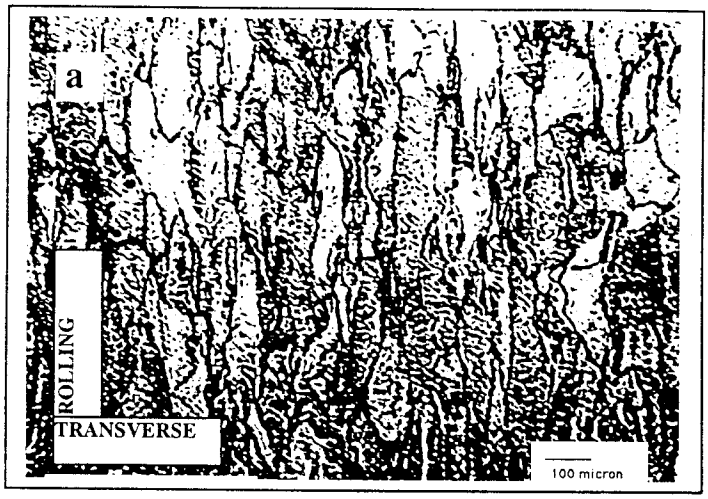

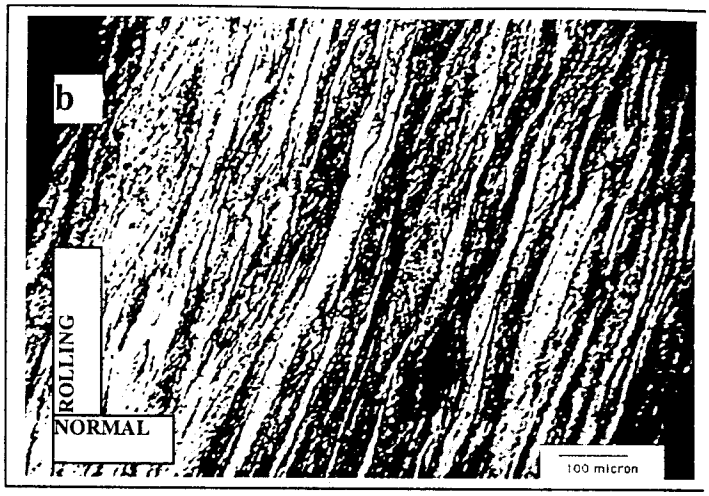

Figure 3-15a,b: Grain Structures of 80 pct. cold-rolled followed by continuous annealing at 1220°F peak temperature pre-annealed material.

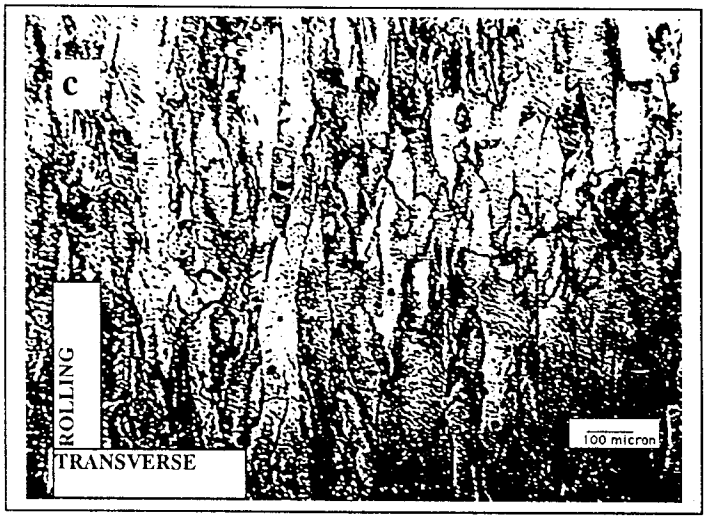

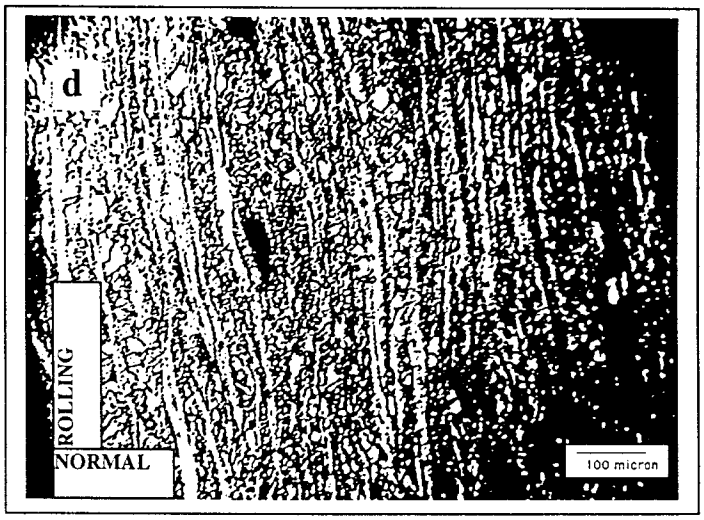

Figure 3-15c,d: Grain Structures of 80 pct. cold-rolled followed by continuous annealing at 1320°F peak temperature pre-annealed material.

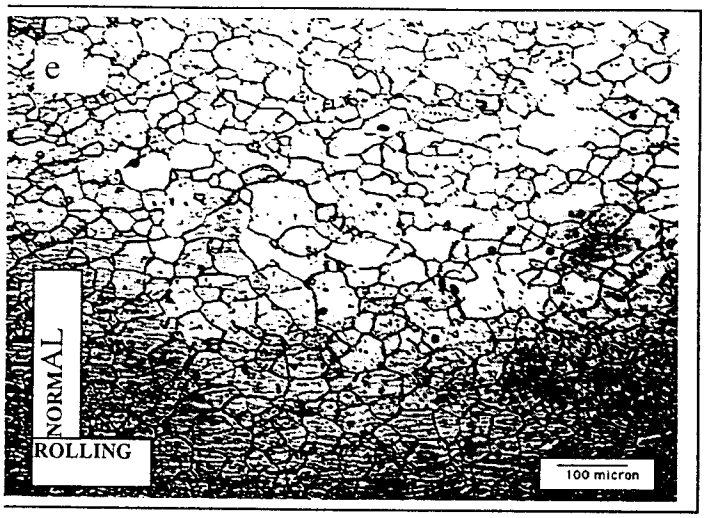

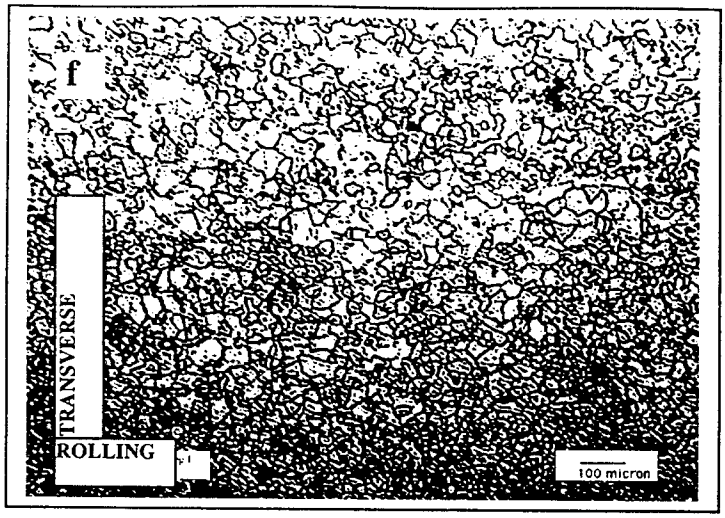

Figure 3-15e: Shows the grain structure of the transverse section of 80 pct. cold-worked pre-annealed material continuous annealed at 1420°F peak temperature.

Figure 3-15f: Shows the grain structure of the longitudinal section of 80 pct. cold-worked pre-annealed material continuous annealed at 1520°F peak temperature.

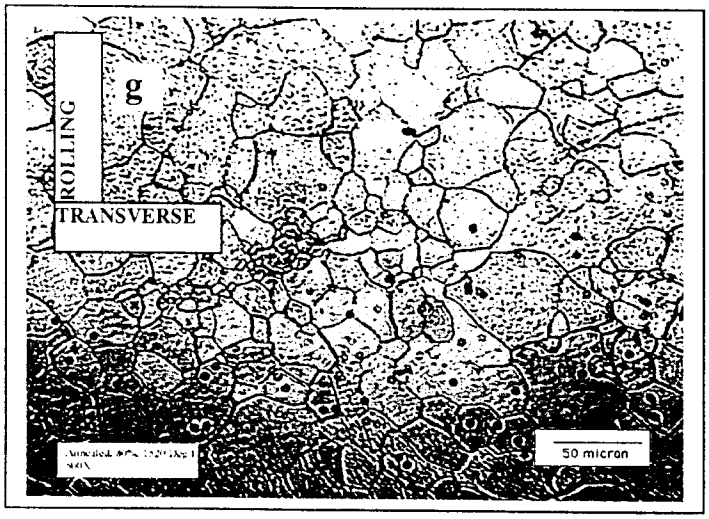

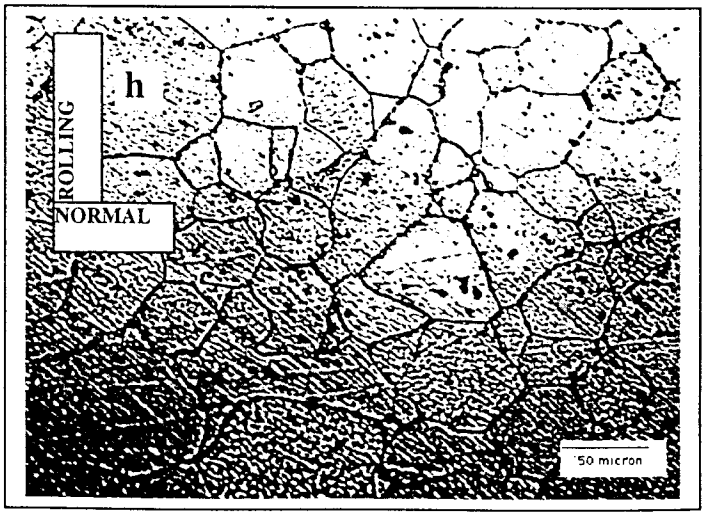

Figure 3-15g,h: Grain structure of 80 pct. cold worked pre-annealed sample continuous annealed at 1520°F (at higher magnification).

References:

3.1 K. Mukunthan and L. Strezov, *Evolution of microstructure and product opportunities in low carbon steel strip casting*, The Brimacombe Memorial Symposium, pp. 421-437.

3.2 A. Guillet, E. Es-Sadiqi, G. L'esprance and F.G. Hamel, *Microstructure and mechanical properties of strip cast 1008 steel after simulated coiling, cold rolling and batch annealing*, ISIJ International, Vol. 36 (1996), No.9, pp. 1190-1198.

3.3 Walter Blejde, rama Mahapatra and Hishahiko Fukase. *Application of Fundamental Research at Project M*, 2000 Belton Symposium Proceedings, pp. 253-261.

3.4 R. I. L. Guthrie, M. Isac, and J. S. Kim, *Steel casting in the third millinium; strip casting, interfacial heat fluxes and microstructures,* The Brimacombe Memorial Symposium, pp. 209-241.

3.5 L.T. Shiang and P.J. Wray, *The microstructure of strip-cast low-carbon steels and their response to thermal processing*, Metallurgical Transactions A, 1989,vol. 20A, pp. 1191-98.

Appendix 4: Texture:

The texture work was focused on cold rolled batch annealed strip cast steel, and its comparison with the conventionally cast, cold rolled batch annealed US Steel. Both the samples were 70% cold reduced before batch annealing. X-ray texture measurements were performed on both the samples. Based on these measurements, the texture was analyzed with a particular interest in the gamma fiber. The microtexture of the US Steel cold rolled batch annealed sample was measured by orientation imaging microscopy. A similar study on the strip cast cold rolled batch annealed sample is being performed. Figure 4-1 shows the (idealized) fiber textures for rolled and annealed steel.

The X-ray pole figure for the two samples is shown in Fig. 4-2. It can be seen from this figure that the pole figures look very similar and both exhibit a prominent gamma fiber, <111> || ND. However, the gamma fiber analysis (Fig. 4-3) shows that the fiber intensity is slightly stronger for the conventionally cast US Steel sample. The important point to mention here is that, although US Steel is Al-killed (automotive grade) compared to commercial quality Si-killed strip cast steel, direct cold rolling and batch annealing of the strip cast steel results in moderately strong gamma fiber, with intensity close to the drawing quality US Steel. This is a very encouraging result and shows the potential of the strip cast sheet for demanding applications, given further development of processing methods.

The orientation imaging microscopy of the US Steel sample shows a grain structure with an average grain size* of 27μm (Fig. 4-4). A total area of 500 X 1000 μm^2 was scanned. The grains are mapped according to the orientation parallel to the normal direction. Deep gray color grains indicate the <111> orientations, which is the most prominent orientation present here. The pole figures obtained from the OIM (Fig. 4-5) is quite similar to that obtained through X-ray pole figure measurement, though the slight presence of <100> and <110> intensity is absent from the center of the OIM pole figures. This could be related to the fact that OIM measures microtexture rather than the macroscopic (average) texture obtained from X-ray measurements. The OIM work on the cold rolled batch

annealed strip cast steel will provide a better comparison of the grain structure and texture of the two samples, which is currently under investigation.

The r-value of the as-cast strip (>0.9) is suggestive of the presence of some γ-fiber, which can be seen from the X-ray pole figure results (Fig. 4-6). The sheet is nearly isotropic, as can be seen from the very small value of ❒r. In-line hot rolling with the current process parameters decreases the r-value, which is apparent from the pole figures (Fig. 4-6), and can be explained in terms of the slight increase of {111} intensity and decrease of {100} intensity as compared to the as-cast strip. The cold rolled, batch annealed sample shows

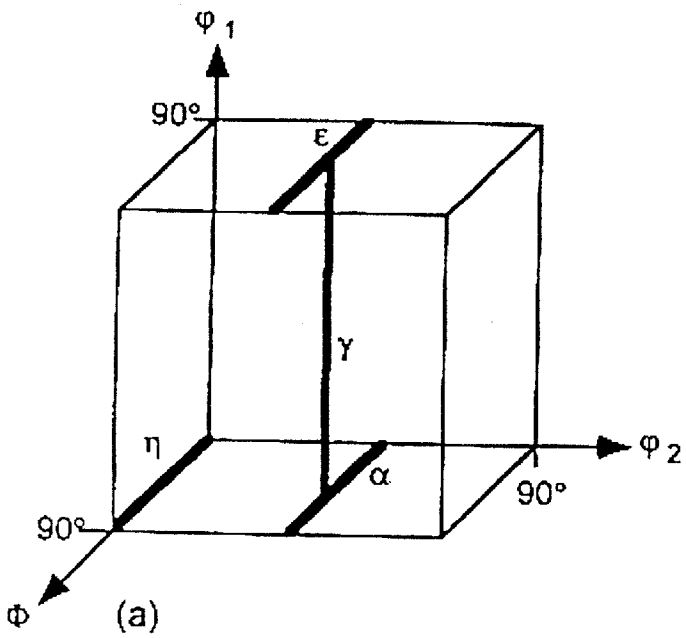

Fiber	Fiber Axis
α-fiber	<110> || RD
γ-fiber	<111> || ND
η-fiber	<001> || RD
ε-fiber	<110> || TD

Figure 4-1: (a) Diagram of the (idealized) fiber textures for rolled and annealed steel. (b) Table of idealized fibers with Miller indices.

significant increase in r-value and there is mild development of gamma fiber (Fig. 4-7), compared to that obtained for Si-killed steels, and is highly encouraging. However, the large anisotropy factor (❒r) suggests that further investigation needs to be done in rolling and annealing schedules to get high r-value, and small ❒r. Increasing the amount of cold reduction improves the development of gamma fiber, needed for deep drawing property.

* grain size obtained after dilation clean-up with minimum confidence index of 0.2, minimum misorientation of 10° and minimum grain size of 12 μm.

This can be illustrated from the {111} pole figures for the 20%, 50%, 60% and 80% cold deformed samples (Fig. 4-8).

Orientation Imaging Microscopy:

The orientation imaging microscopy (OIM) obtained for the as-cast strip confirms the optical characterization of a very inhomogeneous structure, with large regular polygonal ferrite, and bands of Widmanstätten ferrite (Fig. 4-9). The grain size obtained from OIM grain mapping is 22μm, compared to 50-60μm observed by Optical microscopy. This significantly finer grain structure obtained from the OIM explains the enhancement of the strength properties for the as-cast strip. Fig. 4-10 shows the mapping of grains in a region dominated by Widmanstätten ferrite side plates, with a particular orientation selected within a tolerance angle of 10°. The image illustrates the presence of parallel laths of ferrite with similar orientation. OIM has successfully emerged as a great research tool for studying the morphology of grain structure, the orientation of grains, grain size statistics, and the grain boundaries. These various aspects of the grain structure using OIM is currently under investigation, and will throw some more light into this material.

Table 4-1: Plastic Strain Ratio of as-cast, in-line hot rolled, and cold rolled, batch annealed sheet

Processing Type	r-value (r_m)	Plastic Anisotropy factor (Δr)
As-Cast	0.93	0.07
In-line Hot Rolled	0.79	-0.11
Cold Rolled, Batch Annealed	1.1	0.45

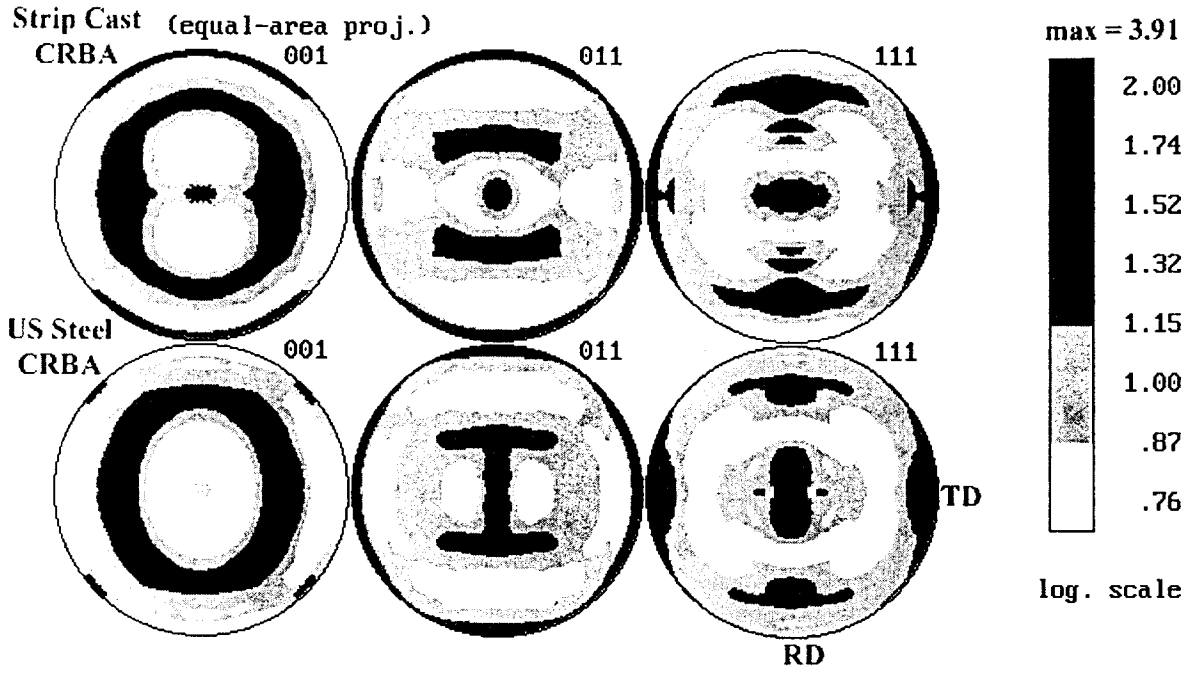

Fig. 4-2: X-ray pole figure for 70% cold rolled batch annealed strip cast company 'B' steel and conventionally cast US Steel.

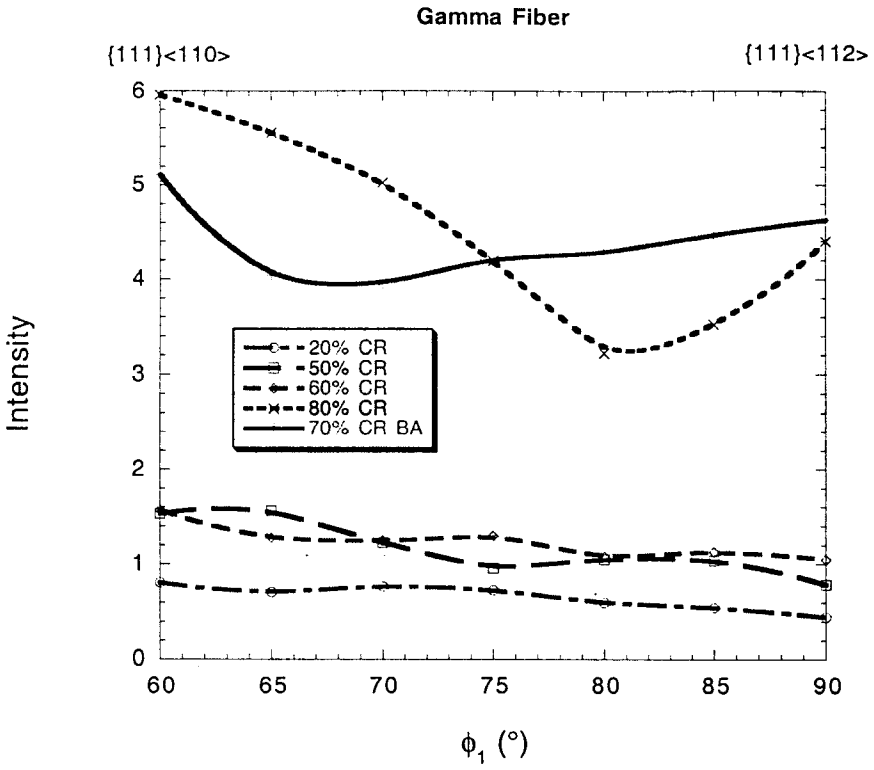

Fig. 4-3 a: Showing the intensities along the gamma fiber for various reductions in thickness of cold rolled strip cast steel and also cold rolled and annealed. Annealing does not reduce the intensity of the gamma fiber.

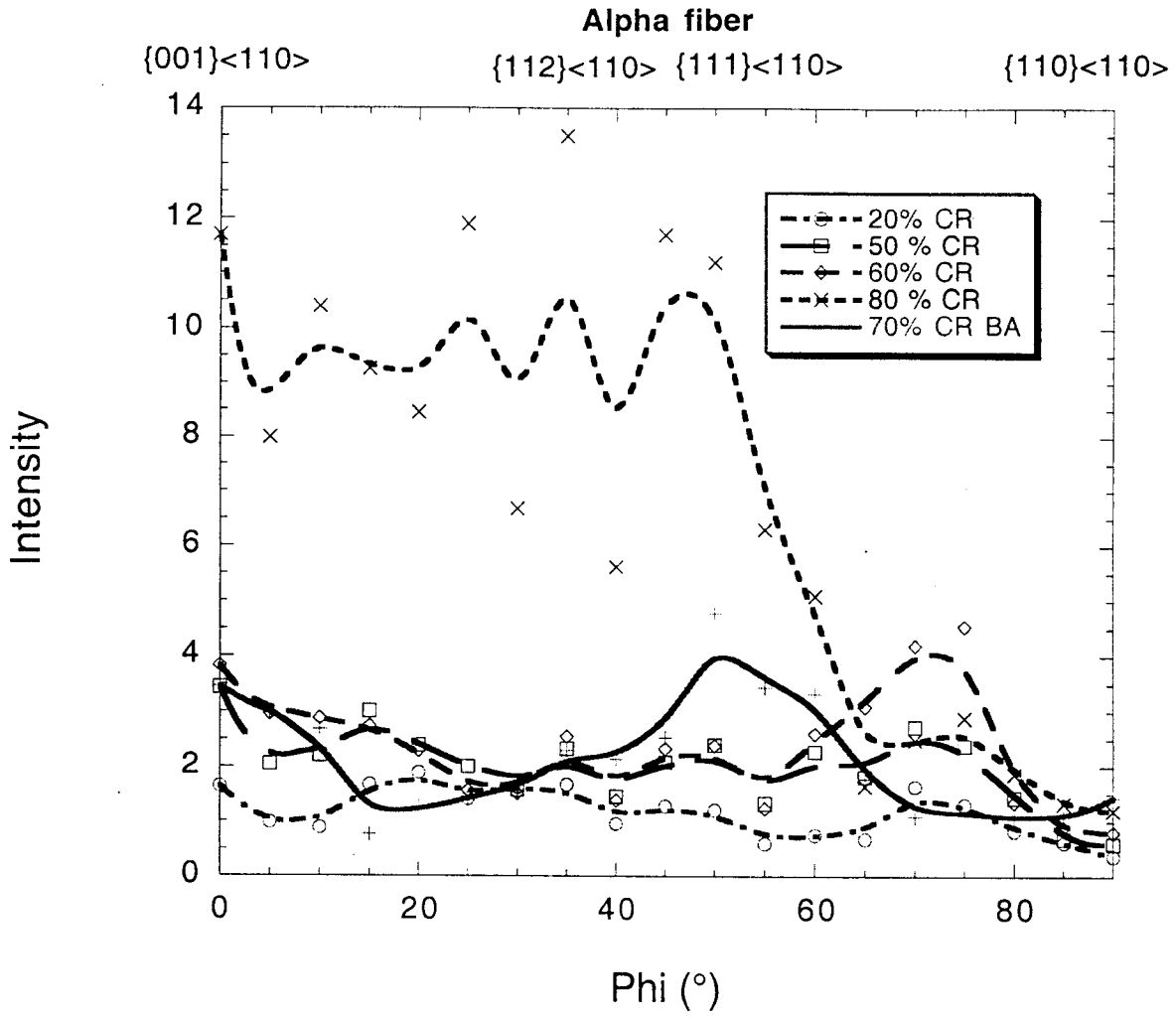

Figure 4-3 b. Showing intensities along the alpha fiber (<110> // Rolling direction) with various reductions in thickness in cold rolling and also cold rolled and annealed. Annealing lowers the intensity on the alpha fiber to levels similar to undeformed material.

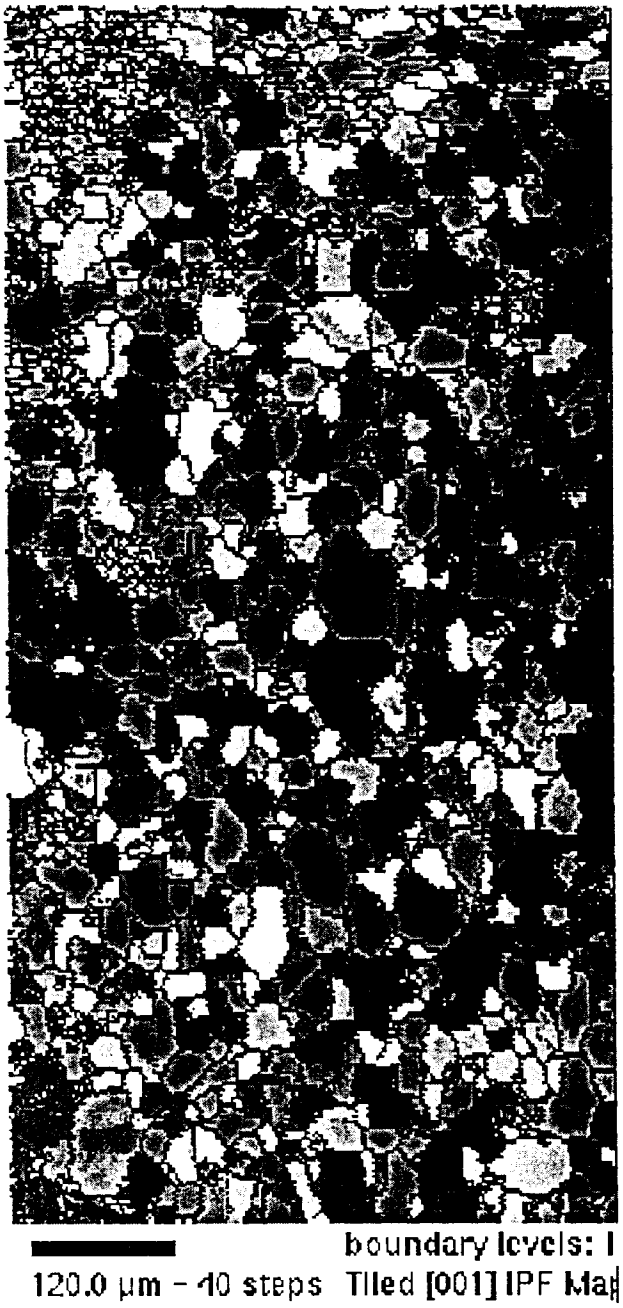

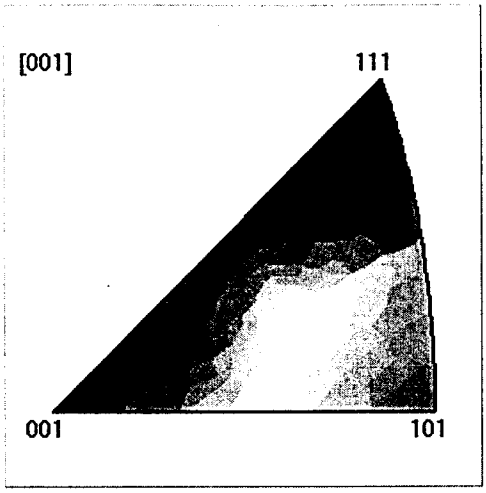

Fig 4-4: Grain mapping of cold rolled batch annealed conventionally cast US Steel under OIM with respect to their orientations parallel to the normal direction. Rolling direction is vertical and transverse direction is horizontal.

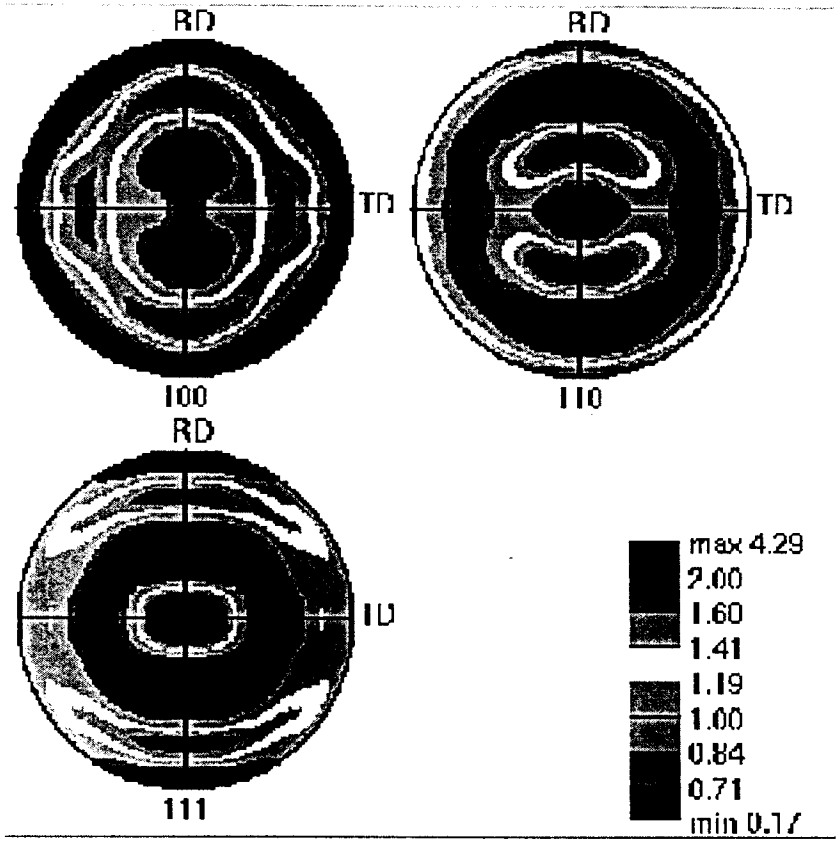

Fig. 4-5: Pole Figures for US Steel sample obtained from orientation imaging microscope.

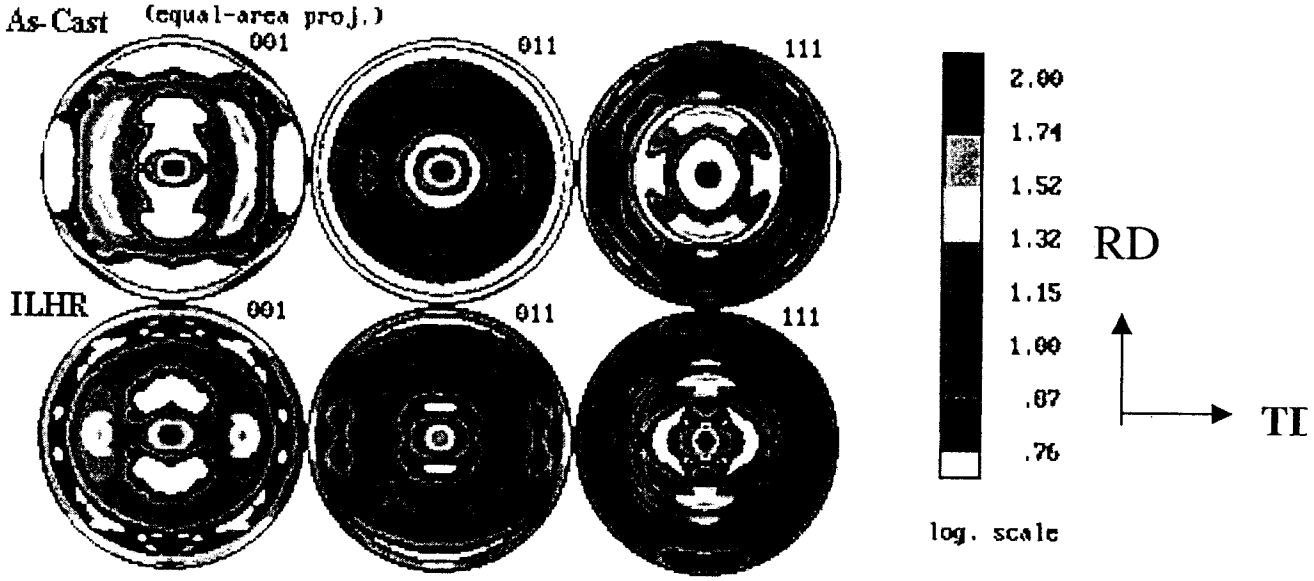

Figure 4-6: Pole figures for as-cast and in-line hot rolled samples

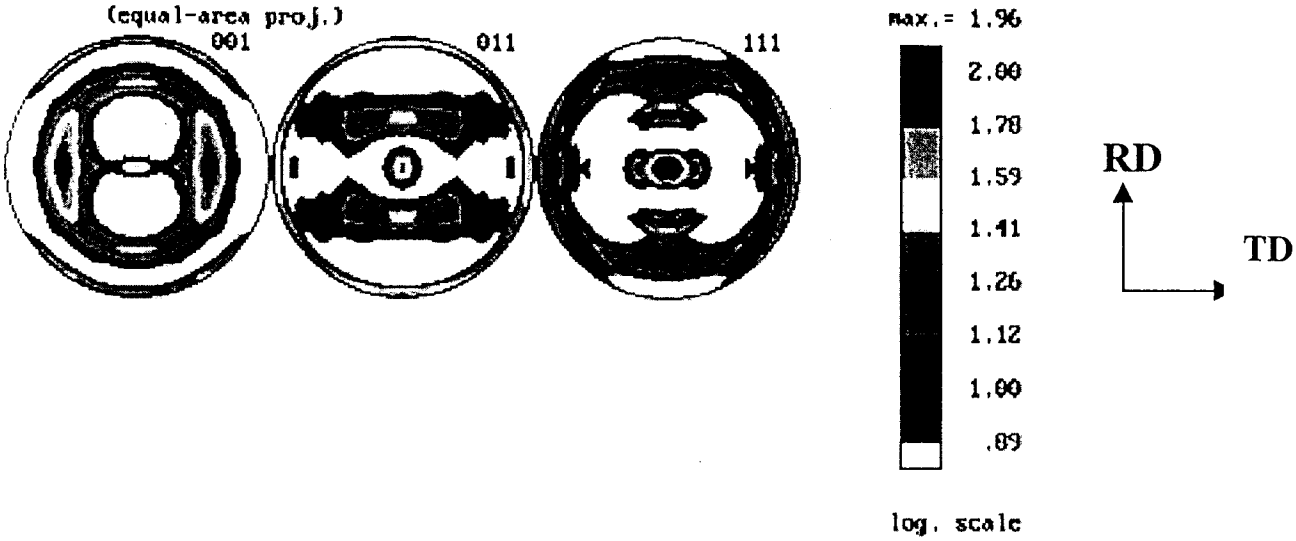

Figure 4-7: Pole figures for 70% cold rolled, batch annealed sample

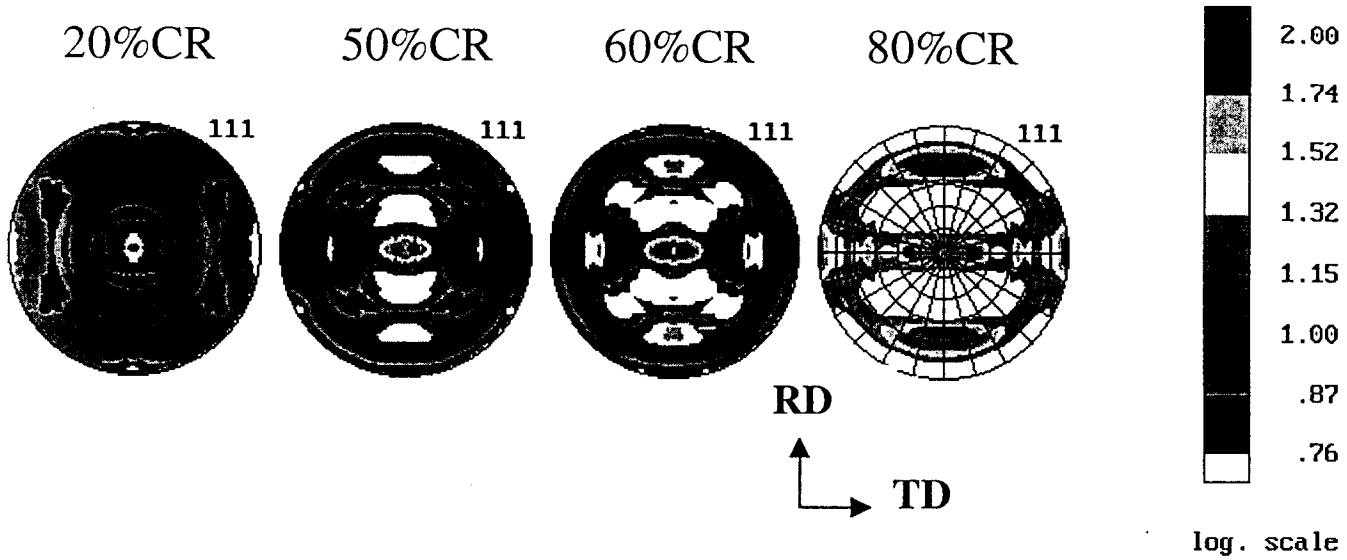

Figure 4-8: (111) pole figures for 20%, 50%, 60% and 80% cold rolled strip cast samples to show the evolution of gamma fiber

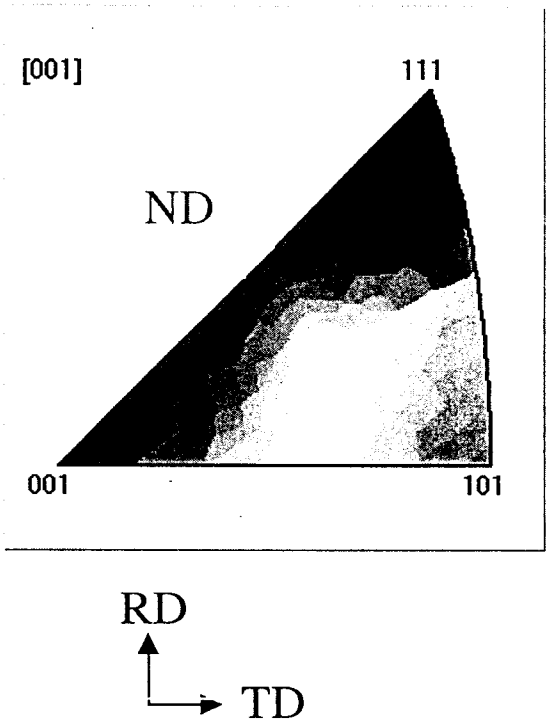

Figure 4-9: OIM Mapping of grains with respect to their orientations parallel to the normal direction. Different colors of grains indicate the different orientations present in the sample.

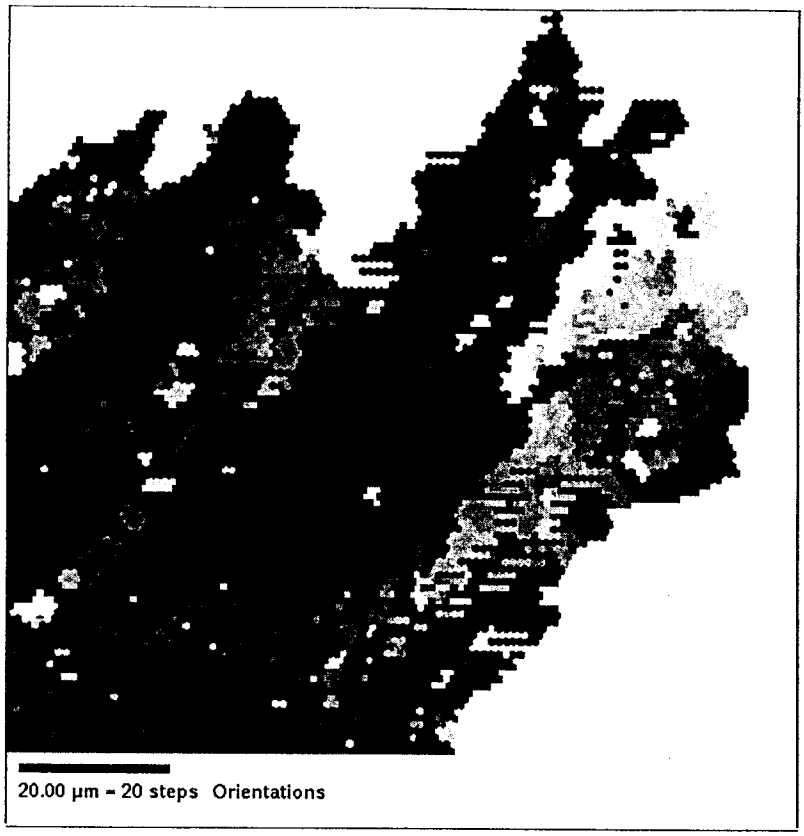

Figure 4-10: OIM mapping in a region dominated by Widmanstätten ferrite, shaded within a tolerance of 10° of a selected orientation inside the Widmanstätten ferrite structure.

Summary

The various observations in this project related to microstructure, texture and anisotropy can be summarized as follows.

- Strip cast steel has an acicular, Widmanstätten ferrite grain structure compared to polygonal ferrite observed in the conventionally cast and hot rolled steel. This microstructure is consistent with previous observations of low carbon steels that have been rapidly cooled through the gamma to alpha transformation as in the heat affected zone of a weld, for example.
- The material supplied by British Steel exhibited a mixture of Widmanstätten and polygonal ferrite indicative of lower cooling rates than for the material from "Company B."
- Cold rolling induces the typical texture observed for low carbon steels with development of a moderately strong γ-fiber, i.e. <111> // ND.
- Annealing of the cold rolled sheet does not change the gamma fiber intensity but lowers the alpha fiber intensity. This behavior is typical in low carbon steels.
- Cold rolled, batch annealed sheet shows mild development of the γ-fiber, i.e. <111> // ND, so that its r-value (of slightly over one) is comparable to that of conventionally cast Si-killed steel.
- Cold rolled, batch annealed sheet has promising ductility (close to 50%), and reasonably high strength.
- In-line hot rolling with the current processing parameters does not increase the ductility or r-value of the as-cast sheet.

Appendix 5: Confocal Experiments

5.1 Introduction:

In order to better understand the melting solidification behavior of the material, confocal scanning laser microscopy (CSLM) was employed. CSLM facilitates direct in-situ observation of the metallurgical melts at temperatures as high as 1700° C. The 1LM21H microscope, equipped with features of CSLM was installed within Carnegie Mellon University in 1998.

All the experiments discussed below involve melting a small piece of metal kept in an alumina crucible of inner diameter 4 mm and observing from the top using CSLM. All the heat required for the process is supplied from a bulb by converging all the light from it on the metal. A He-Ne laser with wavelength 692 nm serves to illuminate the surface. The laser beam strikes the plane it is focused at and the reflected signals reaching the detector are integrated on a TV monitor. A pinhole aperture makes sure that any beam reflected from a plane not in the focus is obstructed from hitting the detector. Only one point is observed at a time and the whole sample surface is scanned to give a complete real time image.

In the last few years, CSLM has been applied to various interesting application in high temperature metallurgy. [Ref. 5-1 to 5-6].

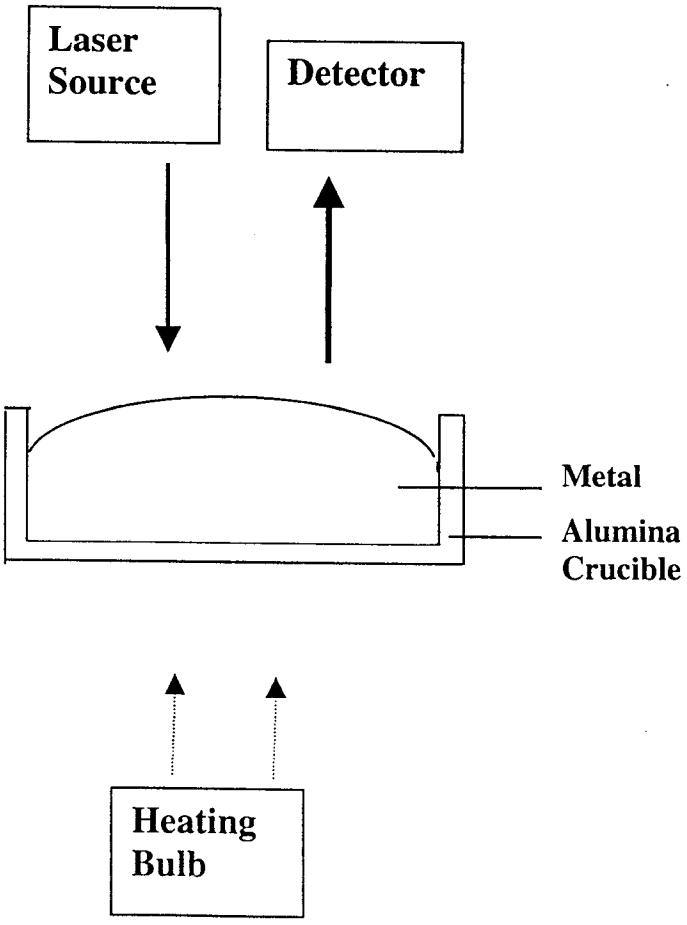

Figure 5-1: Schematic of confocal laser scanning microscope set up

The various phenomena observed using CSLM have been divided into three categories.

5.2a: Movement of liquid inclusions in molten steel:

Strip cast metal was heated above its melting point. At temperatures close to 1650 C, large number of liquid inclusions were observed to emerge from close to the crucible-metal interface and move towards the center of the melt. Originally < 2-3 μm , these inclusions would then agglomerate into sizes as big as 30-40μm.

When the melt was cooled a reverse phenomena was observed. At around 1590 C, inclusions were observed to move from the center of the melt to the periphery (crucible-metal interface).

The driving force behind this motion appears to be Marangoni flow. On heating the inner melt is at higher temperature than the outer melt closer to the crucible while the situation is reversed when cooling. Changes in temperature could cause change in surface tension thus leading to flow of inclusions to minimize surface energy.

The observations also highlight the importance of metal-crucible interactions. The role of crucible material in the flow of liquid inclusions can not be ruled out. In an actual strip caster, hot metal is in contact with edge-dams, made of refractory material, and thus any metal-refractory interplay can have important effect on the process control as well as the quality of the product.

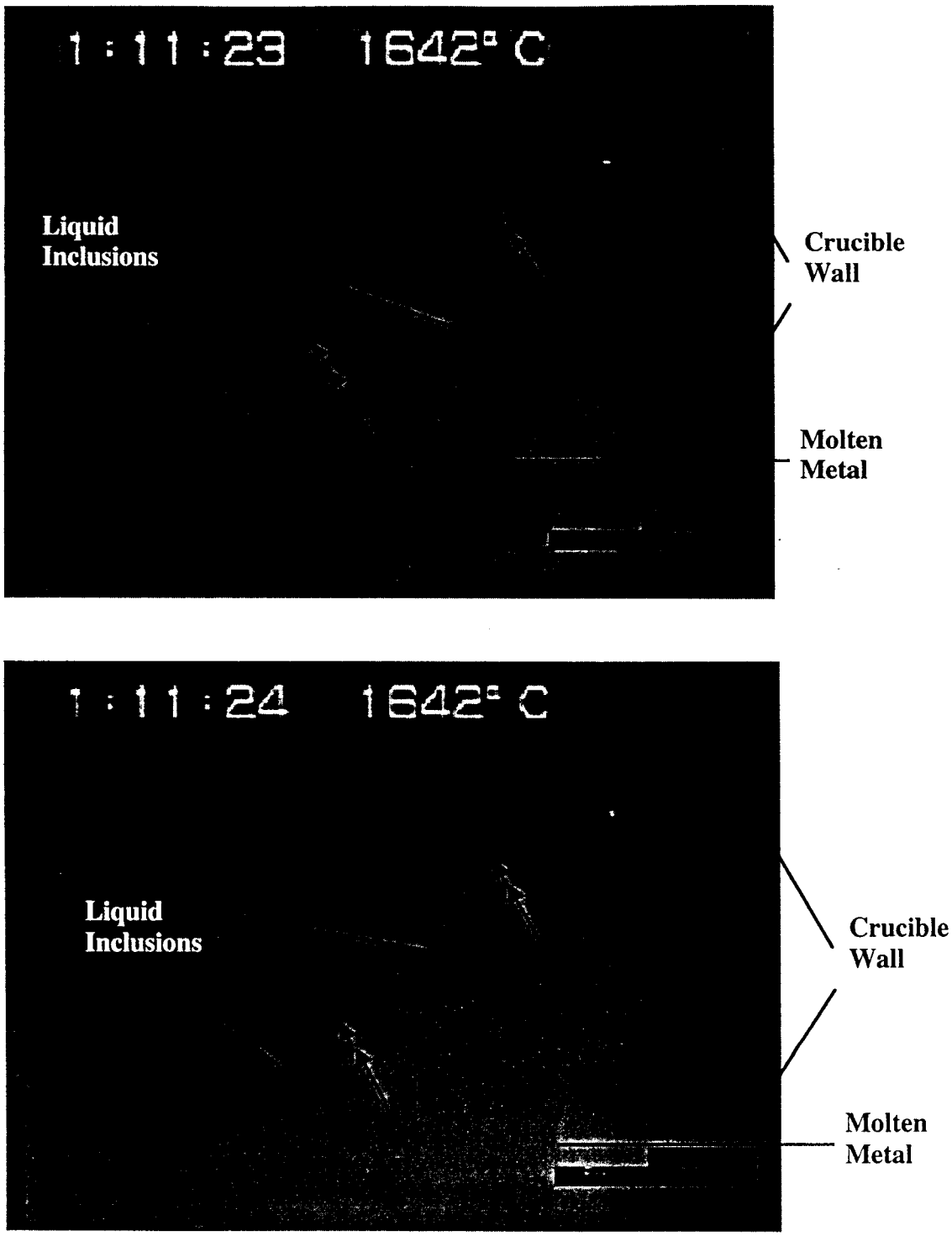

Figure 5-2: Liquid inclusions coming out from the crucible-metal interface on heating

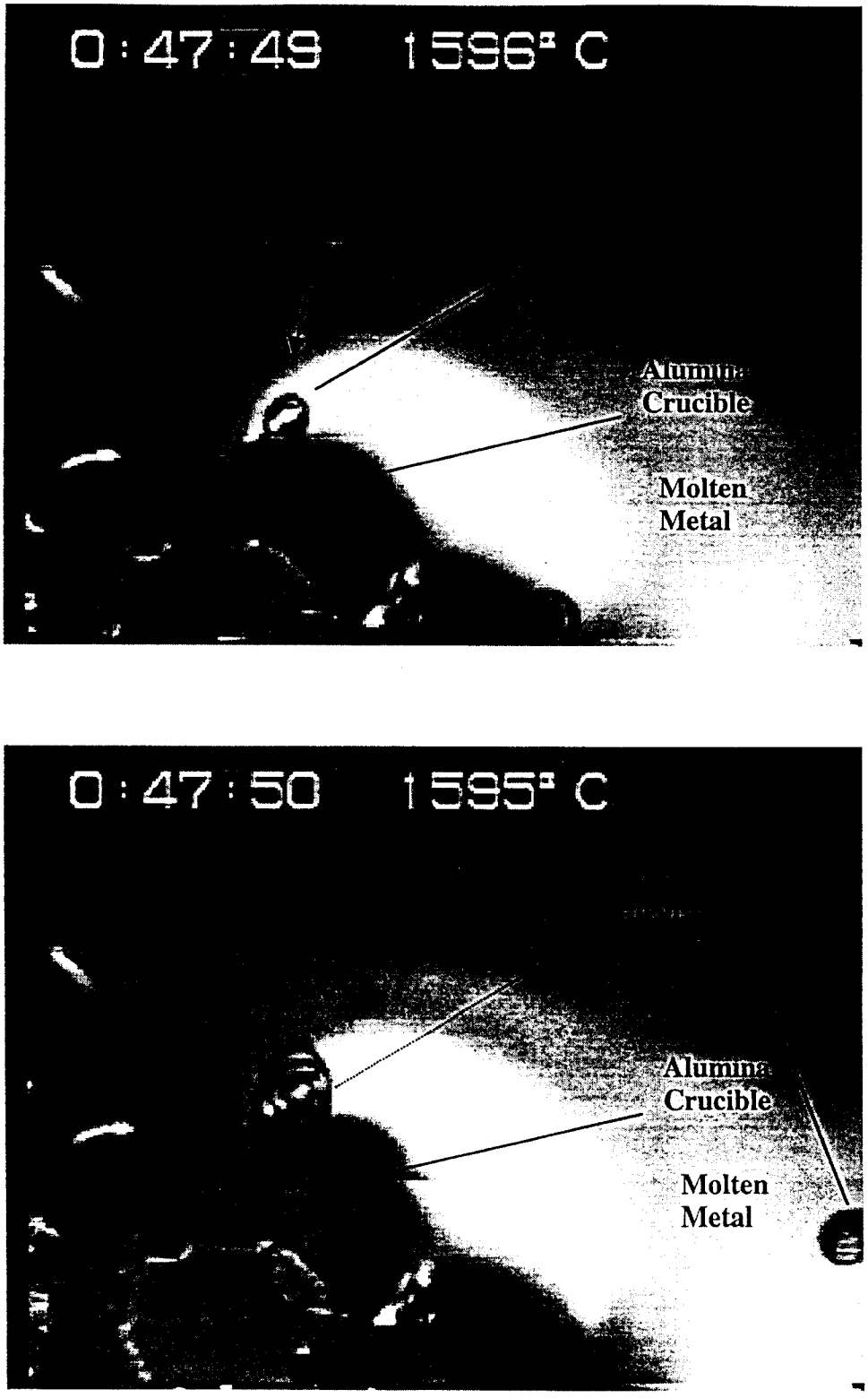

Figure 5-3: Liquid Inclusions going back to the crucible-metal interface on cooling

5.2b: Inclusion Agglomeration:

In the molten metal pool it was easy to observe liquid inclusions agglomerating. These liquid inclusions are present as lens-like particles on the surface of the metal. Since the thickness of these inclusions is very small, it leads to observation of light and dark bands due the constructive and destructive interference.

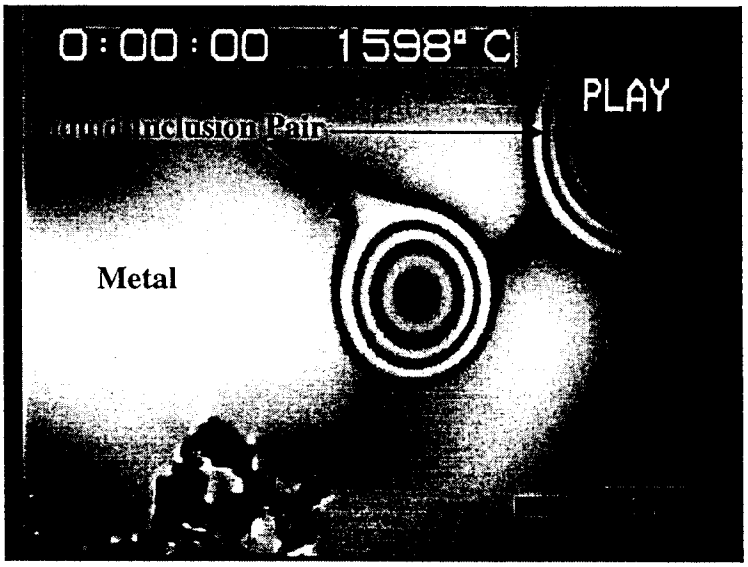

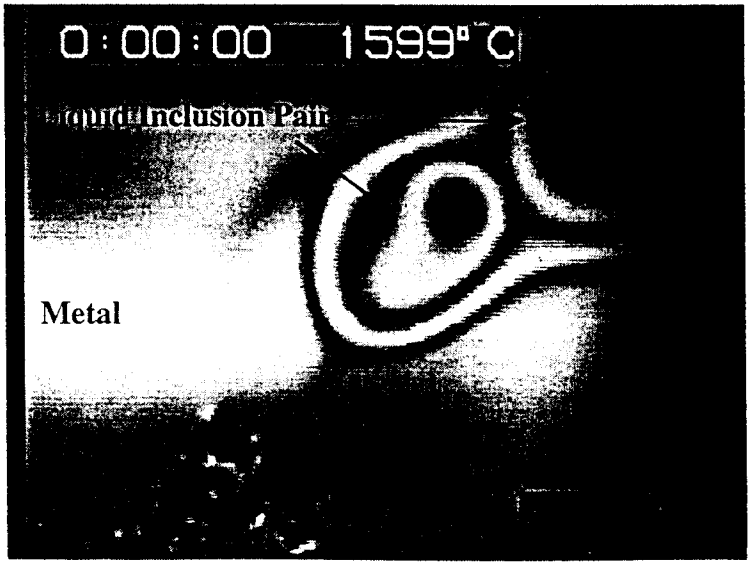

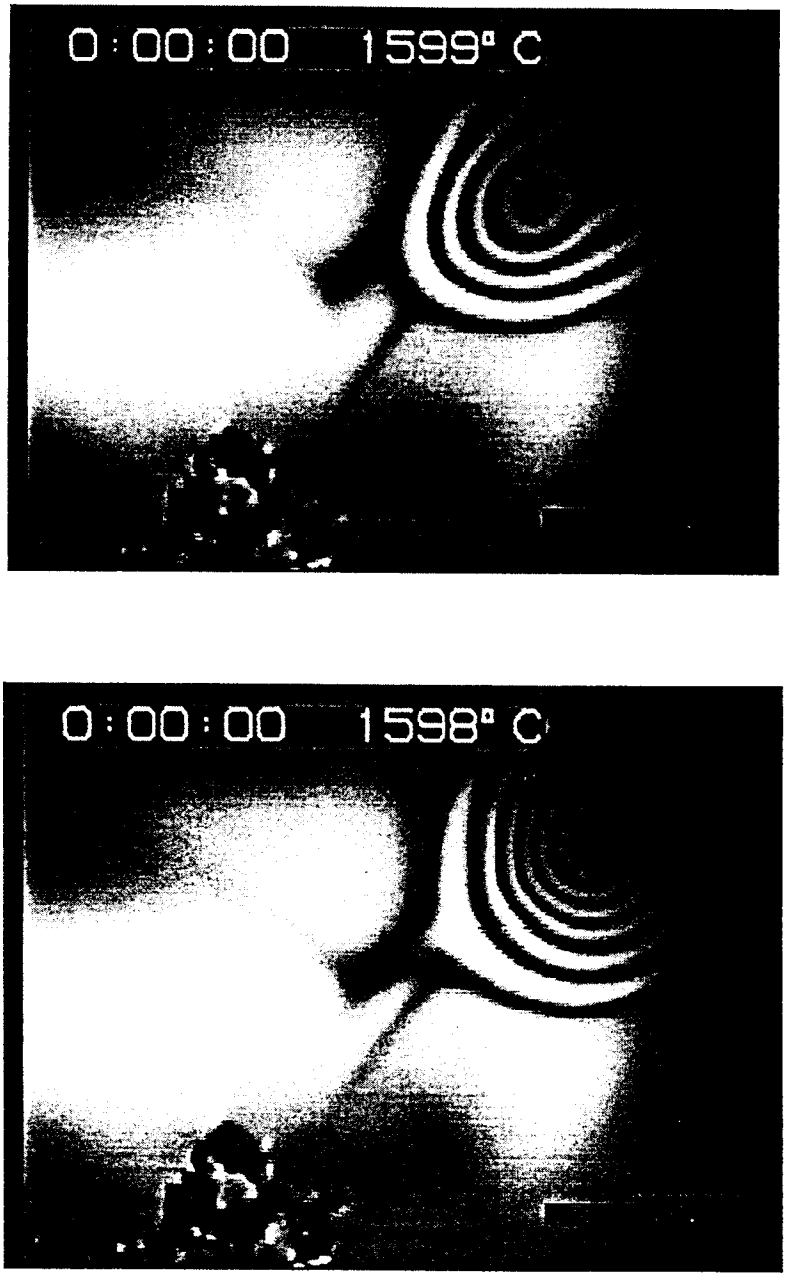

Figure 5-4: Series of pictures showing agglomeration of two liquid inclusions sitting on the surface of molten metal.

5.2c: Liquid film covering the surface of the melt:

After metal was cooled from the molten state on which it solidified, its surface was observed to be covered with a liquid film. The liquid film solidifies at a lower temperature, in the vicinity of 1350 C.

EDX analysis of the film revealed the presence of Mn-Si-O in it. Liquid films like these have been reported elsewhere too [Ref. 5-7] and CSLM videos together with EDX results indicate that their source lies in the natural inclusions content of the material.

These liquid films can have an important effect on the heat transfer during solidification. Metal shrinks after solidification thereby creating an air gap between the solidifying shell and the copper rolls. This air gap offers the greatest resistance to the heat transfer from the metal to the copper rolls. However a liquid film sitting on the surface of the metal can fill up this air gap, consequently increasing the heat flux. It is to be noted that in strip casting conditions the surface flux is very high (15 MW/m^2) and the solidification time are as low as a few hundreds of milliseconds. Thus liquid films can make a significant difference in the heat transfer capacity of the caster.

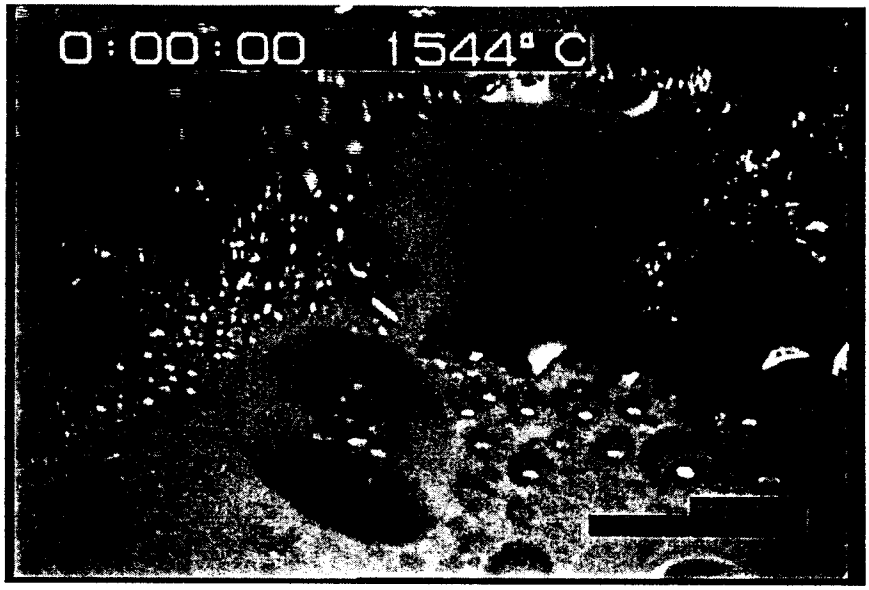
0:00:00 1544° C

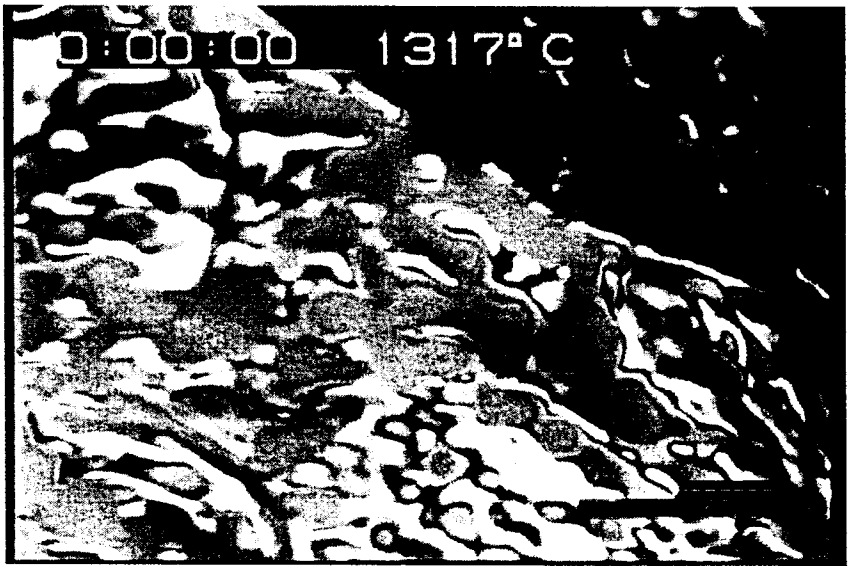
0:00:00 1317° C

Figure 5-5: Precipitation of surface liquid film from molten metal. As the molten metal (A) is solidified and subsequently cooled to low temperature (B), the film separates out and solidifies (C).

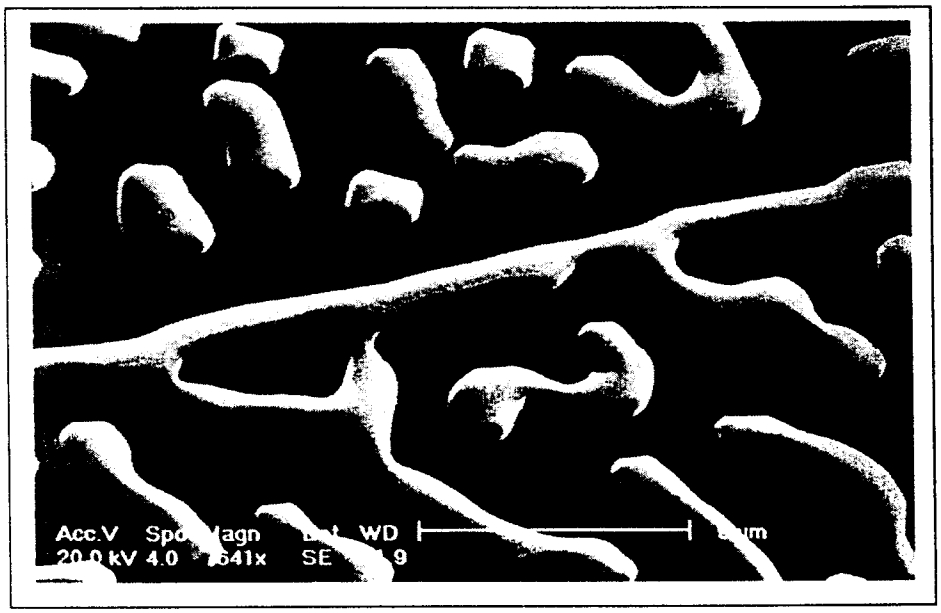

Figure 5-6: SEM picture of the sample after the experiment shows the solidified film. EDX analysis indicates their origin in the natural inclusion content of the material

References:

5.1 Hongbin Yin, Hiroyuki Shibata, Toshihiko Emi and Mikio Suzuki, *In-situ observation of collision, agglomeration and cluster formation of alumina inclusion particles on steel melts*, ISIJ International, Vo. 37 (1997), No. 10, pp. 936-945.

5.2 Hongbin Yin, Hiroyuki Shibata, Toshihiko Emi and Mikio Suzuki, *Characteristics of Agglomeration of Variaous Inclusion Particles on Molten Steel Surface*, ISIJ International, Vol. 37, 1997, No. 10, pp.946-955.

5.3 Toshihiko Emi, *Interfacial phenomena in refining of steel melt*,2000 Belton Symposium Proceedings, pp. 195-207.

5.4 P. Misra, V. Chevrier, S. Sridhar and A. W. Cramb, *In situ observations of inclusions at the Mn-Si killed steel/CaO-Al_2O_3 interface*, Metallurgical and Materials Transactions B, Vol. 31B, October 2000, pp. 1135-1140.

5.5 P. Misra, S. Sridhar and A. W. Cramb, *In-situ observation of TiN precipitates at stainless steel/CaO-Al_2O_3-MgO-SiO_2 Interface*, Metallurgical and Materials Transactions B, to be published.

5.6 S. H. Lee, C. Tse, K. W. Yi, P. Misra, V. Chevrier, C. Orrling, S. Sridhar, A. W. Cramb, *Separation and dissolution of Al_2O_3 inclusions at slag/metal interfaces*, Journal of Non-crystalline Solids, 282 (2001), pp. 41-48.

5.7 Les Strezov, Joe Herbertson and Geoffery R. Belton, *Mechanisms of initial melt/ substrate heat transfer pertinent to strip casting*. 2000 Belton Symposium Proceedings, pp. 289-299.

Appendix 6: The Effect of Oxide Films on Heat Transfer Rate

The Effect of Surface Tension, Superheat and Surface Films on the Rate of Heat Transfer from an Iron Droplet to a Water Cooled Copper Mold

Natthapong Phinichka

Department of Materials Science and Engineering
Carnegie Mellon University
Pittsburgh, Pennsylvania

July 25th, 2001

Committee : Prof. Alan W. Cramb (MSE, Advisor)
Prof. Cristina H. Amon (ME)
Prof. Richard J. Fruehan (MSE)
Prof. Sridhar Seetharaman (MSE)

Submitted to Carnegie Institute of Technology
in partial fulfillment of the requirements of the degree of
Doctoral of Philosophy in Materials Science and Engineering

Table of Contents

List of Figures

List of Tables

Chapter 1

Introduction

In the past decade attempts to improve the economics of steel production have been directed towards casting processes[1] and, as a result, the direct casting of steel strips has been developed. This process is attractive because it decreases the investment cost of the steel-making process as there is a possibility that slab re-heating and hot-rolling can be eliminated and that coiled strip with the properties and geometry of hot rolled strip can be produced in one step. According to calculations by Emoto et al. the energy saved by strip casting can be up to 800 KJ/ton compared to the conventional continuous casting process.[2] The potential investment cost savings for strip casting is quite high. Operating cost savings are however more modest as the benefit is in the elimination of reheating and hot rolling. For carbon steels potential savings could be of the order of $25 per ton; however, details of actual operating cost savings have yet to be documented.

Unlike conventional continuous casting, strip casting is carried out without mold flux to moderate the heat transfer and the cast surface becomes the product surface. No steel casting process, before strip casting, ever used the cast surface as the product surface. Due to this fact, strip that is directly cast must have the shape and geometrical tolerances normally found during hot-rolling as a treatment of the cast surface is not possible after casting. For the strip casting process, it is, therefore, very important to obtain a uniform thickness in order to prevent surface cracks, laps and marks and to avoid surface shrinkage that could lead to porosity and internal shrinkage cavities.

The most important factor that influences strip casting surface quality is the heat transfer rate during the early stage of the solidification as the details of surface formation will be determined by the initial heat transfer rate and the fluid flow conditions at the meniscus. High heat fluxes may cause wrinkling of the steel strip and an uneven transverse heat transfer between casting and roller could lead to defects on the cast strip.

The behavior of a liquid steel droplet upon contacting a mold (where it impinges, spreads and solidifies on a copper substrate) is relevant to strip casting manufacturing processes. At the point of contact between the steel meniscus and the rotating mold, fresh liquid steel continuously contacts a copper chill mold. Thus the phenomena that occur during this process are similar to that found when a droplet is ejected and spreads on a substrate. In this study, steel alloys are melted and then ejected onto the copper chill. Droplet spreading and solidification behavior determines the roughness of the cast surface.

A study of transient heat transfer between the molten droplet and the copper chill mold at the early stage of solidification will allow one to understand its profound influence on the solidification behavior and surface quality of cast products. The main goal of this work is to develop fundamental understanding of factors controlling strip casting and the primary objective of this study is to better understand the role of processing parameters such as superheat, steel chemistry and mold surface condition on initial solidification phenomena, heat transfer rate and the formation of the cast steel surface.

Chapter 2

Literature Review

To understand strip casting fundamentals, the heat transfer behavior between a molten metal and a water-cooled copper mold must be studied. Several researchers have focussed on transient heat transfer behavior in the early stage of solidification of a metal alloy on a metal substrate. In the following reviews three different kinds of topic will be discussed.

The first topic is the technique to determine the initial heat transfer behavior between a molten metal and metal substrate. Each technique will be summarized and discussed in detail.

The second topic will be focused on how the process variables affect the initial heat transfer and solidification behavior. The following issues will be discussed in this section.

1. The chill mold
2. The metal-mold interface condition
3. Alloy composition
4. Superheat
5. Microstructure

The third topic is the mathematical model used to estimate the interfacial heat transfer rate through the metal-mold interface.

2.1 Technique for determination heat flux and heat transfer coefficient during the initial solidification process

During a solidification process, one of the factors that influences cast microstructure and the surface quality of cast products is the magnitude of the heat transfer rate during the initial solidification process. To prevent crack formation, control cast structure and promote uniform shell growth, the heat transfer rate during a casting process has to be well controlled.[3)] A number of researchers have attempted to study initial solidification phenomena. Some of their studies have been carried out with laboratory scale experiments while others have used prototype twin rolls casters. The solidification of metals is mainly dependent on the heat flow from a metal to a mold that is in turn proportional to an overall heat transfer coefficient h. Therefore in this section several techniques that were used to determine the initial heat transfer behavior during a casting process are reviewed.

Ho and Pehlke[5)] used two different techniques to determine the interfacial heat transfer coefficient between an aluminum based alloy and a copper mold.

The interfacial heat transfer coefficient, h, was determined from the computer solution of an inverse heat conduction problem by using the temperature profile measured at the selected position in a casting and mold. A relationship between calculated h and time is shown in Figure 2.1. A computer program in Pascal language was written to solve the inverse heat conduction problem. The solution of the inverse heat conduction depends on the minimization of the function $F(h)$ shown in equation 2-1.

$$F(h) = \sum_{i=1}^{N_1 N_2} (T_i - \theta_i)^2 \qquad \textbf{2-1}$$

Where Ti and θi = Calculated and measured temperature at various thermocouple locations and times.

N_1 = Number of finite difference time steps per temperature measurement.

N_2 = Number of temperature measurements per interval over which the derived heat transfer coefficient is constant.

To find the correction of the heat transfer coefficient at each iteration step the function is minimized by an iterative procedure using a Taylor series expansion and also by applying the condition of $(\partial F / \partial h = 0)$ to the equation 2-1.

$$T_i(n+1) = T_i(n) + \frac{\partial T_i(n)}{\partial h_i(n)} (T_i(n+1) - T_i(n))$$

The interfacial heat transfer coefficient was derived from heat transfer data across the static gap where the variation of its size was measured by two transducers during the experiments. The conductive heat transfer coefficient h_c can be calculated from the equation 2-2

$$h_c = \frac{k_g}{x_g} \qquad \textbf{2-2}$$

k_g = The average thermal conductivity of gas in the gap.

x_g = Gap width.

They found that the interfacial heat transfer coefficient determined from two different methods were in a reasonable agreement and that they could provide further insight into the characteristic of gap formation. By both methods the interfacial heat transfer coefficient had a maximum value of 2000 W/m^2K, in about 100 seconds.

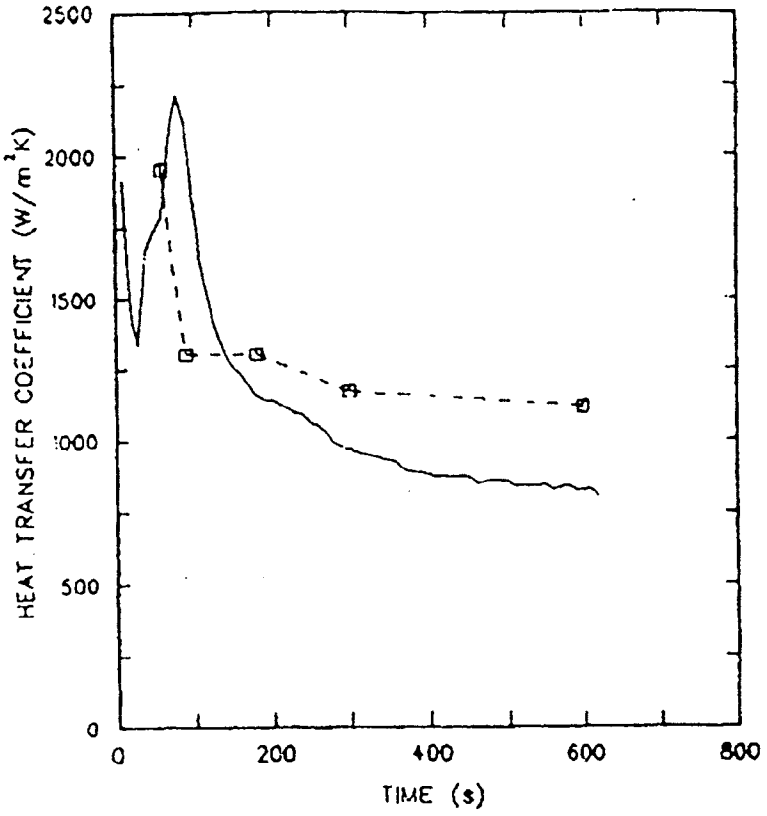

Figure 2.1 The relationship between the heat transfer coefficient and time. Solid lines represent the results obtained by solving the inverse heat conduction problem. Dashed lines represent the values calculated from interfacial gap widths.[5]

Nishida, Droste and Engler[6] designed an experiment, Figure 2.2, to determine the heat transfer coefficient at the casting-mold interface with the present of air gaps. They used both pure aluminum and aluminum with 13.2% silicon to study the air-gap formation process at a casting mold surface and the heat transfer mechanism through the gap. They measured 1) the displacements of both casting surface and mold surface during the solidification process 2) the temperature profiles in the casting and mold. The heat transfer coefficients, h, at the casting- mold interface can be determined from both measured temperature profiles.

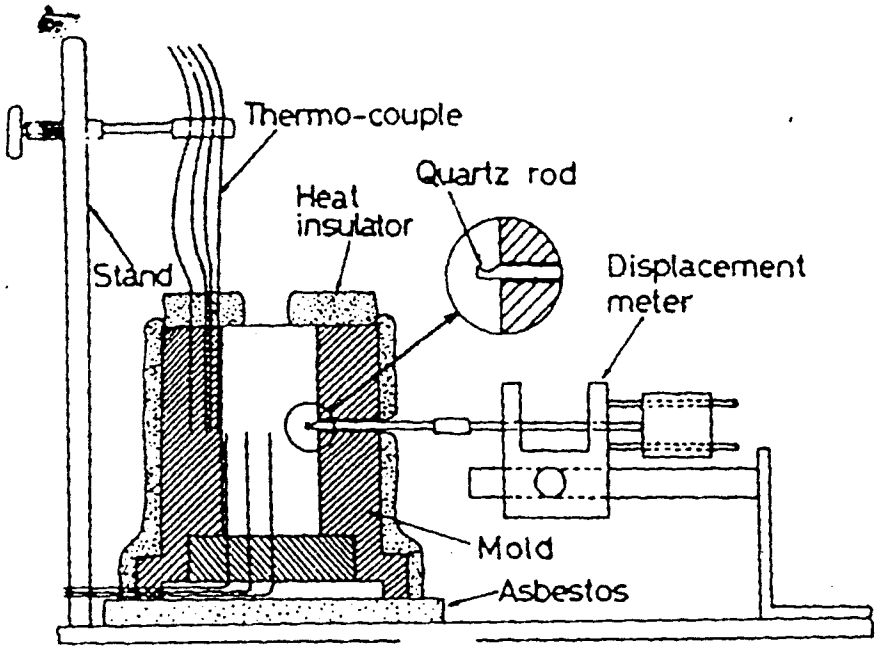

Figure 2.2 Apparatus for measurement of casting displacement and temperature.[6)]

Two kinds of mold were used in this work.

1) For a flat casting, initially, just after pouring, the mold began to move toward a casting, pushing the casting, and the maximum in heat transfer coefficient appeared. After the heat transfer coefficient reached the maximum value the mold moved in a reverse direction and a contraction of casting began. The relationship between the heat transfer coefficient and time for flat casting is shown in Figure 2.3.

2) For a cylindrical casting, the inner surface of the mold began to move outward right after pouring. The casting surface stayed until solidification progress to a great extent then a contraction began. After the contraction began the interfacial heat transfer coefficient decreased quickly. The relation between the heat transfer and time for cylindrical casting is shown in Figure 2.4.

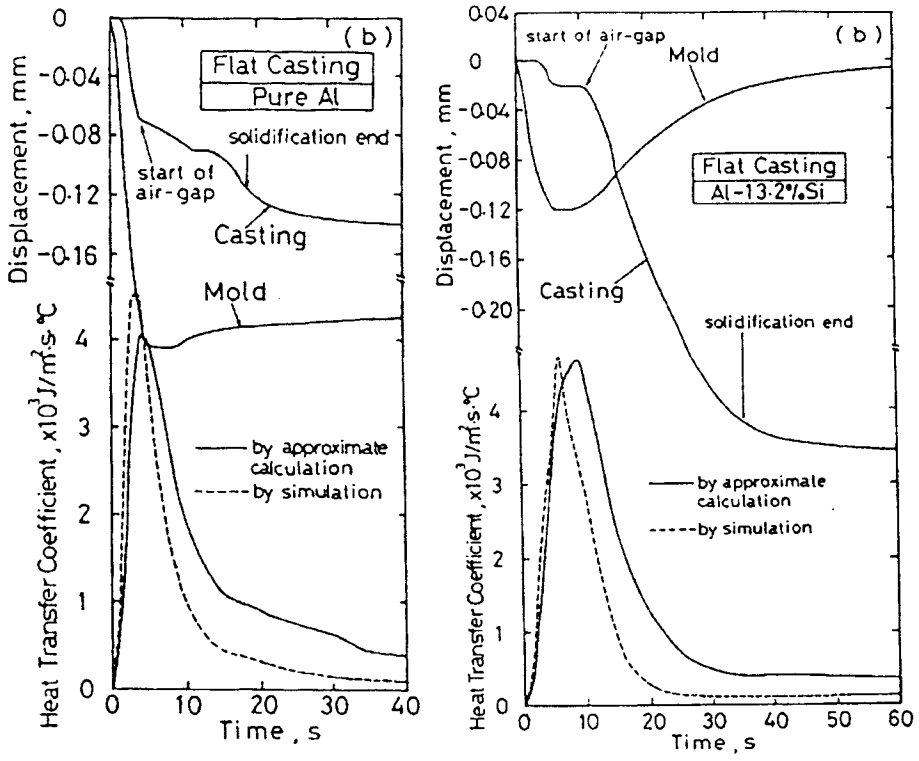

(a)

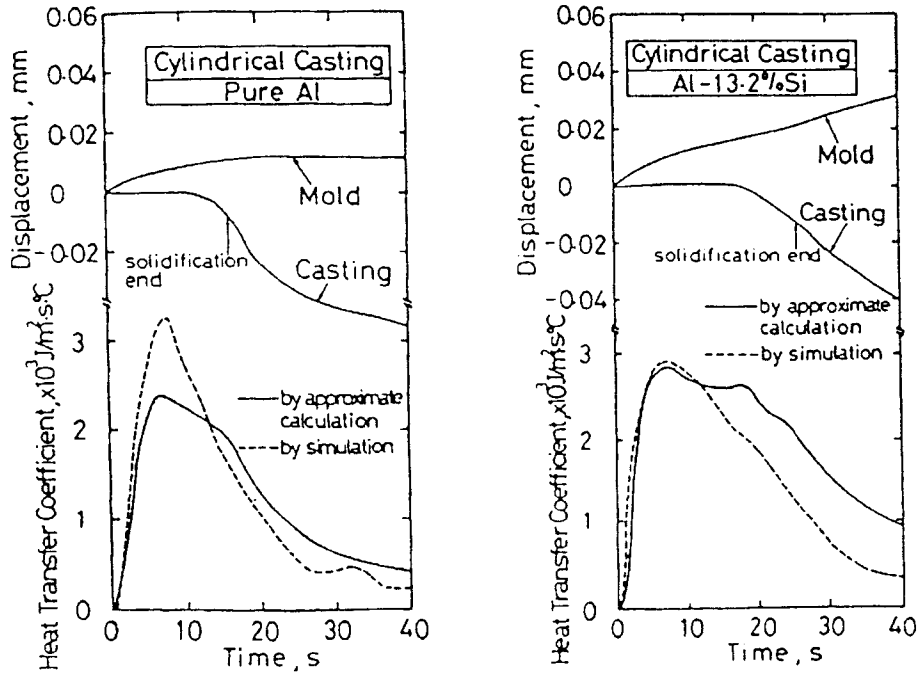

(b)

Figure 2.3(a)-(b) Heat transfer coefficient compare with mold and casting displacement for (a) flat pure Al and Al-13.2%Si casting. (b) cylindrical pure Al and Al-13.2%Si casting.[61]

Mahallawy and Assar[7] evaluated the heat transfer coefficient as a function of time by using a finite difference model for solving a one-dimension heat transfer problem. The aluminum was heated and seated on a copper chill and cooled by a water spray. The experimental apparatus is shown in Figure 2.4. Three thermocouples were inserted into a specimen at different positions and another one was inserted into a copper chill at position 2 mm from the surface. Figure 2.5 shows the cooling curves measured from thermocouples at several positions along the specimen at different chill temperature. It was found that the heat transfer coefficient was found to be a function of time and gap temperature. The heat transfer coefficient reaches its maximum value when the surface temperature is equal to the liquidus temperature of the metal.

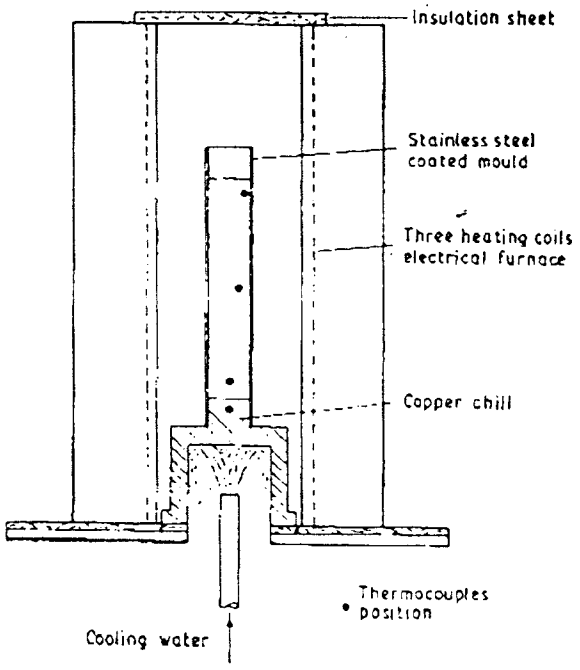

Figure 2.4 Schematic drawing of the experimental apparatus.[7]

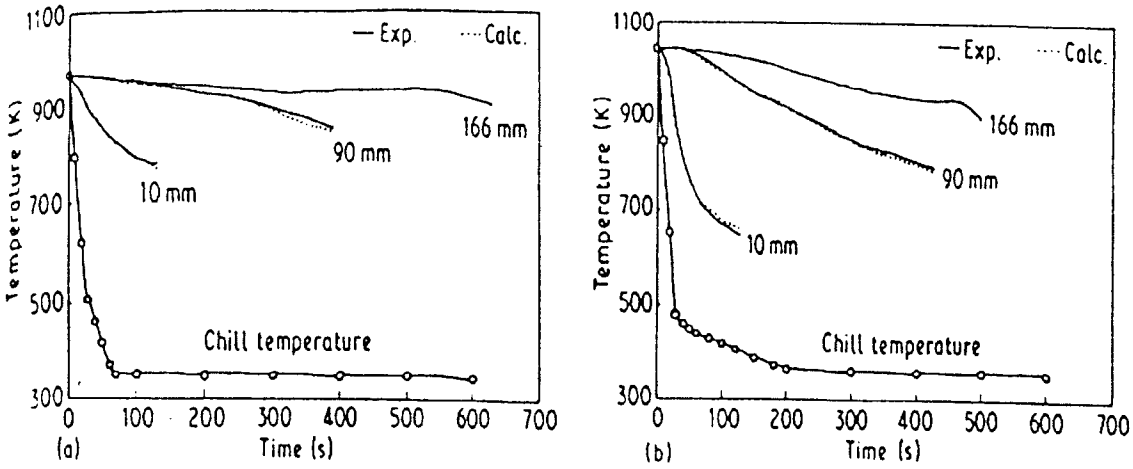

Figure 2.5 Experimental and computed cooling curves of these points along the specimen (1, 90 and 166 mm from the chill) together with chill temp. 40°K and 115°K.[7)]

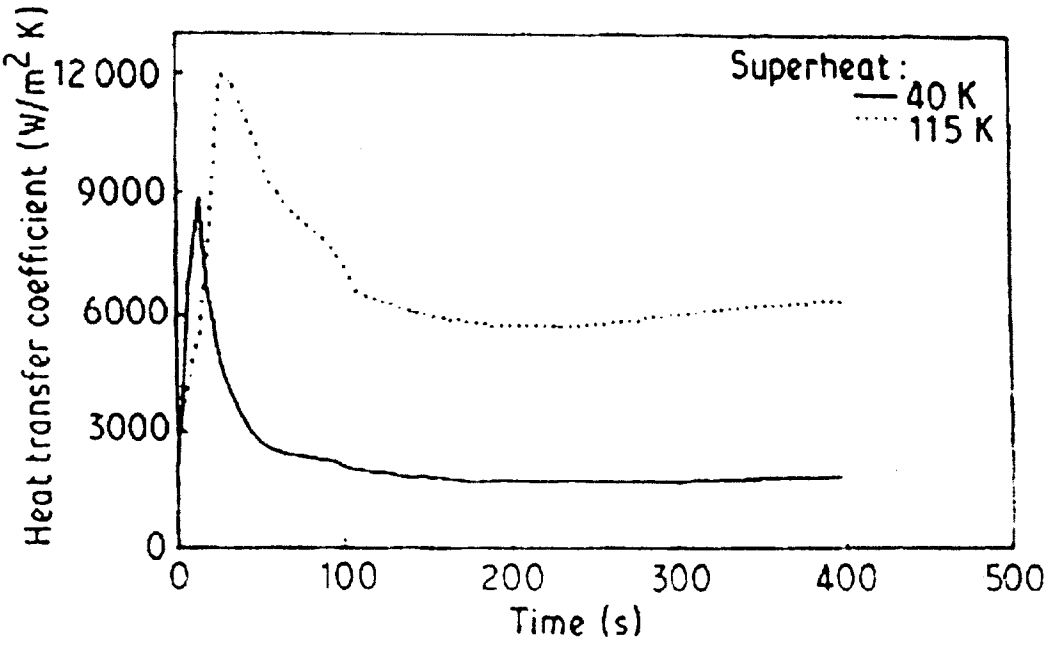

Figure 2.6 The relationship between heat transfer coefficient and time for 40°K and 115°K superheat. [7)]

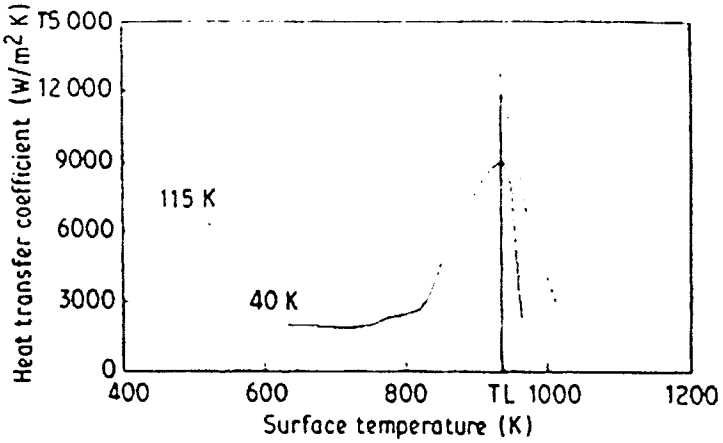

Figure 2.7 The relationship between heat transfer coefficient and surface temperature for 40°K and 115°K superheat. [7)]

The heat transfer coefficient reach a maximum value at 9000 and 12000 W/m^{2}K for 40 K and 115°K melt superheat during the first 20 to 50 seconds, as shown in Figure 2.6 and the relationship between the heat transfer coefficient and the surface temperature is shown in Figure 2.7. The heat transfer from a metal to copper mold through an air gap can be calculated from the equation 2-3 that combines heat conduction, convection and radiation together. However the gap is usually small so that the convection part as indicate by the corresponding Grashof number can be neglected.[5)] The variation of h_{cond} and h_{rad} versus gap temperature is shown in Figure 2.8.

$$h = h_{cond} + h_{rad} = \frac{K_{gap}}{X_{gap}} + \frac{\sigma\left(T_c^3 + T_c^3 T_m^2 + T_m^3\right)}{\left(\frac{1}{\varepsilon_m}\right) + \left(\frac{1}{\varepsilon_c}\right) - 1} \qquad \textbf{2-3}$$

σ = Stefan-Boltzmann constant.

$\varepsilon_m, \varepsilon_c$ = Corresponding emmisivities.

X_{gap} = Gap size.

K_{gap} = Average thermal conductivity of the gas in the gap evaluated from the average temperature of metal surface.

Tc = Chill surface temperature.

Tm = Metal surface temperature.

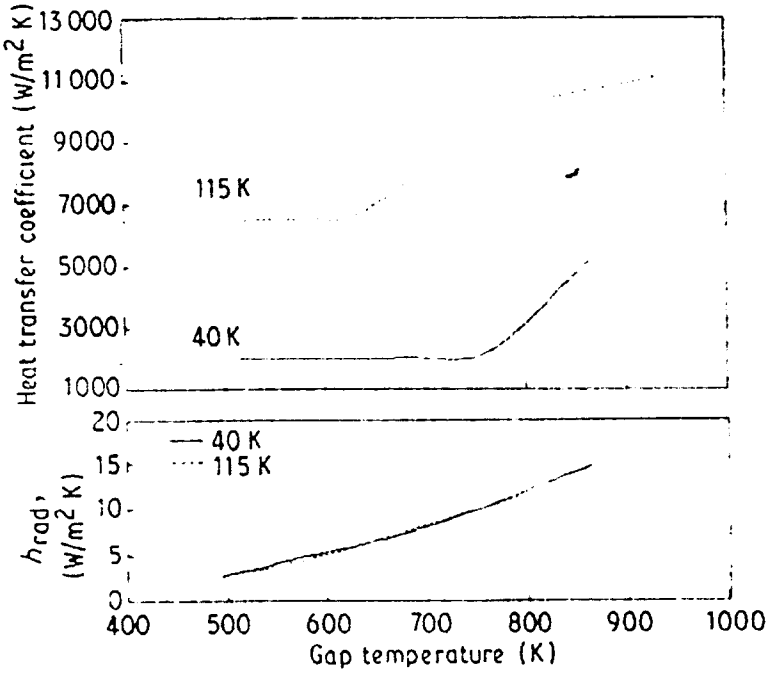

Figure 2.8 The variation of h_{cond} and h_{rad} versus gap temperature.[7)]

Richard Sun[8)] developed a technique to approximate surface conductance, h, for convergent heat flow at the early stage of casting. The schematic of his experimental apparatus is shown in Figure 2.9. His one-dimension heat transfer calculation is based on convergent heat flow into a 1-1/4 inches diameter cylindrical rod. The equation of heat flow, in term of finite difference method, into an infinite cylindrical rod was used as follows and the surface heat conductance, h, was calculated from the heat flow data as follow.

(1) At the center

$$T_{0,n+1} = \frac{4}{M} T_{1,n} + (1 - \frac{4}{M}) T_{0,n}$$

(2) At general intermediate point

$$T_{r,n+1} = \frac{1}{M} \cdot \frac{2 + \frac{1}{r}}{2} (T_{r+1,n} - T_{r,n}) + \frac{2 - \frac{1}{r}}{2} (T_{r-1,n} - T_{r,n}) + T_{r,n}$$

(3) At the surface

$$T_{s,n+1} = \frac{8r - 4}{M[4r - 1]} T_{s-1,n} + \frac{8rN}{M[4r - 1]} T_1 + [1 - \frac{8rN + 8r - 4}{M[4r - 1]}] T_{s,n}$$

Where $M = (\Delta r)^2 . C_p . \frac{\rho}{(k \Delta t)}$

$N = \frac{h \Delta x}{K}$ (Biot Number)

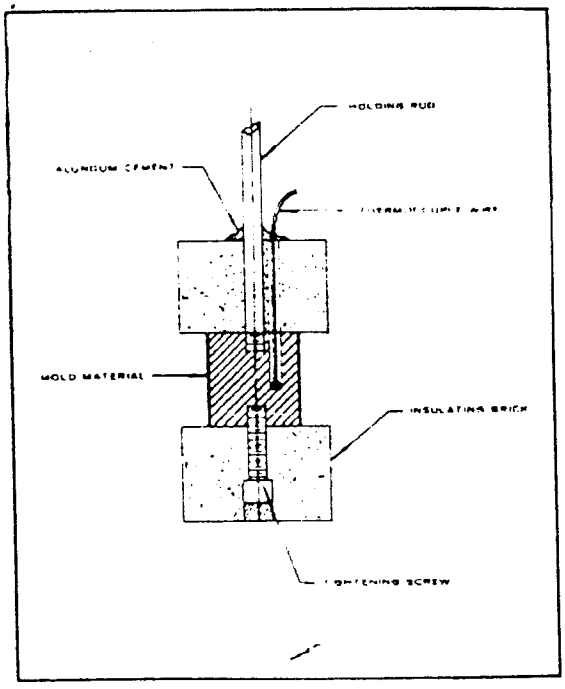

Figure 2.9 The schematic of Sun's experiment apparatus.[8]

The experiments were also conducted in order to compare the observed heating curve with the calculated heating curves. His calculated heating curves are shown in Figure 2.10. He immersed different kinds of samples, made into a rod shape, into a bath of Hastelloy X or Aluminum. He moved the rod continuously and slowly to keep the sample in contact with the molten alloys. A thermocouple was located at the mid-radius of the sample. The calculated and measured heating curves for the uncoated mold show the same value of surface conductance, h. However he proved that the experimental heating curves do not follow any of the theoretical curves assuming constant heat transfer coefficient value, as shown in Figure 2.11, since h values change with immersion time or surface temperature.

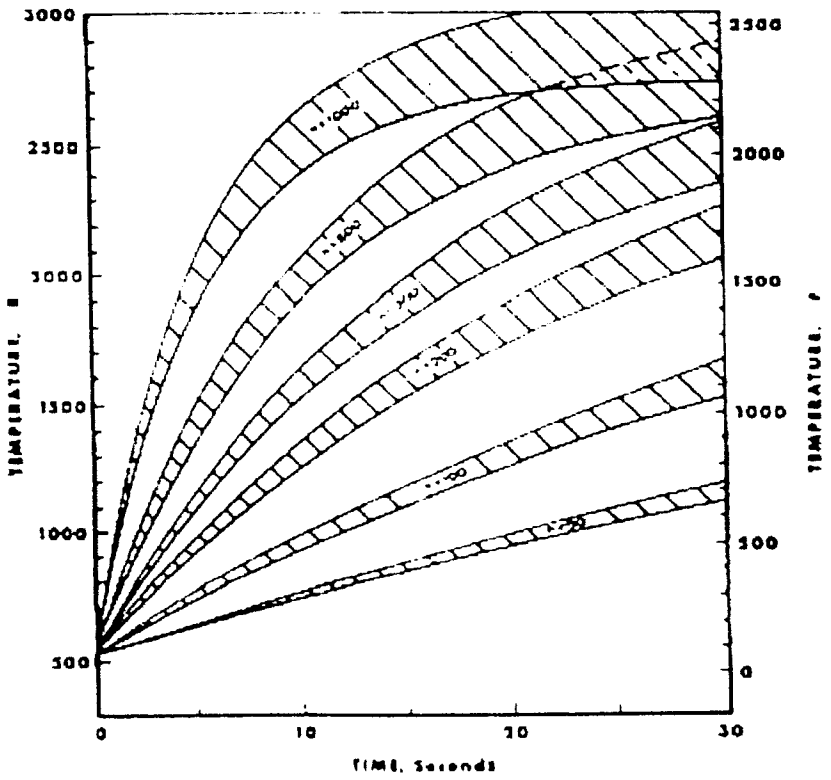

Figure 2.10. Calculated heating curves for copper sample rods immersed in molten metal at 1260°C and 1427°C.[8)]

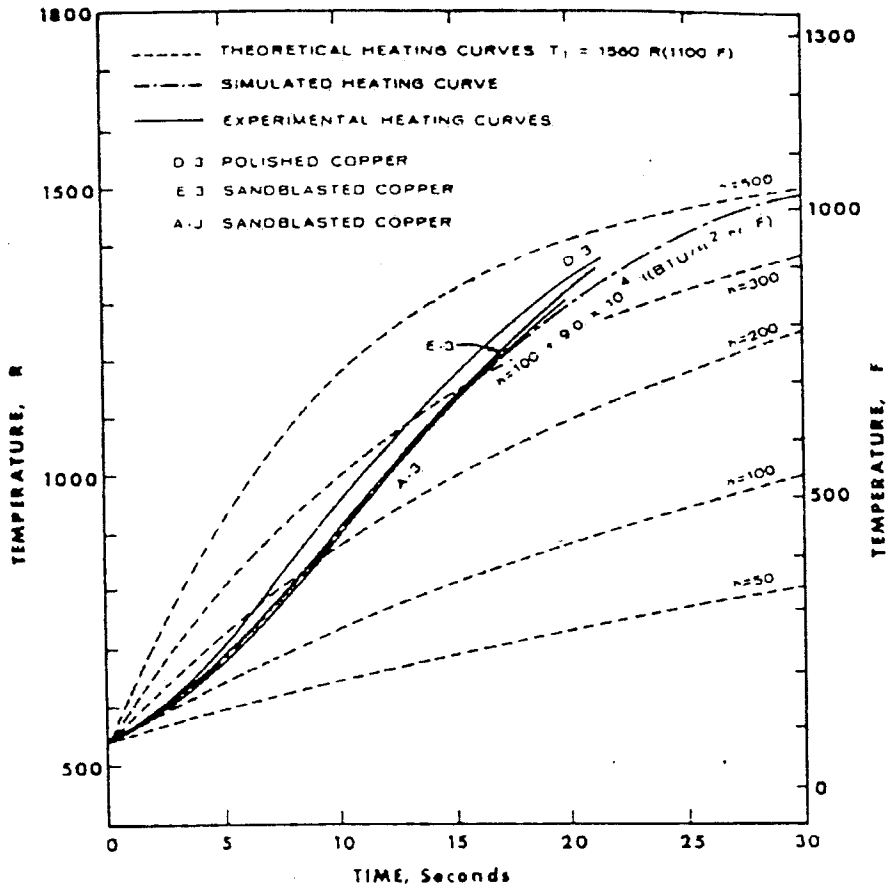

Figure 2.11 Comparing between calculated and measured heating curves for copper rods immersed in molten aluminum at 1250°F (667°C).[8]

Prasana Kuma and Naraya Prabhu[9] poured aluminum based alloys into the mold with a square chill made from different kinds of material located at the end. A thermal history was monitored by thermocouples and an interfacial heat flux was estimated by solving a one-dimension Fourier heat conduction equation inversely. Figure 2.12 shows the relationship between the heat flux and time obtained from this experiment.

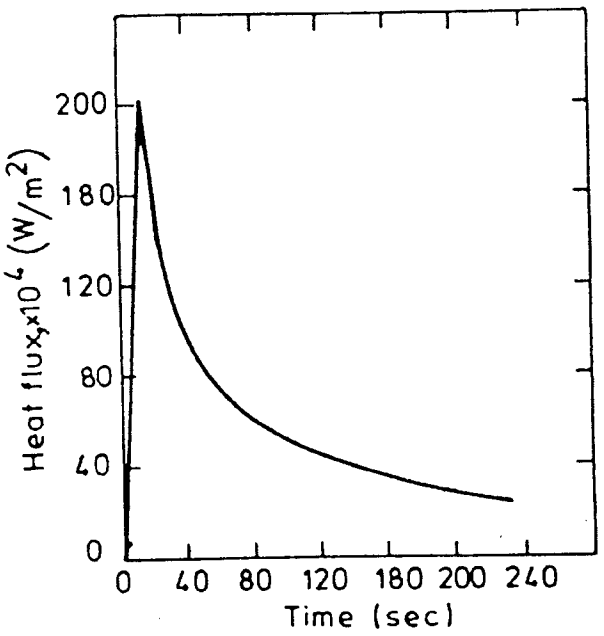

Figure 2.12 Estimated heat flux values for Al -13.2 % silicon alloy, using 50 x 50 x 50 mm copper chill without coating.[9)]

The heat flux curve indicated a maximum at 20 seconds after pouring then it rapidly decreased. It was suggested that during solidification the contact became less perfect, resulting in the decreasing of the heat flux across the interface.

Prates, Fissolo, and Biloni[10)] also poured molten aluminum into a chilled mold made from different materials. *Prates* et al. used a large mold in order to make it semi-infinite metal-mold system. The schematic of his experimental apparatus is shown in Figure 2.13. Two pairs of K-types thermocouples were used to measure the temperature at different positions during the experiment. Both pairs of thermocouples were placed in the lower half of ingot to avoid effects of heat losses at the free surface of the liquid.

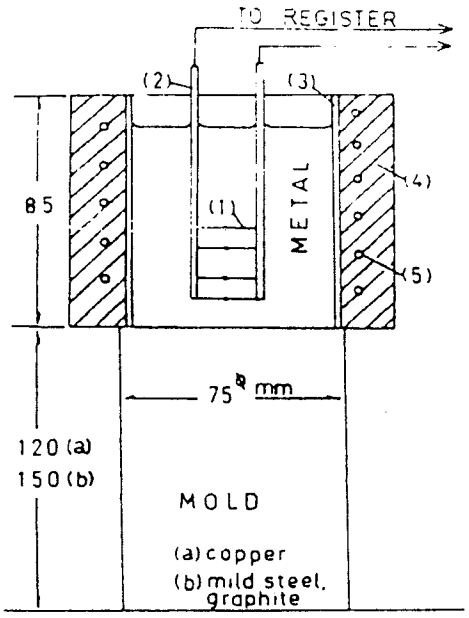

Figure 2.13 Illustration of apparatus 1) Two pairs of thermocouple 2) Thermocouple protection 3) Stainless wall protection 4) Furnace wall 5) Kanthal electric resistance.[10]

The experimental results show that the position of solid/liquid interface (X) varied with time (t) follows the relationship $X(t) = A.t^{1/2} - B$. Where B is a constant that only depends on superheat through the parabolic law and A is another constant that is independent of a superheat but dependent on mold sink capacity parameters such as mold temperature and the heat transfer coefficient h. The values of A increased with increasing heat transfer coefficient. From his experiment, pouring aluminum in a mild steel mold, the following results were obtained.

Aluminum coat	$h = 0.02$ $A = 0.41$
Zirconate coat	$h = 0.04$ $A = 0.53$
Clean surface	$h = 0.08$ $A = 0.65$
Calculated (Lyubov's model)	$h = \infty$ $A_\infty = 0.66$

Muojekwu, Samarasekera and Brimacombe[11] studied transient heat transfer in the early states of solidification of aluminum alloys on a water-cooled chill. The water-cooled chill mold were instrumented with thermocouples and dipped into the aluminum silicon alloy melted in a graphite crucible. The data acquisition system was used to record the temperature profiles at various positions in the chill and solidifying metal at the sampling speed rate 2Hz. The chill was dipped 2 mm below the melt surface and left in contact with the molten alloy for 60 seconds. The temperature profiles measured from thermocouples at different positions were shown in Figure 2.14. The temperature went up to its maximum value within the first 10 seconds.

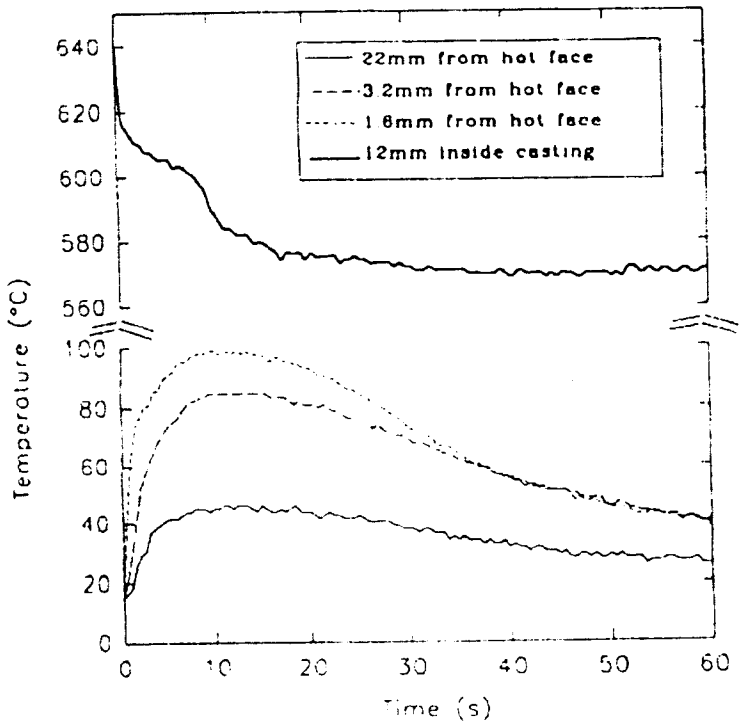

Figure 2.14 The typical temperature profiles measured when copper chill was dipped into Al-7%Si melt.[11]

After cooling to room temperature a solidified shell thickness was measured. The interfacial heat flux, heat transfer coefficient and the temperature profile increase steeply upon the contact during the first 10 seconds, decrease steeply for a few seconds and then gradually decline to a fairly steady value. The typical heat flux and heat transfer coefficient as a function of time was shown in Figure 2.15. *Muojekwu et al.*[11] also ran experiments to understand the influence of process variables such as the mold surface roughness, mold material, metal superheat, alloy composition and lubricant. The result of these works will be discussed later in the section 2.2, "The effect of casting parameters".

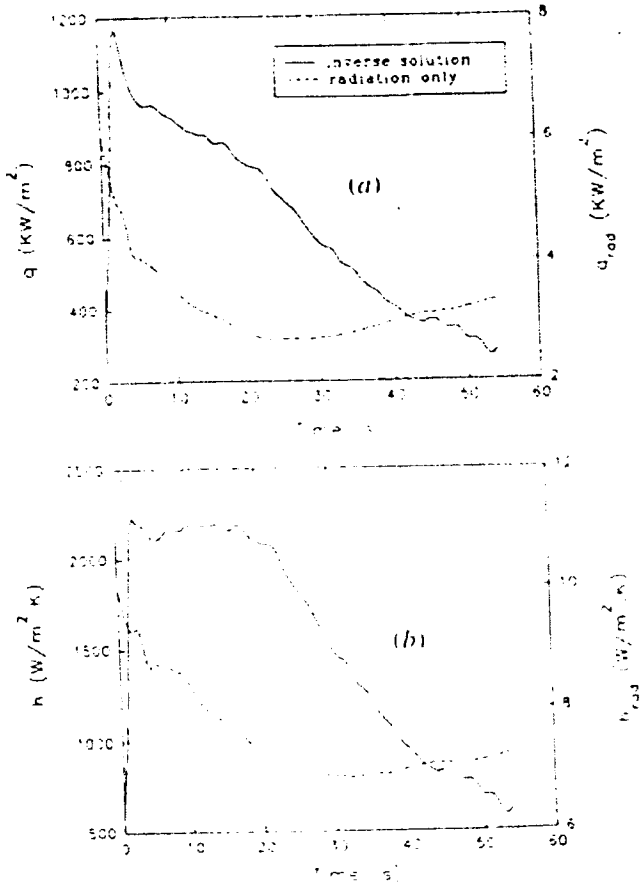

Figure 2.15 The Typical results of (a)interfacial heat flux and (b)heat-transfer coefficient as a function of time for Al-7%Si alloy and copper chill.[11]

Wang and Matthy[31] measured the temperature profile of a solidified metal at various locations and used the inverse heat transfer model to estimated the variation in interfacial heat transfer coefficient as a function of time. Their experimental set up consisted of two parts: a metal substrate and crucible. The metal substrate was made from long metal rod and the crucible is made from smaller size alumina tube, shown in Figure 2.16.

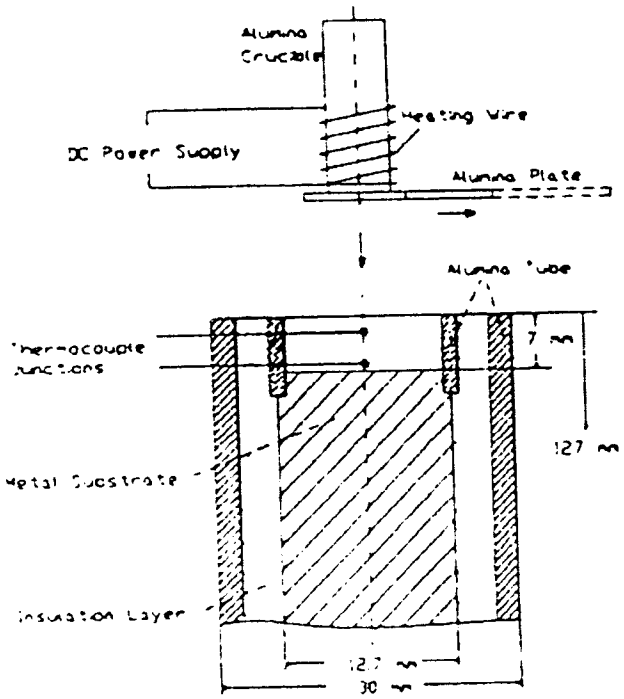

Figure 2.16 The schematic of Wang's experimental apparatus.[31]

The substrate temperature profile was measured by two thermocouples placed at position 0.9 and 3.1 mm from the surface of the substrate, Figure 2.17. The calculated heat transfer coefficient plotted as a function of time shown in Figure 2.18. The heat transfer coefficient increases to a maximum value, 50 KW, within 0.2 second and then decreases sharply and finally reaches a relatively steady state.

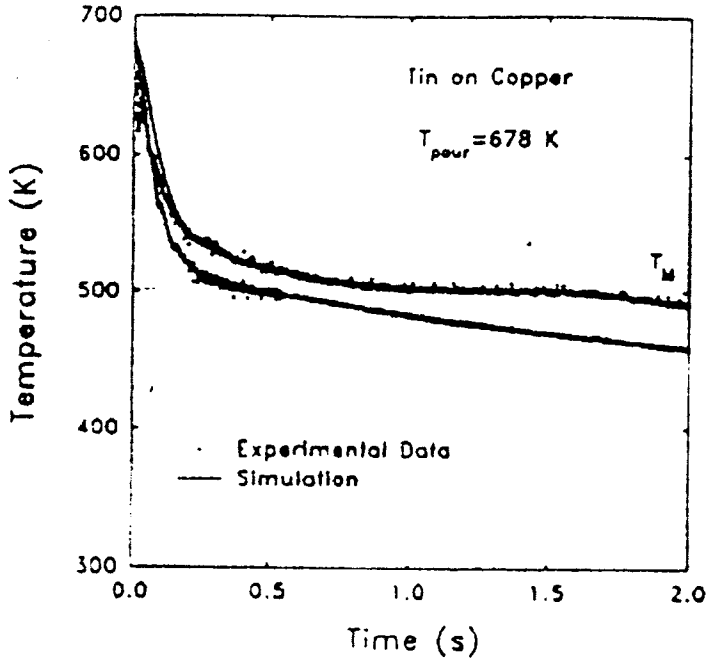

Figure 2.17 The temperature history measured from thermocouples at different positions.[31]

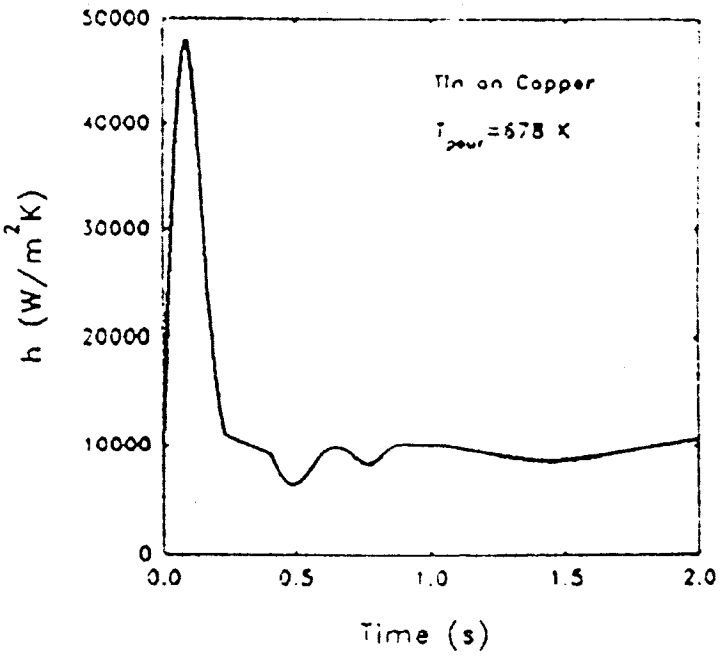

Figure 2.18 The calculated interfacial heat transfer coefficient, h, as a function of time.[31]

Mizukami, SuZuki and Umeda [81,82] studied the undercooling during the initial solidification of a 18Cr-8Ni stainless steel. Figure 2.19 shows his experimental set up. The specimen was melted in the induction furnace and the photo-diode sensor was used to measure the cast surface temperature profiles of the cast specimen, Figure 2.20. Their results indicated that the undercooling, at initial solidification, has a linear dependence on cooling rate Figure 2.21.

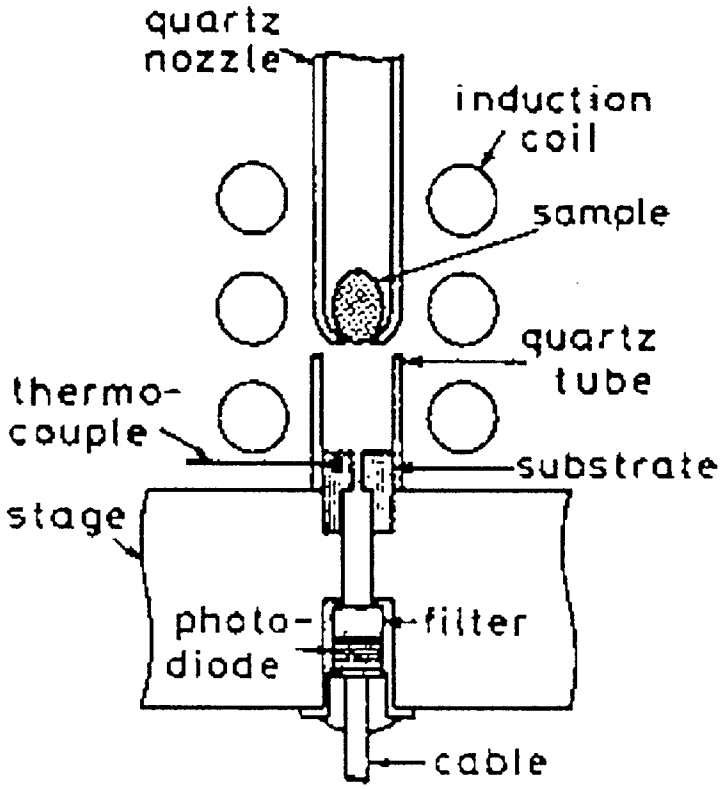

Figure 2.19 The experimental apparatus of Mizukami et al.[81]

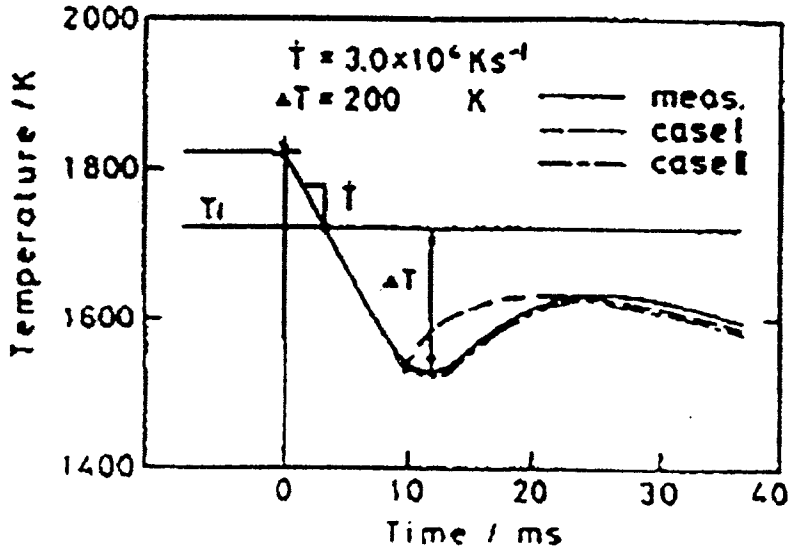

Figure 2.20 The cast surface temperature profile of 18Cr-8Ni stainless steel.[82)]

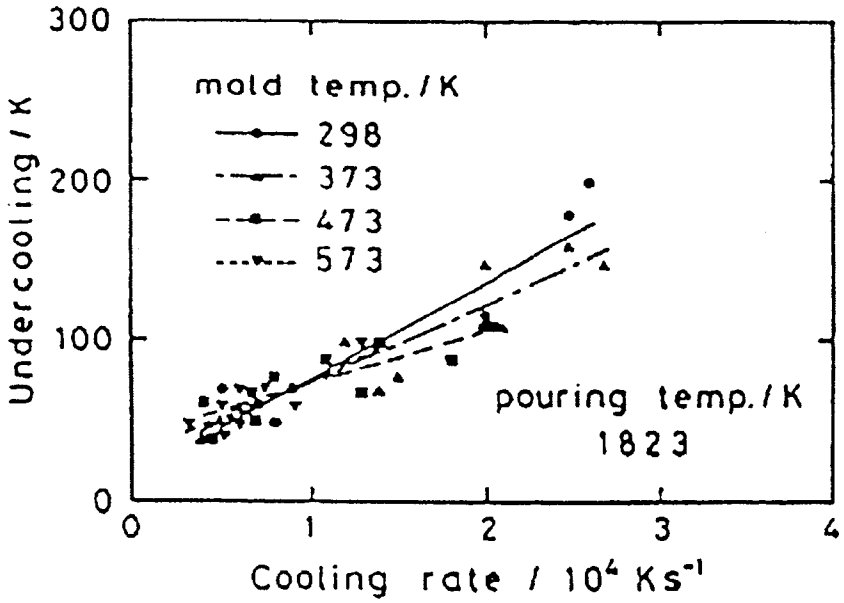

Figure 2.21 The relationship between undercooling and cooling rate of solidified 18Cr-8Ni stainless steel.[81)]

Todoroki, Lertarom, Suzuki and Cramb[12,13] studied heat transfer behavior of pure Iron, Nickel and 304 stainless steel against a water-cooled copper mold during the initial stage of solidification. The metal was melted in the quartz nozzle and then ejected onto the copper mold under an argon gas atmosphere. The temperature within the chill mold was measured by a set of K-type thermocouples, installed at position 1 mm and 4 mm from the surface at different 3 locations in the mold. The superheat temperature was measured by using a two-color pyrometer and the surface temperature of a cast metal was measured by using a photo-diode sensor.

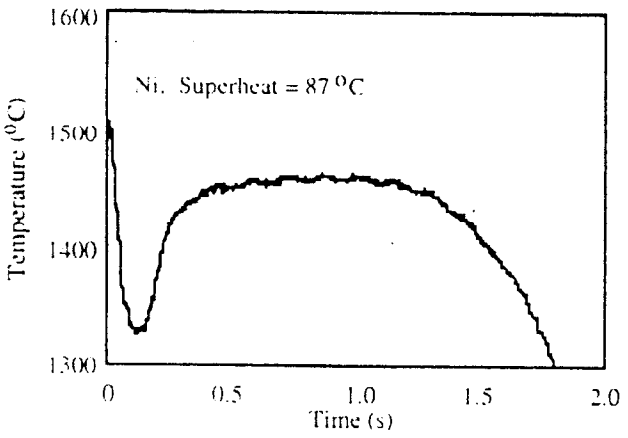

Figure 2.22 The surface temperature profile of cast nickel of the experiment of 87°C superheat.[13]

Figure 2.22 shows one of the surface temperature profiles of the cast metal, Ni, in this figure the undercooling and recallescence can be observed. Figure 2.23 shows the substrate temperature profiles measured from the thermocouples position 1 and 4 mm from the surface. The thermocouple at 1 mm. from the surface is more sensitive than those at 4 mm. so it gives a higher temperature if we compare at the same time.

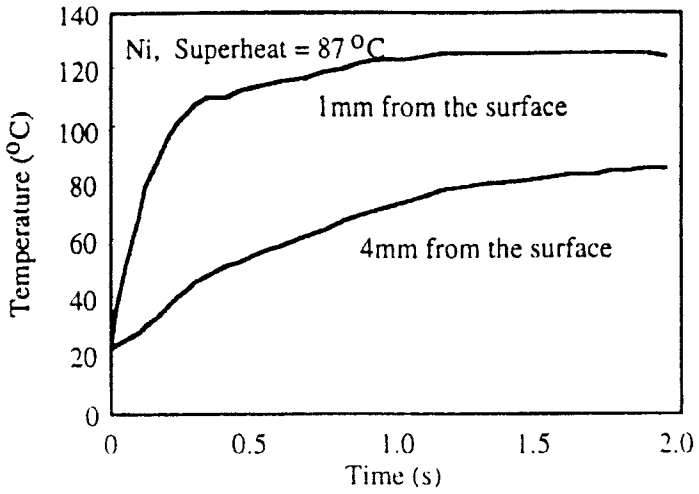

Figure 2.23 Temperature profiles in the chill mold in the case of nickel experiment of 87°C superheat.[13]

The heat flux and heat transfer coefficient can be calculated by using the mold and cast surface temperature profiles. Figure 2.24 shows typical relationship between heat transfer coefficient and time calculated from temperature profile measured at various thermocouples locations.

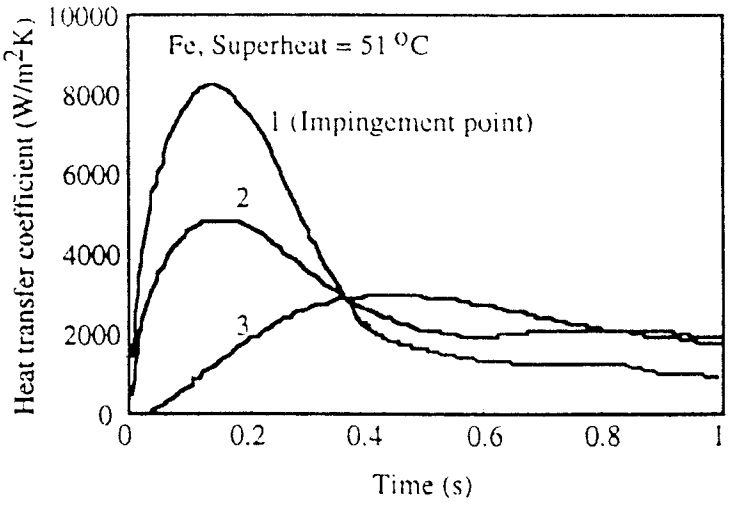

Figure 2.24 Heat transfer coefficients of a cast iron as a function of time. Numbers indicate the locations of thermocouples.[13]

Strezov and Herbertson[18] used a different technique to determine the initial heat transfer rate during the initial solidification process. They studied the interfacial heat transfer rate and the initial solidification behavior that is pertinent to strip casting by immersion of various substrates attached to a moving plate into a liquid 304 austenitic stainless steel, Figure 2.25. The cooled plate was inclined at an angle similar to the melt/roll contacting geometry of the meniscus region of a twin roll caster. 0.25 mm K-typed thermocouples were placed near the surface of the substrate surface to measure the temperature during the immersion. The substrate temperature acquisition rate was 2KHz per channel.

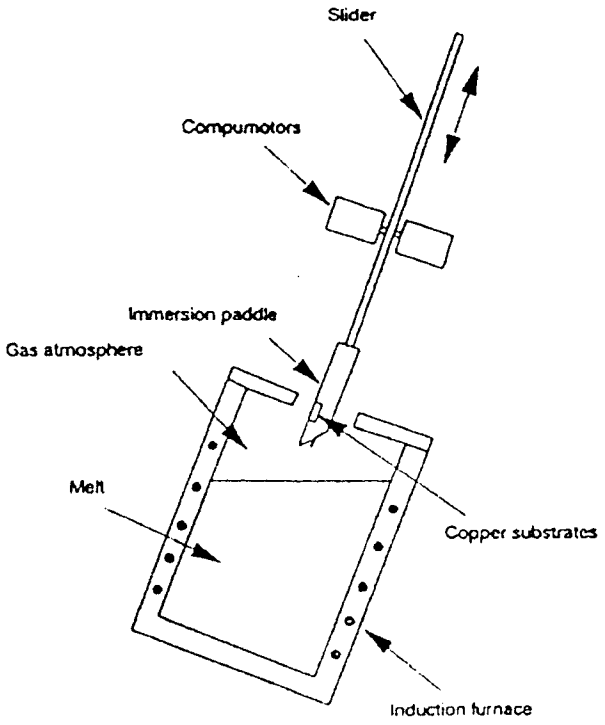

Figure 2.25 The schematic of Strezov's apparatus.[18]

The apparatus and instrumentation was designed for millisecond resolution of heat transfer behavior. The noise obtained in the raw data was filtered using a polynomial

regression method and the transient heat flux was calculated by using inverse heat conduction algorithm. Figure 2.26 shows the heat flux histories for a sample solidified on the various substrate surfaces. A spike appeared in the calculated heat flux value within the first 10 milliseconds due to the contact conditions.

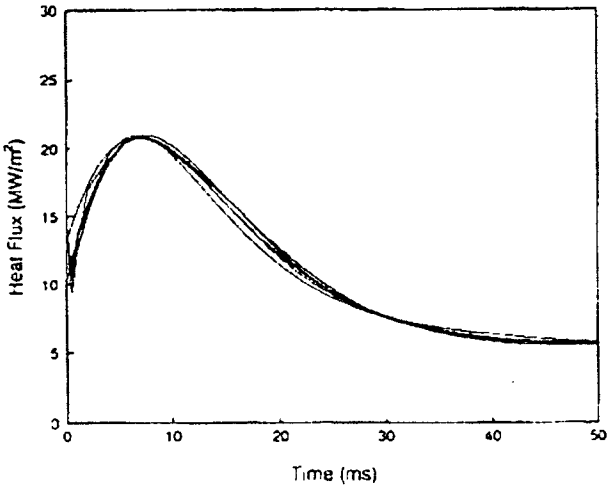

Figure 2.26 The typical heat flux histories.[18]

T. Evans [45] developed a modified levitated drop apparatus, Figure 2.27, which consisted of top and bottom coil for levitation and heating. The temperature of droplet was measured by a modified Capintec Series 30 two-color pyrometer through the 8 mm Spectrosil B prism. After a melt reached a desired temperature the induction furnace was turned off and the droplet started to fall on the substrate surface and the heat flux to the substrate was calculated from droplet temperature profile. Figure 2.28 shows the temperature profile of the droplet before and after contact the substrate and Figure 2.29 shows the typical calculated heat transfer coefficient as a function of time.

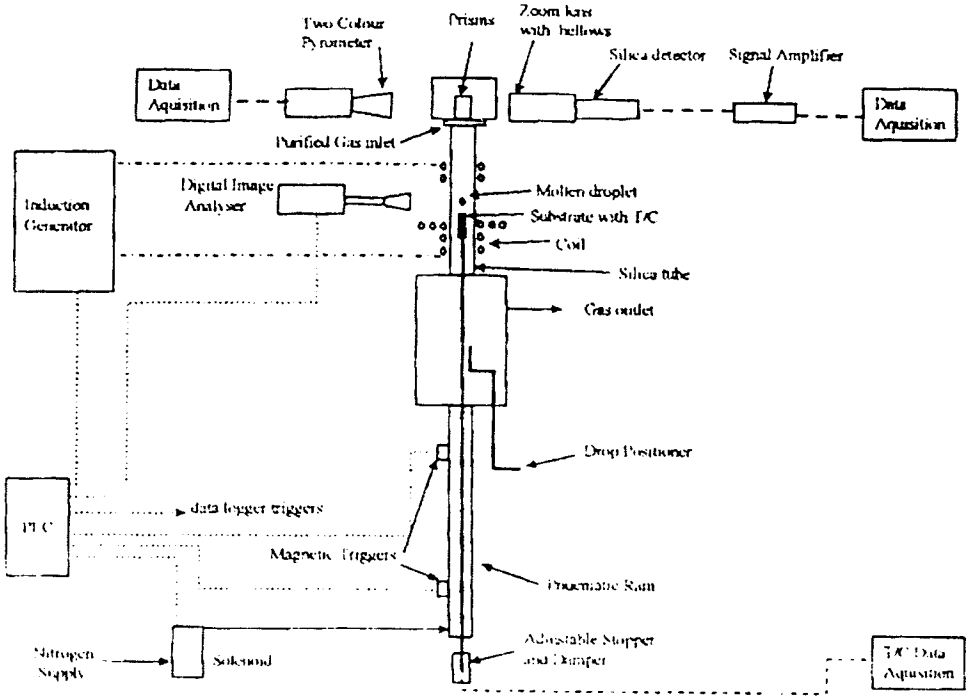

Figure 2.27 The modified levitation apparatus.[45]

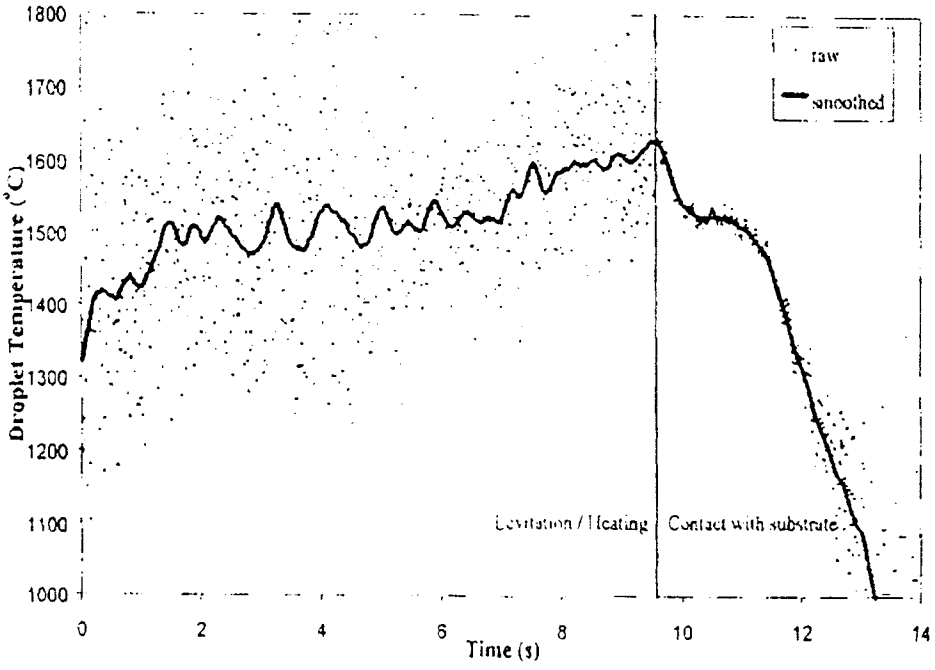

Figure 2.28 The droplet temperature during the levitation and contact.[45]

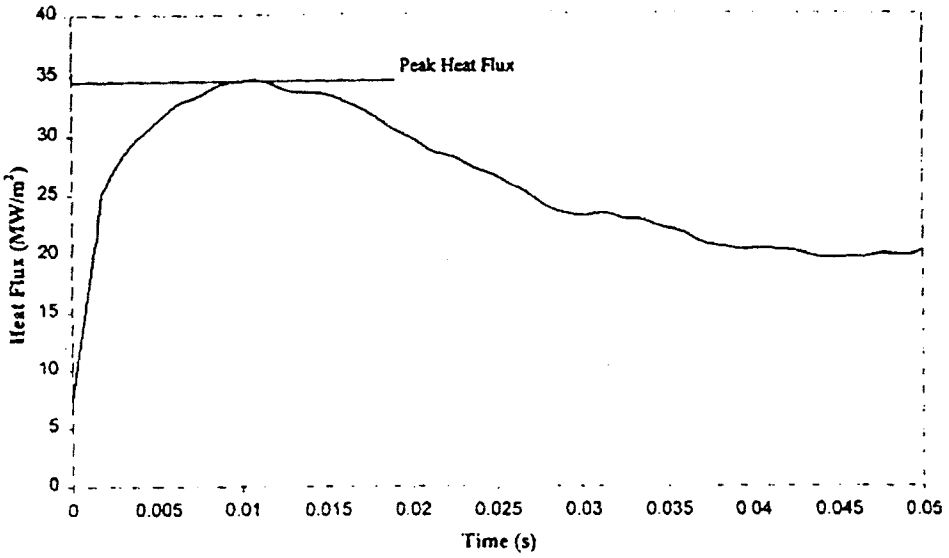

Figure 2.29 The typical heat flux calculated from the mold temperature profile.[45]

2.2 Effect of Casting Parameters

During the casting process, there are several parameters, such as mold material, mold surface roughness, superheat of liquid metal and alloy composition, that effect the initial heat transfer behavior and quality of product including its microstructure. Many studies were conducted to investigate and understand the effect of those parameters and to use this knowledge as a tool to predict and improve the product quality in the future.

2.2.1 Chill Mold

The chill mold works as a heat extraction source for liquid steel. It can be made from different kinds of material. Each of them has their own heat extraction behavior that can be attributed to different properties of the cast product.

Prates and Biloni[26] made their molds from mild steel, nuclear graphite and electrolytic copper. Their metal /mold interface varied from a clean mold surface to the one coated by thin film of alumina or zirconia. For molten aluminum poured into different kinds of mold, Figure 2.30, the mold made from copper gave a highest value of heat transfer coefficient. This is in a good agreement with other studies when increased the thermal diffusivity of a chill material heat flux and heat transfer increased [8, 9, 26, 27].

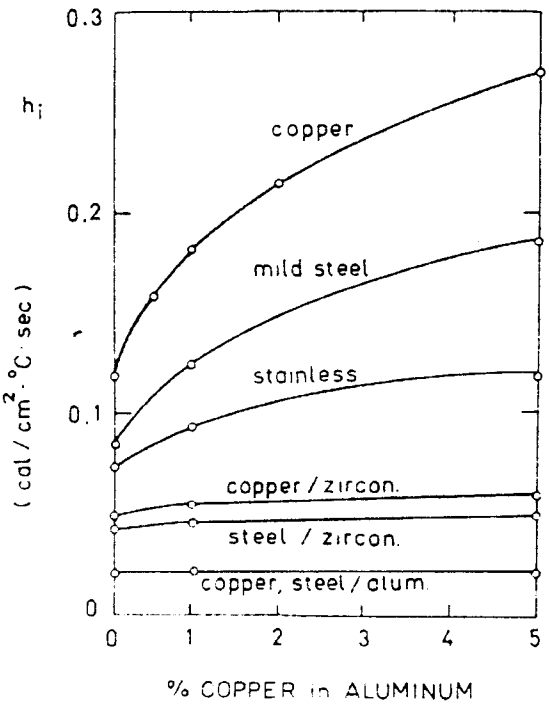

Figure 2.30 Values of the coefficient "h" obtained for different aluminum copper alloys and different substrates.[26]

Richard C. Sun[8] coated his mold with different kinds of material. He believed that the increase of heat transfer coefficient with metal contact time is due to an increase of thermal conductivity of the coating layer of a coated mold. It was concluded that the heat transfer coefficient was mainly controlled by conduction at the interface in the early stage of casting for both uncoated and coated molds. Figure 2.31 shows the theoretical, simulated, and experimental heating curves of the uncoated copper mold. Also there is no difference in the magnitude of observed h values when uncoated samples are immersed into molten metal baths heated at different temperature since the h value depends neither on a molten bath temperature nor a mold surface temperature.[8] The different degree of a mold surface roughness can also be attributed to the different degree of heat extraction.

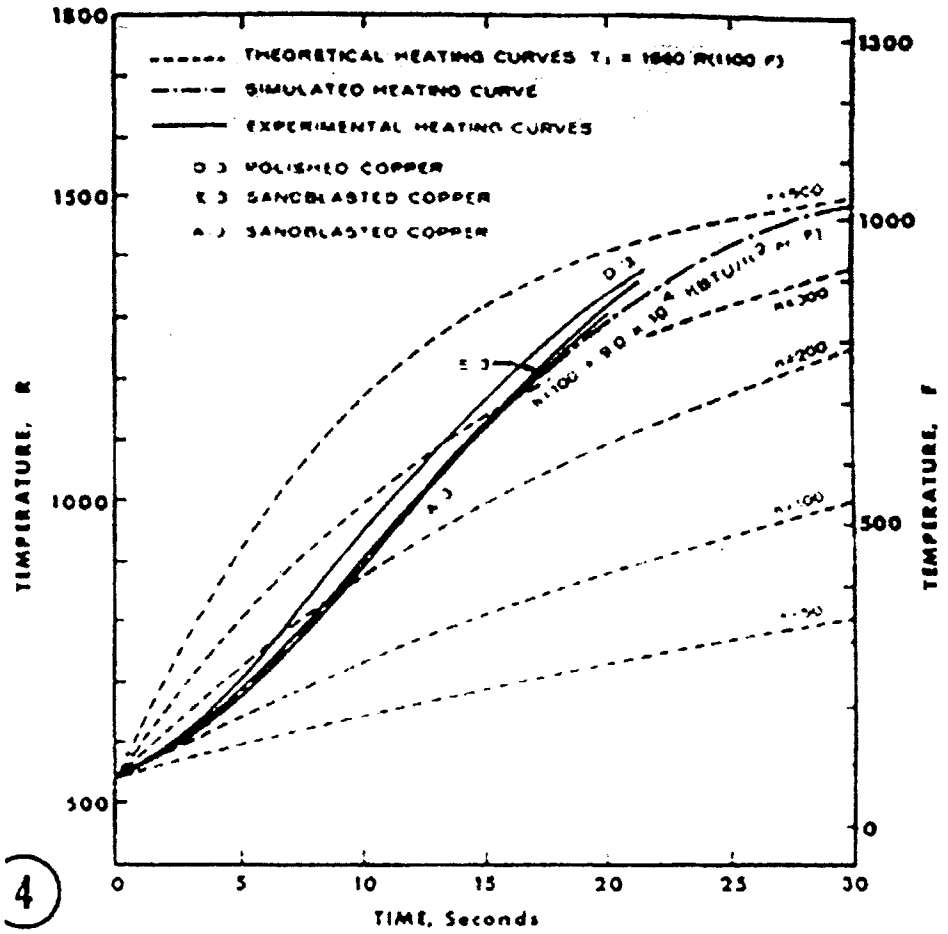

Figure 2.31 The heat curves of uncoated copper mold.[8]

Moujekwu, Samarasekara and Brimacombe [10] polished and filed the chill surface in order to obtain the various degree of surface texture. They found that heat extraction increased with increasing surface smoothness of the copper chill and resulting in an increase in shell thickness and decrease in secondary dendrite arm spacing. Figure 2.32, shows the effect of surface roughness on heat flux, heat transfer coefficient, shell thickness and secondary dendrite arm spacing.

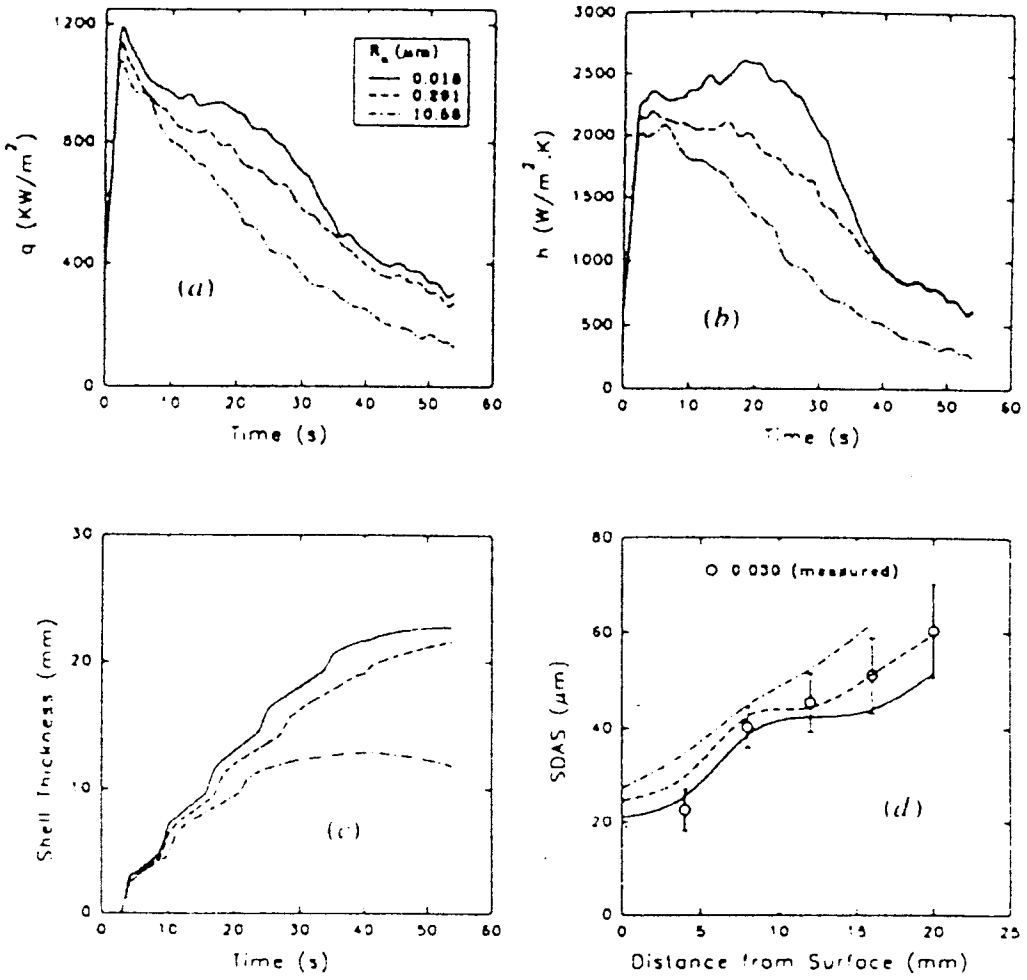

Figure 2.32 The effect of chill surface roughness on (a) Interfacial heat flux (b) Heat transfer coefficient (c) Shell thickness profile and (d) SDAS for Al-7%Si and copper chill (superheat = 30°C).[10]

Moujekwu et al.[10] observed that a 16-fold increased in roughness from 0.018 to 0.291 μm decreased the heat flux by an average of 12.5% while the heat transfer coefficient decreased by 17%. If the roughness is further increased more than 500 fold, 10.56 μm, the heat flux will decrease 32% while the heat transfer coefficient decreases 42%. It was also observed that as the chill surface roughened, the surface of the solidified shell smoother than that of the chill.

The results of his work also show the effects of chill material, Figure 2.33, on the heat flux and heat transfer coefficient. Both value increase with thermal diffusivity of chill materials [10].

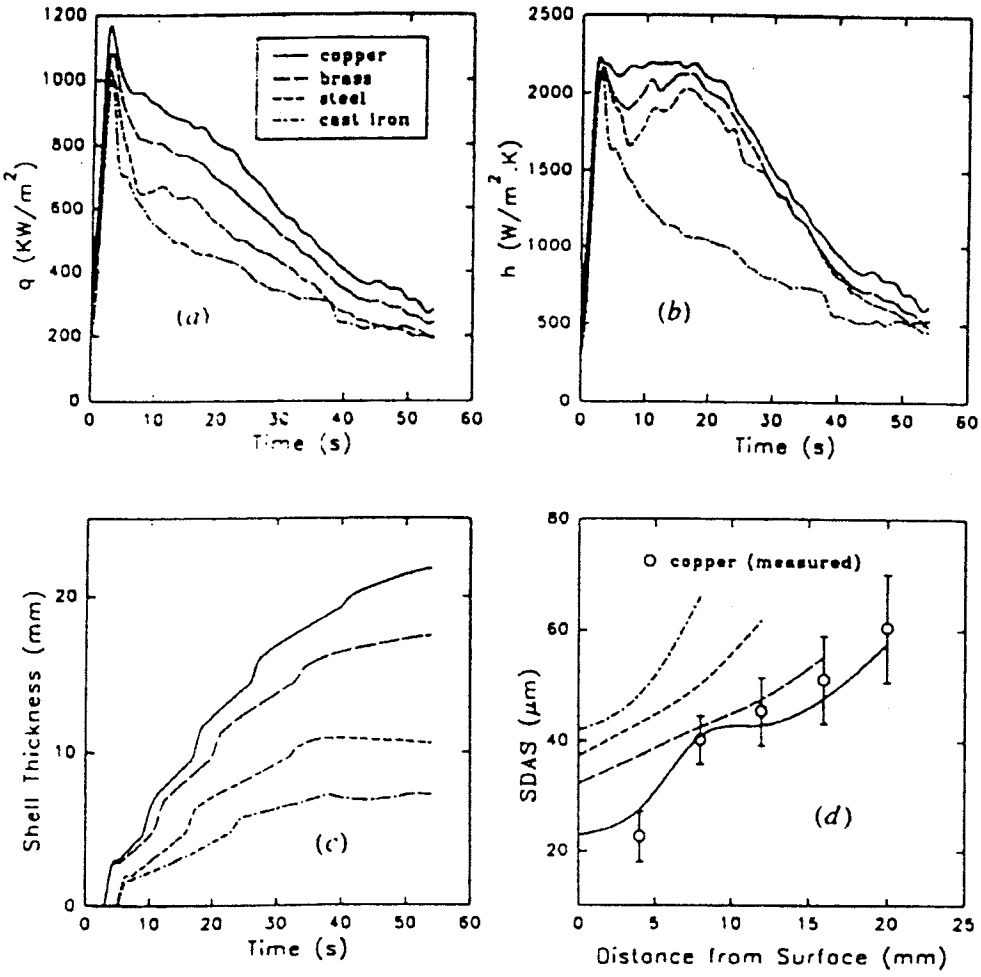

Figure 2.33 Effect of chill materials on (a) Interfacial heat flux (b) Heat transfer coefficient (c) Shell thickness profile (c) SDAS for Al-7%Si (superheat = 30°C).[10]

Les Strezov and Joe Herbertson[18.64] demonstrated the importance of substrate texture. Their experiments had both smooth and textured surface substrates. The texture surface had ridges of varying pitch, Table 2.1, with a constant depth as shown in Figure 2.34.

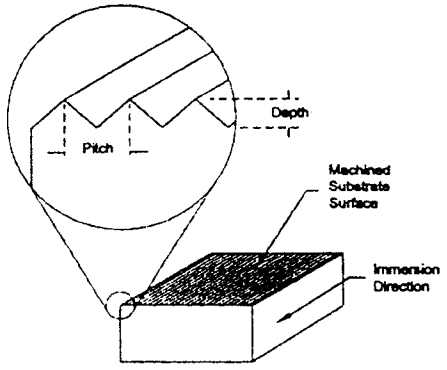

Figure 2.34 Schematic of substrate surface texture showing machined ridges parallel to an immersion direction.[18]

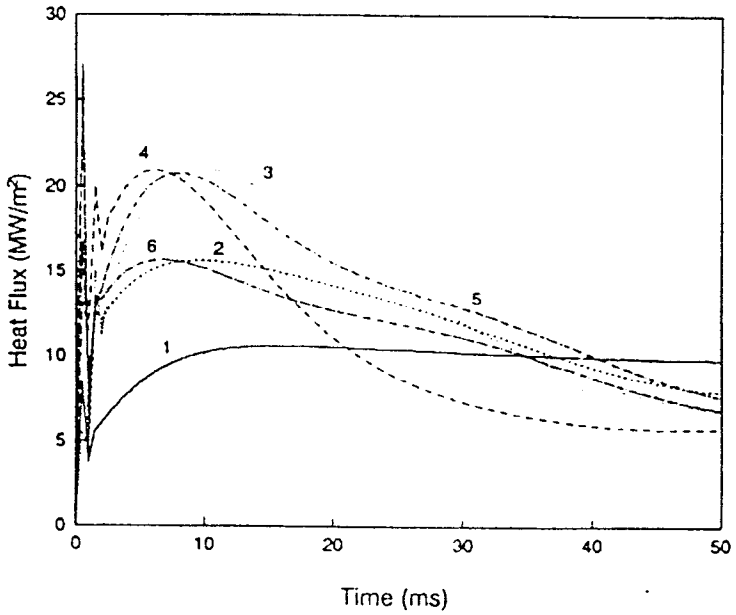

Figure 2.35 Heat flux histories for samples solidified on various substrate surfaces (detail shown in Table 2.1).[18]

Table 2. Substrate Surface Textures

No.	Pitch (μm)	Depth (μm)
1	Smooth	0.15 Ra
2	75	30
3	100	30
4	150	30
5	200	30
6	300	30

Table 2.1 The substrate surface texture.[18]

Figure 2.35 shows the calculated heat flux histories within 50 ms of the solidification on different substrate surfaces. The peak heat flux of the textured substrate was significantly higher than those of the smooth substrate. The surface structure of the samples solidified on the smooth surface shown coarse surface dendrites, Figure 2.36, and one solidified on the textured substrate shown fine surface dendrites nucleated along the ridges of the substrate texture, Figure 2.37.[18,64]

Figure 2.36 The surface structure of the samples solidified on the smooth substrate.[18]

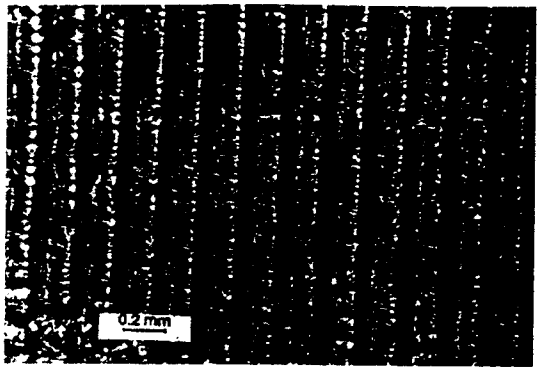

Figure 2.37 The surface structure of the samples solidified on the texture substrate.[18]

Liu, Wang and Matthys[28] studied the effect of a substrate material on splat cooling rate. The experimental apparatus was shown in Figure 2.38. The droplet is levitated in an open-bottom quartz tube. Two high-temperature IR two color pyrometer were used to measure initial droplet temperature and the surface temperature of the splat Figure 2.39 shows the measured top surface temperature profile of the splat at various substrates. The substrates were made from three different materials, Cu, Al, and stainless steel. It was found that the splat cools down faster as the thermal diffusivity of the substrate increases.

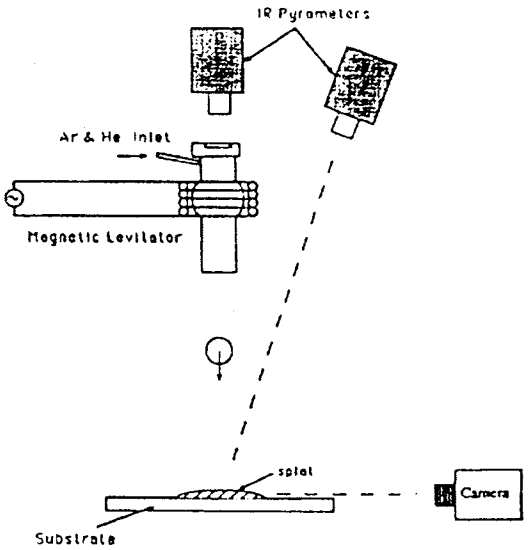

Figure 2.38 *Liu* et al.'s experimental apparatus.[28]

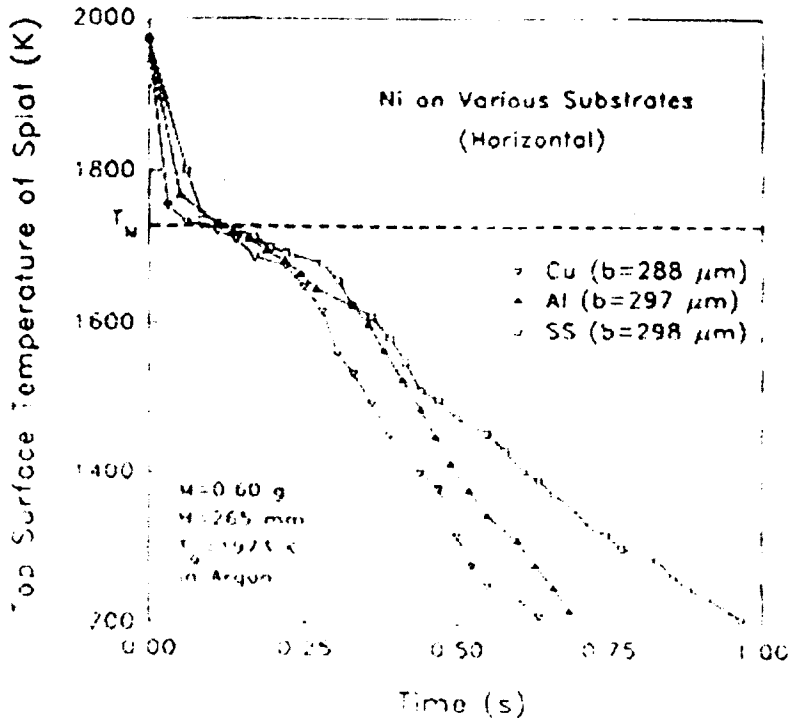

Figure 2.39 The top surface temperature of the splat as a function of time at various substrates.[28]

Irsid and Thyssen Stahl AG [24]developed the double roll strip casting process on a small-scale machine. They investigated the strip casting process over a wide range by varying the main parameters of mass flow, roll speed, roll roughness and strip thickness. They found that roll roughness appears to have a significant influence on heat extraction. Their results suggested that heat flux decreases when the roll roughness increases, Figure 2.40.

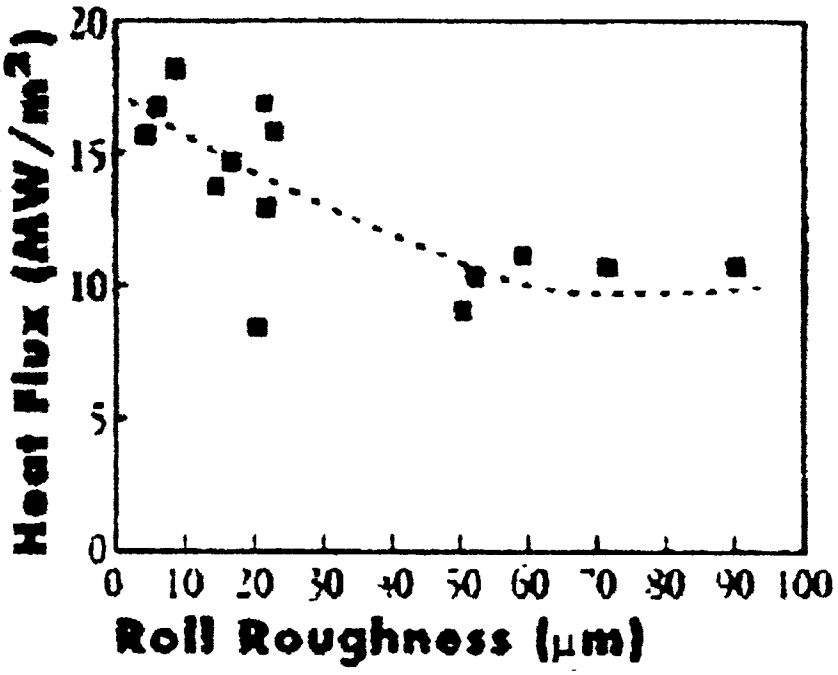

Figure 2.40 The effect of mold roughness on mean heat flux.[24]

2.2.2 Metal – Mold Interface Condition

The subject of metal-mold interfacial heat transfer has been of interest to many researchers due to its importance influence on the solidification rate of metal casting. Since in the strip casting process liquid steel contacts the rotating mold directly, therefore, the change in metal-mold interface condition is expected to influence the change in the interfacial heat transfer significantly.

Ho and Pehlke[48,49] proposed physical mechanism at the metal and mold interface during the solidification process. As the solidification progresses the thermal condition at the metal-mold interface may change in 2 directions: 1) The metal and mold stay in contact along isolated asperities on the microscopically rough surface or 2) gradually developing an interfacial gap, as the mold and metal walls recede, which separate the metal and mold apart.

Prate and Biloni[26] proposed a mechanism to explain the initial formation of metal-mold interface with solid-solid contact, Figure 2.41. Due to the fact that the interface of the substrate is not completely smooth but consists of small asperities protruding from its surface profile the liquid metal deposited on the substrate will contact the peak of the asperities first and start solidifying. At the same time, the surface tension of the liquid metal and subsequent rapid growth of solidification from the nucleation site prevents the solidifying metal from wetting the valleys on the substrate surface. One of the conclusion in their work is the metal-mold interface condition will not remain static but will change with time after the initial formation of solidified skin.

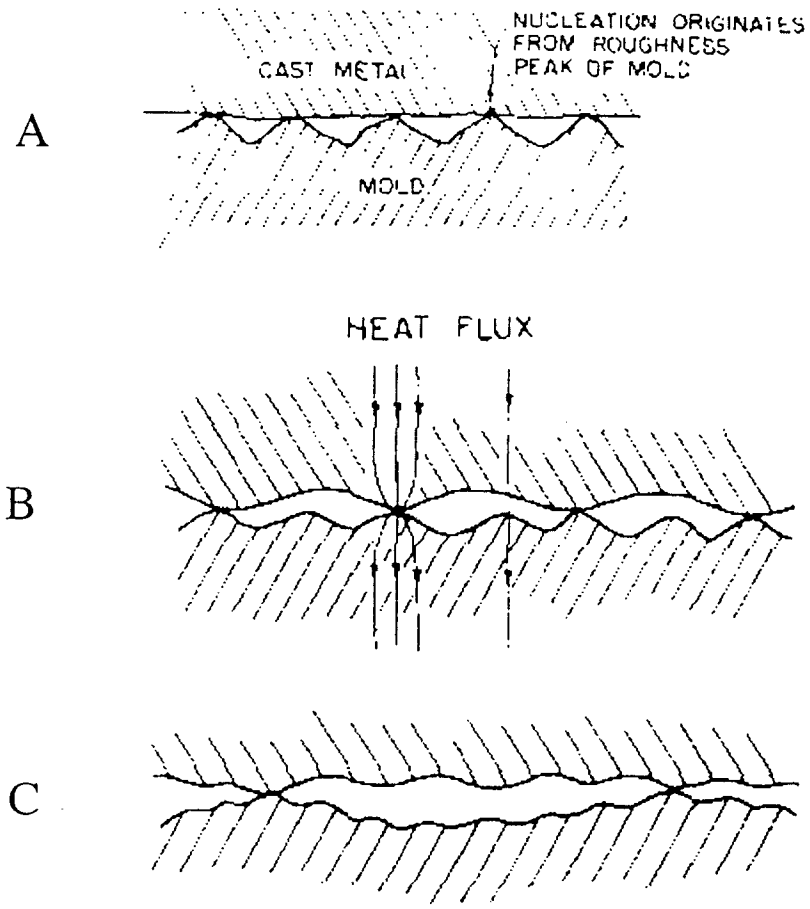

Figure 2.41 A) Metal-mold interface at the start of solidification B) Conforming solid contact at an interface. The preferential flow of heat along the points of solid contact is also illustrated C) Nonconforming solid contact at an interface.[26]

Huang and Fiedler[43] studied the effect of wheel conditions on the casting of amorphous metal ribbons. The castings were carried out in air on the water-cooled copper with 1% chromium wheel. There were two kinds of wheel surface used in this work; a smooth wheel surface and a matte wheel surface. From their studies, two distinct mechanism of air pocket formation are found for different casting wheel surface conditions. For a smooth wheel surface, the air pockets are nucleated homogenously the wetting angle $\theta < \theta^*$, Figure 2.42. The air pockets nucleated in this mechanism are

elongated along the length of the ribbon. When the casting on a matte wheel surface air pockets are nucleated heterogeneously at the low spot of the wheel surface and oriented themselves transverse to the wheel spinning direction which helps the ribbon easily separated from the wheel, Figure 2.43.

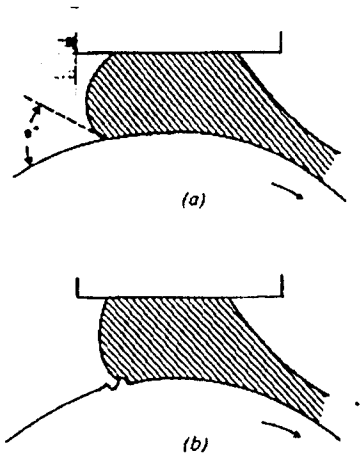

Figure 2.42 Schematic of a) The homogenous nucleation mechanism of air pockets on a smooth casting surface, and b) The heterogeneous nucleation mechanism of air pockets on a matte surface. [43]

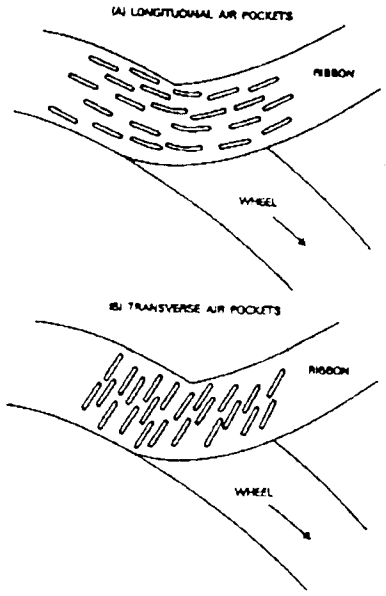

Figure 2.43 Schematic showing the direction of air pockets relative to the direction of peeling off the ribbon from the wheel for the case of (a) casting on a smooth wheel surface, and b) casting on a matte wheel surface.[43]

Strezov and Evans [42] studies the nucleation and early growth pertinent to near net shape casting. Their calculation shows that, at the initial contacting region of a twin roll caster, the thermal resistance of the growing shell in early stages of contact has relatively minor influence. In fact the total resistant of heat flow is coming from the interface thermal resistance.

Another interesting work done by *Strezov, Herbertson and Belton*[20] showed that the initial melt/substrate heat transfer is shown to be strongly influenced by the interfacial conditions between two surfaces and the dynamic wetting phenomena. By dipping the copper substrate into the a SUS304 stainless steel melt many time the oxide layer mainly composed of manganese and silicon build up on the substrate surface. They found that wetting condition was also enhanced when manganese and silicon oxides deposited on the interface melted. Large increases in heat flux were observed when the wetting condition was improved, Figure 2.44.

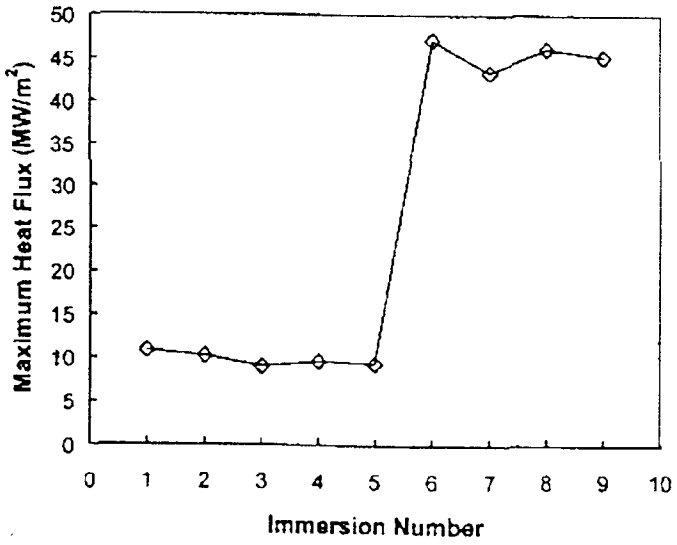

Figure 2.44 Effect of oxide build up on maximum heat flux.[20]

2.2.3 Alloy Composition

There are many researchers who studied the effect of alloy composition on heat flux, heat transfer coefficient, surface quality and microstructure of the cast specimen. *Moujekwu et al.* ran the experiment to see the effect of alloy composition. With decreasing silicon content in his Aluminum silicon alloys, both heat flux and heat transfer coefficient increased and the secondary dendrite arm spacing also increased with decreasing silicon content[11], Figure 2.45.

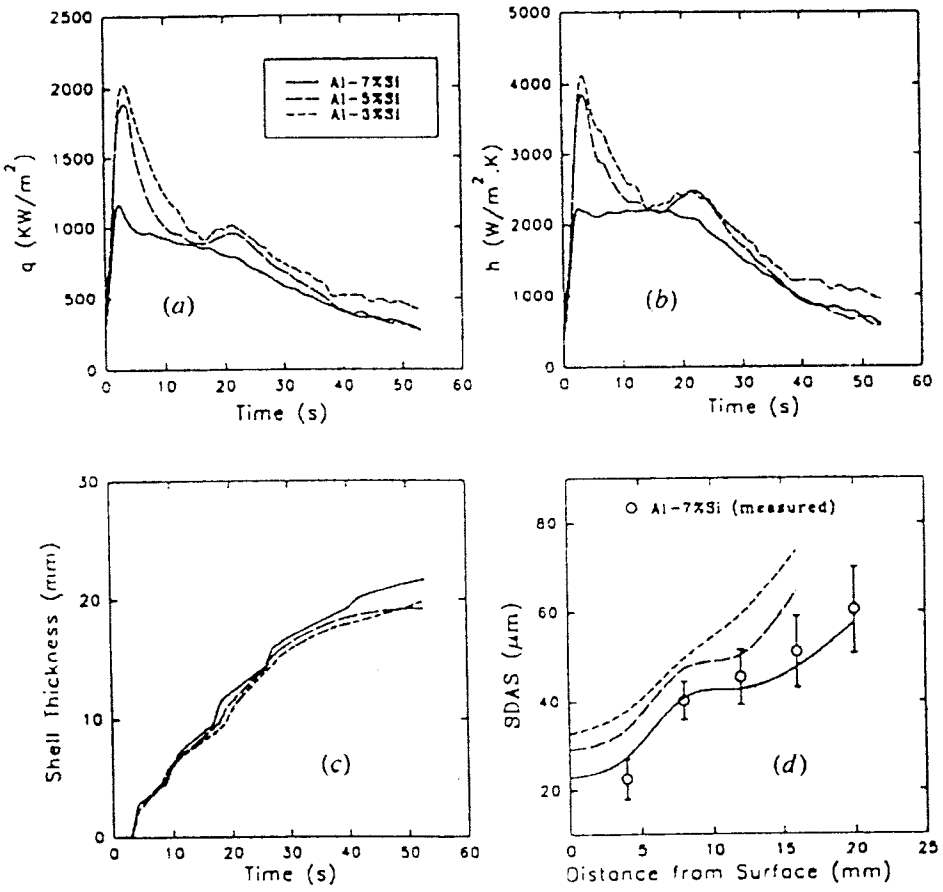

Figure 2.45 The effect of alloy composition on (a) interfacial heat flux (b) heat transfer coefficient (c) shell thickness profile and (d) SDAS for Al-Si alloys and copper chill (superheat = 30°C).[11]

They explained their results as follows: First, the casting temperature must be higher as the silicon content decreased due to the increase in liquidous temperature. Second, as the silicon content decreased the thermal diffusivity of the alloy slightly increased. These results agreed with Bamberger, Weiss and Stupel 's results who studied heat flow and dendrite arm spacing of aluminum silicon alloys.[4)]

Spittle and Lloyd[32)] measured the primary and secondary dendrite arm spacing of hypoeutectic Pb - Sb alloys. Both primary and secondary dendrite arm spacing were observed to decrease when initial alloys composition increased.

Todoroki et al.[33)] studied the initial solidification of 304 stainless steel which contain 0.002% and 0.088% of sulfur and found that at high superheat heat flux increased when the amount of sulfur content in 304 stainless steel decreased. However, at low superheat, sulfur content in a 304 stainless steel did not show much effect on heat flux.

2.2.4 Superheat

Superheat plays a major roll on the initial heat transfer behavior of alloys. Most of the work in this field has measured this effect. *Wang et al.* determined the interfacial heat transfer of free-jet melt spinning. When comparing the heat transfer coefficient under two superheat conditions he found that the higher melt superheat greatly improves the thermal contact at the interface[28,30,31].

Muojekhu et al. found a similar result. The interfacial heat flux and heat transfer coefficient increased with increasing superheat, Figure 2.46.[11] It was found that the solidified shell became smoother when the superheat increased.

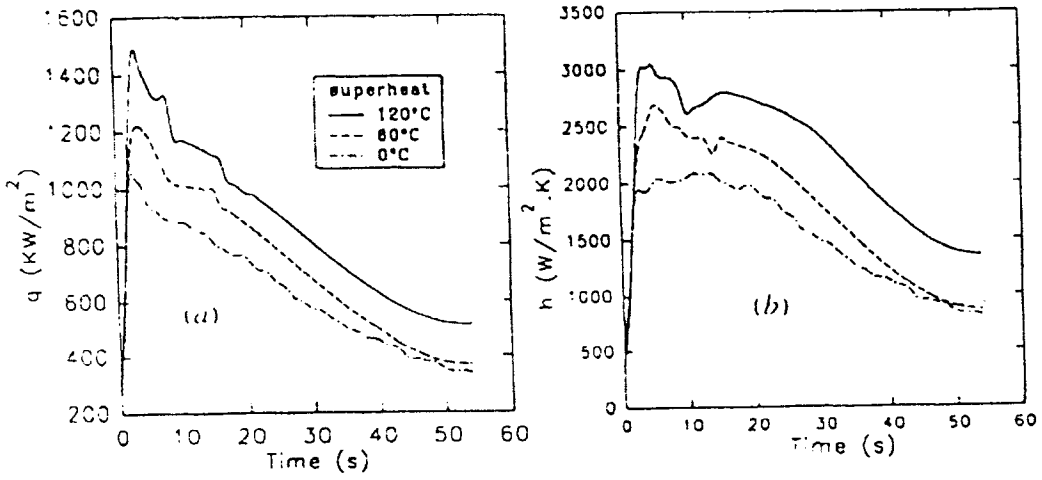

Figure 2.46 Effect of superheat on interfacial (a) heat flux (b) heat transfer coefficient.[11]

Ozbayraktar and Koursaris investigated the effect of superheat on solidification structure of AISI 310S austenitic stainless steel. His results suggested that the microstructure of a cast material responded differently to variation in casting temperature.[34] Figure 2.47 shows that when the casting temperature was increased the

primary dendrite arm spacing decreased. In the other words, the microstructure was refined when pouring from higher temperatures.

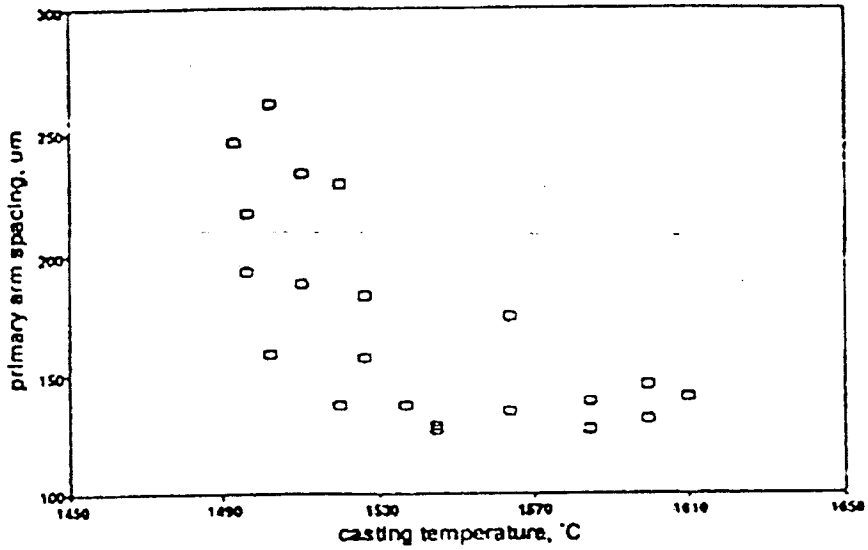

Figure 2.47 Variation in primary dendrite arm spacing with casting temperature.[34)]

Todoroki, Lert-a-rom and Cramb investigated heat transfer behavior of pure iron and nickel against the water-cooled copper mold. The heat transfer coefficient of both materials increased with increasing superheat, as shown in Figure 2.48 and 2.49. [14,33)]. The results suggested that the heat transfer behavior reaches the maximum value within the first 0.2-0.4 seconds of the droplet solidification process. *Lert-a-rom*[44)] also studied the relationship between the secondary dendrite arm spacing and the melt superheat of the 304 stainless steel. His results agree well with other previous works. When the superheat increased the secondary dendrite arm spacing decreased, Figure 2.50 - 2.51.

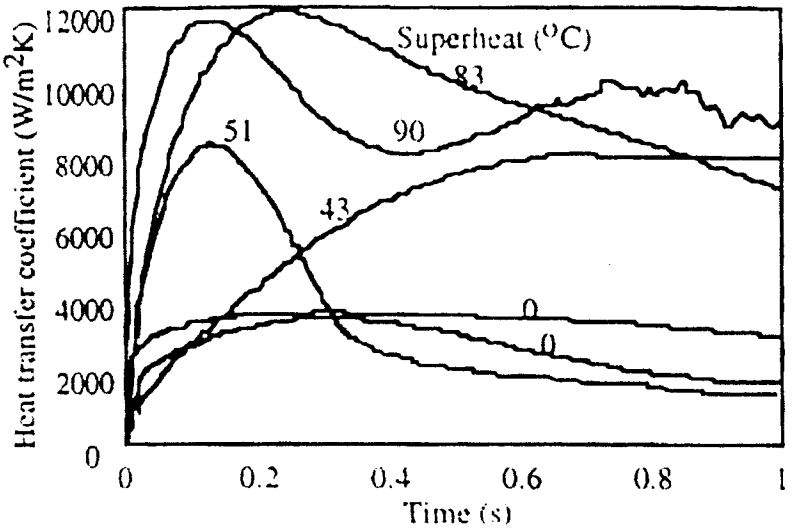

Figure 2.48 Relationship between the heat transfer coefficient and time of iron at different superheat.[33]

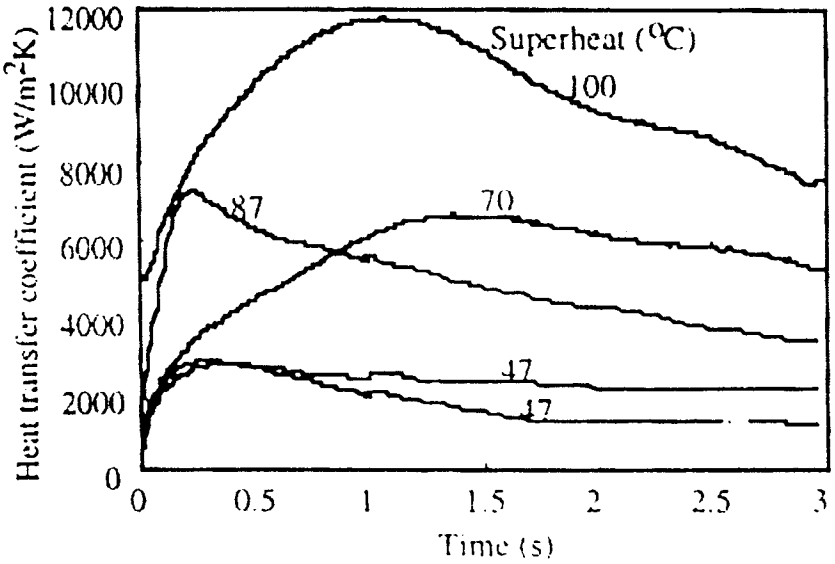

Figure 2.49 Relationship between the heat transfer coefficient and time of nickel at different superheat.[33]

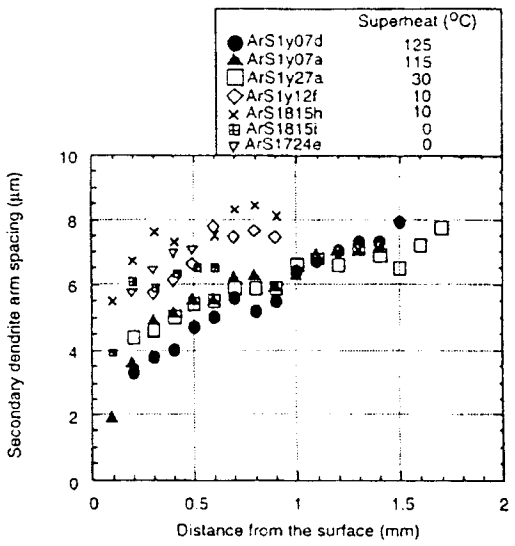

Figure 2.50 The secondary dendrite arm spacing of 304 stainless steel at various superheat.[44]

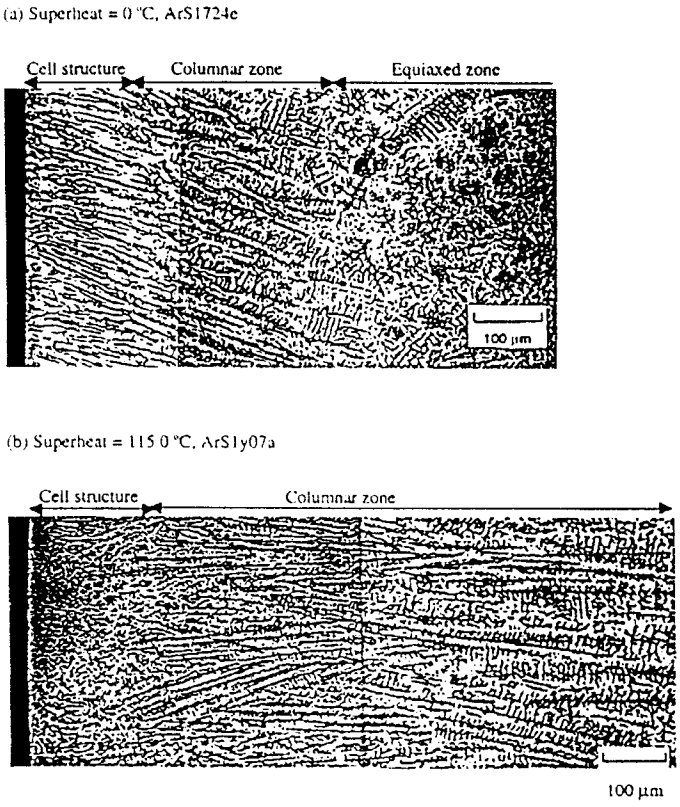

Figure 2.51 The actual pictures of the secondary dendrite arm spacing of 304 stainless steel at superheat 10°C and 60°C[44]

Liu, Wang and Matthys studied the behavior of a molten metal droplet impinging, spreading and solidifying. Nickel was dropped onto different substrates, copper, aluminum and stainless steel. The detail of their experimental set up was discussed earlier in section 2.3.1. *Liu et al.* found that, at high superheat, the splat cool down slower than the low superheat one after solidification, even though the splat thickness decrease with increasing the level of superheat, Figure 2.52. This result can be explained due to the fact that the higher the superheat, the higher the temperature of the substrate surface becomes before and during solidification.[28]

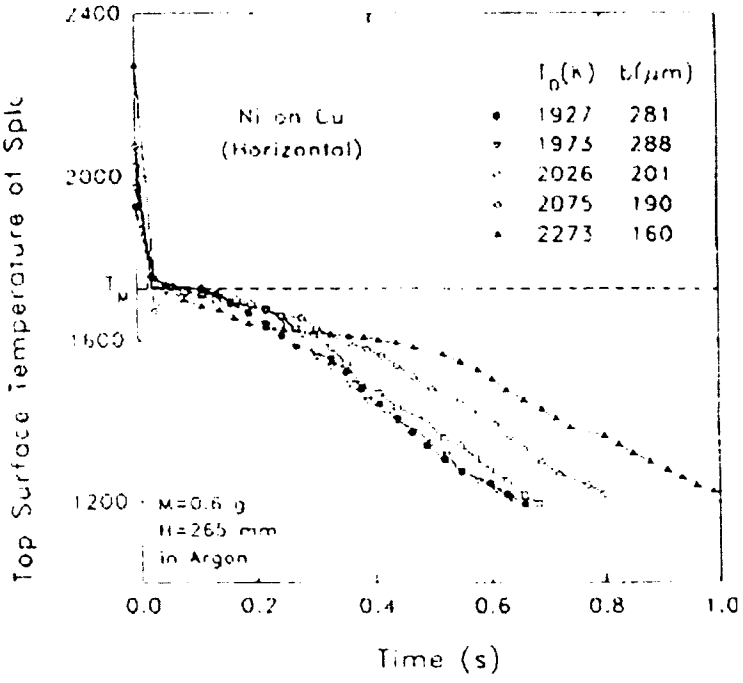

Figure 2.52 The relationship between top surface temperature of spat as a function of time at different initial meat temperature.[28]

El-Mahallawy and Assar also studied heat transfer coefficient for aluminum solidifying against a copper chill. The results show that the heat transfer coefficient sharply increases from 3 KW/m^2K to the maximum value during the first 20-50 seconds according to superheat, Figure 2.53.[7)]

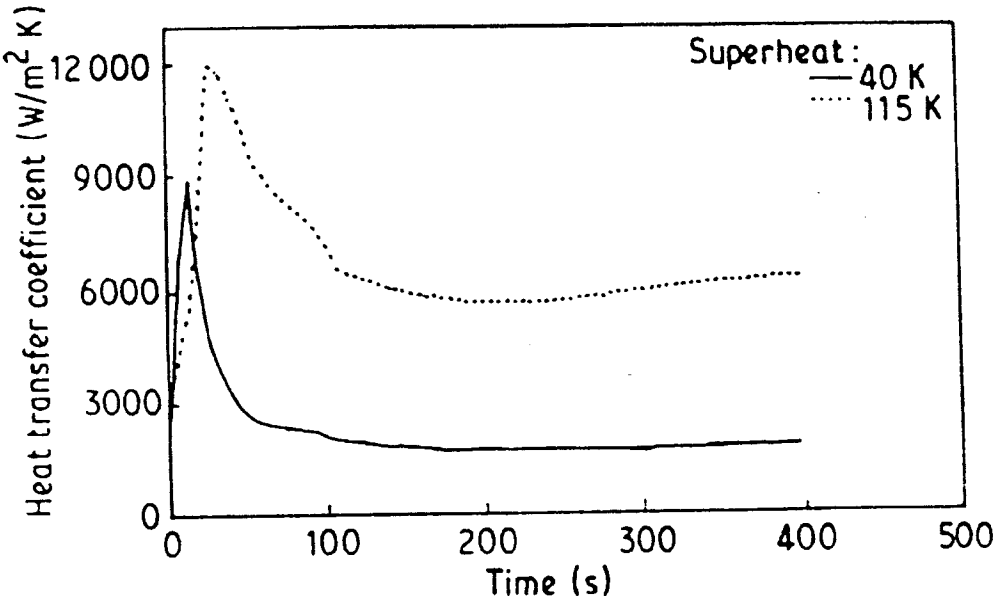

Figure 2.53 Variation of heat transfer coefficient with time for 40 °K and 115 °K superheat.[7)]

Les Strezov et al. immersed a smooth copper substrate into the melt of a 304 austenitic stainless steel at various superheat. At the initial of 50 milliseconds of melt/substrate contact time, the maximum heat flux decrease with increasing melt superheat, Figure 2.54, and the dendritic became coarser when superheat increased. Strezov's result is opposite to all other previous studies.[18)]

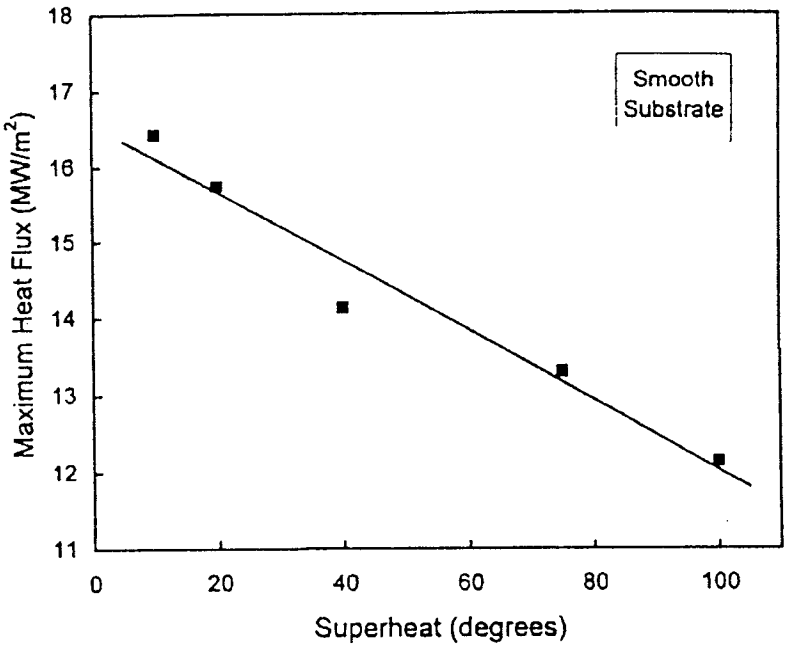

Figure 2.54 The effect of melt superheat on the maximum heat flux.[18]

In the melt spinning work area, done by *Wang et al.*, the solid-liquid interface velocity, for both aluminum and Titanium spun, decreased when a superheat increased. For aluminum spun, with a higher conductivity, a larger heat flux can be achieved when superheat increased.[30] Another work done by Wang and Matthys[29], discussed earlier in section 2.3.1, shows the effect of the melt superheat on the interfacial heat transfer during the early stages of splat solidification process. As shown in Figure 2.55, the strong effect of melt superheat on heat transfer coefficient, h, exists for nickel on a copper substrate. The results also shown that the smoother the surface is, the stronger the effect of superheat on h will be.

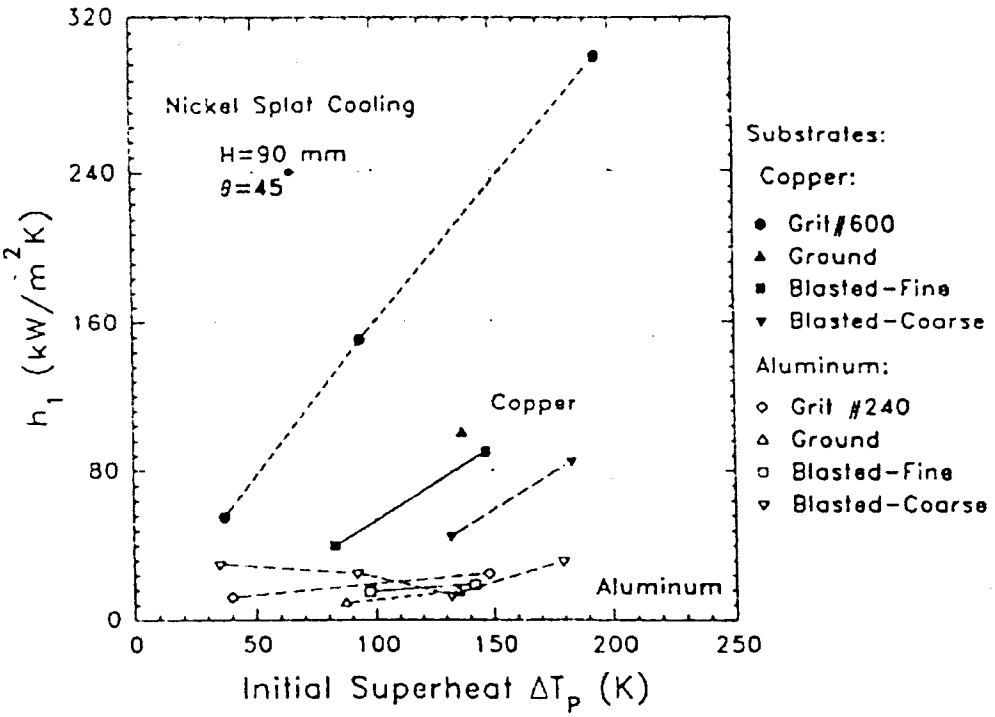

Figure 2.55 The interfacial heat transfer h during the liquid cooling as a function of melt superheat for nickel on several substrates of various finishes.[29]

2.2.5 Microstructure

To predict the properties and soundness of a cast product the formation of a microstructure during the solidification of alloys has to be known.

Muojekwu et al.[10] found that when the superheat increased the heat extraction is higher, the shell is thicker, and the dendrite arm spacing is smaller. His result is well agreed with all previous studies. [6, 34-37]

Grosjean et al. studied microstructure of the product cast from a small-scale double rolls caster. Due to a high undercooling and heat extraction rate a grain size is much finer than one found in the conventional continuous casting process.

In the case of the 304 stainless steel with 0.002% Sulfur content, which was ejected to solidified on to the copper chill mold under the laboratory condition, done by Lert-a-rom [33], the grain size is getting smaller when a superheat increase as shown in Figure 2.56 In this work the molten metal was ejected on to the copper mold therefore the size of the grain is varied with the distance from the impingement point, as shown in Figure 2.57. The grain size near the impingement point is obviously smaller than that far from the impingement point. This result can relate to the variation in heat transfer coefficient over the chill surface. It can be said that higher heat transfer rate at the impingement point makes the grain size smaller because of higher nucleation rate due to the higher cooling rate.

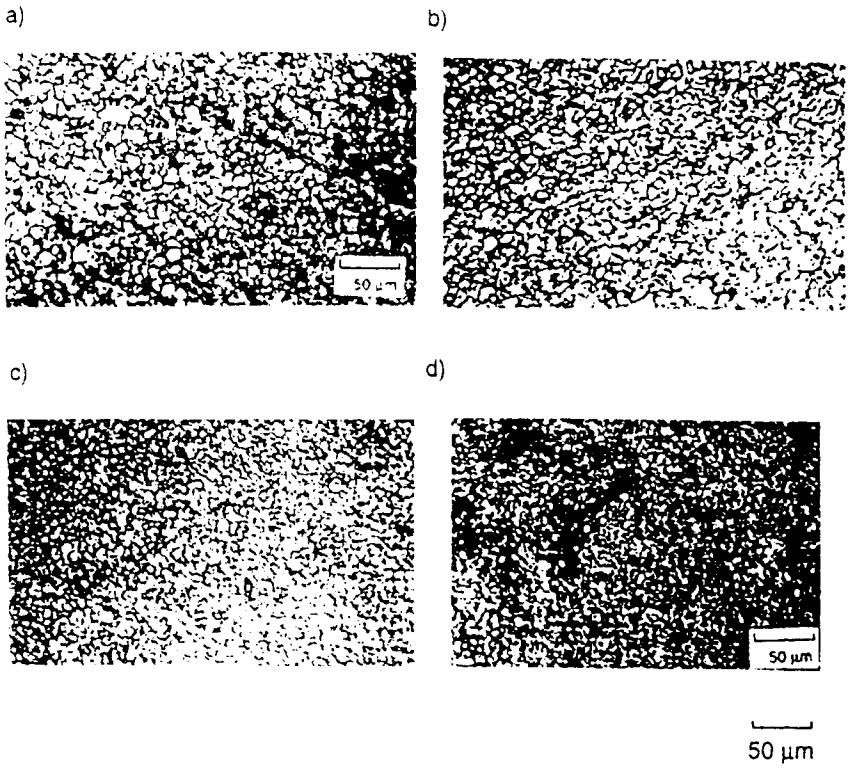

Figure 2.56 Effect of superheat on a surface grain size
(a) 10°C (b) 50°C (c) 60°C (d) 80°C [33]

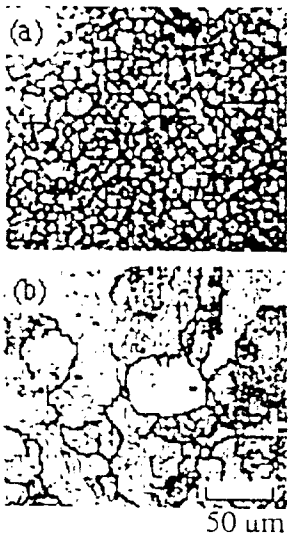

Figure 2.57 Surface grain structure (a) near an impingement point (b) far from an impingement point [33]

2.3 Mathematical Model

In order to investigate the interfacial heat transfer rate through the metal–mold interface both numerical and analytical technique were used in many works. The heat transfer coefficient can be estimated from the cooling rate by assuming an isothermal, newtonian, cooling condition. *Burden, Jones and Davies* employed this method to their melt spinning and splat cooling work.[41,42] Without the newtonian cooling assumption Huang and Fiedler analytically estimated heat transfer coefficient from solidification time and the thickness of his melt-spinning ribbon.[43]

The finite difference method and finite element method are the numerical methods that are widely used by many researchers in both materials science and mechanical engineer field.[38] One of the challenge is to use this method to determine the surface temperature or heat flux from the knowledge of other conditions such as temperature histories at interior points. The determination of the interfacial heat flux or surface temperature or heat transfer coefficient is an inverse problem, not a direct problem. Unfortunately many of concepts which work very well for direct problems (given the differential equation, properties ,boundary conditions and initial conditions) do not apply for this inverse problem. It is like the difference between obtaining a derivative and integral; evaluating the integral is an inverse problem and it is generally much more difficult than evaluating a derivative. The main objective of the inverse solution is to estimate the surface heat flux history, q(t). (An equivalent problem estimates the time-varying temperature at the heated surface) The problem can be solved by making calculated temperatures agree in a least squares sense with measured temperatures. The

agreement is accomplished by using a sequential least squares procedure and the Crank-Nicolson volume method is introduced to solve the partial differential equation and associated boundary and initial condition.

The difficulty of the solution of the inverse heat conduction problem arises as a consequence of the diminished and delayed thermal response in the interior of a body. Error associate with the use of truncated temperature data at an exterior point are numerically amplified during the determination of the time varying thermal conditions at the surface. The inverse heat conduction becomes nonlinear when the solidification of an object involve a change of phase and temperature variable thermal properties.[48-49]

One of the first efforts to solve this problem is reported by *Stoz*[38,49] He subdivided the time domain into intervals such that the observed temperature, in each time interval, at a given interior point is considered to be the result of a step change in surface heat flux at the beginning of the time interval. By using the Duhamel's theory the observed temperature in this time interval is expressed in term of an integral involving the step change in surface heat flux, thereby enabling the reverse determination of surface heat flux through a numerical inversion of this intergral.

Sparrow[49,74] solved the inverse heat conduction problem by using the Laplace transformation on transient equation of heat conduction, the surface temperature is expressed in term of internal temperature history at a point in the transformed s-domian. Subsequent application of inverse Laplace transformation to this relation then gives the surface temperature in term of an integral involving the internal temperature history.

A numerical technique, from the standpoint of effective treatment of experimental data, that will allow a solution to the inverse heat transfer problem was introduced by

Beck[38] This numerical scheme, a least square method [29,38] can be used to solve the inverse heat conduction problem by using the measured temperature at one or several locations in the system. The result gives the interfacial heat flux or interfacial heat transfer coefficient as a continuous function of time.[27,38] However, if the thermocouples which were used to provide the internal history of the body and the heat flux change rapidly, the temperature history can be corrupted by the effect of inherent thermocouple sensor dynamic.[39] This problem also occurred with Strezov's work and to solve this problem a modified version of Beck's IHCP algorithm had to be employed in his study.[18,20]

2.4 Conclusions from literature review and the objective of the present study

Conclusions of the literature review

Based on literature survey, the following conclusions were drawn.

1) Research has been conducted which focused on the transient heat transfer behavior in the early stage of solidification of a metal alloy on both a metal substrate and a twin roll caster. These studies tried to identify the importance of process variable such as melt superheat, substrate material, substrate finish and alloy composition on both interfacial heat transfer and initial solidification behavior.

2) Different techniques have been used to measure substrate temperature profiles and determine the interfacial heat transfer rate between a molten metal and a substrate. However most of these studies lack information on the initial heat transfer behavior during the first milliseconds of contact time between the molten metal and chill mold as their experimental technique was not designed for millisecond resolution of heat transfer behavior. Therefore the magnitude of the heat transfer rate during that time is missing from their data and it is not possible to predict initial solidification phenomena.

3) The technique to study the initial solidification and heat transfer behavior of melt on a substrate has been established by many researchers. Most of the work carried out by predicting the initial solidification behavior of the melt from the thermal result and solidified specimen microstructure. None of those techniques can simultaneously in-situ observe the initial solidification process of the molten droplet and measure the heat flux.

4) Although several of the previous workers paid attention to the effects of mold surface roughness, only a few investigated the effect of the casting parameters on the surface roughness profile of the cast specimens. The surface roughness profile of the cast specimen will form very quickly after the metal contacts a mold surface. Therefore, the phenomena that happen during the first few milliseconds of contact between the droplet and the mold can determine the surface of the specimen. If the relationship between casting parameters and the surface roughness can be clearly understood, and also the relationship between the initial heat transfer behavior of the specimen and the surface roughness profile can be established, then the occurrence of surface defects due to initial solidification phenomena (ripples and laps) can be predicted.

5) It has been demonstrated by many workers that the substrate surface condition has a strong influence on the rates of interfacial heat transfer in the initial period of the melt/substrate contact. However only one literature reported the role of oxide accumulation on the 304 stainless steel melt/copper substrate interface on the

interfacial heat transfer behavior in the system using the substrate embedded in a inclined moving paddle similar to melt/roll contacting geometry of the meniscus region of a twin-roll.

Objectives of the present study

In this present study, steel alloys are melted and then ejected onto the copper chill mold and the study of a transient heat transfer between the molten droplet and the copper chill mold at the early stage of solidification was carried out.

Based on the conclusion from the literature review, the objectives of this study were established as follows.

1) To develop an experimental apparatus for the measurement of the interfacial heat transfer rate at the initial stage of solidification in millisecond scale.
2) To develop an experimental technique capable of simultaneous in-situ observation and measurement of rapid heat transfer enables a coupling between the interfacial heat transfer rate measurement and droplet solidification observation.
3) To investigate the influence of process variables such as superheat, mold condition and alloy composition on initial heat transfer rate, solidification behavior and surface roughness.

The work focuses on

1) the effects of sulfur content on the initial heat transfer between the droplet and the substrate. Varying sulfur levels can strongly affect the surface

tension of the droplet and the wettability between the droplet and the copper substrate.

2) The effect of the oxide film deposited during the solidification process of Mn-Si killed steel. The additions of Mn/Si in steel can also affect the heat transfer behavior as liquid inclusions can be formed within the droplet and a black substance is deposited onto the surface of the copper mold during experimentation. Both Mn and S affect the initial heat transfer rate, the spreading behavior and surface roughness of the droplet. However details of these effects are still unknown. In order to investigate these effects the work has been focused in two parts

- Investigation of the effects of the black substance, deposited at the surface of the copper substrate, on the interfacial heat transfer behavior of the Mn-Si killed steel.
- A study of the formation and identification of the deposited oxide film in order to understand how it relates to the steel chemistry and the process variables, and the formation of the surface of the solidified droplet during the casting process.

Chapter 3

Experimental Design

3.1 The Requirements

To study the initial heat transfer and solidification behavior of the molten steel on the chill substrate the experimental technique was designed based on the following requirements.

1) The experimental apparatus should imitate the strip casting process. Since the intervening flux used in a continuous casting process to moderate and homogenize heat flux could not be used in strip casting the apparatus was designed to allow the molten steel to directly contact the copper substrate.

2) To gain information on the initial heat transfer and solidification behavior that occurs during the first milliseconds of a contact time between the molten metal and chill mold, as the phenomena that happens during that time can determine the surface of the specimen, the experimental technique should be designed for millisecond resolution of interfacial heat transfer behavior.

3) The experiment technique should enable the influence of process variables to be investigated in order to better understand the role of processing parameters such as superheat, steel chemistry and mold surface condition on the initial solidification phenomena, heat transfer rate and formation of the cast steel surface.

3.2 Development of the Experimental Apparatus

The experimental apparatus involved the ejection of molten metal droplet onto a water-cooled copper mold. The apparatus has gone through three different revisions to solve problems discovered during operation of the equipment and to meet all the requirements.

3.2.1 The First Experimental Set Up

3.2.1.1 The Apparatus

The first set up is shown in Figure 3.1. Initially this design was developed by Todoroki, Lert-a-rom, Suzuki, and Cramb[13] for determination the initial heat transfer rate of nickel, iron and 304 stainless steel in contact with a chill mold.

The apparatus consisted of an outer quartz cylinder, inner quartz nozzle with a hole at the bottom, induction coil, and a water-cooled copper mold. The specimen was melted in the quartz nozzle by induction furnace. The melting temperature was measured by two-color pyrometer through a quartz prism. The argon gas was introduced into the outer and inner quartz cylinder in order to control the atmosphere. The six exposed tip K-type thermocouples, Figure 3.3, were installed inside the copper mold in order to measure the temperature within the chill mold during the experiment. The thermocouples were installed in three different locations underneath the copper mold (No.1, No.2 and No.3) as shown in Figure 3.2. In each position, there are two thermocouples horizontally installed at 1 mm and 4 mm from the surface of the copper substrate.

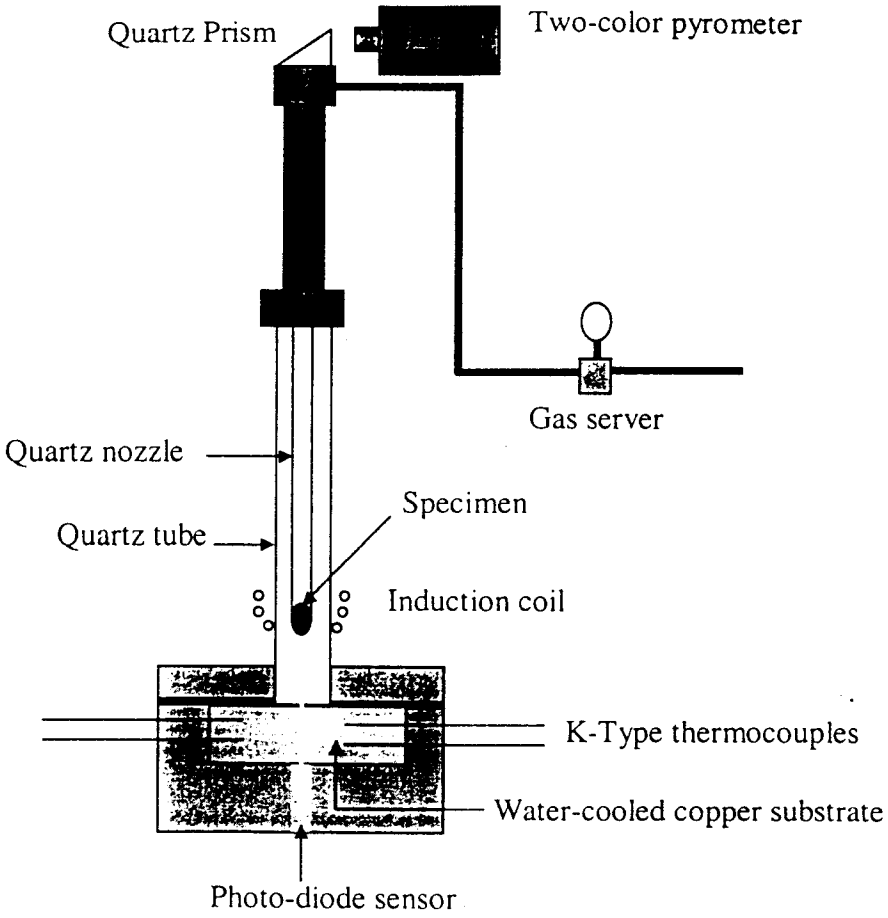

Figure 3.1 The experimental apparatus (the first set up).

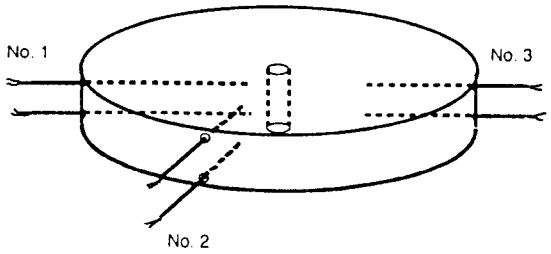

Figure 3.2 The copper mold.

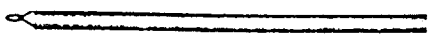

Figure 3.3 Exposed tip K-type thermocouple.

The thermal data received from the thermocouples was recorded on personal computer by using a data acquisition system, the DynaRes of the Strawberry Tree Inc., with a sampling rate 20 milliseconds or 50 Hz. The surface temperature of the cast steel was measured by using a photo diode sensor developed by Suzuki and Mizukami et al.[14,15] A half a millimeter diameter hole was drilled in the copper chill mold to collect the emitted light from the surface of the cast specimen and the signal was transferred to a photo diode sensor through a quartz mirror and optical fiber. The output voltage from the sensor was documented by another data acquisition system, the Daqboard of IO tech., of sampling rate 500 Hz. After that the voltage was converted to a surface temperature.

3.2.1.2 The Experimental Procedure

After placing the specimen inside the inner quartz nozzle, which has a small hole at the bottom, the argon gas was substituted for the air. Then the induction power was turned on and the specimen was heated and melted. The temperature was controlled by a two-color pyrometer. After the molten metal reached a desired temperature the induction power was turned off and the liquid metal was ejected from the nozzle onto the copper chill mold by pressurized argon gas stored in a gas server. The ejection pressure is 15 Psi in every experiment. Mold temperatures were measured by six K-type thermocouples installed at different positions inside the substrate and the heat flux was calculated by using finite difference method.

3.2.1.3 The Calculation

1) The Heat flux calculated from the copper mold temperature

Heat flux can be calculated from copper mold temperature profiles and the heat transfer coefficient can be calculated from the surface temperature of solidified droplet and the surface temperature of the copper mold. The surface temperature of the solidified droplet, Tsm, was measured by photo diode sensor and surface temperature of the substrate, Tsc, was calculated from measured chill temperature profiles, T1 and T4, by using finite difference method.

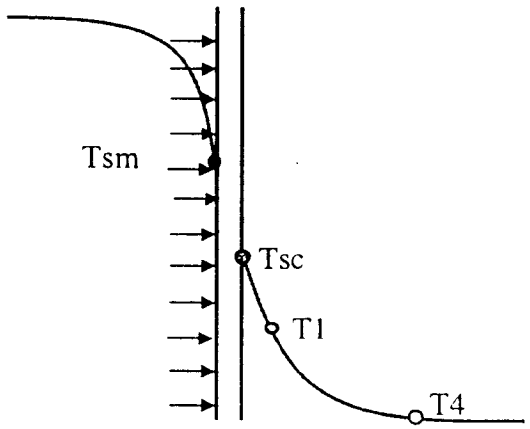

By assuming a one-dimensional heat flow, heat flux and heat transfer coefficient were calculated from the following relationships:

$$\frac{dT}{dt} = \alpha \frac{d^2T}{dx^2} \qquad \textbf{3-1}$$

Where α = Thermal diffusivity and x = distance in the copper chill.

Heat flux from cast to chill. $$q_{in} = h(T_{sm} - T_{sc})$$ **3-2**

Heat flux from chill to cooling water. $$q_{out} = -k\left(\frac{dT}{dx}\right)$$ **3-3**

Where Tsc and dT/dx can be calculated from a finite difference method by using the temperature profiles getting from thermocouples installed at 1 and 4 mm and the heat transfer coefficient, h, can be calculated from equation 3-4.

$$h = -\frac{K\left(\frac{dT}{dx}\right)}{(T_{sm} - T_{sc})} \quad \textbf{3-4}$$

Where k = Thermal conductivity.

The principle of finite difference method

By applying finite difference method, in equation 3-1, the temperature of i-th element of copper chill mold from time step j to j+1 can be described as follows:

$$\frac{dT}{dt} = (\frac{k}{\rho Cp})\frac{d^2T}{dx^2} \quad \textbf{3-5}$$

$$\frac{dT}{dt} = (\frac{k}{\rho Cp})\left[\frac{T_{i-1,j} - 2T_{i,j} + T_{i+1,j}}{\Delta x^2}\right] \quad \textbf{3-6}$$

$$dT = (\frac{k\Delta t}{\rho Cp\Delta x^2})[T_{i-1,j} - 2T_{i,j} + T_{i+1,j}] \quad \textbf{3-7}$$

$$T_{i,j+1} = T_{i,j} + r(T_{i-1,j} - 2T_{i,j} + T_{i+1,j}) \quad \textbf{3-8}$$

Where $r = \frac{k\Delta t}{\rho Cp\Delta x^2}$

k = Thermal conductivity.

ρ = The density of copper chill.

Cp = The heat capacity.

Δx = The element size.

Δt = The time interval.

From the equation 3-8, the heat input at time step j-th can be calculated from

$$\Delta q_j = h_j(T_{s,j} - T_{0,j})\Delta t \qquad \textbf{3-9}$$

Where h_j = Heat transfer coefficient.

$T_{s,j}$ = The surface temperature of the solidified steel measured by photo diode sensor.

$T_{0,j}$ = The surface temperature of the copper chill calculated from the temperature profiles measured by K-type thermocouples at position 1mm and 4 mm underneath the substrate surface. The Δx was set equal 1mm and Δt was set equal 0.02 second similar to the acquisition speed of the thermocouples.

The surface temperature of the copper chill $T_{0,j+1}$ is calculated from the energy balance of the element in the substrate. The heat balance at the surface contact between the copper chill and metal, i = 0, is as follows:

$$\frac{d(\frac{kdT}{dx})}{dx} = \frac{\rho CpdT}{dt} \qquad \textbf{3-10}$$

$$(q_{in} - q_{out}) = \rho Cp \frac{\Delta x}{2} \frac{dT}{dt} \qquad \textbf{3-11}$$

$$(\Delta q_{in} - \Delta q_{out}) = \rho(\frac{\Delta x}{2}) Cp dT \qquad \textbf{3-12}$$

Where q_{in} is the heat flux from the solidified shell into the metal-mold interface and q_{out} is the heat flux away from the interface into the mold.

Therefore the temperatures of the element i=0 of the copper mold from time j to j+1 is:

$$T_{0.j+1} = T_{0.j} + \frac{2(\Delta q_{in} - \Delta q_{out})}{\rho Cp \Delta x} \qquad \textbf{3-13}$$

From the boundary conditions, equation 3-2 and 3-3, Δq_{in} and Δq_{out} are described as:

$$\Delta q_{in} = h_j (T_{s.j} - T_{0.j}) \Delta t \qquad \textbf{3-14}$$

$$\Delta q_{out} = k(T_{0.j} - T_{1.j}) \Delta t \qquad \textbf{3-15}$$

Where h_j can be calculated from equation 3-13, 3-14 and 3-15 if $T_{0,j}$ and $T_{0,j+1}$ were solved through the numerical analysis.

2) The heat flux calculated from the cast surface temperature variation

When the surface temperature Y(t) of the semi-infinite body is known continuously as a function of time. The temperature distribution in a body is given by Duhamel's theorem as the following equation:

$$T(x,t) = T_0 + \int_0^t u(x,t-\lambda)\frac{dY(\lambda)}{d\lambda}\,d\lambda \qquad \textbf{3-16}$$

Where u(x,t) is the temperature response function for a body. λ is a dummy time variable and $Y(\lambda)$ is the continuous surface temperature variation with time. Heat flux variation with time at the surface is given as the following equation [75]:

$$q(t)\Big|_{x=0} = \sqrt{\frac{k\rho Cp}{\pi}}\int_t^t \frac{Y'(\lambda)}{\sqrt{t-\lambda}}d\lambda \qquad \textbf{3-17}$$

Where k = Thermal conductivity, ρ = Density, Cp = The specific heat capacity.

Before latent heat is released during time 0 to time t, by using the cast surface temperature variation measured by photo diode sensor, the heat flux can be calculated by equation 3-16.

The cooling rate of the molten metal at surface $Y'(\lambda)$, $dT/dt_{|x=0}$, can be assumed as a constant because the slope is quite close to the linear function, Figure 3.4. Therefore the equation 3-17 can be simplified as the following equation:

$$q(t) = A * \frac{dT}{dt_{|x=0}}\sqrt{t} \qquad \textbf{3-18}$$

Where $A = \sqrt{\frac{K\rho Cp}{\pi}}$

Figure 3.5 shows the heat flux calculated from both cast surface temperature and chill temperature profiles.

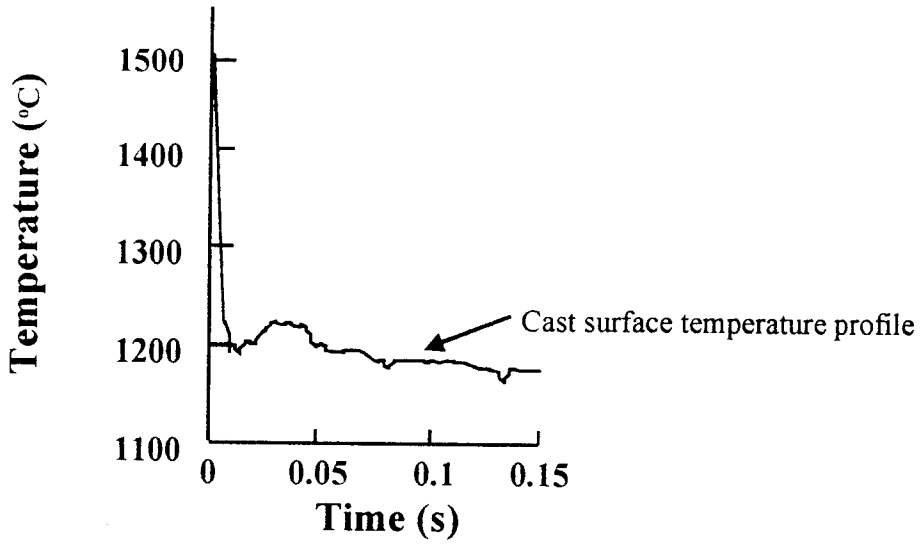

Figure 3.4 The cast temperature profile measured by photo diode sensor.

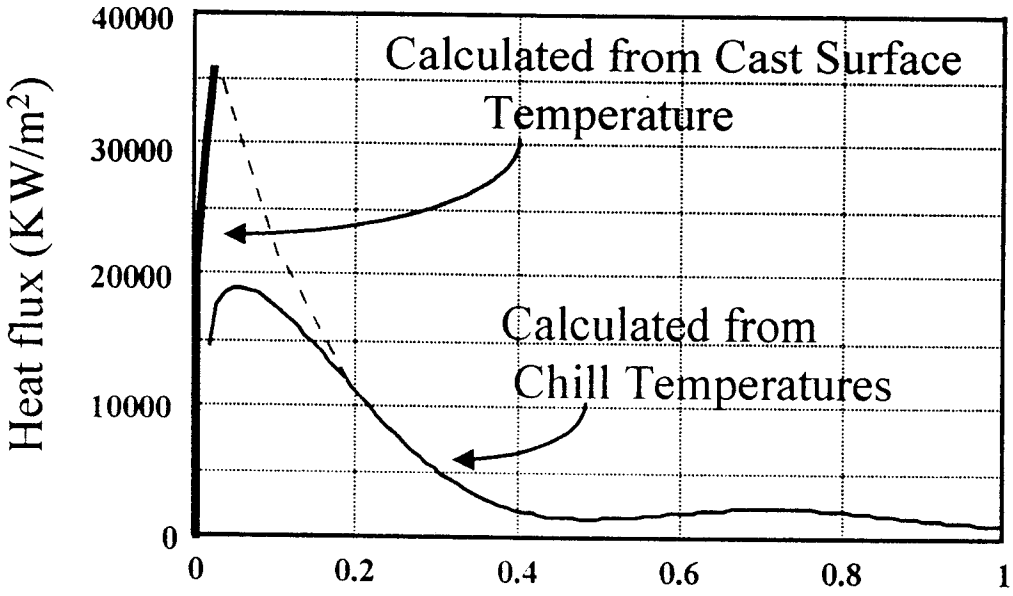

Figure 3.5 The heat flux calculated from copper chill and cast surface temperature.

If we compare heat flux calculated from both methods, during the first milliseconds of the metal-mold contact time, the heat flux curve obtained from the cast surface temperature gives a significantly higher value than the one determined from the chill temperatures, Figure 3.5. The result implies that the response time of the thermocouple was still not fast enough to detect the transient temperature variations. The relationship between heat flux and time can only be obtained by connection of heat flux curves calculated from both methods.

3.2.1.4 The Limitation of the First Set Up

1) The lack of the information of the heat flux curves, obtained from chill temperatures, during the first milliseconds of the contact time was a major limitation of the method. Even though the method of calculating heat flux from the cast surface temperature was introduced to minimize this problem the method could only be applied during the time before the latent heat is released, with an assumption that the relationship between temperature and time is linear. After the latent heat is released heat flux curved has to be calculated directly from the chill temperatures. Since both calculations have their own limitations and are also prone to the introduction of errors when both curves were connected, it was important to find a calculation method that was capable of calculation of the heat flux for the entire solidification process.

2) It was not possible to measure mold temperatures with millisecond resolution due to the set up of the thermocouples and data acquisition system. Besides the fast sampling speed of the data acquisition system, the type, size, response time and position of the thermocouples play importance roles on the system temperature measurement ability. In order to develop a millisecond resolution temperature measurement system the response of the thermocouples and speed of the data acquisition had to be improved. If a millisecond resolution of the temperature measurement can be achieved the variation of the transient temperature will be detected with actual resolution and the initial heat transfer behavior between the droplet and the substrate can be obtained.

3.2.2 The Second Experimental Set Up

3.2.2.1 The Apparatus

The second set up was developed from the first set up in order to allow the measurement of temperature and calculation of heat transfer parameters with millisecond resolution. The data acquisition system was upgraded for a faster sampling speed. A Keithley DAS1801ST board with STP-50/C terminal panel and Testpoint software were chosen to collect and record the data from T-type thermocouples. The sampling speed was set to 16 KHz for each channel that is about 300 times faster than the previous set up. The personal computer with a faster processor, Pentium II 333 MHz, and bigger memory, 64 MB RAM was installed and hooked to the new data acquisition system. The copper mold was restructured, Figure 3.10, by 1) Reducing the distance of the thermocouple from surface from 1mm. to 0.5 mm and from 4 mm to 3.5 mm for better mold surface temperature response and heat flux calculation; 2) Isolating the copper substrate from the interfering environment by increasing its height from 5 to 6 mm; 3) Thermocouples installed underneath the copper chill mold surface were changed from K-type to be T-Type for a faster response by using Mr. Todoroki and Mr. Lert-a-rom 's technique as shown in Figure 3.7. The temperature can be measured directly at point "a" because two different kinds of metal, constantan and copper wire, are contacted each other and generate some small voltage at that point. Small diameter 0.0076mm (0.003 inches) of shield T–type thermocouples were used in this set up. The hole at the bottom of the glass nozzle was better made, Figure 3.12, resulting in a precise ejection position of the liquid steel on the copper substrate. A gas purification system was added in order to control the atmospheric oxygen content.

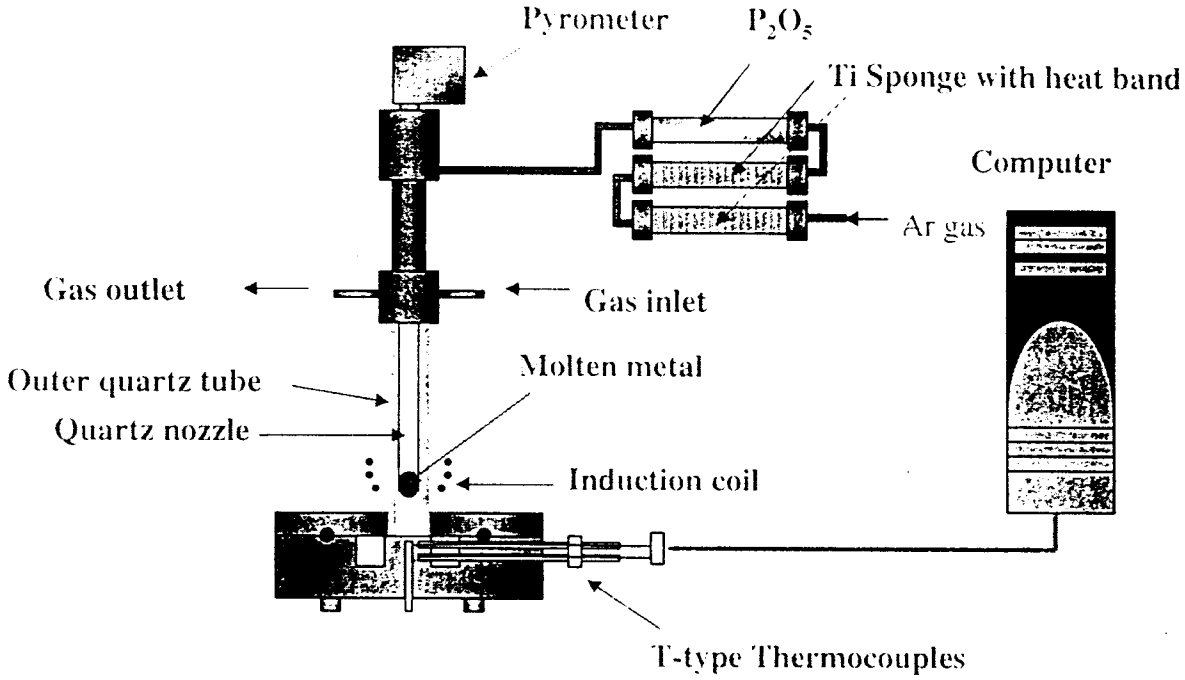

Figure 3.6 The schematic of the experimental apparatus.

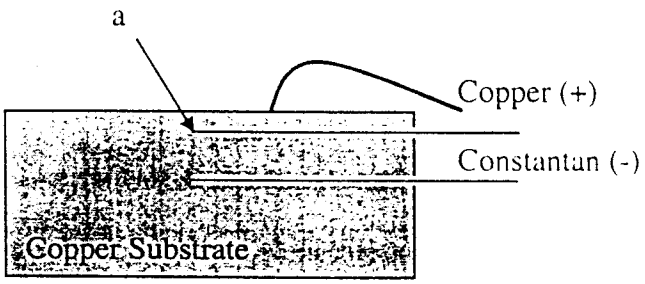

Figure 3.7 The schematic of T-type thermocouple installing technique.

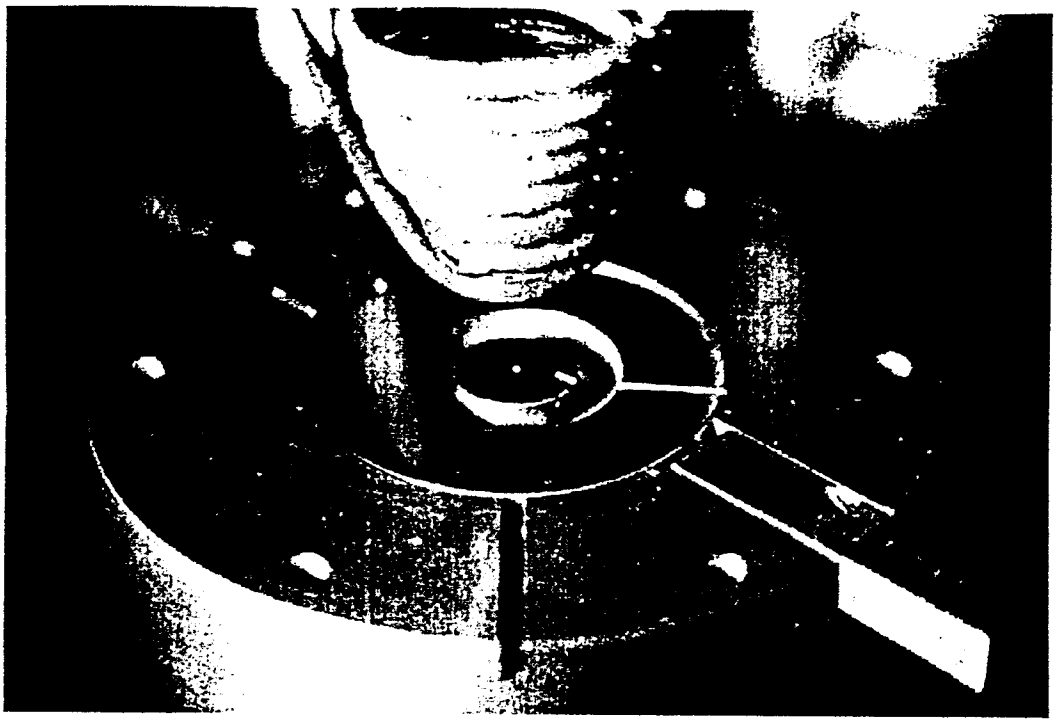

Figure 3.8 The close up look of the copper substrate and the induction coil.

Figure 3.9 The close up look of the substrate and solidified droplet.

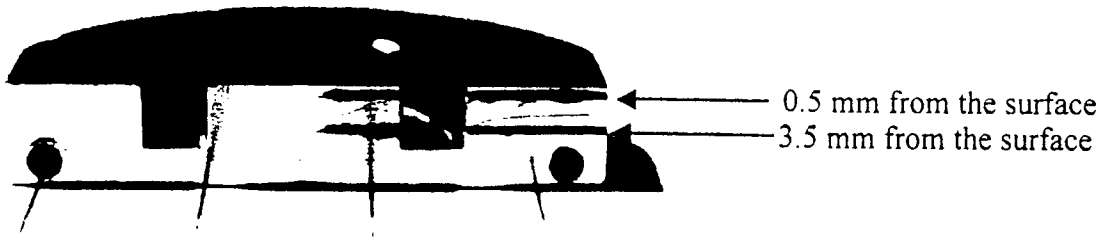

Figure 3.10 The cross section of the copper substrate.

Figure 3.11 The copper mold with the inserted T-type thermocouples.

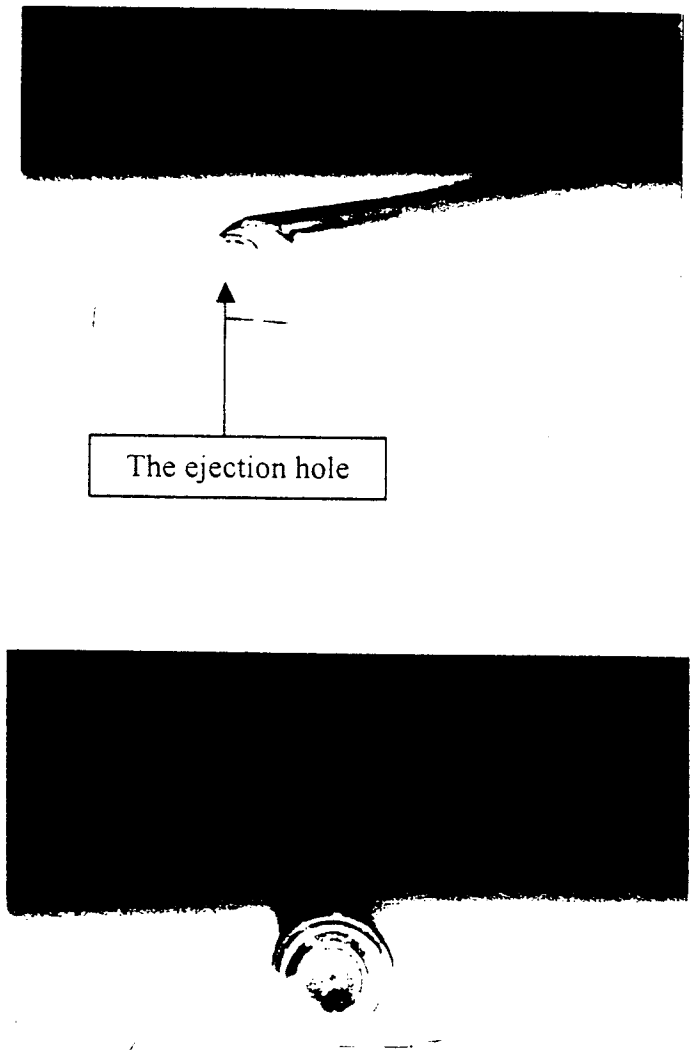

Figure 3.12 The glass nozzle.

3.2.2.2 The Experimental Procedure

The procedure is almost the same as the first set up. The superheat of the molten steel was measured by a two-color pyrometer, placed above the quartz nozzle where it can directly see the liquid steel. Mold temperatures were measured by two T-type thermocouples in order to examine the variation of heat transfer rate over the mold surface. These data were recorded on a personal computer through a new high-speed data acquisition system with a 16KHz sampling speed for each channel. After obtained the temperature profiles inside the copper mold, the heat flux during the initial solidification was calculated by new IHCP software that was specially customized for this work by Prof. J.V.Beck.[3, 39, 40] at Michigan State University. The surface heat flux as a function of time was estimated based on IHCP algorithm which is more precise than the previous finite difference method developed by Prof. T. Suzuki.

3.2.2.3 The Calculation

The common technique for calculating interfacial heat fluxes is to use the inverse heat conduction problem (IHCP) algorithm. The inverse heat conduction problem seeks to determine the surface temperature of heat flux from other known conditions[40] such as temperature history at interior point. The difficulty to solve this problem is the diminished and the delayed thermal response in the interior of the body. Moreover the solidification of the metal relates to both phase change and temperature variable thermal properties so that the inverse heat conduction becomes nonlinear. This technique is used estimate the transient interfacial heat flux and surface temperature of the chill mold based on interior temperature measurement taken from the substrate and the sequential

nonlinear estimation technique which is based on Crank-Nicolson procedure and least squares minimization. With adequate insulation on the cylindrical surface of chill mold, heat flow pattern through the chill can be reasonably approximated as one dimension heat transfer problem.

The governing differential equation

$$\frac{1}{\alpha}\frac{\partial T}{\partial t} = \frac{\partial^2 T}{\partial^2 X} \qquad \textbf{3-19}$$

The initial and boundary conditions

$$t = 0 \qquad T = T_0 \qquad \textbf{3-20}$$

$$t > 0 \qquad 0 < x < H_{chill}\ , \qquad -k\frac{\partial T}{\partial x} = q(t) = h(t)(T_{melt} - T_{chill}) \qquad \textbf{3-21}$$

$$t > 0 \qquad x = H_{chill}\ , \qquad T = T_{water} \qquad \textbf{3-22}$$

The interfacial heat flux was estimated by following equations

$$q^n = q^{n-1} + \frac{\sum_{i=1}^{r}\sum_{j=1}^{n}(TM_j^{n+i-1} - TC_j^{n+i-1})Z_j^{n+i-1}}{\sum_{i=1}^{r}\sum_{j=1}^{n}(Z_j^{n+i-1})^2} \qquad \textbf{3-23}$$

$$Z = \frac{\partial T_j^{n+i-1}}{\partial q^n} \qquad \textbf{3-24}$$

where

Z = Sensitivity coefficient.

TC = Calculated temperature (^oC).

TM = Measured temperature (^oC).

r = The number of future time steps.

n = The number of thermocouple sensors.

q = Heat flux (W/m^2).

α = Thermal diffusivity m^2/s.

H_{chill} = The height of a chill cylinder.

When the interfacial heat flux changes rapidly, as the case of this study, the inherent thermocouple sensor dynamics can introduce measurement errors[39]. A modified version of Beck's inverse heat conduction problem algorithm, which can minimize those errors, was used in this study.

3.2.2.4 The Improvement of the Results

The millisecond resolution of the temperature measurement was achieved and the variation of the transient temperature was detected properly.

Figure 3.13 (a)-(b) and Figure 3.14 (a)-(b) show a typical mold temperature profiles from the first experimental set up. The temperature profiles were measured, at 20 ms (50Hz) sampling speed, by K- type thermocouples at position 1mm and 4mm from the substrate surface. From the temperature profiles, it took approximately 1 sec for the mold temperature to rise up to the maximum value.

Figure 3.15 (a)-(b) show a typical mold temperature profiles from the modified version of the experimental system, the second set up. The mold temperature profiles were measure by T-type thermocouples at sampling speed of 16 KHz. The results show that the mold temperature rose to the maximum value within 50 ms. Figure 3.16 shows the comparison between the mold temperatures profile from the two different temperature measurement systems.

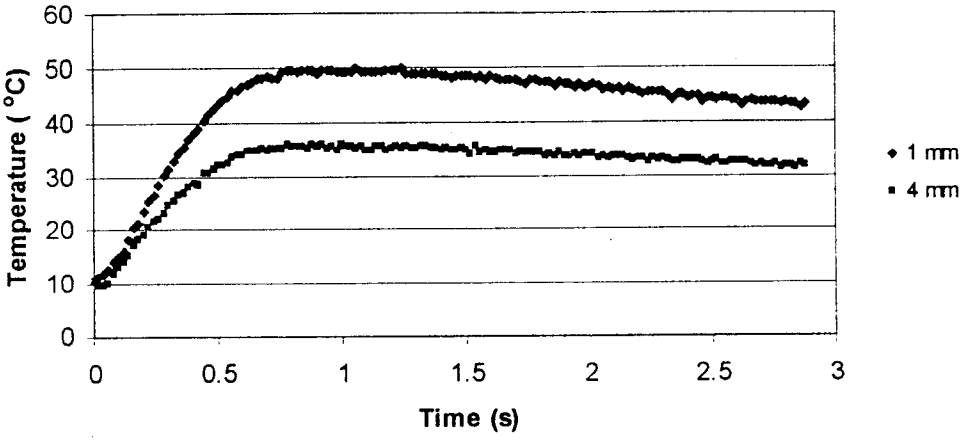

(a)

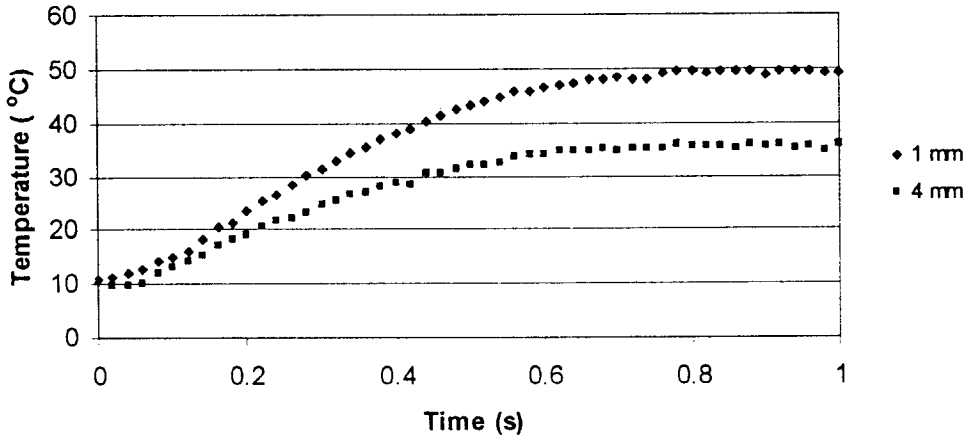

(b)

Figure 3.13(a)-(b) The mold temperature profile measured at position 1 mm and 4mm from the mold surface at sampling speed 20 ms(50Hz). during the first 3 sec (a) and 1 sec (b) of the contact time.

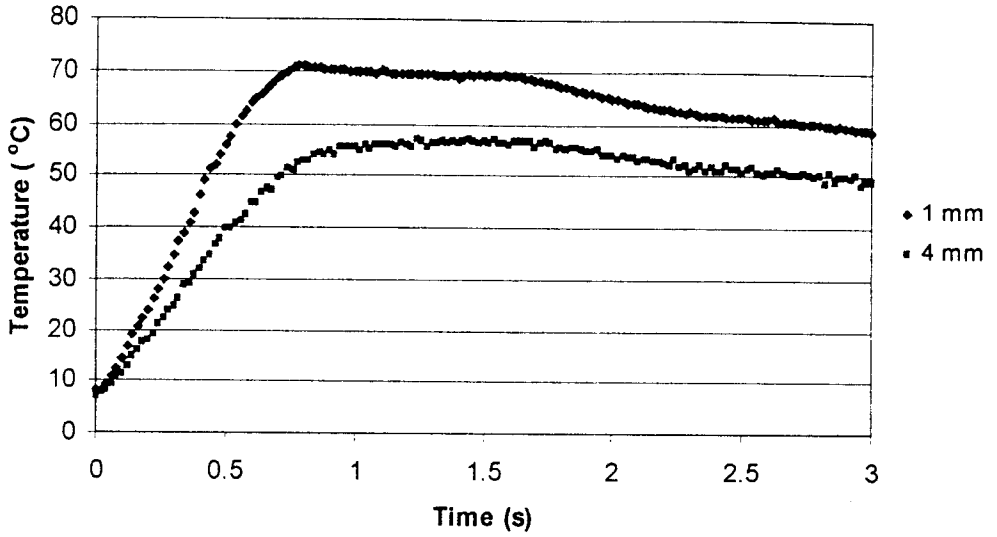

(a)

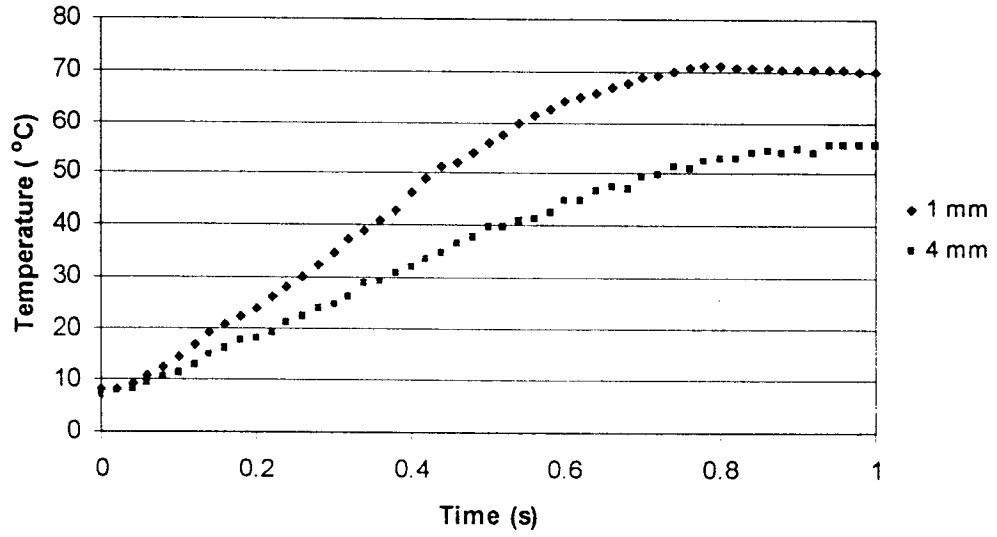

(b)

Figure 3.14(a)-(b) The mold temperature profile measured at position 1 mm and 4mm from the mold surface at sampling speed 20 ms (50Hz). during the first 3 sec (a) and 1 sec (b) of the contact time.

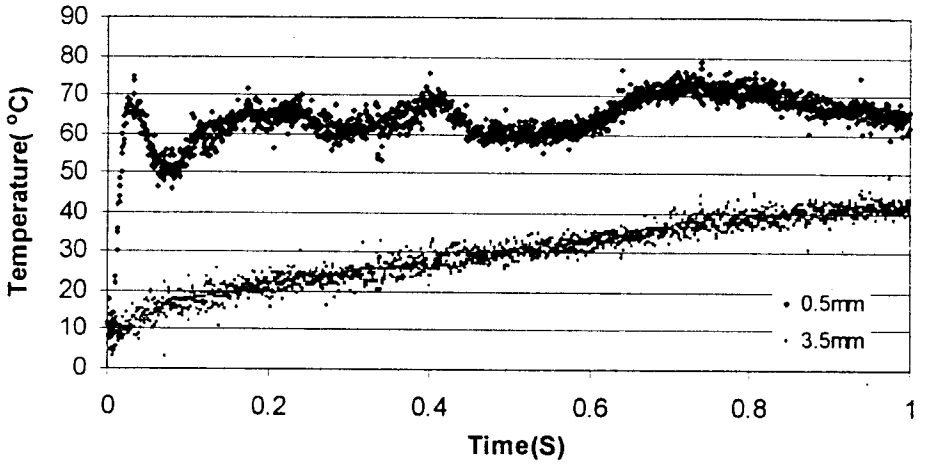

(a)

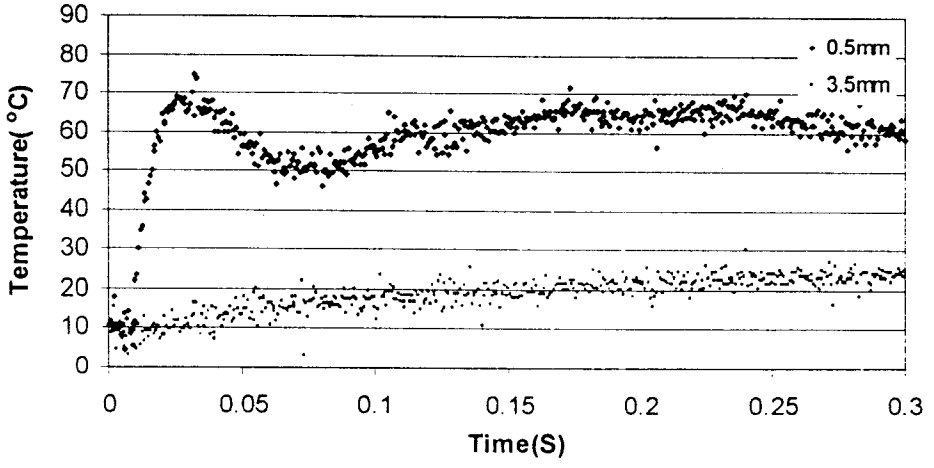

(b)

Figure 3.15(a)-(b) The mold temperature profile measured at position 0.5 mm and 3.5 mm from the mold surface at sampling speed 16KHz. during the first 1 sec (a) and 0.3 sec (b) of the contact time.

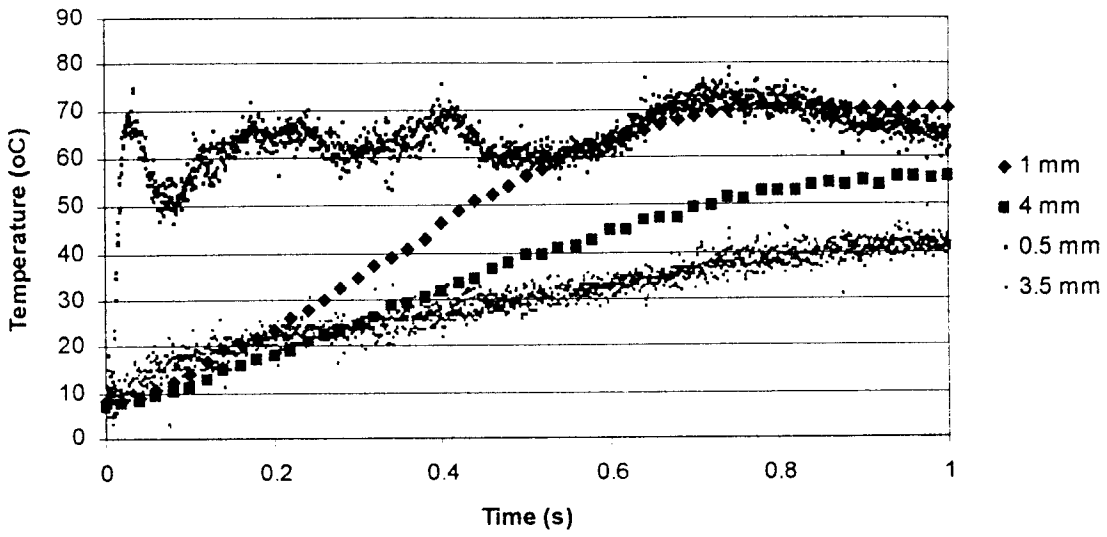

Figure 3.16 The comparison between the mold temperature profiles from the first and second experimental set up. The thermocouples were at position 0.5 mm and 3.5 mm for the second set up and at 1mm and 4 mm for the first set up.

It can be seen that the temperature profile from the old temperature measurement system, the first experimental set up, has less detail than that of the new system, the second experimental set up. The fluctuation of the temperature profile, which is probably due to the movement of the droplet could not be observed in the old system. The significant difference in detail of both temperature profiles could be observed during the first 500 ms when the profiles from the old system were still rising to their maximum value.

3.2.2.5 The Influence of Process Variables on Initial Heat Transfer Using the Modified Apparatus

To better understand the role of processing parameters the experimental apparatus should enable the influence of the process variables to be investigated. Figure 3.17 shows the mold temperature profiles of Fe-0.33%S droplets from two different experiments with a similar experimental condition except one droplet was ejected at 40°C superheat and another one at 100°C superheat. The mold temperature was set at 7°C at the beginning of both experiments and, in both cases, thermocouples were placed at a position of 0.5 mm and 3.5 mm from the substrate surface.

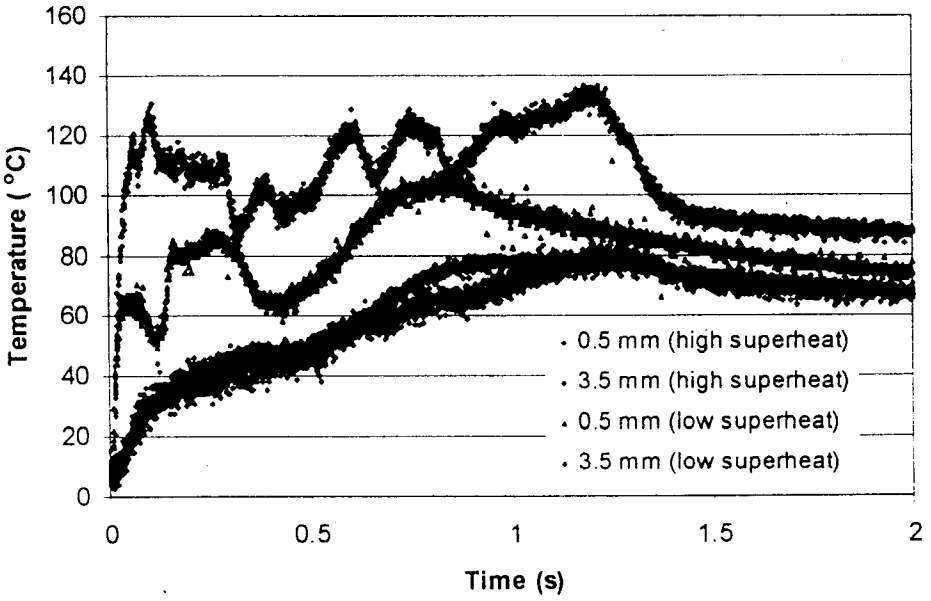

Figure 3.17 The comparison between mold temperature profiles from two different experiments with the same experimental condition except the melt superheat.

It can be seen that the superheat affected the initial heat transfer between the droplet and the copper substrate significantly. The substrate temperature increased with increasing melt superheat. The effect of superheat was clearly shown in the results and indicated that

the influence of the process parameters can be investigated by this experimental technique.

3.2.2.6 The Limitation of the Second Set Up

Although the information of the initial heat transfer behavior that occurs during the first milliseconds of contact time between the molten metal and chill mold can be gained by this set up the phenomena that happened during the initial metal-mold contact time and the solidification behavior of droplet are still unknown. It's important to reveal and record the phenomena that happen during the ejection and solidification period since the visual data allows determination of droplet movement, spreading and solidification rate. Therefore only appropriate data, with a good experimental condition, should be selected for heat flux calculation.

3.2.3 The Current set up

3.2.3.1 The Apparatus

The current set up was designed to allow the solidification process of the droplet to be seen and recorded by VCR. For this set up the copper chill mold was moved inside the bell jar, Figure 3.18 and 3.19, and the outer quartz tube and the mold cover was removed. The experiment was recorded by using a CCD camera with Minolta 50 mm f3.5 lens. The solidification front of the droplet can be observed and solidification time can be estimated by using a timer. The atmosphere is well controlled by applying a vacuum pump into the system and then refilling with treated argon. The temperature of the copper mold can be controlled by circulation either warm or cold water inside the mold.

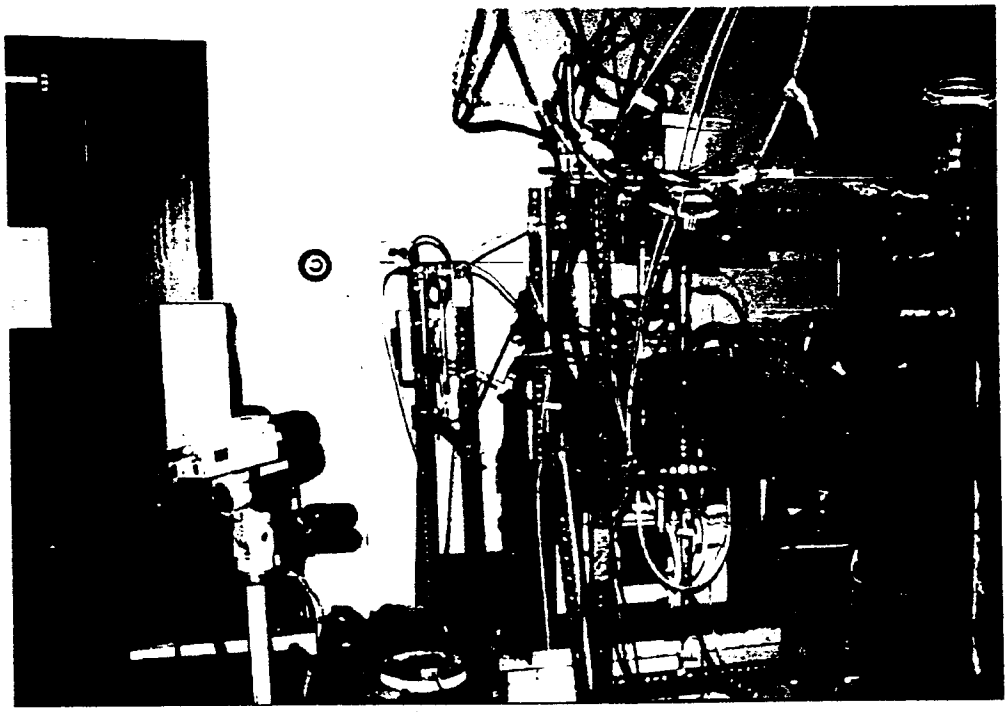

Figure 3.18 The current experimental set up.

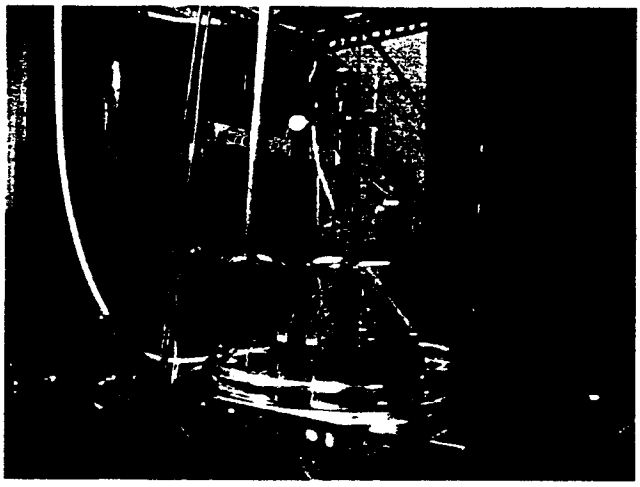

Figure 3.19 The close up look at the glass chamber.

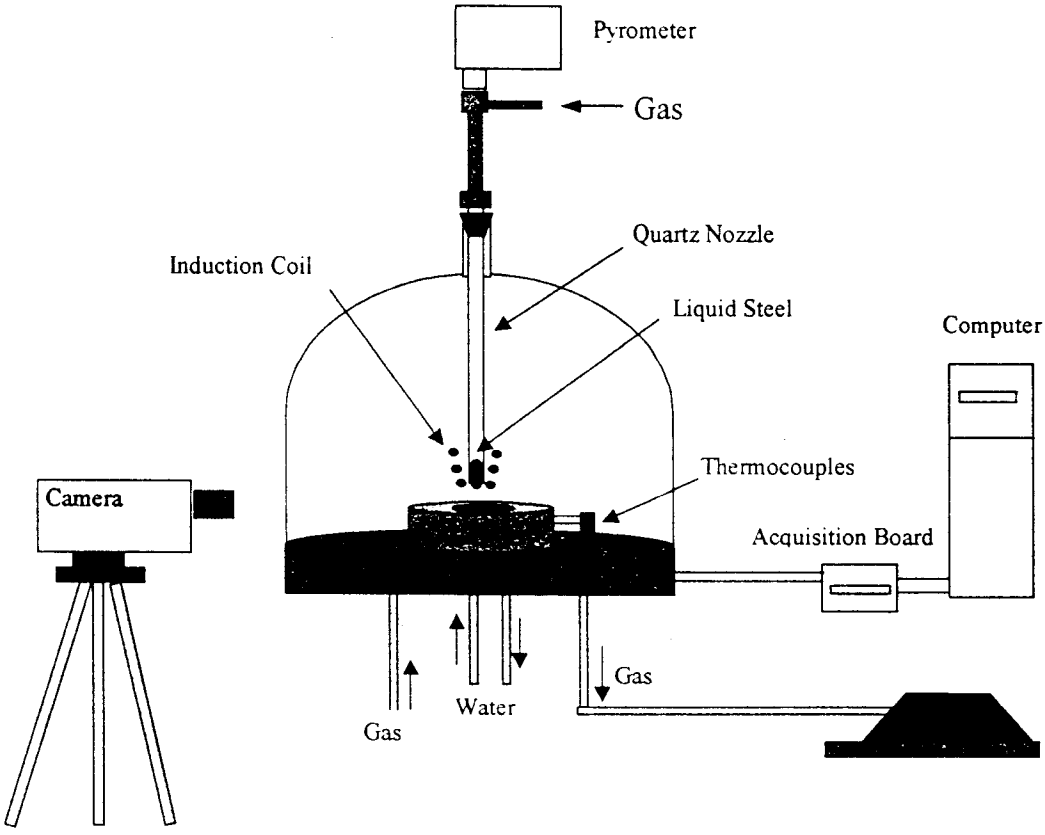

Figure 3.20 The Schematic of the experimental apparatus with a video recording system.

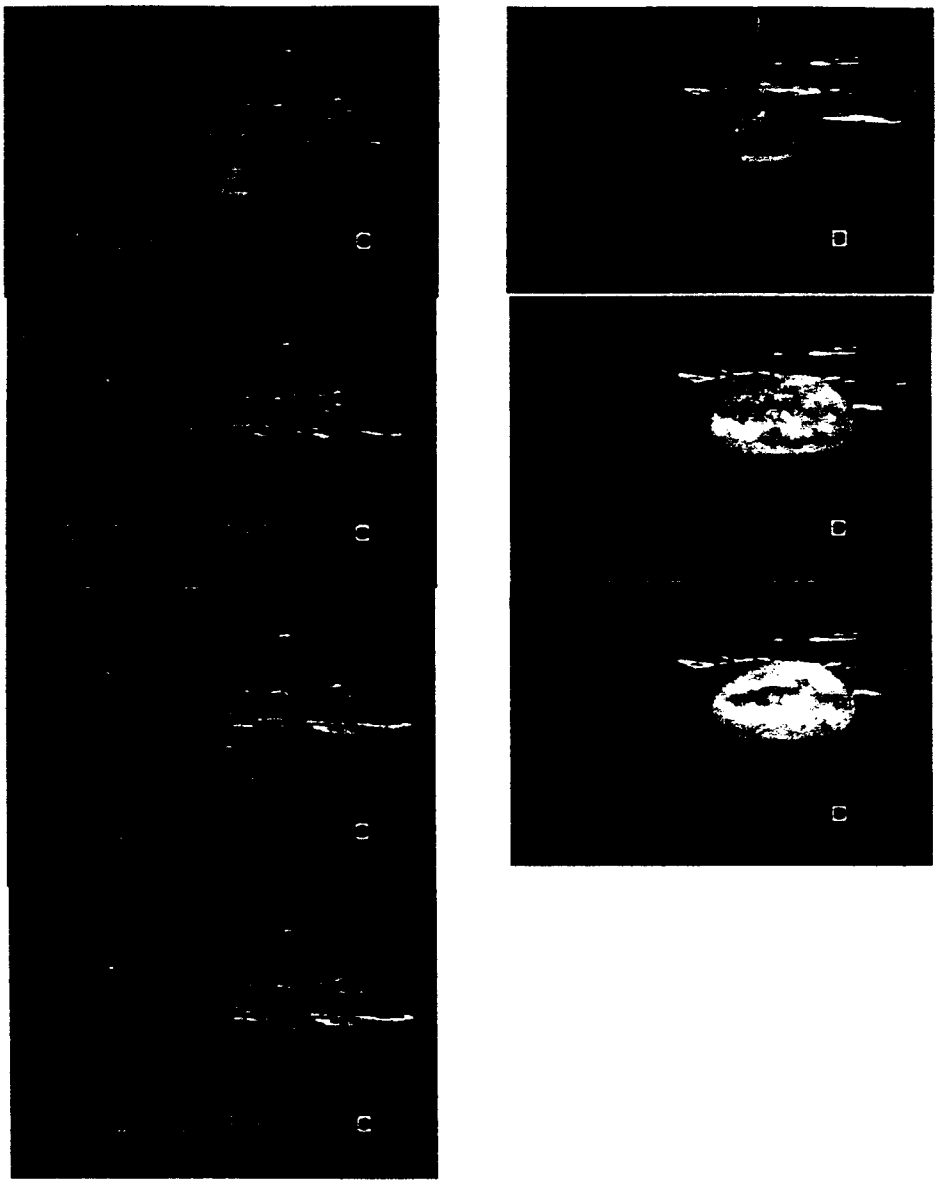

Figure 3.21 The solidification process of the droplet captured by CCD camera.

3.2.3.2 The Experimental Procedure

The specimen was placed inside the inner quartz nozzle that is longer than the one that usually used in the previous set up. However the distance between the coil and substrate remained the same as previous set up. The mold cover and the outer quartz tube were removed in this set up. The atmosphere inside the bell jar was controlled by evacuating and flooding argon gas inside. The substrate cooling water was turned on. The water temperature can be kept constant at any temperature between 15-70°C if both hot water and cold water was turned on and mixed together. The light was turned on and adjusted properly in order to help observing solidification front clearly. After the melt reached a desired temperature the induction furnace was turned off and molten metal was ejected onto the copper mold while the CCD camera was turned on and together videotaped.

3.3 The Reproducibility of the Interfacial Heat Flux Data

In order to check the reproducibility of the interfacial heat flux during the first millisecond of metal-mold contact, each experiment was repeated at least twice. Figure 3.22 shows heat flux curves from two repeated experiments with the same experimental condition. Fluctuations of the heat flux curves can be seen during the first milliseconds of the metal-substrate contact time due to the movement of the liquid steel during the ejection process which takes approximately 300-400 ms, revealed by CCD camera. The results show the fluctuation of heat flux curve gradually decreased at around 100 ms after the ejection process started. Even though fluctuations of the heat flux curves, especially during the first 50-100 ms, can't be avoided the calculated heat flux results, Figure 3.22, still show good agreement between both curves. Heat flux curves for two repeated experiments at two different melt temperature are given in Figure 3.23. The experimental results, again, show a good agreement in the peak heat obtained with some small difference existing between repeats. The peak heat flux values and the total heat remove reported throughout this work were average values of two or more experiments.

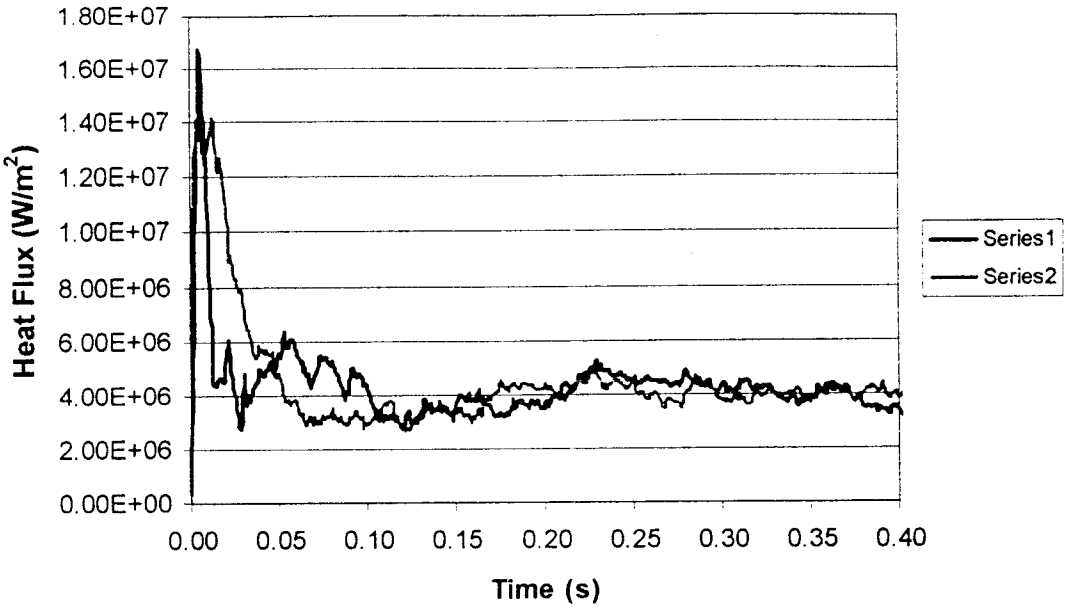

Figure 3.22 Reproducibility of the interfacial heat flux.

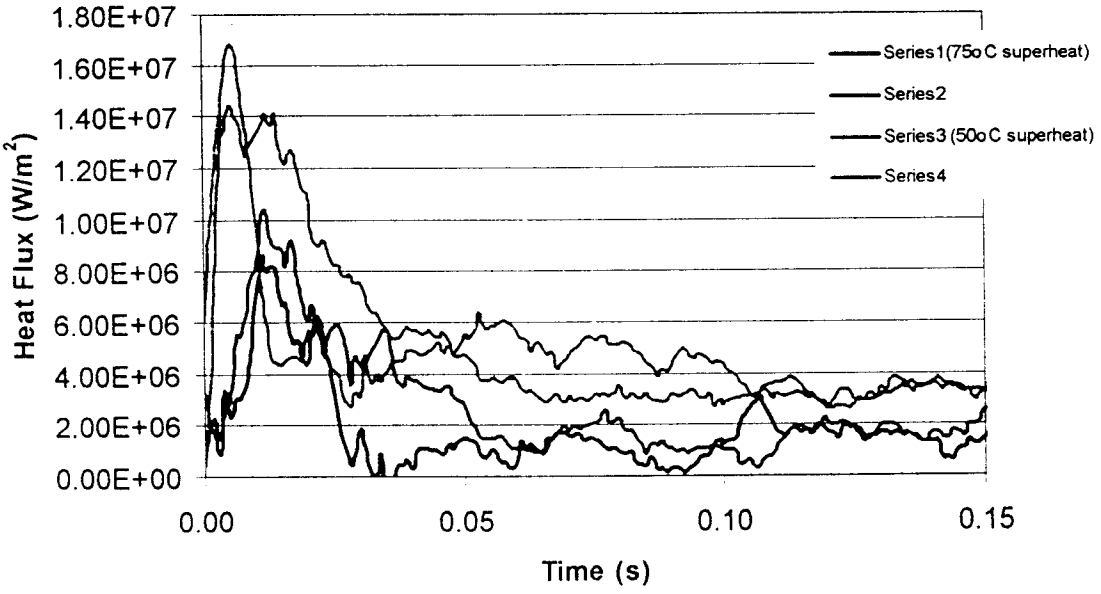

Figure 3.23 Reproducibility of the interfacial heat flux for two repeated experiments at two different melt temperature.

3.4 Specimen Preparation

The Apparatus

The specimen was made under a well-controlled atmosphere in order to prevent the unwanted oxidation reaction. The apparatus, Figure 3.24, consisted of an aluminum crucible with diameter of 40 mm and 58 mm height. The aluminum crucible was placed inside the quartz chamber with 2 1/8" diameter and 14" height. The top and the bottom cap of the quartz tube were cooled by cold water. The atmosphere was controlled by evacuating the air inside the chamber and then back filling with argon gas. Small pieces of aluminum or other materials can be added through the quartz tubes inserted through the middle of the upper cap of the quartz chamber.

The Procedure

Three to four hundred grams of raw materials were placed inside the alumina crucible and melted by an induction furnace. After they were melted the desired amount of aluminum was added and the furnace was shut down. The alloy was left inside the chamber until it's completely cooled down under the argon gas atmosphere. After that the specimen was taken off, cut into small pieces, polished, washed in ultrasound and kept in a vacuum dessiccator.

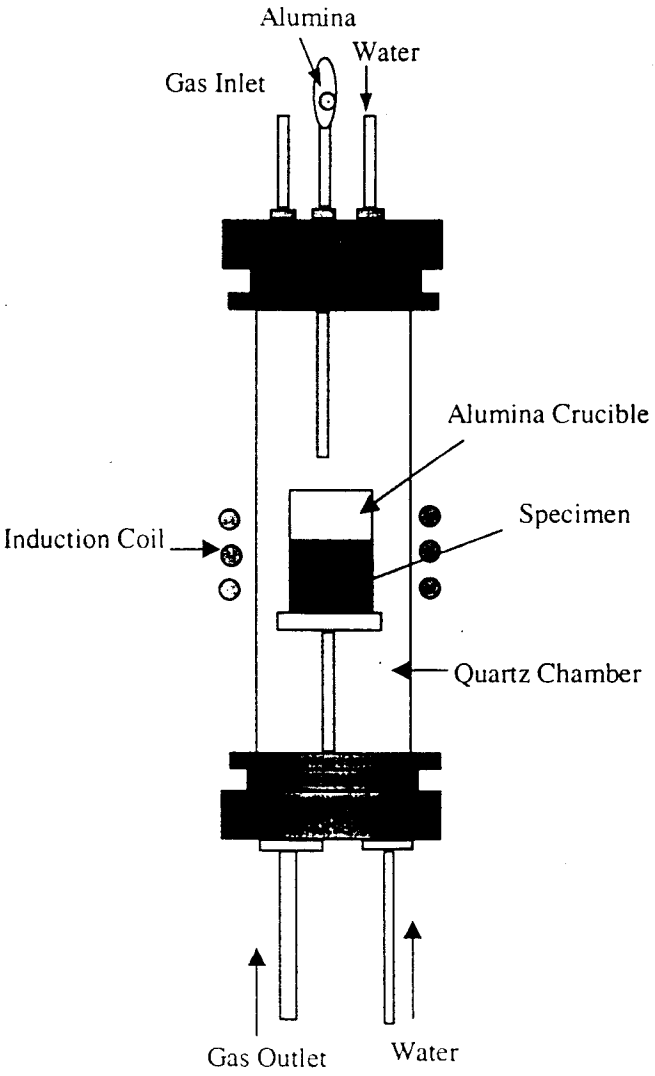

Figure 3.24 The specimen preparation apparatus.

3.5 Surface Roughness and Profile Measurement

A stylus-type surface analyzer (T-500, Thyssen Hommel America Inc), Figure 3.26, was used to measure the surface roughness and profile of a cast. These measurements were conducted by a standard method (4.8 mm traverse length with 0.8 mm cut-off parameter) recommended by the manufacturer of this instrument. In each specimen, 5 readings, Figure 3.25, were taken through the droplet impingement point. The arithmetic mean roughness, Ra, and a maximum profile depth, Pt was used to quantify the surface condition in this study.

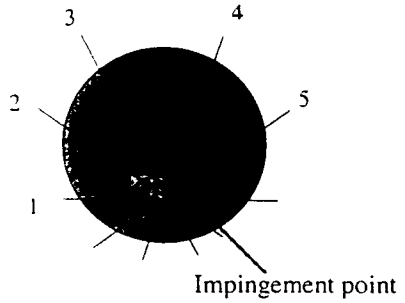

Figure 3.25 The measurement direction.

Figure 3.26 The stylus-type surface analyzer T500.

3.6 Pyrometer Calibration

It is very important to find a standard method to calibrate an optical pyrometer. Figure 3.27 shows a schematic of the experimental set up for calibrating the pyrometer. Figure 3.28 shows a typical melt temperature profile of liquid iron and Figure 3.29. shows those of a Mn-Si killed steel measured by a two-color pyrometer at sampling speed of 10Hz.

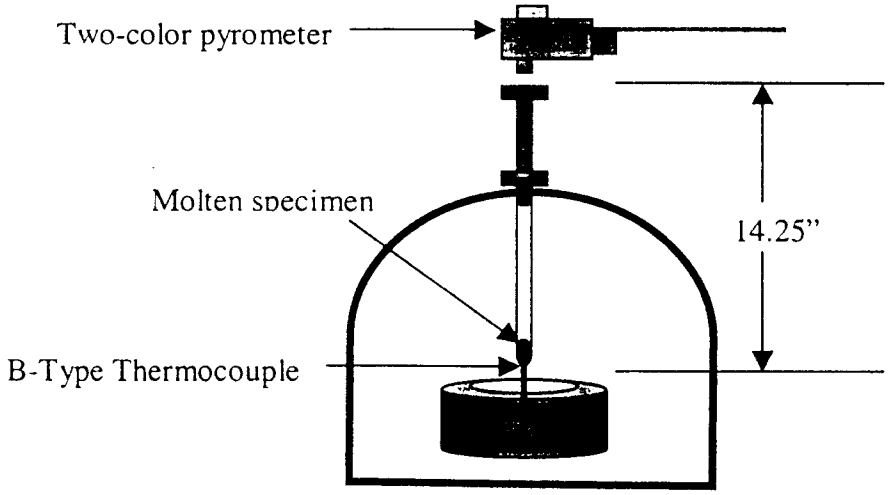

Figure 3.27 The schematic of the experimental set up.

It can be seen that the melting point of Fe, measured by optical pyrometer, is around 1510-1520 °C which is off the true value (1538 °C). For the Mn-Si killed steel the melting point was read around 1520°C however the liquidous temperature for the Mn-Si killed steel is around 1535 °C.[76]

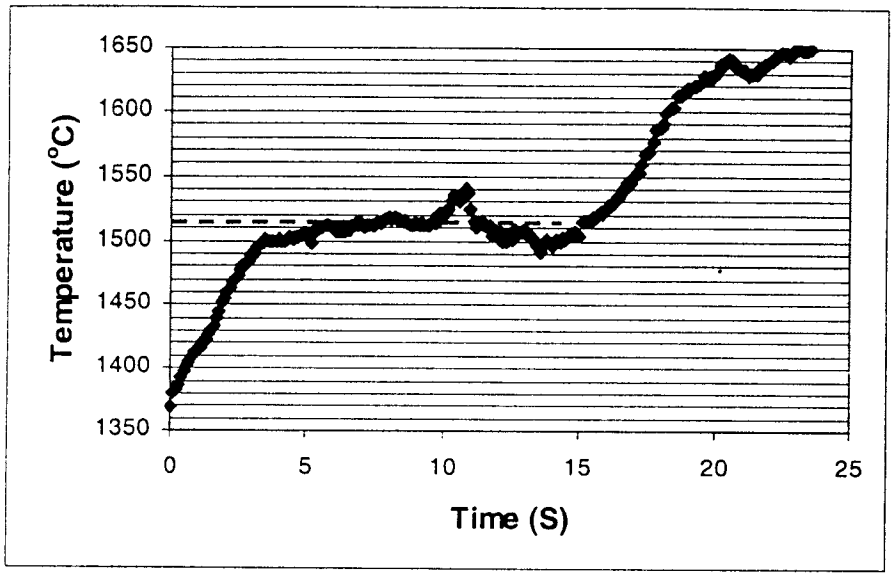

Figure 3.28 The temperature profile of Fe measured by optical pyrometer.

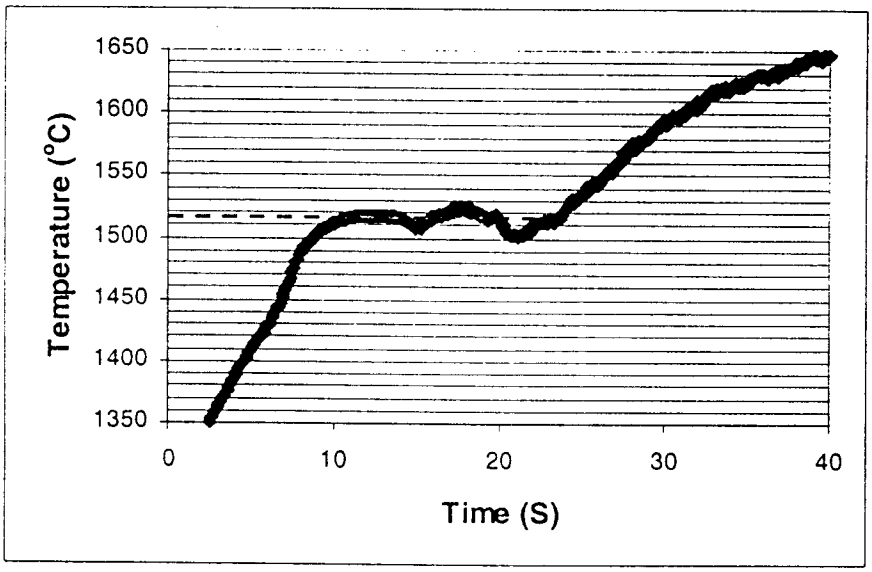

Figure 3.29 The temperature profile of Mn-Si killed steel measured by optical pyrometer.

To calibrate the temperature from the pyrometer, a b-type thermocouple was used to measure the temperature and its result is compared with those from the optical pyrometer, as shown in Figure 3.30 The specimen, Mn-Si killed steel, was melt in quartz nozzle, with a hole at the bottom. The nozzle and the induction coil were place inside the glass chamber. The atmosphere was controlled by flooding the chamber with argon. The b-type thermocouple, diameter 0.010 inch, was inserted through the hole at the bottom of the nozzle. The thermocouple tip was coated by high temperature cement. The optical pyrometer was placed 14.25 inches directly above the specimen. The thermocouple and pyrometer was connected to the data acquisition system and data from both pyrometer and b-type thermocouples were simultaneously recorded at the same sampling speed 10 Hz.

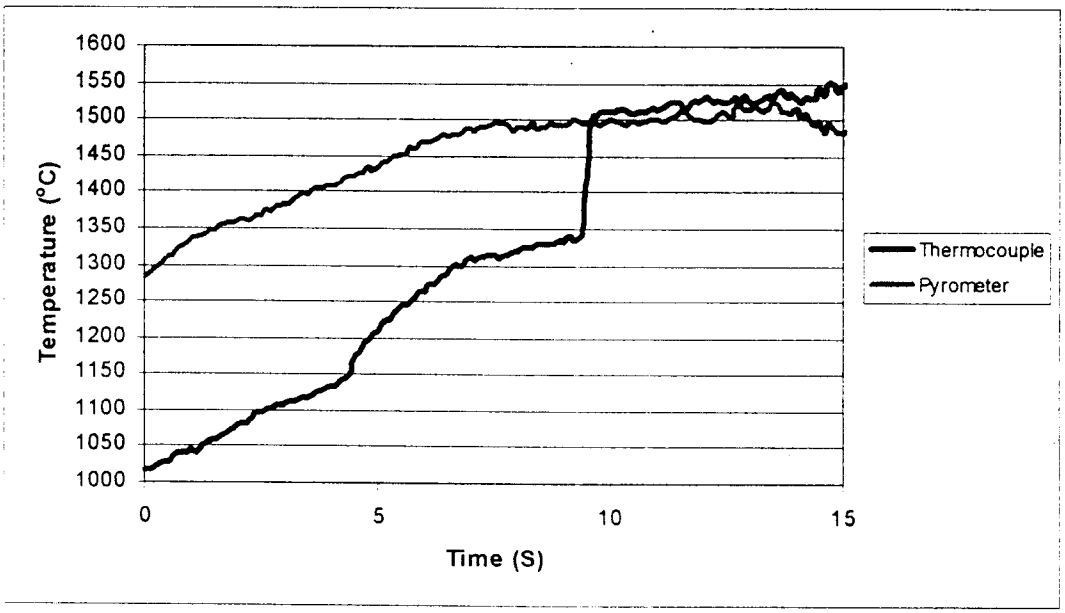

Figure 3.30 The comparison between temperature profile measured by b-type thermocouple and pyrometer.

It can be seen from Figure 3.30 that, at lower temperatures, the value of the temperature measured by pyrometer is a lot higher than the one measured by B-type thermocouple. However when the specimen reached its melting point the gap between both results was closer. Below the specimen's melting point, the contact between the thermocouple and the specimen is fairly poor, however, when the specimen melts and becomes a liquid the contact between the thermocouple and the specimen is dramatically improved. The thermocouple can read the true value of the temperature inside the nozzle when it was completely covered by molten specimen. At the melting temperature, Figure 3.31, the difference between the value of the temperature reading from thermocouple and pyrometer is approximately 15-20°C

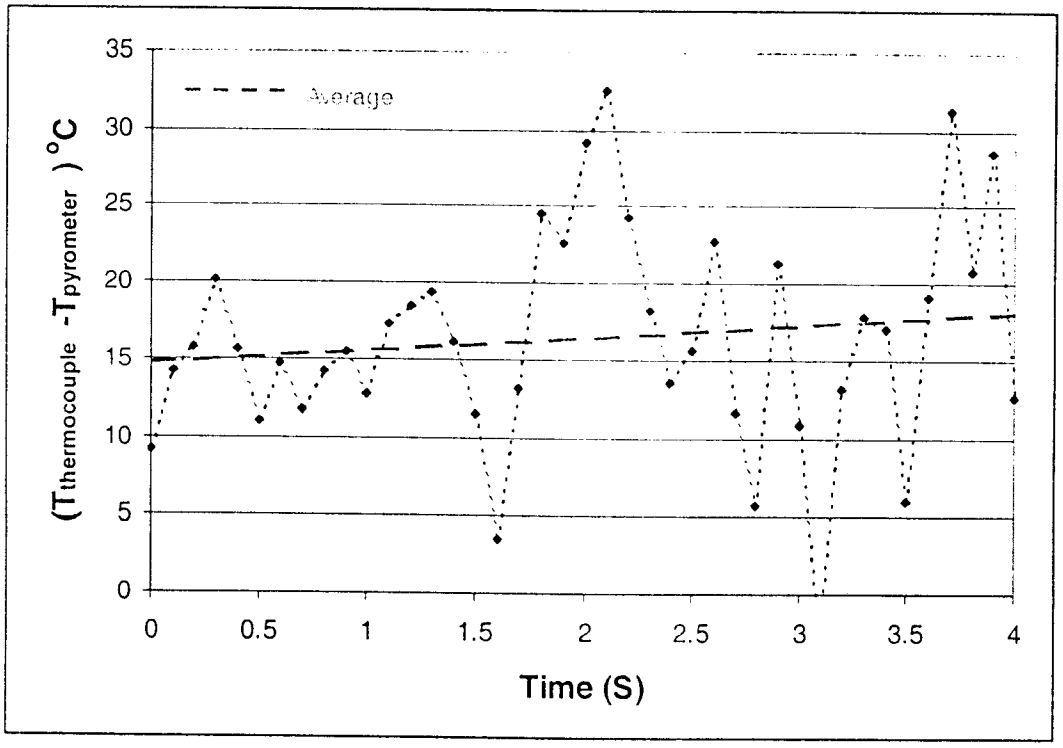

Figure 3.31 The difference between the temperature measured by b-type thermocouple and pyrometer at the melting point.

If we correct the previous results the temperature are reasonable as close to the true value of its liquid temperature.

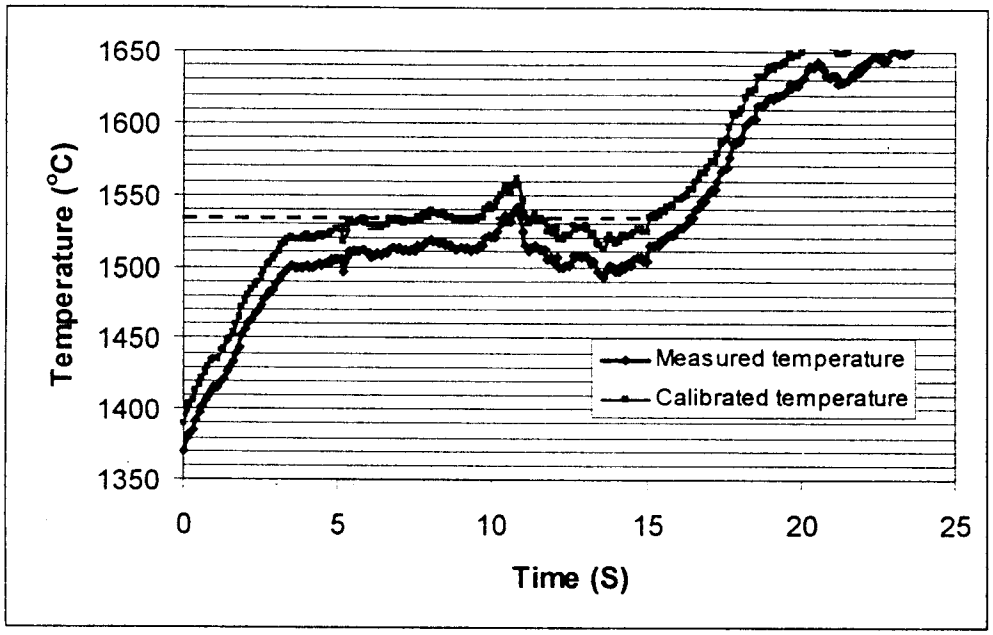

Figure 3.32 The example of the temperature profile after calibrating by using the result of the temperature difference, measured from, between a b-type thermocouple and optical pyrometer.

Chapter 4

In-situ Observation and Measurement of Interfacial Heat Transfer between the melt and substrate

4.1 Investigation of Interfacial Heat Transfer Phenomena by Using Video Camera

In order to conduct the measurement of the interfacial heat transfer properly, it is critical to control the rate of fall at the impact area of the droplet. The process had to be monitored continuously in real time to ensure that the droplet impact occurred as expected. A video recording system was thus designed to record the process as it happened. Figure 3.20 shows the experimental set up of this experiment. The experiment was recorded by a video recording system using a CCD camera with a Minolta 50 mm. f3.5 lens. The atmosphere was controlled by evacuation of the system and back-filling the chamber with ultra high purity argon gas.

The video camera allowed documentation of the phenomena that happened as the molten metal contacted the copper mold, as shown in Figure 4.1. The mold temperature profile developed from the thermocouples indicated that there were temperature profile fluctuations that might happen because of the movement of the molten metal droplet that was deposited onto the mold. Therefore the new experimental set up was established in order to see what was really happening when the molten droplet contacted the copper mold.

Results

The phenomena that occurred from the first contact of the molten metal onto the copper mold until it was fully solidified was videotaped. Furthermore, the movement of the solidification front can be observed and the solidification time can be estimated. This advantage allowed coupling between the interfacial heat transfer and droplet solidification rate.

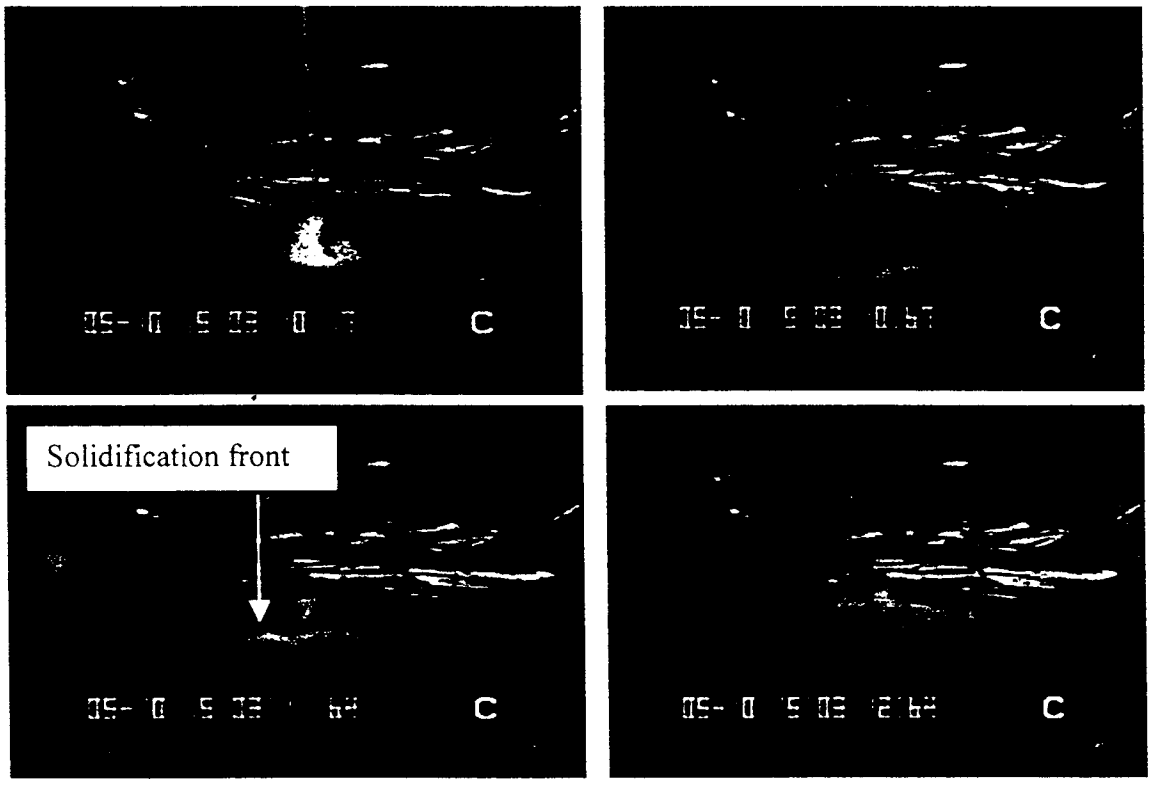

Figure 4.1 The solidifying iron droplet captured from CCD camera during the experiment.

The new set up allowed us to select only proper results and revealed interesting phenomena that occurred during ejection and solidification. Figure 4.2 shows the example of a failed experiment that was unable to be identified during the experiment prior to the time that the video camera was applied to this work.

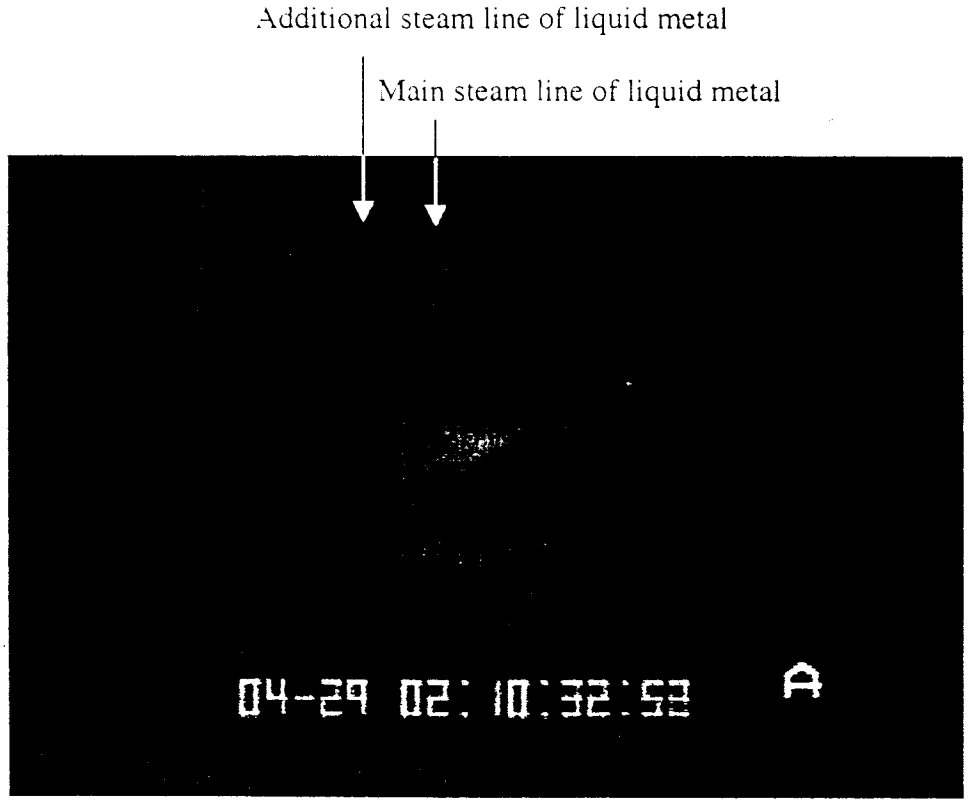

Figure 4.2 The example of the failed experiment that can't be detected without using CCD camera. There are two stream lines of molten metal came of from the nozzle.

Figure 4.3 shows another problematic experimental issue. Instead of having a continuous line of liquid metal hitting the mold surface, the molten metal formed as a line of small droplets.

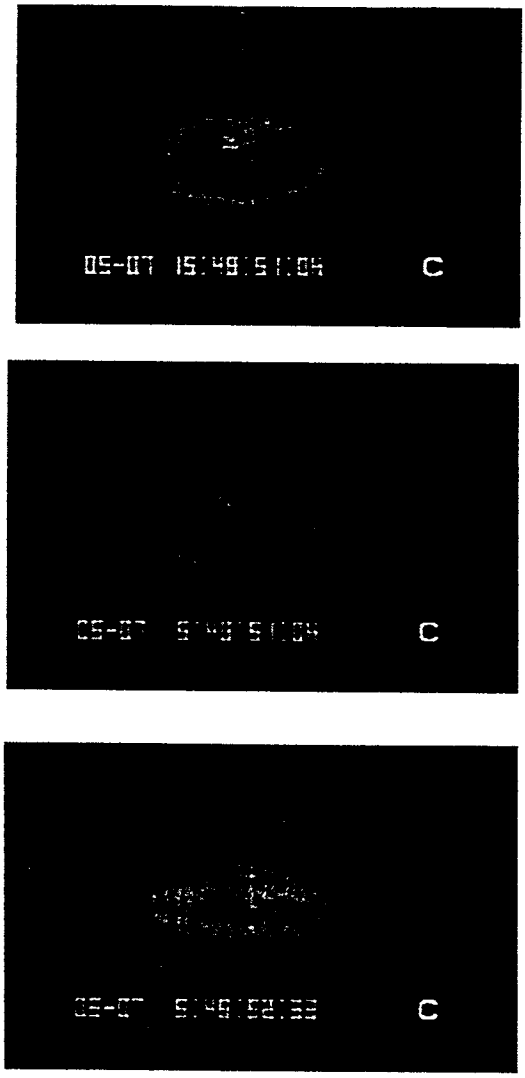

Figure 4.3 Another example of the failed experiment. The molten metal came of from the nozzle by gravity force.

4.2 Coupling Thermal Data to Visual Data

The new experimental apparatus was equipped with a video recording system that was designed to record the experiments and to document the onset of solidification. The solidification front position and growth rate was studied with this technique along with the interfacial heat transfer behavior of the droplet. This novel approach of simultaneous in-situ observation and measurement of rapid heat transfer enables a coupling between the interfacial the heat transfer and droplet solidification.

4.2.1 Visual Data

Figure 4.4 shows a picture of the solidification of a 99.97% iron droplet with 65°C superheat. The droplet weighed 1.9 grams. It took 450 ms to eject the molten metal to the copper mold, Figure 4.4(a) to 4.4(f). During that time the droplet changed its shape, moved and spread on the mold. The solidification front started to be seen clearly at the bottom of the droplet in Figure 4.4(g) and sporadically on the top of the droplet due to the impingement of the argon gas stream used to push the liquid metal from the nozzle; however, this initial solidification on top of the droplet remelts and does not persist. The solidification front moves from the bottom to the top of the droplet, as shown in Figure 4.4(g) to 4.4(m). and this step takes approximately 1.74 seconds.

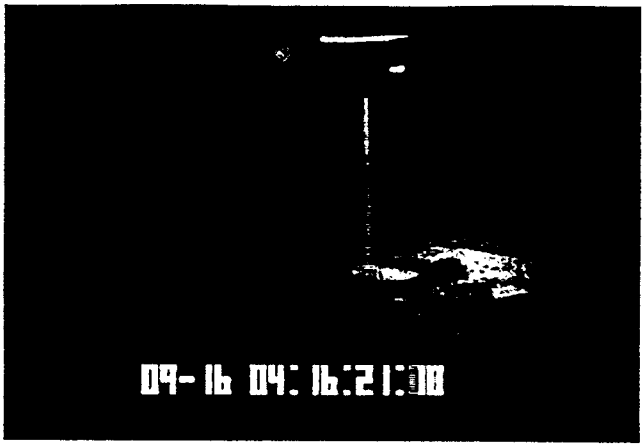

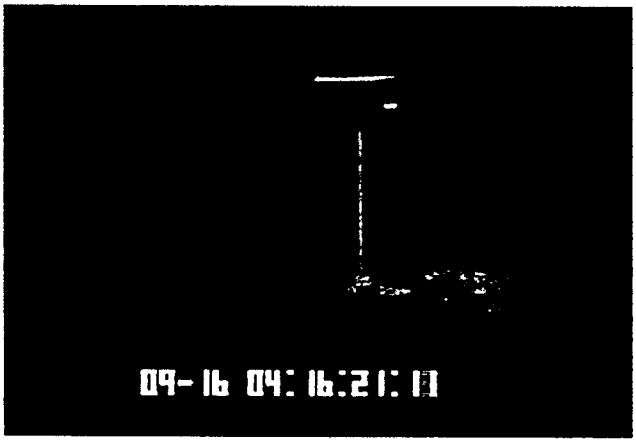

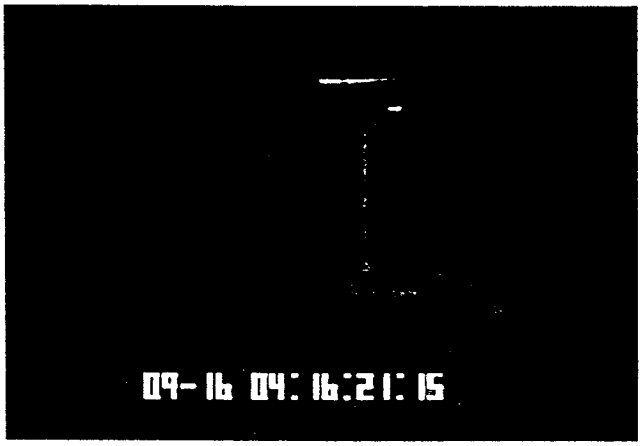

Figure 4.4 (a) – (c)

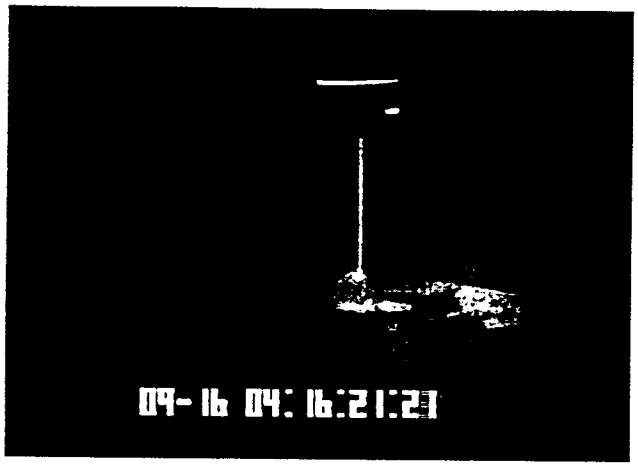

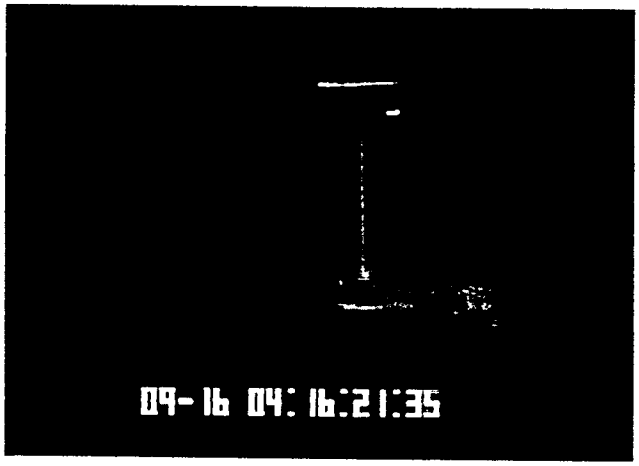

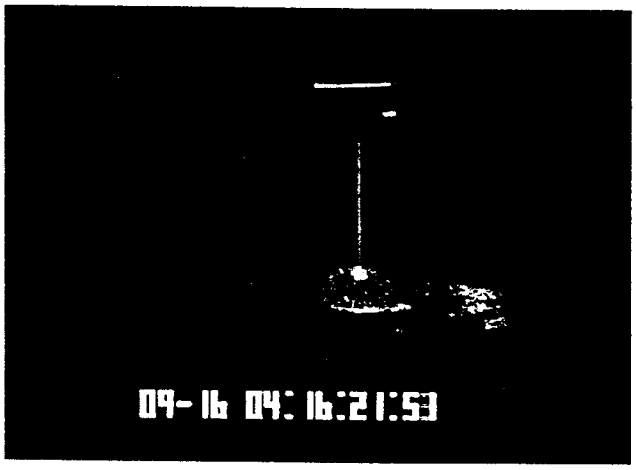

Figure 4.4 (d) – (f)

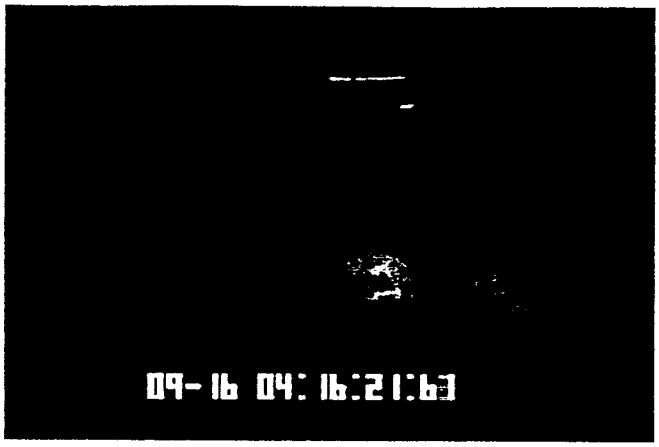

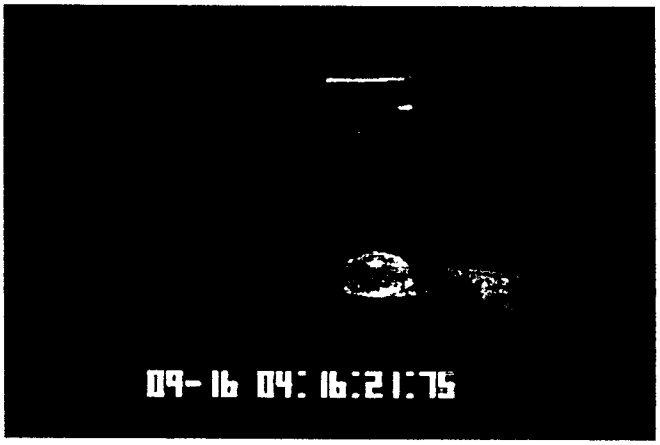

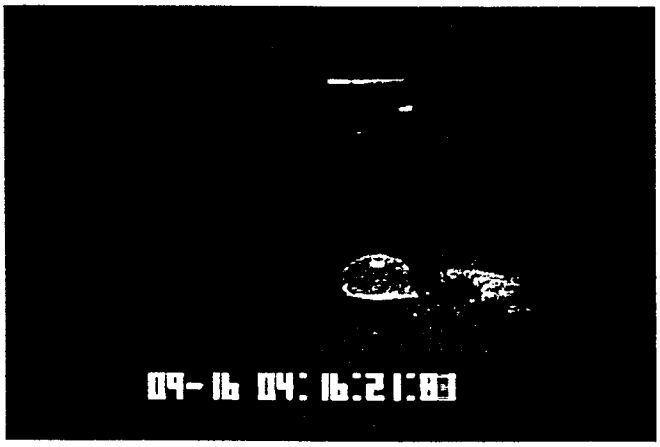

Figure 4.4 (g) – (i)

Figure 4.4 (j) – (l)

Figure 4.4 (m)

Figure 4.4 (a)-(m) The solidification process of the molten droplet on the copper substrate captured by CCD camera.

4.2.1.1 Documentation of Droplet Spreading Behavior

The spreading behavior of droplet was documented, as shown in Figure 4.6, from the video recording of the droplets. Figure 4.5 shows a schematic of the droplet spreading behavior during the ejection process. The liquid metal first hit and spread on the copper substrate during the first 10 ms. Between the first 10–50 ms the droplet shape was formed. After 50 ms the droplet size significant increased and resulted in the spread of the metal/mold contact area. After 200 ms, the droplet size increased but the droplet/substrate contact area was constant.

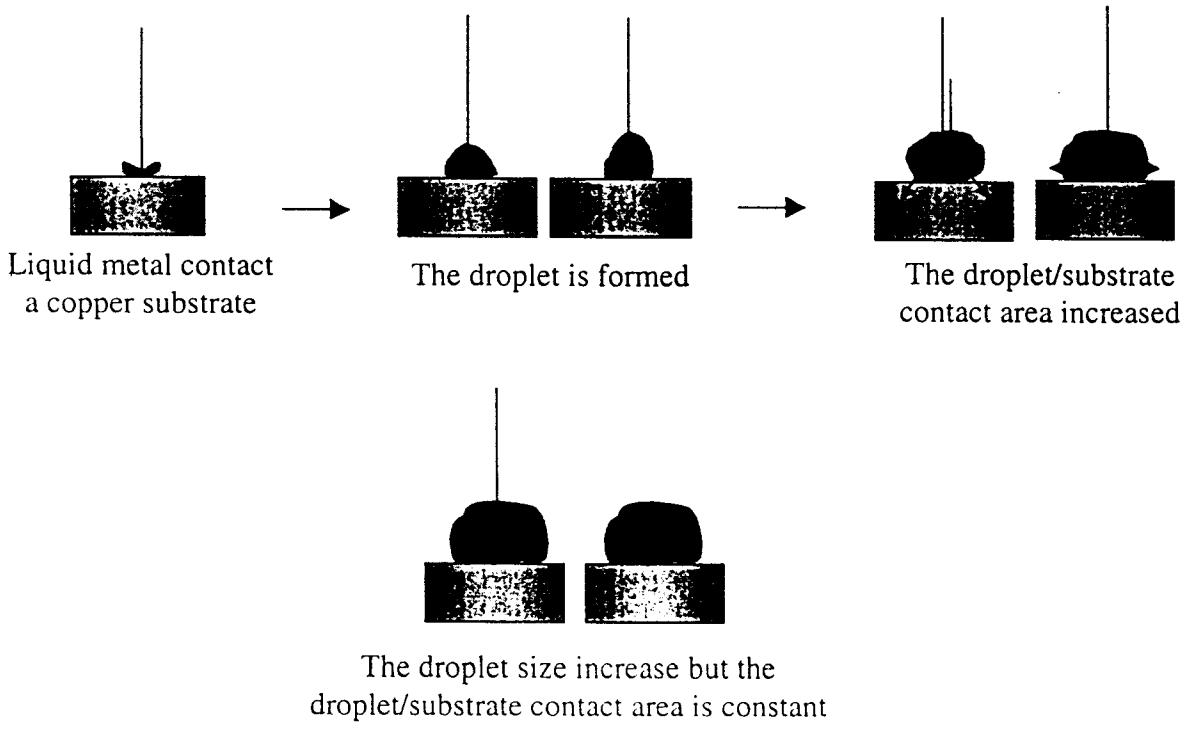

Figure 4.5 The schematic of the droplet spreading behavior.

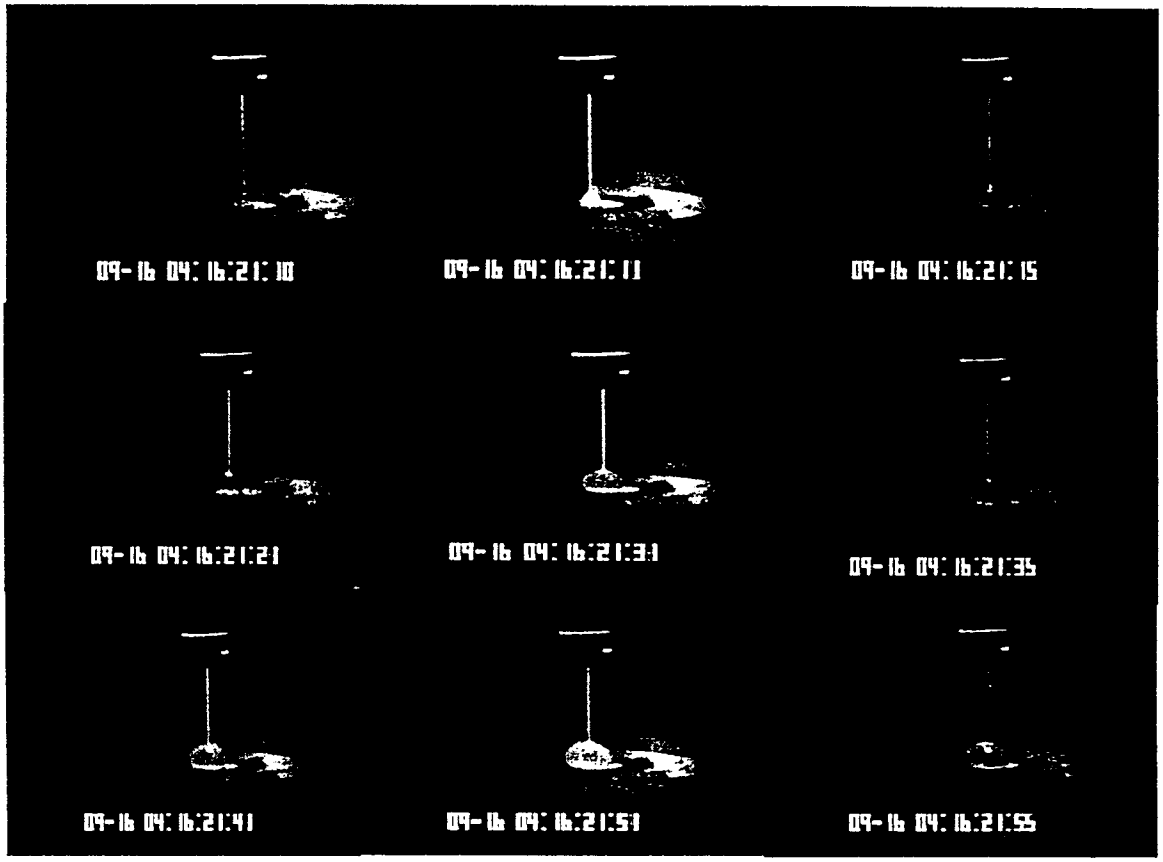

Figure 4.6 The droplet pictures captured by CCD camera during the ejection process.

4.2.1.2 Estimated Solidification Rate

The solidification rate was estimated from the varying position of the solidification front as captured by CCD camera. Figure 4.8 shows the pictures of the moving solidification front. The initial solidification started when the liquid steel hit the copper substrate however the droplet solidification process could only be documented when the solidification front could be seen clearly and started to move. The solidification shell moved upward after the ejection process was completed. During the ejection process, the liquid steel was continuously hitting the droplet and remelting the solidified shell. This result prevented the growth of the solidification front, as shown in Figure 4.7 and Figure 4.9. In the case where 99.97% Fe droplets, with 55°C and 65°C superheat, were ejected onto the copper substrate at 32°C ± 2°C the relationship between the growth of the solidification front and solidification time started after the ejection process was completed, when the remelting process stopped, as shown in Figure 4.8 and Figure 4.10.

Figure 4.11 and Figure 4.12 show the relationship between the thickness of shell and time measured from solidified droplet pictures captured by CCD camera. The total solidification time measured from the experimental data agrees well with the theoretical empirical equation, [78] Figure 4.13.

$$Xs = 2.33\ t^{0.575} \qquad \textbf{5.1}$$

Where Xs in mm and t is in seconds. The equation can be used to represent the data over the wide range from Xs = 0.2 mm to 5 mm. However the details of the growth rate are quite different.

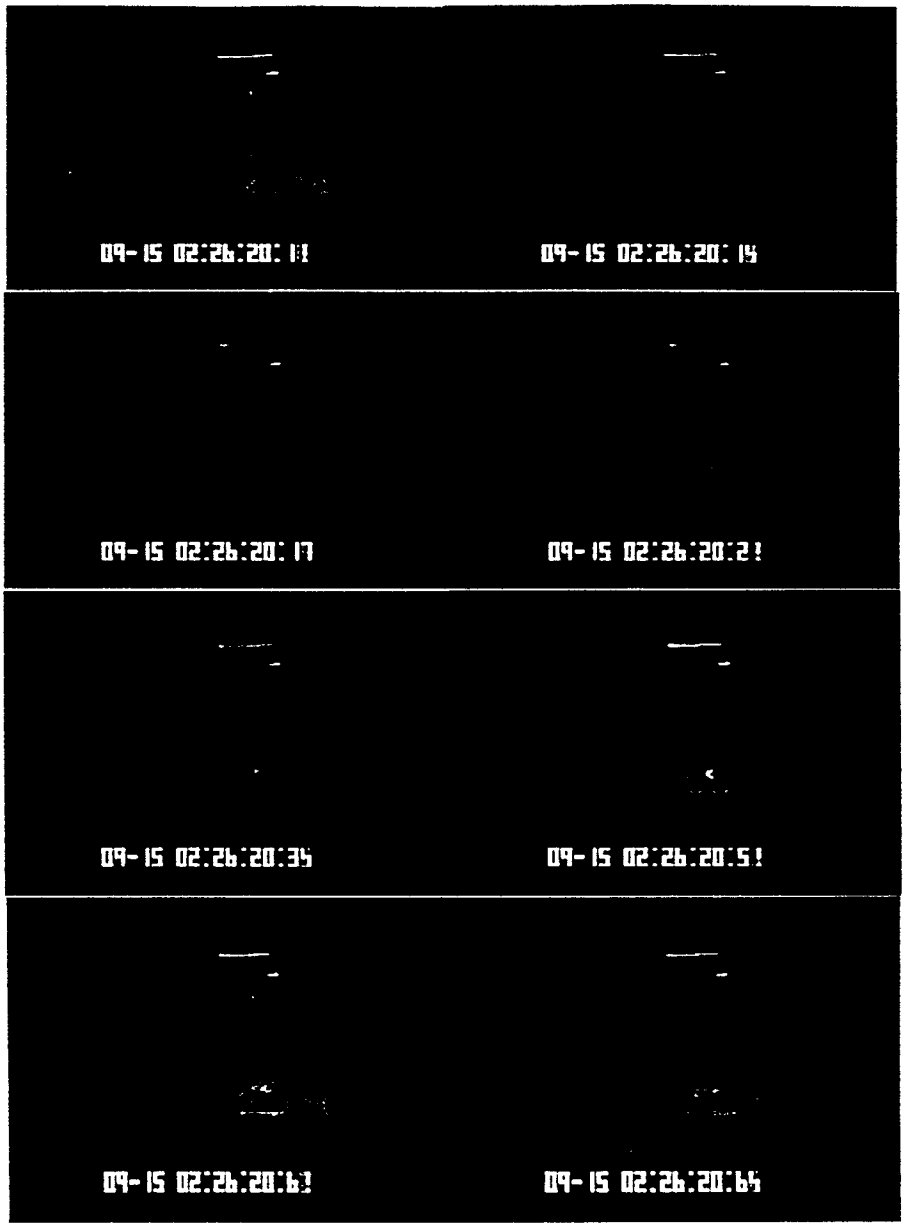

Figure 4.7 The droplet during the ejection process. The growth of the solidification front could not be seen when the liquid steel was continuously hitting the droplet. (melt superheat = 55°C).

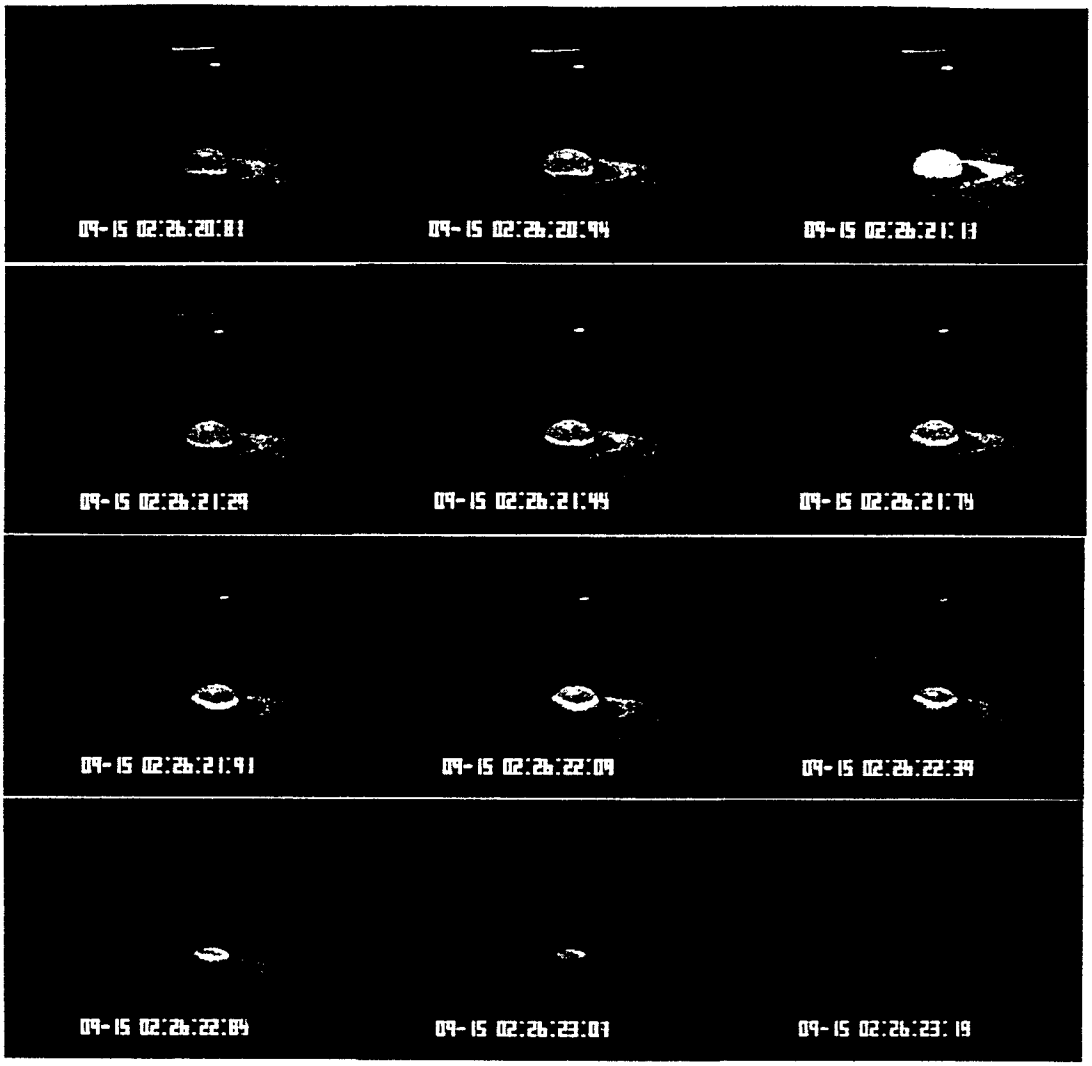

Figure 4.8 The growth of the solidification front. (melt superheat = 55°C) The total solidification time = 2.45 sec.

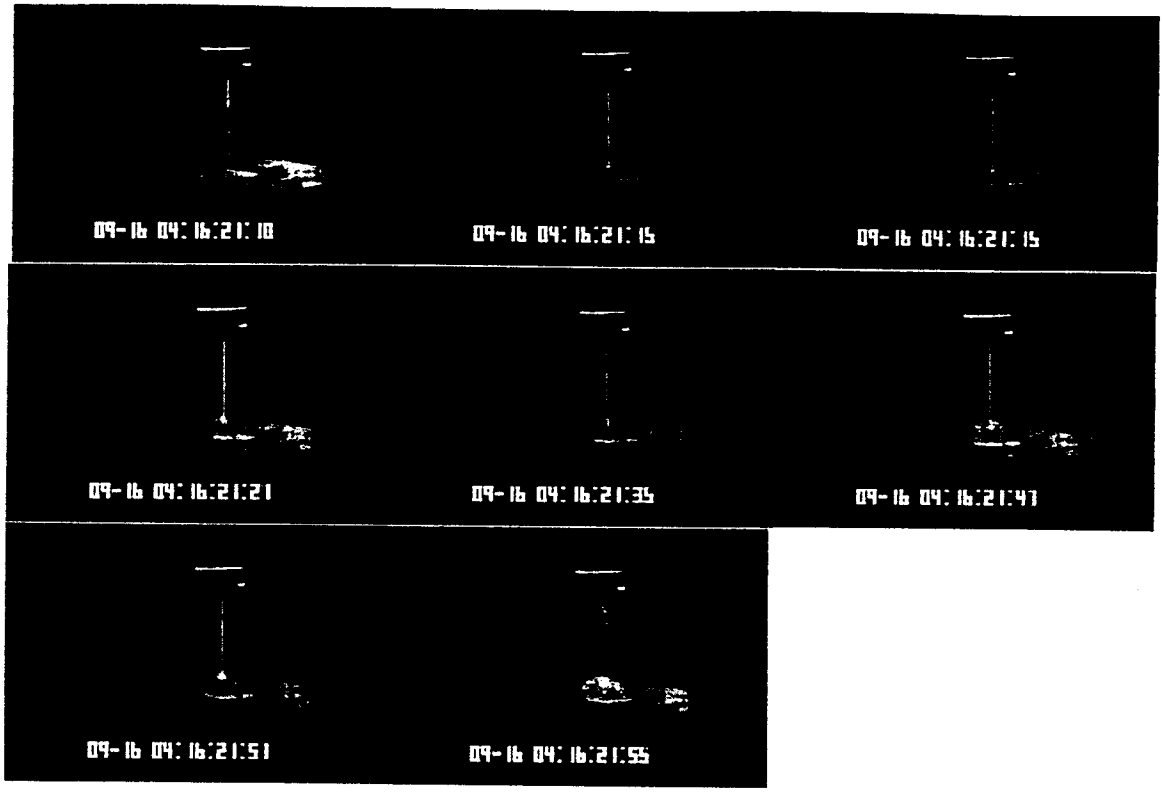

Figure 4.9 Another example of the droplet during the ejection process. The growth of the solidification front could not be seen when the liquid steel was continuously hitting the droplet. (melt superheat = 65°C).

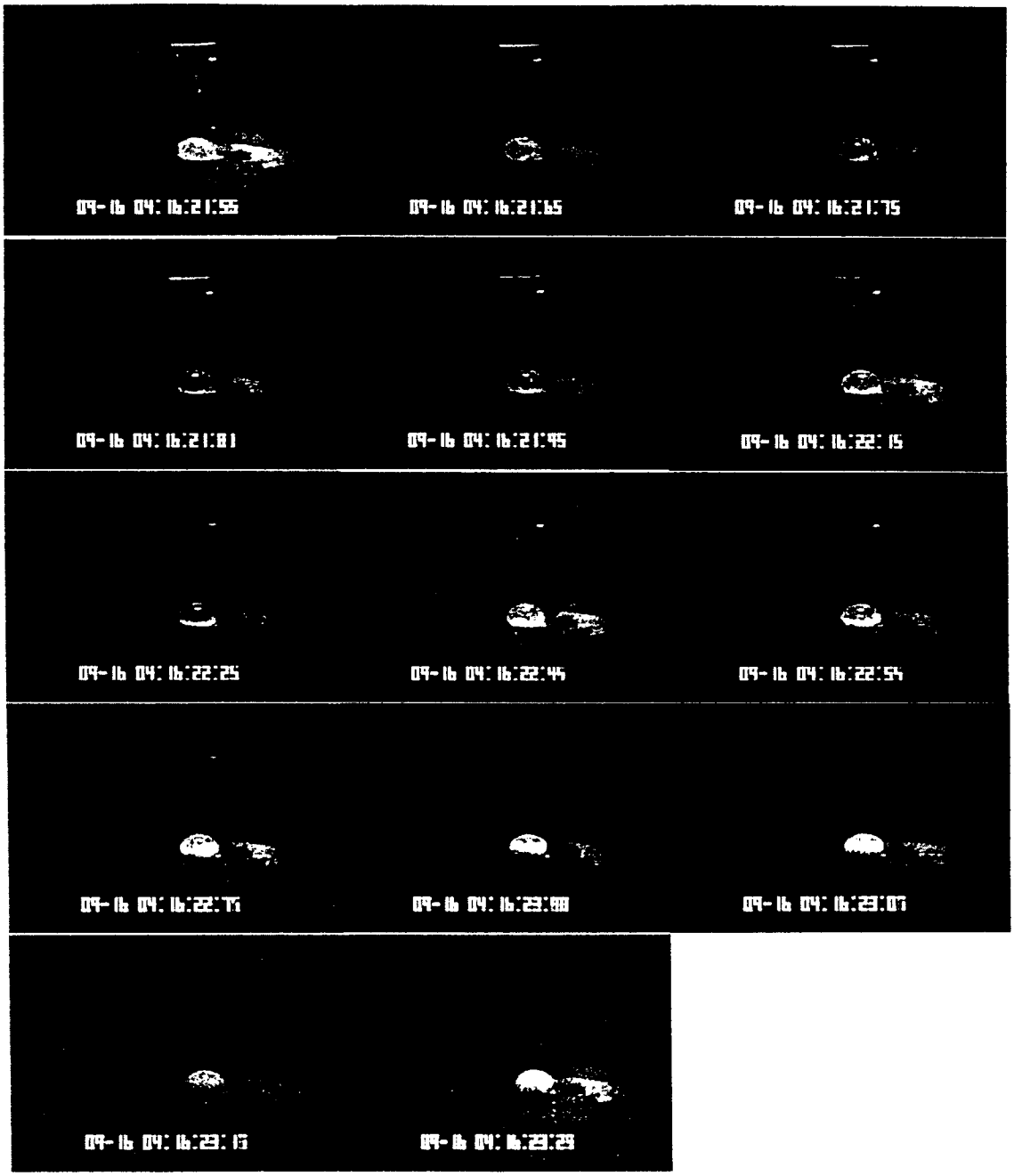

Figure 4.10 Another example of the growth of the growth of the solidification front. (melt superheat = 65°C) The total solidification time = 1.74 second.

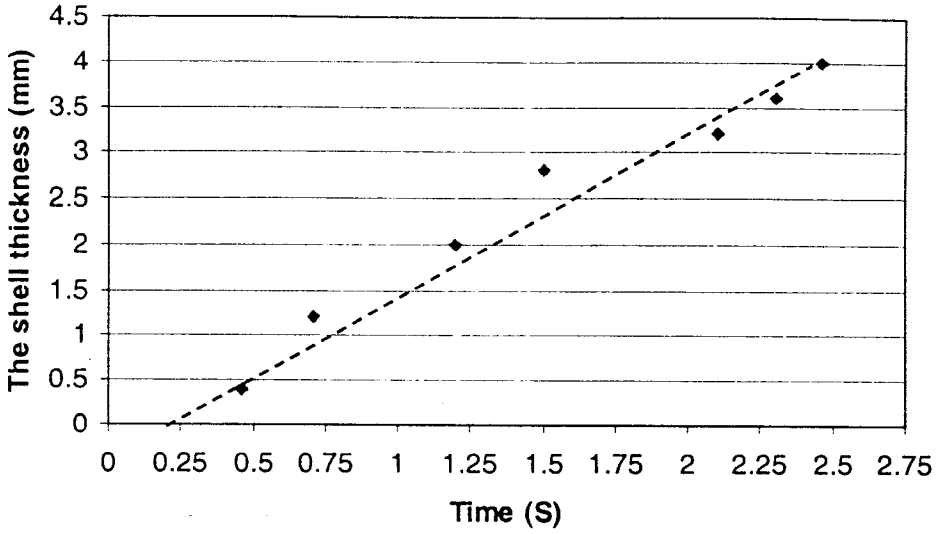

Figure 4.11 The shell growth rate of the droplet thick 4 mm (superheat = 55°C).

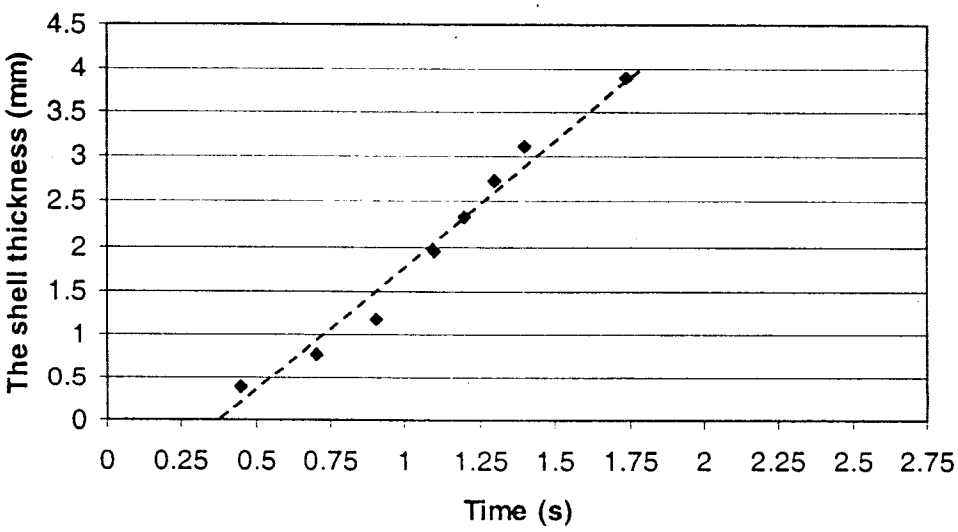

Figure 4.12 The shell growth rate of the droplet thick 3.9 mm (superheat = 65°C).

Time (s)	X (mm)	Time (s)	X (mm)
0.46	0.4	0.45	0.39
0.71	1.2	0.7	0.78
1.2	2	0.9	1.17
1.5	2.8	1.1	1.95
2.1	3.2	1.2	2.34
2.3	3.6	1.3	2.73
2.46	4	1.4	3.12
		1.74	3.9

● Actual Data 55°C superheat, 4.0 mm thick droplet
Documented from video recording of the droplet, Figure 4.8.

● Actual Data 65°C superheat, 3.9mm thick droplet
Documented from video recording of the droplet, Figure 4.10.

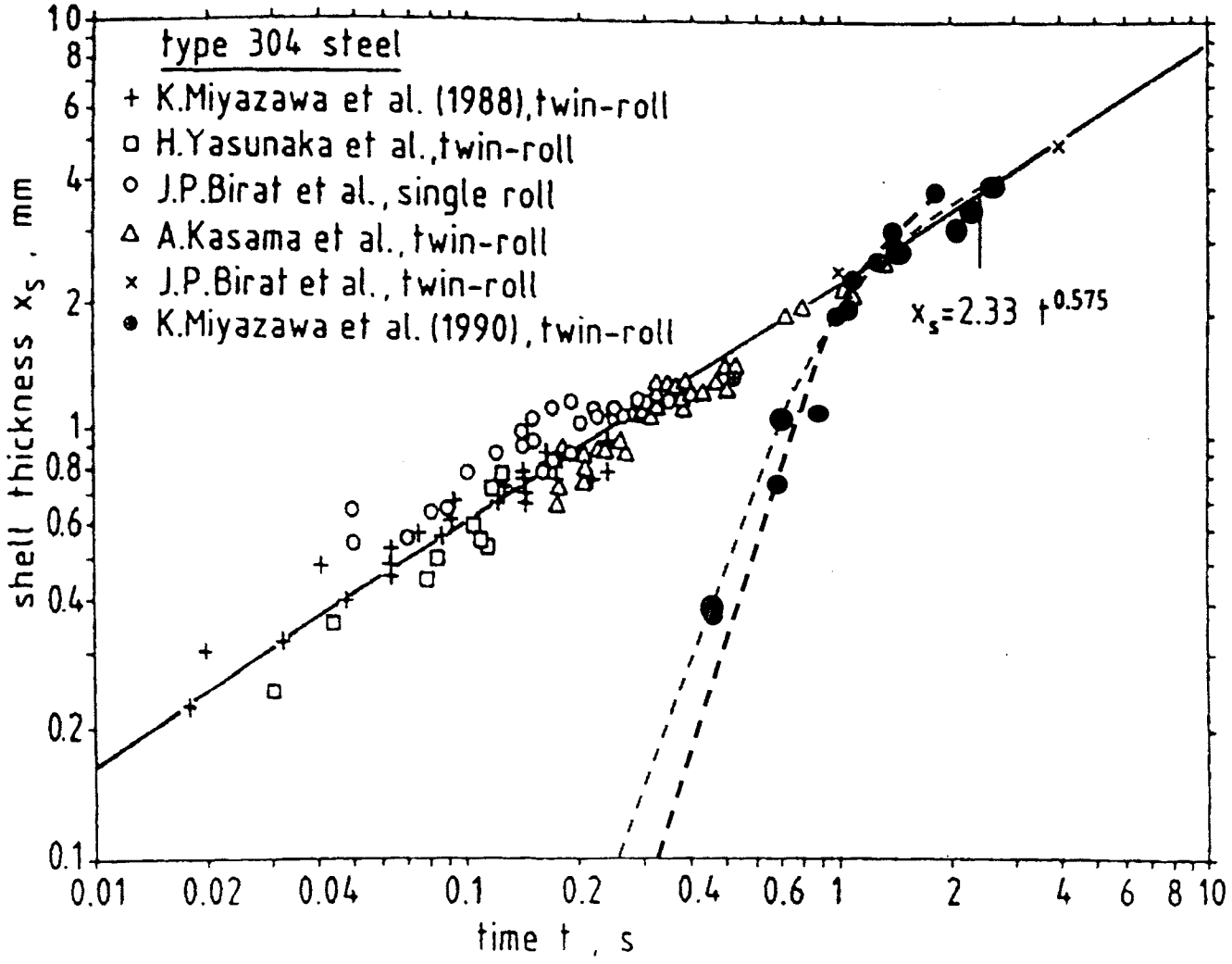

Figure 4.13 Data on shell growth.[78)]

It is interesting to find that the droplet did not start to solidify immediately after the liquid steel hit the copper mold. The shell started to grow only when ejection process stopped. This could happen because the initial solidification, precipitated on the mold surface, was washed away by the liquid steel that was continuing to hit the droplet. If we extrapolated the curve in order to find the time when the solidification front started to form it was found that the time was approximately 0.2 - 0.3 seconds. Therefore the first 200-250 ms of contact time could be the time that the liquid droplet was undercooling.

A previous work done by Todoroki et al.,[13] who ejected the droplet onto the copper substrate and measured the surface temperature of the cast droplet by using the light sensor. The cast surface temperature that he measured showed a long period of undercooling which could not be explained. If we look at some of his results, as shown in Figure 4.14 to 4.15 it is interesting to find that his iron and IF steel droplets with superheat varying from 43°C–70°C undercooled for approximately 200-250 ms.

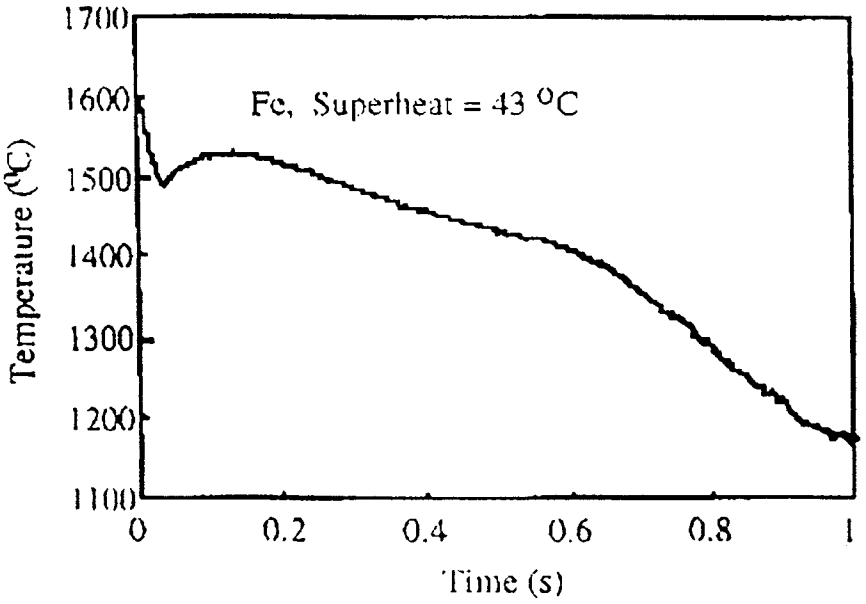

Figure 4.14 Surface temperature profile of the cast iron.[13]

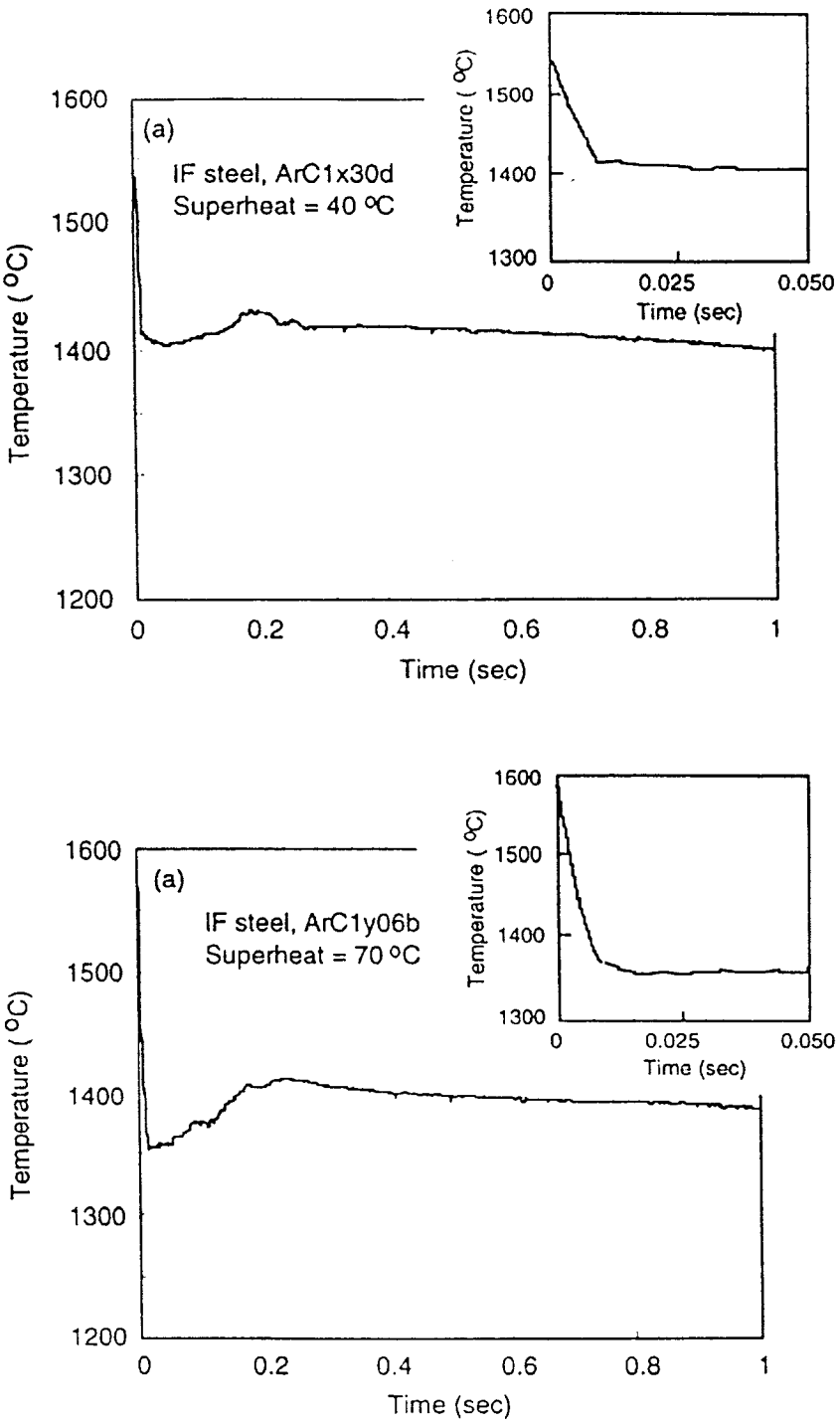

Figure 4.15 Surface temperature profiles of the cast IF steel.[80)]

His results agree reasonably well with the results that we have seen in the videotape. By comparing both results it's clear that the superheat was the most influential casting parameter in our system controlling the initial solidification process of the droplet since the amount of superheat determines how long the liquid droplet can sit and spread on the substrate mold before it develops a solidification shell that acts as resistance to heat transfer at the droplet/substrate interface.

If we look at Figure 4.13 we can see that the total solidification time and the solidification curves of the droplet, especially when the droplet is nearly complete solidified, are close to that of 304 stainless steel but not exactly the same. This is reasonable as the different alloys should wet the mold differently and lead to differing heat transfer balances.

As heat is continuously removed, the droplet must significantly undercool. Thus the solidification front when it initiates will grow by heat dissipation into the undercooled liquid and into mold. This difference in heat flux is shown schematically in Figure 4.16. Therefore the slope of the shell growth curve should be steeper since the heat can be dissipated in both directions as can be seen in Figure 4.17. After the undercooling process was completed the droplet dissipated heat only to the copper substrate resulted in the less steeper gradient.

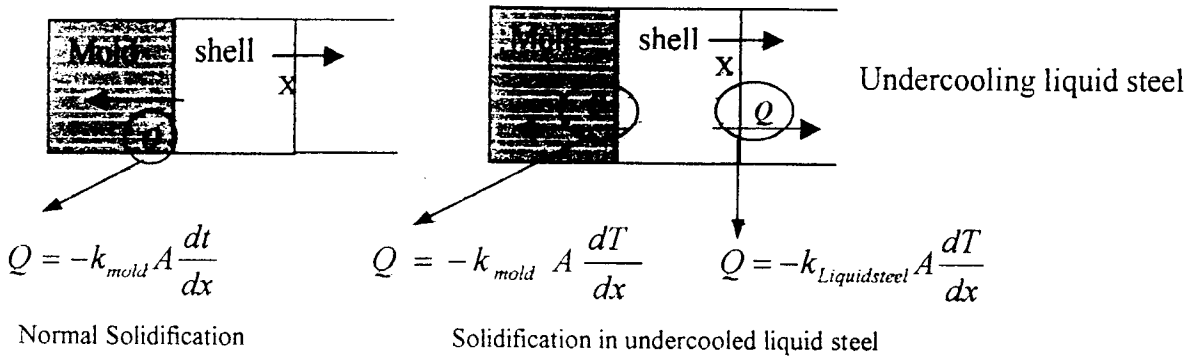

Figure 4.16 Schematic of heat flux in normal solidification and during solidification in undercooled liquid steel.

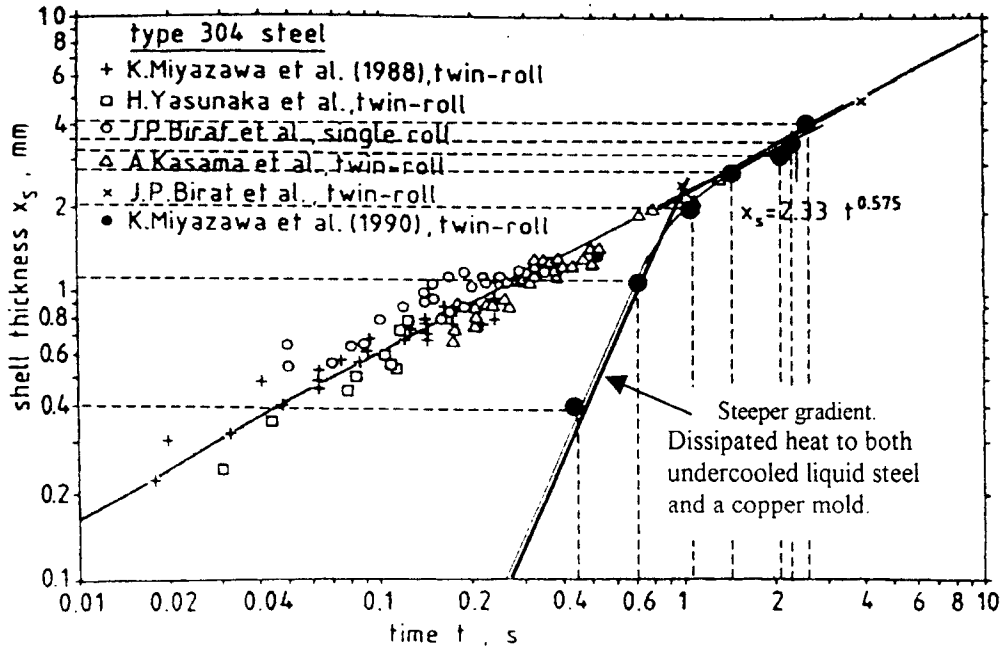

Figure 4.17 The growth rate of shell.

4.2.2 Thermal Data

Copper mold temperature profile

Figures 4.18 and 4.19 show the mold temperature profiles of molten iron droplet that was ejected onto the mold surface with 65°C superheat. The mold temperature profiles were measured from the thermocouples installed at position 0.5 and 3.5 mm from the surface of the substrate.

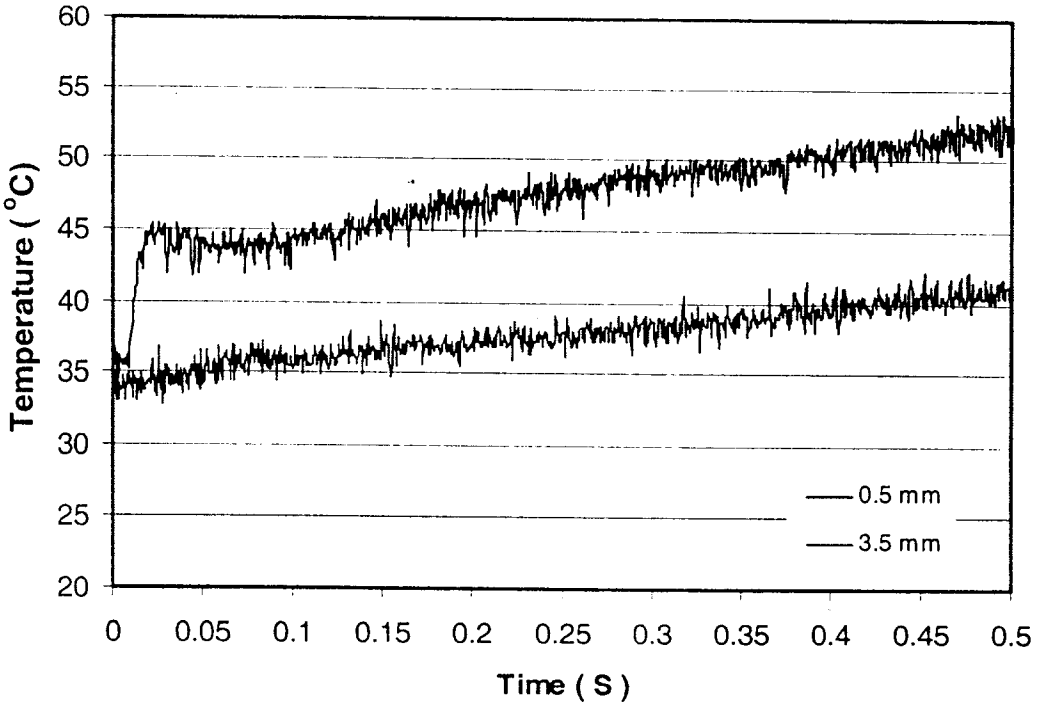

Figure 4.18 The mold temperature profile measured from T-type thermocouples. The droplet superheat is 65°C.

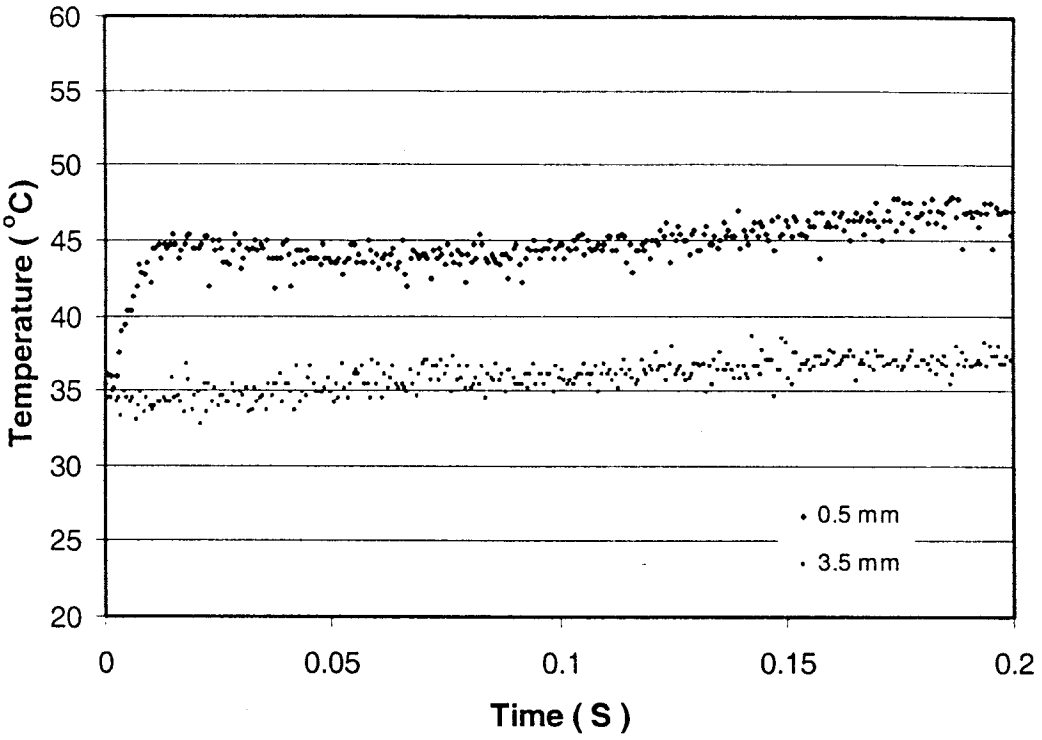

Figure 4.19 The mold temperature profile measured by thermocouples during the first 200 milliseconds.

4.2.3 Coupling Visual Data to Thermal Data

The mold temperature and the heat flux profile rapidly changed during the first 10-50 milliseconds, which is the liquid steel ejection time period. To understand the thermal result better, coupling of the visual data and the thermal data during the first 50 milliseconds is necessary. In this section, the initial heat transfer behavior of an iron droplet during solidification was investigated by both data, as shown in Figure 4.20.

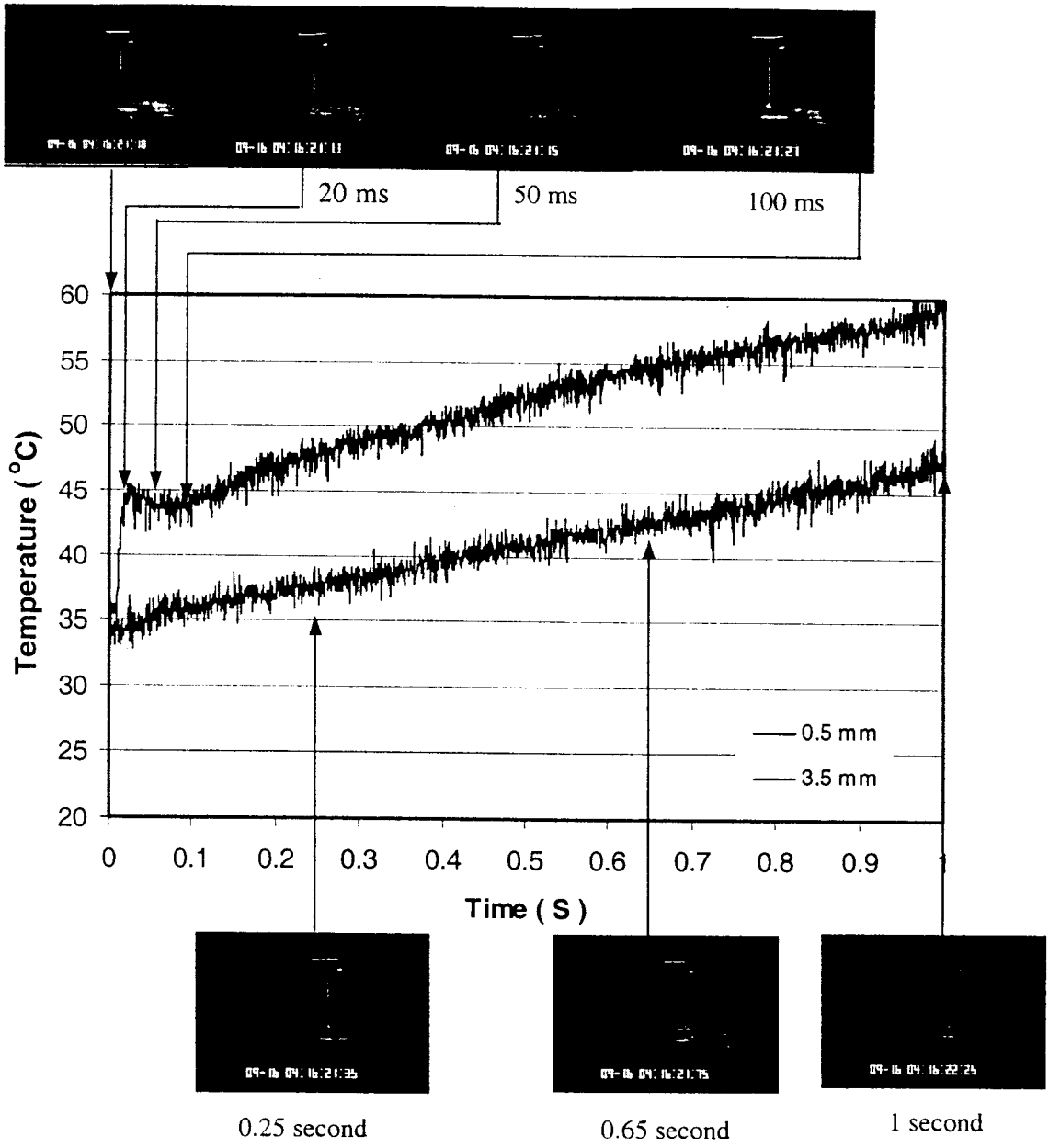

Figure 4.20 The relation between thermal data and visual data.

Heat flux

Figure 4.21shows the relationship between heat flux and time couple with the visual data captured by CCD camera. The heat flux curves were calculated by using IHCP software, written by Prof J. V. Beck.[38)]

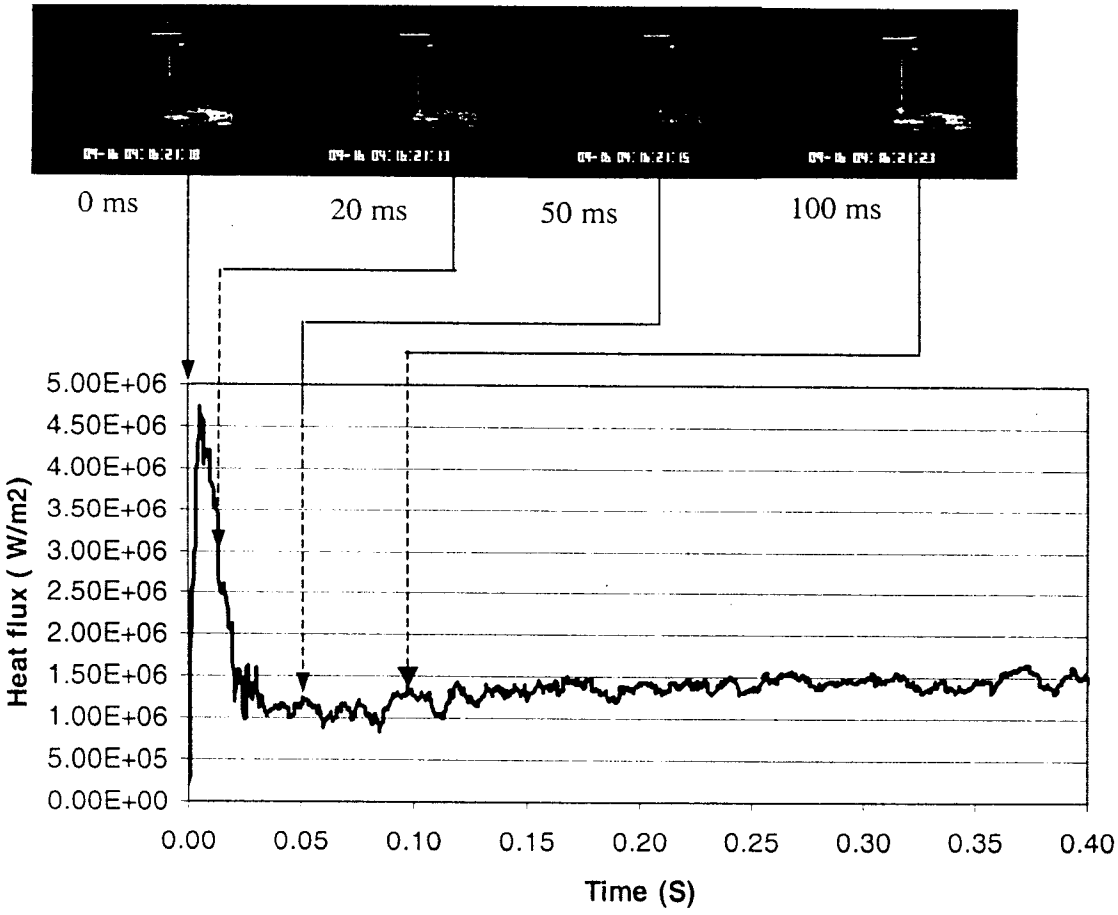

Figure 4.21 The calculated heat flux during the first 400 milliseconds.

Usually, we are interested in the interfacial heat transfer during the first 50 milliseconds time period as the heat flux went up to its maximum value during that time. If we look at the movie recorded during the experiment we can see that the first 50 ms is still within the droplet ejection period. So it can be said that superheat and ejection pressure will play an important role to the initial heat transfer behavior between the droplet and substrate during that time. This result agrees well with the previous work

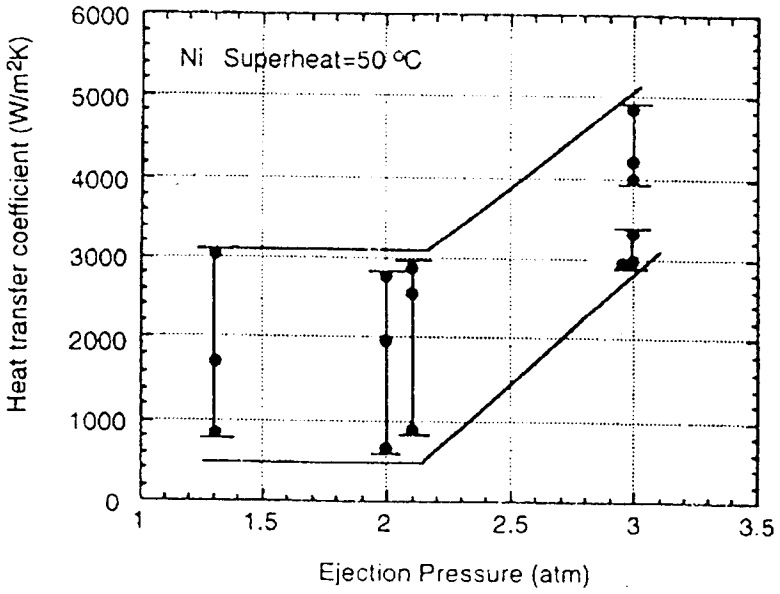

Figure 4.22 The effect of the ejection pressure.[77]

done by Todoroki et al.[77] He found that the ejection pressure affects the heat transfer coefficient. When the ejection pressure increased the heat transfer coefficient increased, as shown in Figure 4.22.

4.3 Summary and Discussion

This novel approach of simultaneous in-situ observation and measurement of rapid heat transfer enables a coupling between the interfacial heat transfer and droplet solidification. The visual data give us accurate information about the position of the droplet impingement point and the solidification behavior therefore only appropriate data, with a good experimental condition, will be selected for heat flux calculation. The spreading behavior of the droplet was documented resulting in the better understand of how the surface of the solidified specimen was formed.

Since the droplet spread and formed the contact surface between the mold and the liquid metal during the ejection process the superheat, ejection pressure and wettability of the liquid metal are the main parameters controlling this step. The impingement point area is a very important area and the effect of the casting parameters on the interfacial heat flux affects the surface quality of the cast specimens in this area. Significant changes of heat flux occurred during the first 20-50 millisecond of contact where, as revealed by CCD camera, the impingement area was formed.

The droplet solidification rate could be estimated from the growth rate of the solidification front. The total solidification time of the droplet fit well with the data obtained by different researchers. It's very interesting that the shell started to grow only after the ejection process had stopped and if we extrapolated the graph representing the shell growth observed from the videotape it was found that it took 200-250 milliseconds for the solidification front to actually started moving upward. This result indicated a significant undercooling period of the droplet during the ejection process. The results can be well explained the earlier works of Todoroki et al.[13] who measured the surface

temperature profiles of the cast specimen. His work shows a long period of droplet undercooling when he ejected the liquid steel on to the copper substrate. If the droplet could be liquid and sit on the copper mold for that period of time the superheat and ejection pressure will be the major casting parameters of our system that significantly influence the interfacial heat transfer.

If we look at the data of shell growth in the strip casting work it can be seen that if the shell grows right as it contacts the roll, at time near zero, the growth rate can be represented by equation 5-1. These results indicated that the system that we have built can represent the strip casting process well when the undercooling process was complete. It is a great advantage of this novel set up in that you can see and understand what your work really represents.

Coupling visual data to thermal data allows better interpretation of the thermal results. The phenomena that occur during the ejection and solidification period can be revealed and related to the interfacial heat transfer behavior between the droplet and mold. The results from coupling visual to thermal data suggested that the measured fluctuation of the heat flux occurred during the time that liquid steel hit the substrate and the droplet was formed. With this information, to obtain a uniform heat transfer rate across the interface that can lead to a uniform roughness surface, the parameters that affected the contact between the droplet and the substrate and the fluid flow within the droplet has to be well controlled.

Chapter 5

Determination of the Effect of Sulfur Content in Aluminum Deoxidized Fe-S alloys on Initial Heat Transfer Behavior

The experiments were conducted to determine the effect of the sulfur content in pure iron on initial heat transfer rate. The wettability between molten iron and a copper chill mold during the initial stage of the solidification strongly affects heat transfer rate. It is well known that sulfur in liquid iron is surface active and that the surface tension of liquid iron at a constant temperature decreases with increasing sulfur content. Therefore the amount of sulfur content can strongly affect the wettability between liquid iron and a copper substrate. A series of experiments were conducted to determine the effect on heat transfer rate of alloy varying sulfur contents from 0.009%S to 0.48%S.

The work had been done twice, before and after the improvement of the system. The lack of the information of the heat flux curves during the first milliseconds of contact time and the significant changes of the heat flux curves, comparing the one calculated from mold temperature profiles and the one after connected with the curves determined from the cast surface temperature profiles, can be seen when the experiments were conducted with the old technique. These problems were solved by introducing a faster temperature measurement system and a new heat flux calculation method. After the system has improved the work was conducted again.

5.1 Determination of the Effect of Sulfur Content on the Initial Heat Transfer by Using the Old Technique

The experimental set up and specimens

The experimental work was conducted before the improvement of the experimental system, fastening the speed of a data acquisition and installing a CCD camera. The detail of the experimental system was clarified in Chapter 3, "The first set up". The specimens were made in the apparatus as shown in Figure 3.24. 180 grams of Fe and a desired amount of sulfur, based on weight percent calculation of Fe-36%S, were wrapped in a Fe foil and put into an alumina crucible which had a diameter of 40 mm. and a height of 58 mm. Small pieces of aluminum were added into the molten Fe-S alloy and the furnace was shut down. The specimen was taken off from the crucible, cut into small pieces, washed and kept in a vacuum desiccator. The chemical composition of the specimens were analyzed by the Spectrochemical Laboratories, Inc. and the result is shown in Table 5.1. The soluble aluminum levels are above 0.045% resulting in oxygen activities less than 10 ppm. and the oxygen values in Table 5.1 is the total oxygen level.

No.	S(%)	O(%)	AL(%)	N(%)
1	0.009	0.003	0.089	0.0007
2	0.073	0.006	0.064	0.0007
3	0.094	0.004	0.088	0.0005
4	0.18	0.013	0.057	0.0005
5	0.33	0.016	0.069	0.0010
6	0.48	0.028	0.045	0.0010

Table 5.1 Chemical Analysis of the specimens analyzed by the Spectrochemical Laboratories, Inc.

The experimental condition

A 3.0±0.2 grams of the specimen was used in each experiment. The copper mold temperature was at 7±5°C at the beginning of each experiment. The diameter of hole at the bottom of the hand made quartz nozzle was 0.5±0.1 mm

5.1.1 Results

The heat flux between the specimens and the substrates were calculated by using finite difference method. Besides the determination of heat flux by copper mold temperature profile thermocouples, the initial heat flux was also determined by using the cast surface temperature measured by the photo-diode-sensor, Figure 5.1 and connected to the other curves calculated from mold temperature profiles to obtain the overall heat flux during the 1 second, as detail were discussed earlier in Chapter 3. Figure 5.2 and Figure 5.3 show the method of calculation and connection heat flux from the cast surface temperature profiles.

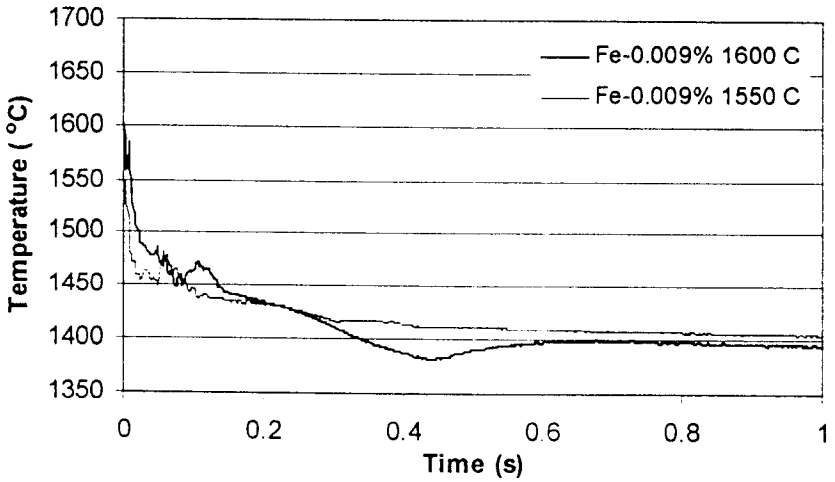

Figure 5.1 The typical cast surface temperatures of the specimens, measured by photo-diode-sensor.

The result of the heat flux calculated from the mold temperature profiles were shown in Figure 5.4 and Figure 5.5 It can be seen that the heat flux rose to the maximum value

within 0.2-0.6 second. The heat flux increased when increasing superheat and the effect of sulfur contact was larger at higher superheat.

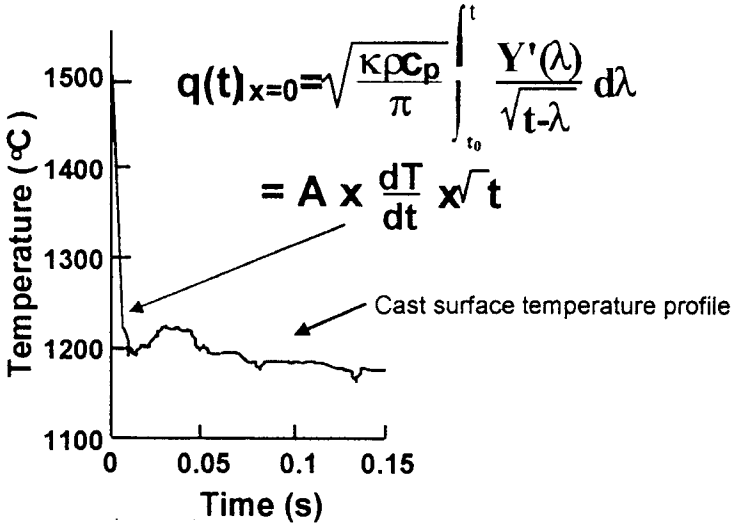

Figure 5.2 The calculation of heat flux by using the cast surface temperature profile of the cast specimens, measured by photo-diode-sensor.

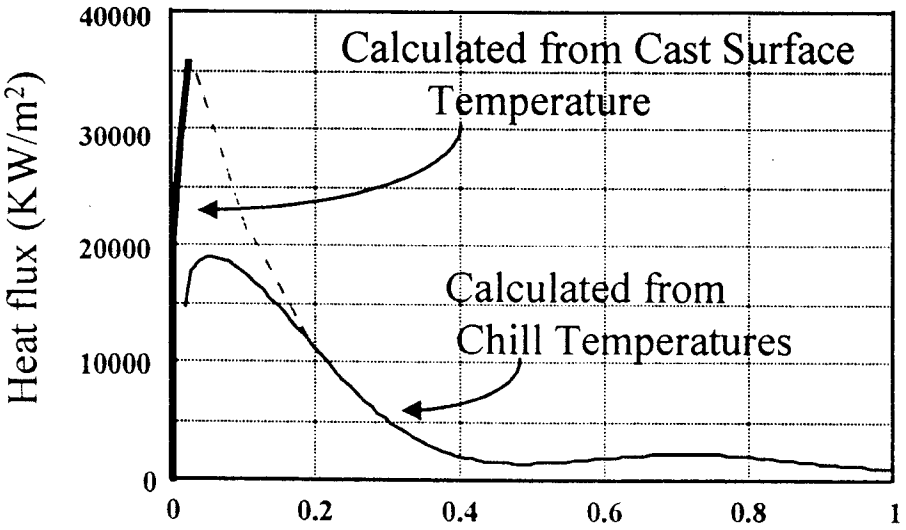

Figure 5.3 The heat flux calculated from copper chill and cast surface temperature.

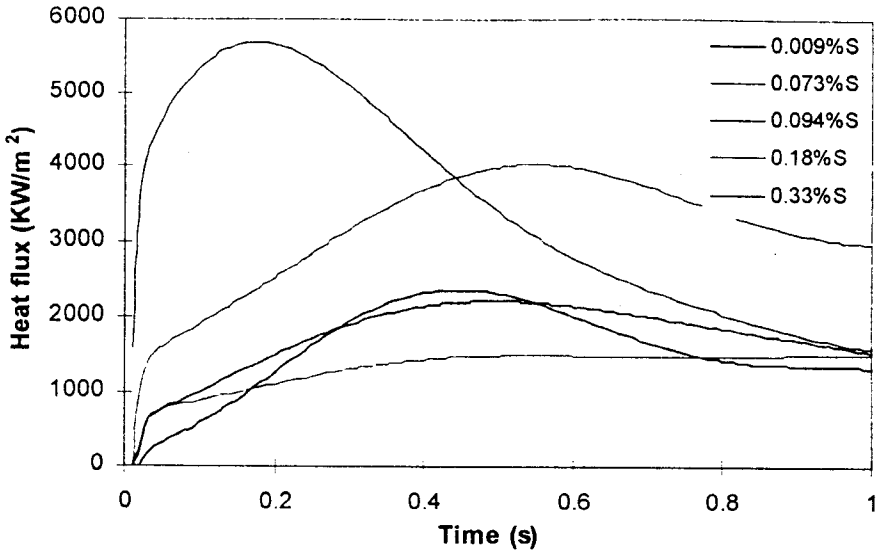

Figure 5.4 The heat flux calculated by using the copper mold temperature profile of Fe-s alloy. (superheat 65°C)

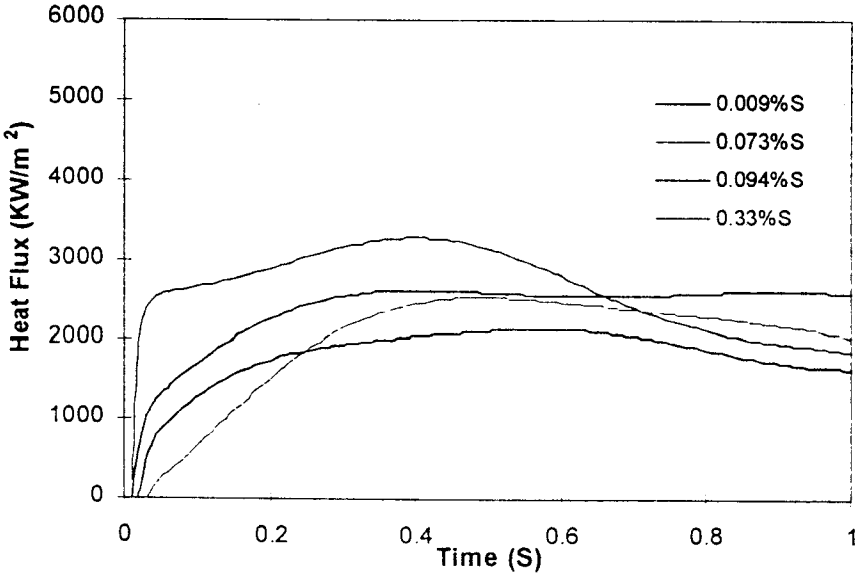

Figure 5.5 The heat flux calculated by using the copper mold temperature profile of Fe-s alloy. (superheat 15°C)

The initial heat flux was also determined by using cast surface temperature profiles and connected to the curves calculated from copper mold temperature profiles. The connected graphs, in both cases15°C and 65°C superheat, were shown in Figure 5.6 and Figure 5.7. After the two curves were connected the heat flux curves were significant changed in their maximum values.

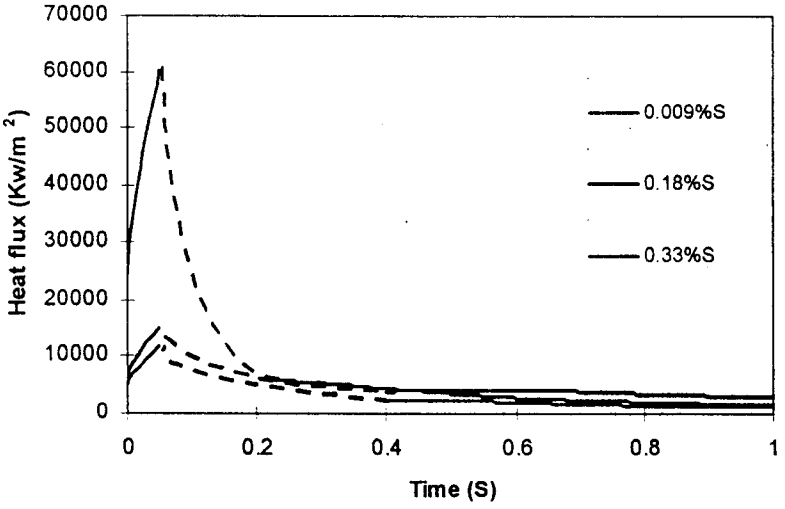

Figure 5.6 The connected heat flux of Fe-S alloys (65°C superheat).

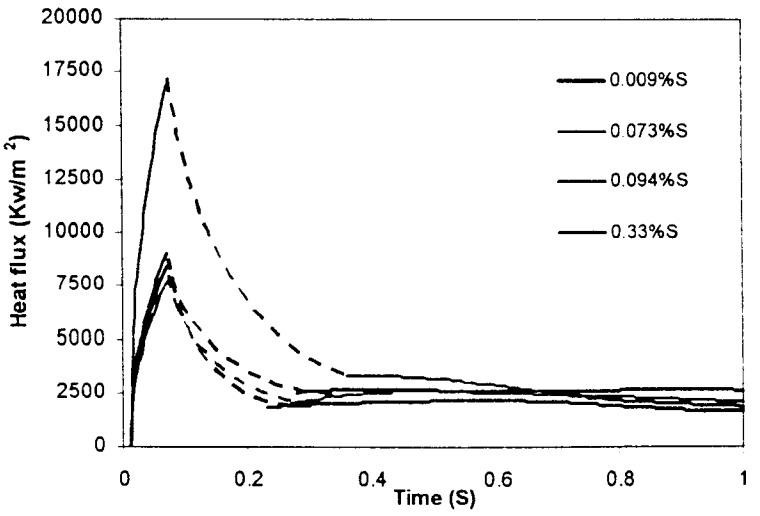

Figure 5.7 The connected heat flux of Fe-S alloys (15°C superheat).

The total heat removed is the total amount of flux that given off in a certain time period. It is the better way to compare the heat flux and can be found from integrating area under the connected heat flux curve. Figure 5.8 shows the relationship between the total heat that given off within the first 1 second after the liquid steel contact the copper substrate. The total heat removed increased with increasing superheat and sulfur content. It was found that at same sulfur content the higher superheat droplets removed more heat during than the lower superheat droplet.

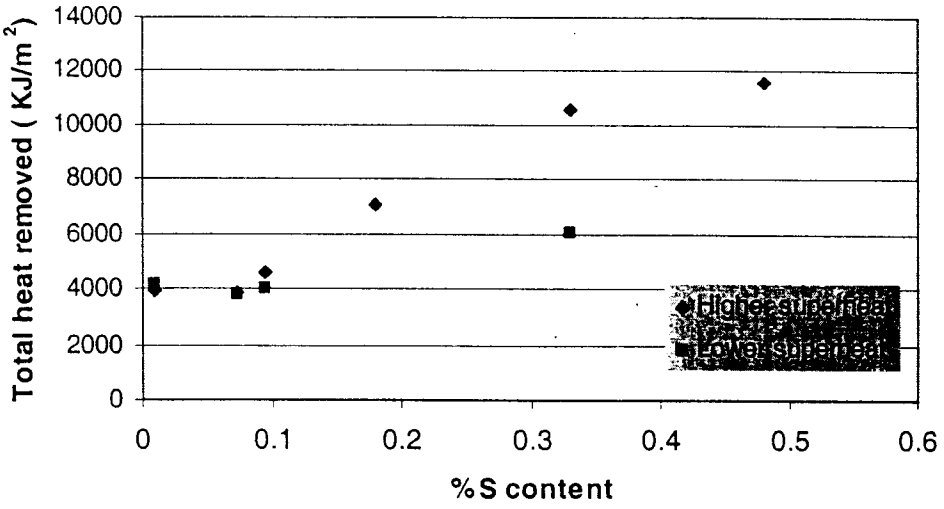

Figure 5.8 The total heat removed within the first second versus % sulfur content.

Since the total heat removed was calculated from the connected heat flux curves, errors can be introduced in the results, as some assumptions have to be made. In order to calculate the heat flux from the cast surface temperature profile and connected it to the heat flux calculated from mold temperatures the results that we found should be confirmed by conducting the experiment under condition where the heat flux can be measured with millisecond resolution.

5.2 Determination of the Effect of Sulfur Content on the Initial Heat Transfer by Using the New Technique

The experimental set up

The experiment was conduct by using a refined experimental apparatus (the second set up) and the new heat flux calculation technique. The thermal data was recorded on a personal computer through a new high-speed data acquisition system with a 0.0625 millisecond, 16KHz, sampling speed. After obtaining the temperature profiles inside the copper mold, the heat flux during the initial solidification was calculated by using the new IHCP software that was specially customized for this work by Prof. J.V.Beck.[40] The surface heat flux as a function of time was estimated based on IHCP algorithm developed by Prof. Beck which is more precise than the previous finite difference method.

The experimental condition

A 3.0±0.2 grams of the specimen was used in each experiment. The copper mold temperature was at 7±5°C at the beginning of each experiment. The diameter of hole at the bottom of the hand made quartz nozzle was 0.5±0.1 mm

5.2.1 Results

The mold temperature profiles

The thermal response of the copper chill mold of Fe-S alloy is shown in Figure 5.9. Because of the faster sampling speed of the data acquisition system and the faster response and closer position of the thermocouples, the details of the chill temperature profile can be observed clearly. It can be seen that the temperature profile tends to rise to the peak point within the first 50 ms of solidification. The fluctuation of temperature during the solidification process can be observed. In the previous work, where the chill temperature profile was recorded at a slower data acquisition speed and by slower response time thermocouples, the fluctuation of the temperature profile which occurred during the ejection process of liquid steel could not be seen.

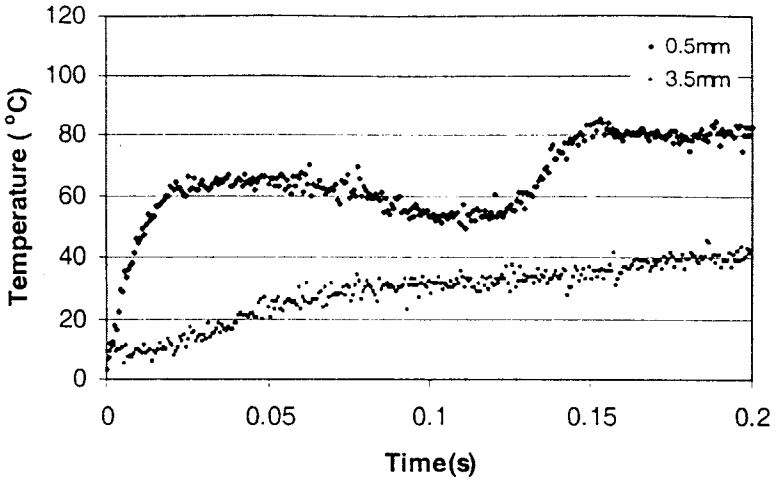

a

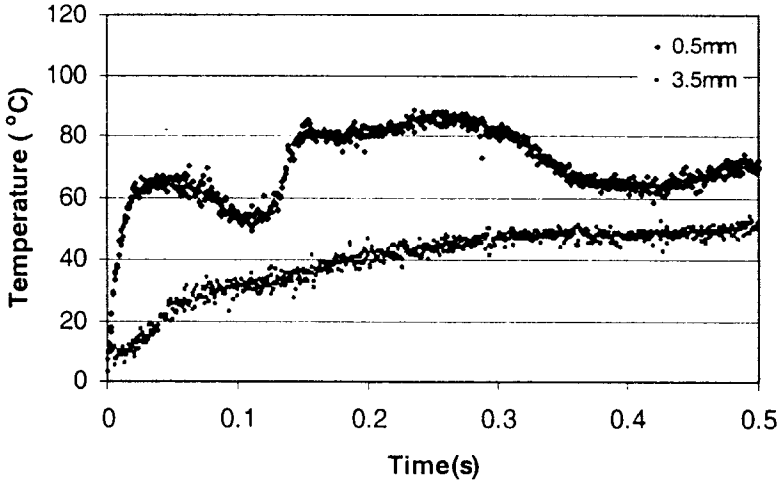

b

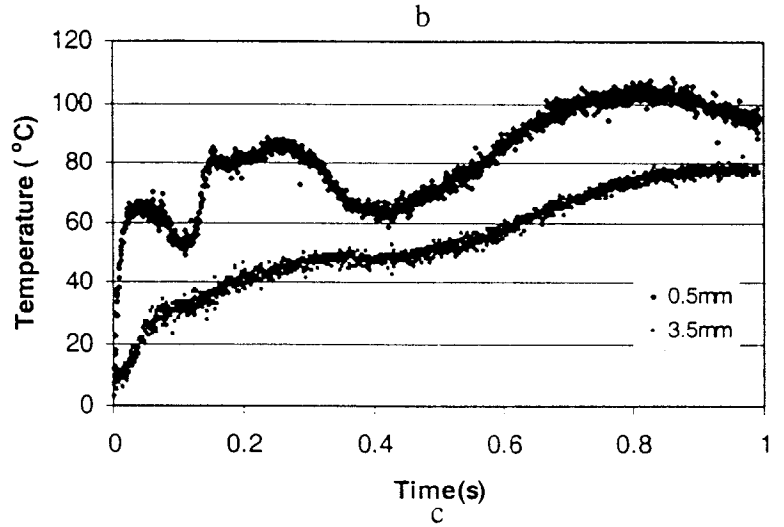

c

Figure 5.9 The example of the mold temperature profiles (0.33%S, 40°C) at different time scales (a) millisecond resolution (b) the first 0.5second of the experiment (c) the first second of the experiment.

Heat flux

The interfacial heat flux between the droplet and the substrate can be calculated from the mold temperature profiles, measured by thermocouples at position 0.5 mm and 3.5 mm beneath the surface of a copper chill substrate, by using IHCP method. Figure 5.10 shows a relationship between heat flux, calculated from temperature profiles, and time. At the same superheat, 40±5°C, each curve rose up to the maximum value within the first 10-15 milliseconds of the contact time and then dropped down when the contact time approach 20 milliseconds. After 100 milliseconds all the curves tend to converge to a similar heat flux value. From the result below, it can be concluded that by increasing %sulfur content the maximum heat flux value gradually increased.

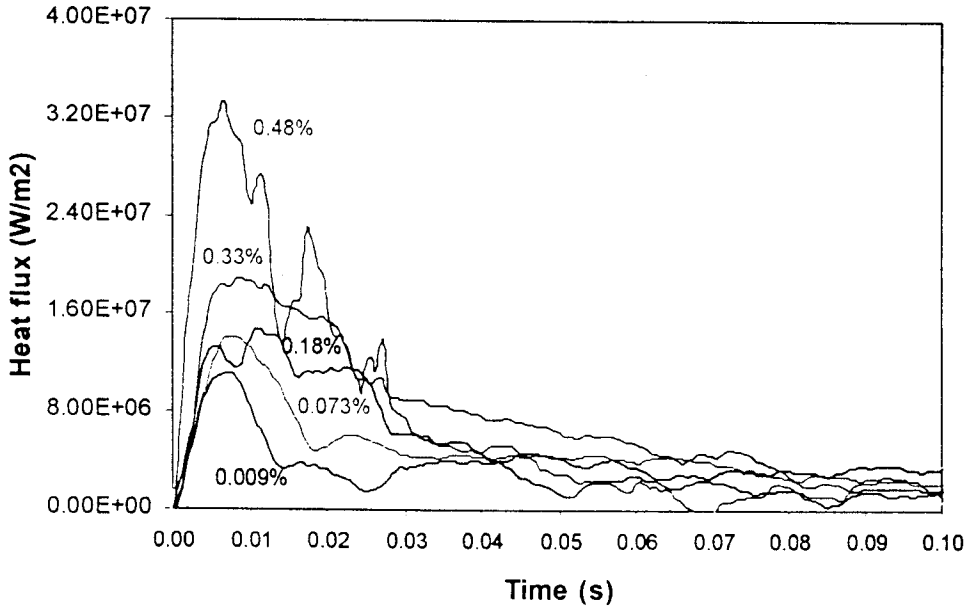

Figure 5.10 The effect of sulfur content on the interfacial heat flux at low copper mold temperature = 7±5°C and the superheat = 40 °C.

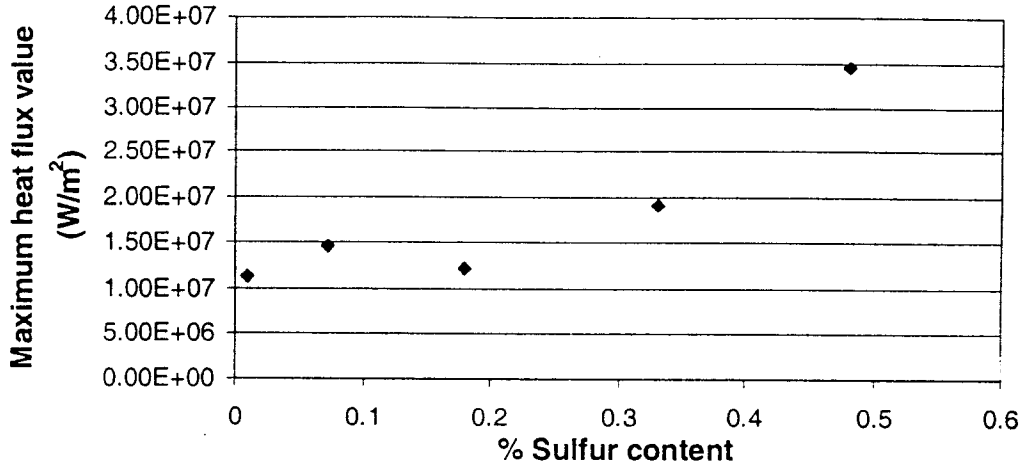

Figure 5.11 The relationship between peak heat flux value and the %sulfur content.

The total heat removed

The total heat removed in a certain time was determined by finding the area under the heat flux curve. Figure 5.12, shows the amount of the heat that given off from the specimen, at various sulfur contents, in 1 second for the both 40±5°C and 70±5°C superheat cases. The amount of heat removed increased with increasing superheat. With increasing % sulfur content the amount of the removal heat is slightly increased. Figure 5.13 and Figure 5.14, show the amount of heat that is given off within the first 50 and 20 milliseconds respectively. Both results have the same trend as Figure 5.12, however within the first 50 and 20 milliseconds, they show a stronger effect of sulfur content on the amount of removal heat.

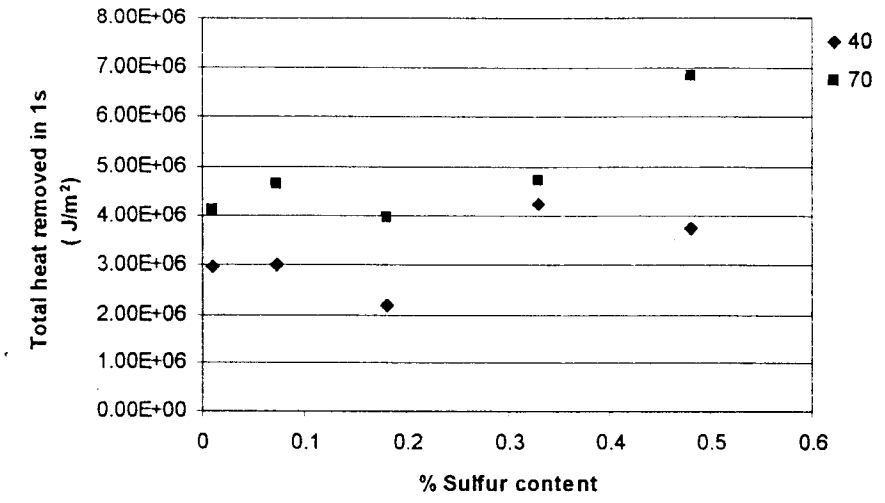

(a)

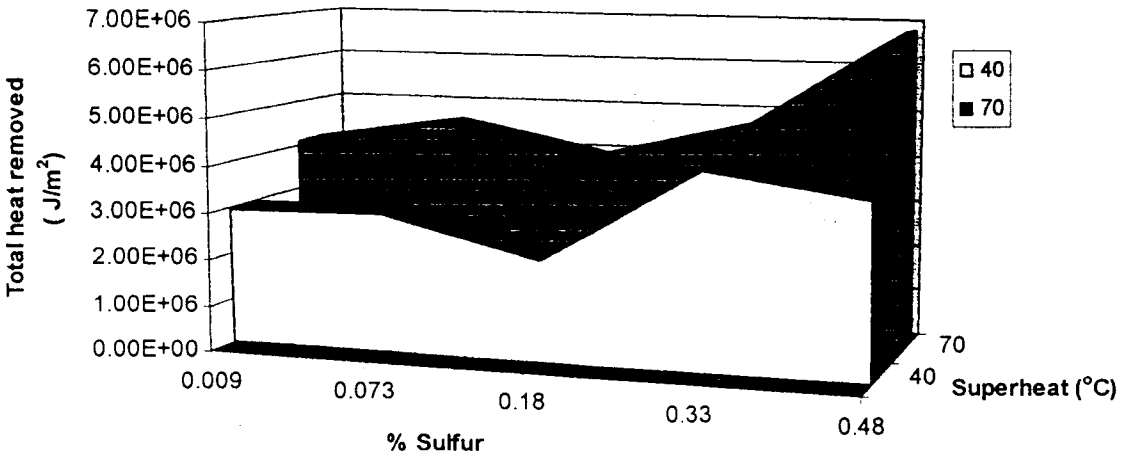

(b)

Figure 5.12 (a) The relationship between the total heat removed within the first second of the contact time and %sulfur content (b) The relationship between total heat removed and %sulfur content and superheat.

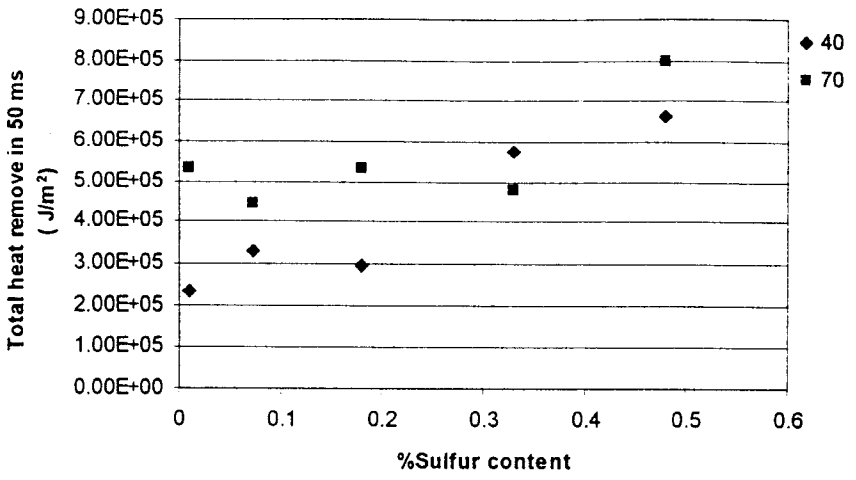

(a)

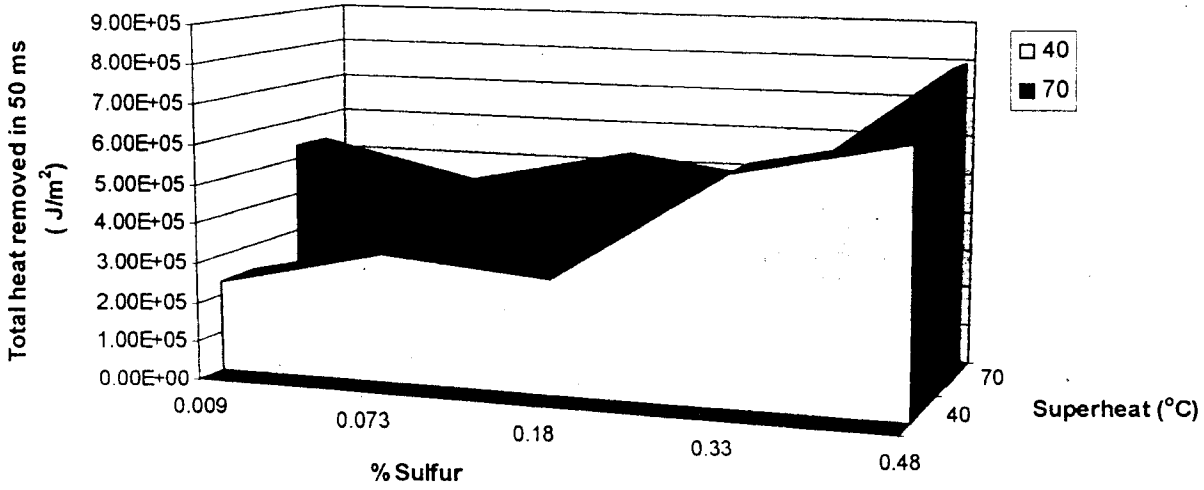

(b)

Figure 5.13 (a) The relationship between the total heat removed within the first 0.5 second of the contact time and %sulfur content (b) The relationship between total heat removed and %sulfur content and superheat.

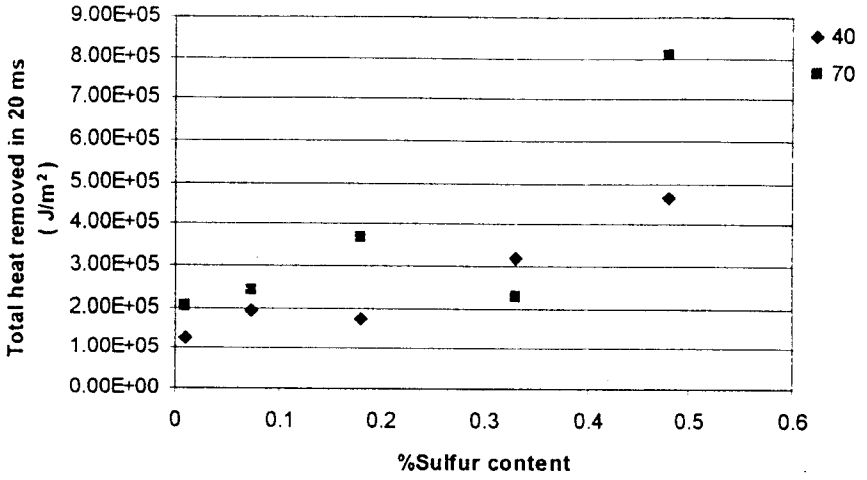

(a)

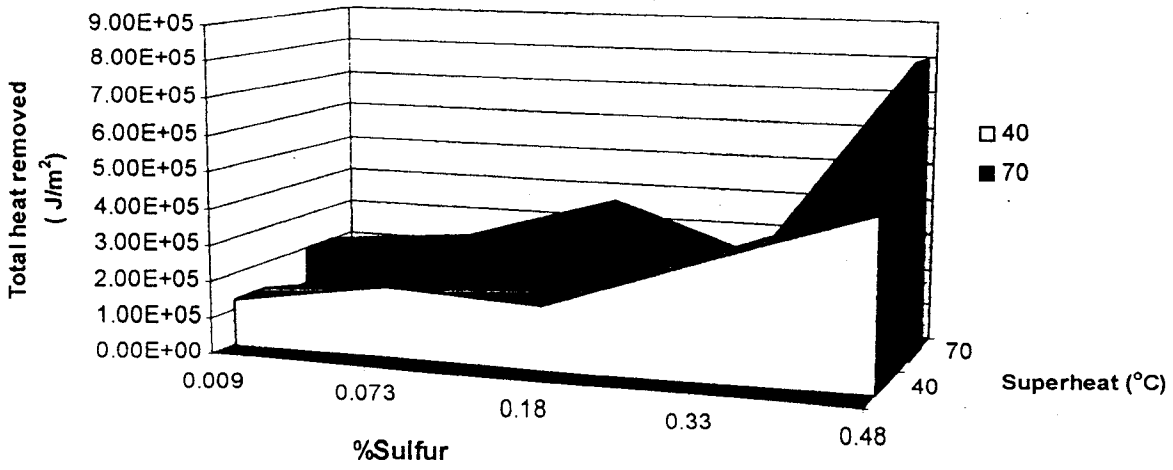

(b)

Figure 5.14 (a) The relationship between the total heat removed within the first 20millisecond of the contact time and %sulfur content (b) The relationship between total heat removed and %sulfur content and superheat.

5.3 Surface Roughness Measurement

Two parameters, Ra and Pt, were selected to define the roughness of the solidified specimens. The roughness was measured by using a stylus-type surface analyzer. The measurement was conducted at a traverse length equals 4.8 mm.

Arithmetric Mean Roughness value, Ra(CLA/AA), is the arithmetic mean of the profile deviation of the filtered roughness profile from the center line within the measuring length lm, Figure 5.15.

Maximum Profile Depth, Pt, is defined as the maximum distance between two parallel threshold lines which contain the unfiltered profile over the traverse length. A description of Pt, which is a waviness parameter, is given in Figure 5.15. Typically Pt is used to monitor a process where waviness rather than roughness is critical parameter.

The effect of sulfur content and superheat on the Ra, Arithmetric Mean Roughness, is presented in Figure 5.16 and the effect of sulfur content and superheat on the Maximum Profile Depth, Pt, is presented in Figure 5.17. Both Ra and Pt values decreased when the superheat increased however the effect of sulfur content on Ra and Pt was not strongly shown. When the sulfur content increased, at a high superheat, the Pt value slightly went down, however this effect could not be seen in Ra value.

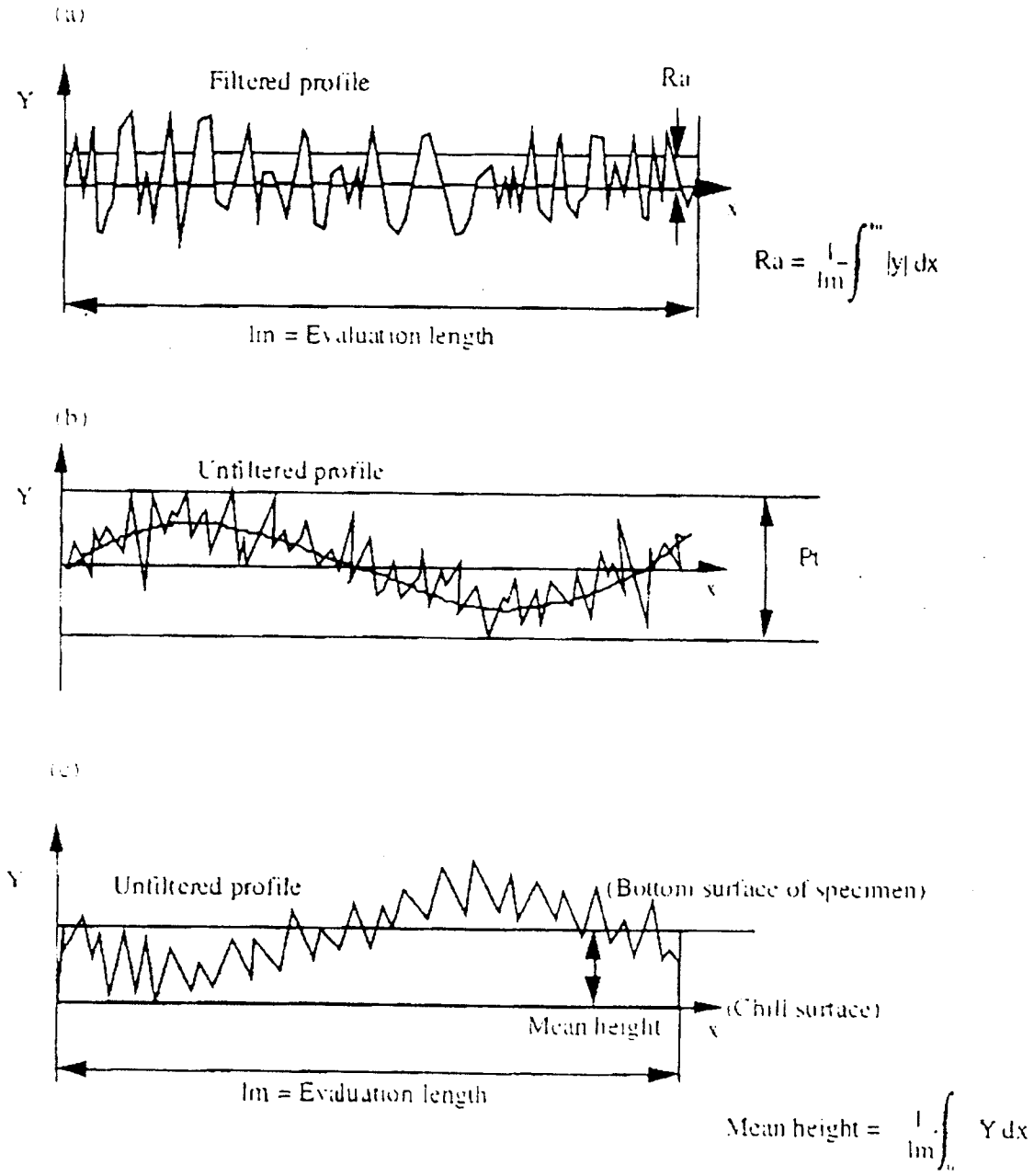

Figure 5.15 Description of (a)Ra, (b)Pt and (c)Mean height.

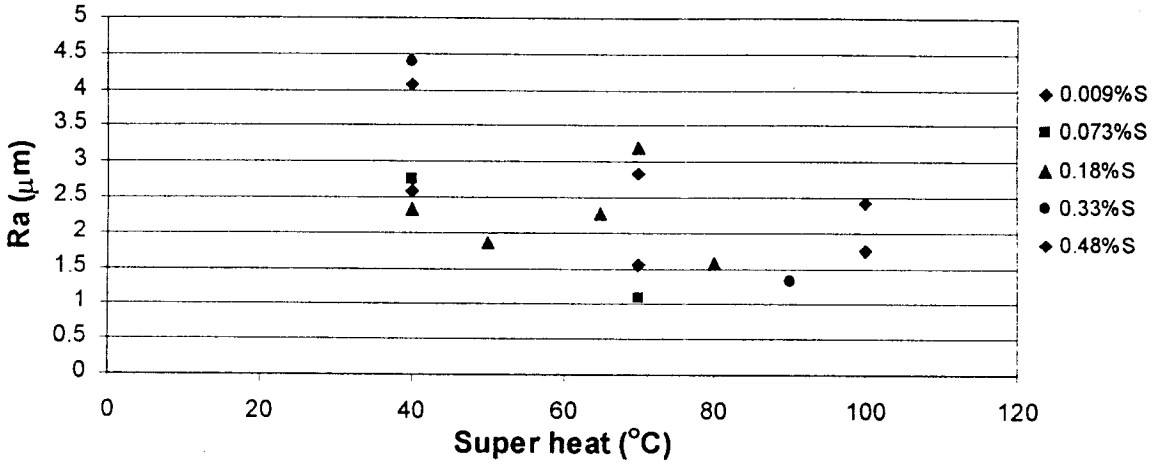

Figure 5.16 The relationship between Ra, % sulfur content and superheat.

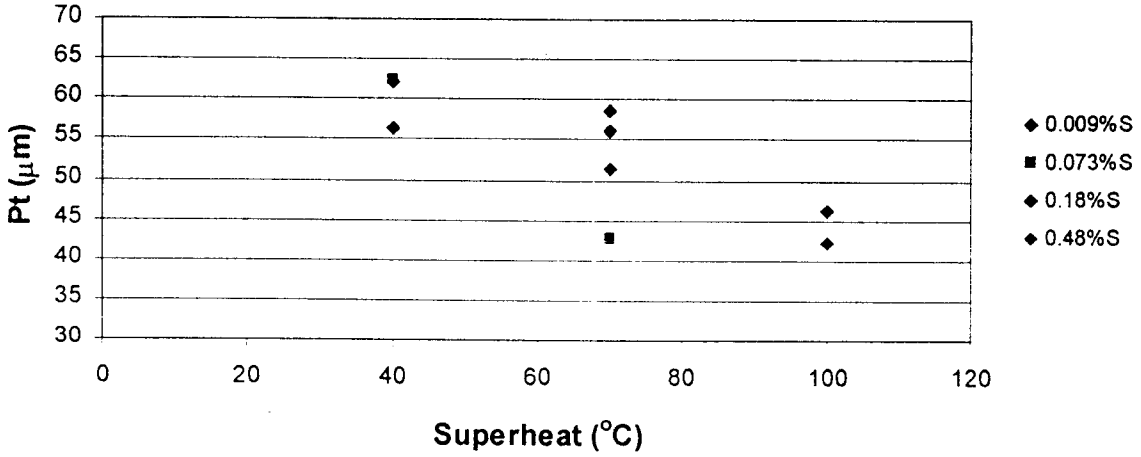

Figure 5.17 The relationship between Pt, % sulfur content and superheat.

5.4 Summary and Discussion

The effects of sulfur content on the interfacial heat transfer were documented in this work. The results show that, at the same sulfur content, increasing superheat (by 30°C) increased the total heat removed. The different in the total heat removed between lower and higher superheat is small in the case of lower sulfur content however it becomes larger in the case of higher sulfur content. If we compare the amount of heat that given off from the droplet to the mold during the first 20 ms, 50 ms and 1 second of the contact time it was found that the effect of sulfur content on the total heat removed can be seen more clear during 20 and 50 ms of contact time. This indicated that the sulfur content strongly affects the interfacial heat transfer during the first millisecond of contact time as the liquid steel was contacted and spreading on the copper substrate.

The sulfur in liquid iron is surface active and that the surface tension of liquid iron at a constant temperature decreases with increasing sulfur content, Figure 5.18. The relationship between the activity of sulfur and the surface tension showed that the surface tension decreased rapidly when the activity of sulfur increased from 0 to 0.1, after that, if sulfur were added more in liquid steel, the surface tension of the liquid steel decreased gradually. Therefore the contact of the liquid steel on the copper substrate will be enhanced by the presence of the sulfur content in the molten specimens, as the liquid can spread and contact the surface profile of the substrate well at low surface tension..

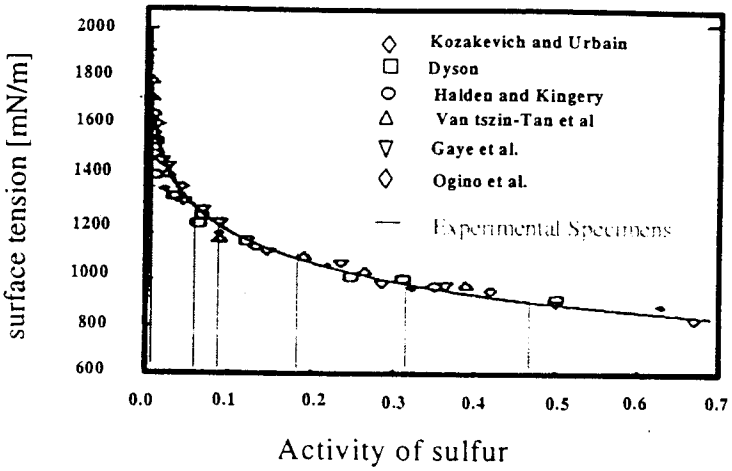

Figure 5.18 The effect of sulfur content on the surface tension of liquid steel.

The surface roughness measurements were conducted by using Ra and Pt as parameters to defined how rough the surface of the specimen was. The result suggested that the melt superheat strongly affected the roughness of the cast specimen. However there was not much effect of sulfur content on Ra and Pt. There are only slightly changes in Pt value as the sulfur content increased. Since Pt values represent only the maximum not average distance between two parallel threshold lines of the unfiltered profile and Ra values represent the roughness after the waviness of the profile was filtered out it might not be the most appropriate way to represent the roughness of metal-mold contact surface by this value.

It is noted that, in every experiment, the solidified droplet left some solidification marks on the surface of the copper substrate. Figure 5.19 show the mark left by 99.97%Fe droplet and its chemical analysis on the copper substrate under the SEM-EDX.

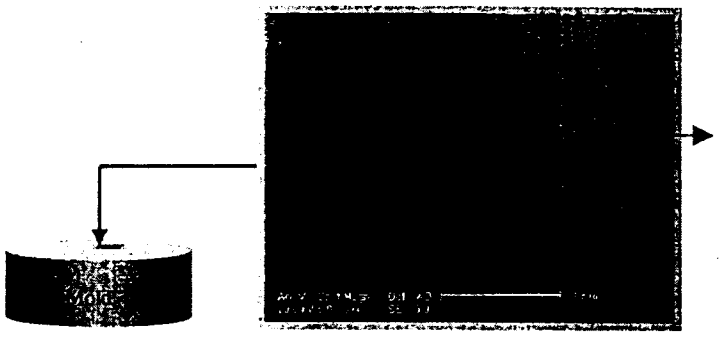

Elmt	Spect. Type	Element %	Atomic %
O K	ED	0.58	2.24
Si K	ED	0.45	1.00
Mn K	ED	0.03*	0.03*
Fe K	ED	1.30	1.44
Cu K	ED	97.64	95.28
Total		100.00	100.00

* = <2 Sigma

Figure 5.19 The chemical analysis of a solidification mark left by the iron droplet.

Since the solidification mark can not be avoided it is interesting to see how it affects the initial heat transfer behavior of the droplet. The next work will be conducted to reveal the effect of the black substance found on the surface of the substrate when the liquid Mn-Si killed steel was ejected onto the substrate.

Chapter 6

Determination of the Effect of Deposition Film Built Up at The Interface of Mn-Si Killed Steel Droplet and Copper Mold Substrate on Initial Heat Transfer Behavior

In strip casting, molten liquid steel contacts the rotating mold directly. Under this condition it is expected that modifications of the interface conditions will result in significant changes in interfacial heat transfer. In order to see the influence of the deposited oxide film on the initial heat transfer behavior of Mn-Si killed steel droplets, under the laboratory conditions, an experiment was designed to imitate the real situation by ejecting the liquid steel continuously onto the copper substrate without cleaning the surface between experiments. As a film built up at the interface between the substrate surface and liquid steel droplet, the effect of the deposited oxide film on the initial heat transfer behavior of the droplet was revealed. To better understand the oxide film the chemical and optical analysis of the film and the solidified specimen was carried out.

In this work, a Mn-Si killed steel was used. It had been found by Strezov et al. that an oxide film built up between SUS304 stainless steel melt and copper substrate strongly effected the heat transfer behavior.[20] It is possible that liquid inclusions or solid inclusions that are formed may interact with the substrate and affect the initial heat transfer behavior via the formation of surface films. The study of the solidified cast specimen surface roughness and measurement of the thickness of the deposited films were also carried out in this work.

6.1 Specimens

A Mn-Si killed steel was used in this study. Table 6.1 shows the percentage of each element in the specimens. A well cleaned 2.90±0.06 grams of the specimens were used in each experiment.

Element	Percentage
C	0.047
S	0.005
Al	0.006
B	<0.001
Si	0.27
Mo	0.03
Ni	0.025
Ti	0.003
Mn	0.64
Cr	0.031
P	0.007
O	0.009
N	0.006
Se	<10 ppm

Table 6.1 The chemical composition of the specimens.

Results

6.2 The Effects of Deposited Film on the Initial Heat Transfer Behavior Between the Liquid Steel Droplet and Substrate

To measure the effect of the deposited film on the initial heat transfer behavior between the steel droplet and the copper substrate the T-type thermocouples were connected to a high speed data acquisition system. The thermal data was collected when the liquid droplet was ejected onto the mold at sampling speed 10 KHz. By continuously repeating the experiment without cleaning the mold surface the effect of the oxide film, deposited on the surface of the copper substrate, on the initial heat transfer behavior can be observed.

Surface Temperature Profile

Figure 6.1 shows the thermal response of the copper substrate. The thermocouple was positioned 0.5 mm underneath the surface of the copper mold when the liquid manganese killed steel was ejected. It can be seen that when the experiment was conducted for 8 times consecutively without cleaning the mold surface between experiments the thermal response of the copper substrate improves significantly

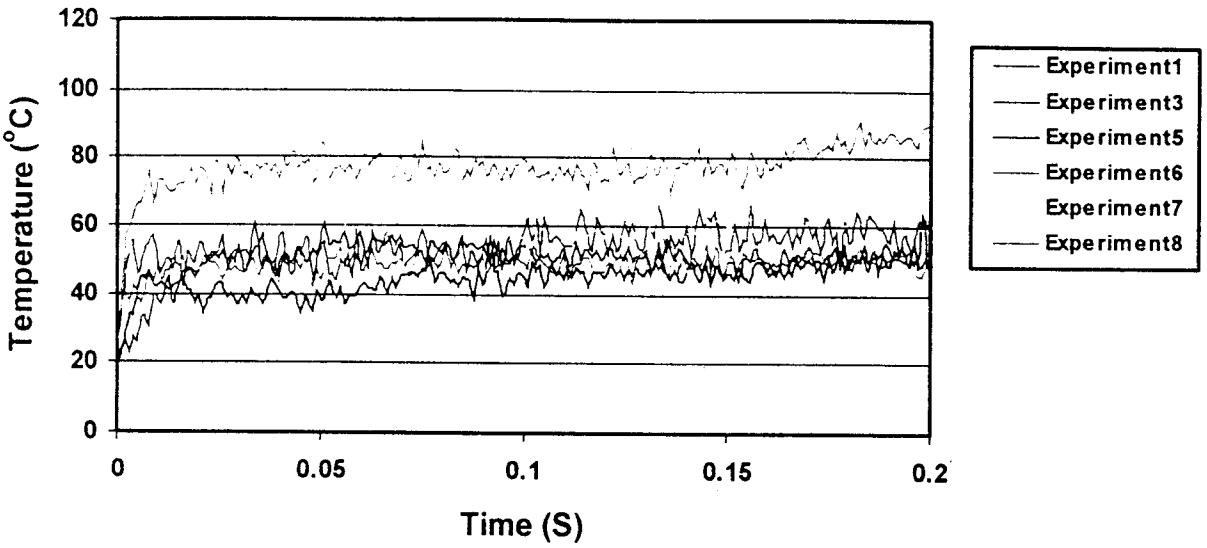

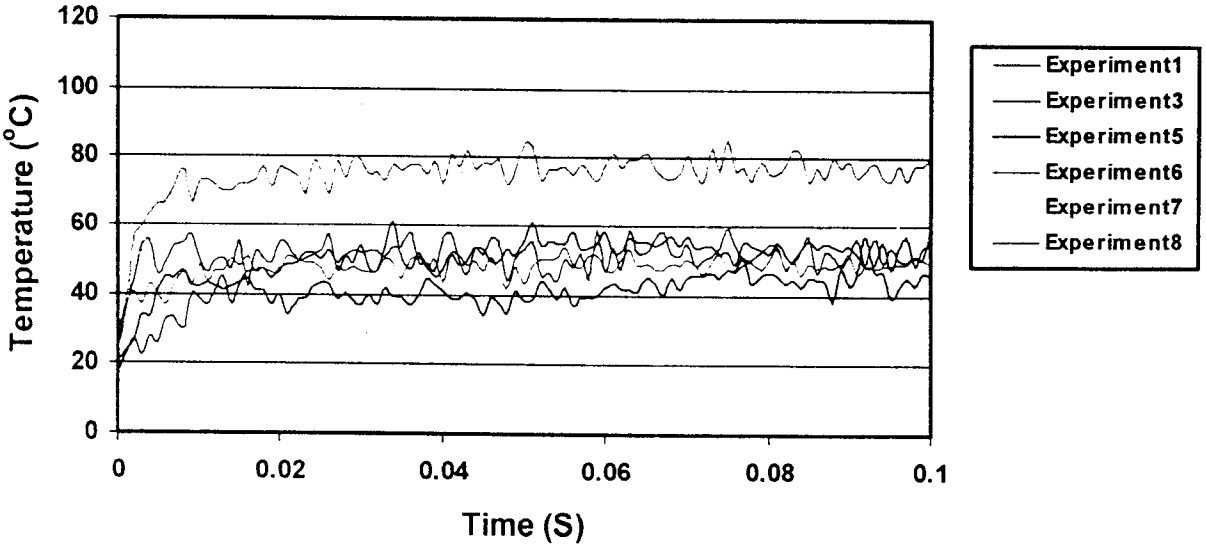

Figure 6.1 The mold temperature profiles recorded from T-type thermocouple at position 0.5 mm from the mold surface during the first 200 and 100 milliseconds.

The calculated heat flux

The heat flux was calculated from the mold temperature profiles measured from both thermocouples installed at positions of 0.5 and 3.5 mm from the mold surface. The modified Beck's version of inverse heat conduction algorithm was employed in this calculation. Figure 6.2 shows the relationship between heat flux and time when the experiments were conduct 8 times consecutively at slightly different superheats. Details of the experiment are given in Table 6.2. The superheat and the mold temperature was maintained at 50 ± 5 °C and 25 ± 2 °C respectively in almost every experiments. However some scattering of superheat value can still be seen in experiment 3 and 6.

Experiment	Superheat (°C)	Mold Temp (°C) (25 ± 2 °C)
1	55	27
3	10	25
5	50	23
6	35	27
7	50	27
8	55	26

Table 6.2 The experimental conditions.

It is interesting that only during the first 50 milliseconds of solidification process the effect of the film layer can be seen clearly; however, when the time approached 0.1 second the difference in heat flux profile in all cases are minimal.

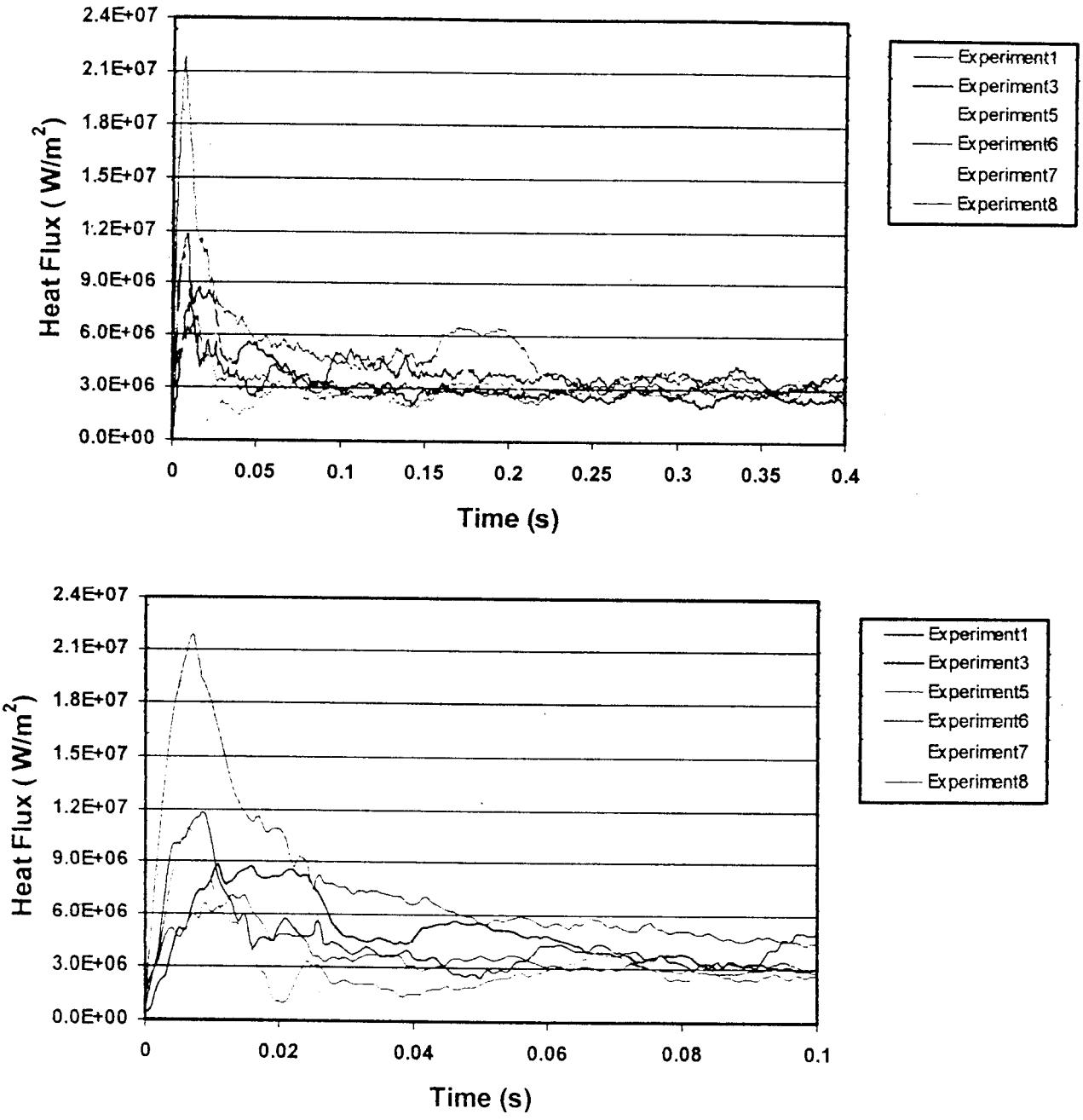

Figure 6.2 The relationship between heat flux and time during the first 400 and 100 milliseconds.

Figure 6.3 shows the relationship between the maximum heat flux and the number of the experiment. It can be seen that with the same experimental conditions the maximum heat flux of the last experiment is higher than the first experiment that the molten metal was ejected onto the clean substrate surface. Figure 6.4 show the total heat that was given off from the melt to the substrate during the first 100 ms in each experiment. Both maximum heat flux and total heat removed were agreed well with each other. They both significantly increased when the number of the experiment increased.

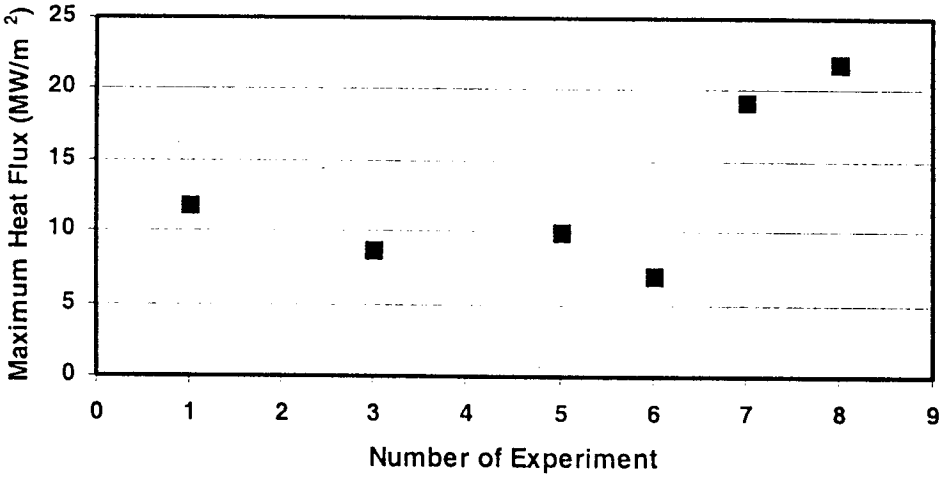

Figure 6.3 The maximum heat flux of each experiment.

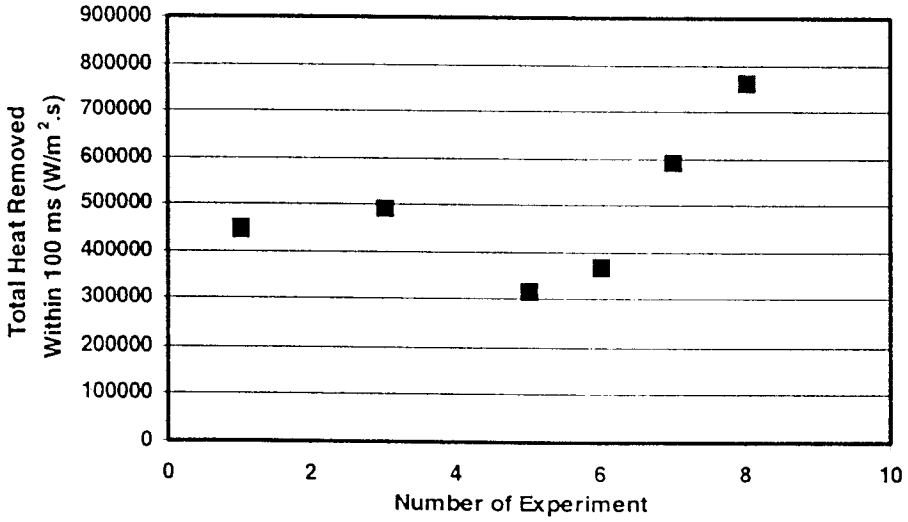

Figure 6.4 The total heat remove during the first second.

6.3 Film Thickness Measurement

To measure the thickness of the film, the optical microscopy was employed. The copper mold surface was dissected into many tiny squares (1 mm^2) and each tiny area was investigated through the microscope, Figure 6.5. The thickness of the film was measured by adjusting the focus of the lens in Z-axis direction between the clean and the deposited oxide mold surface. Figure 6.6 shows the thickness of the film in the area near the tip of the thermocouples after the molten steel was ejected 8 times onto its surface.

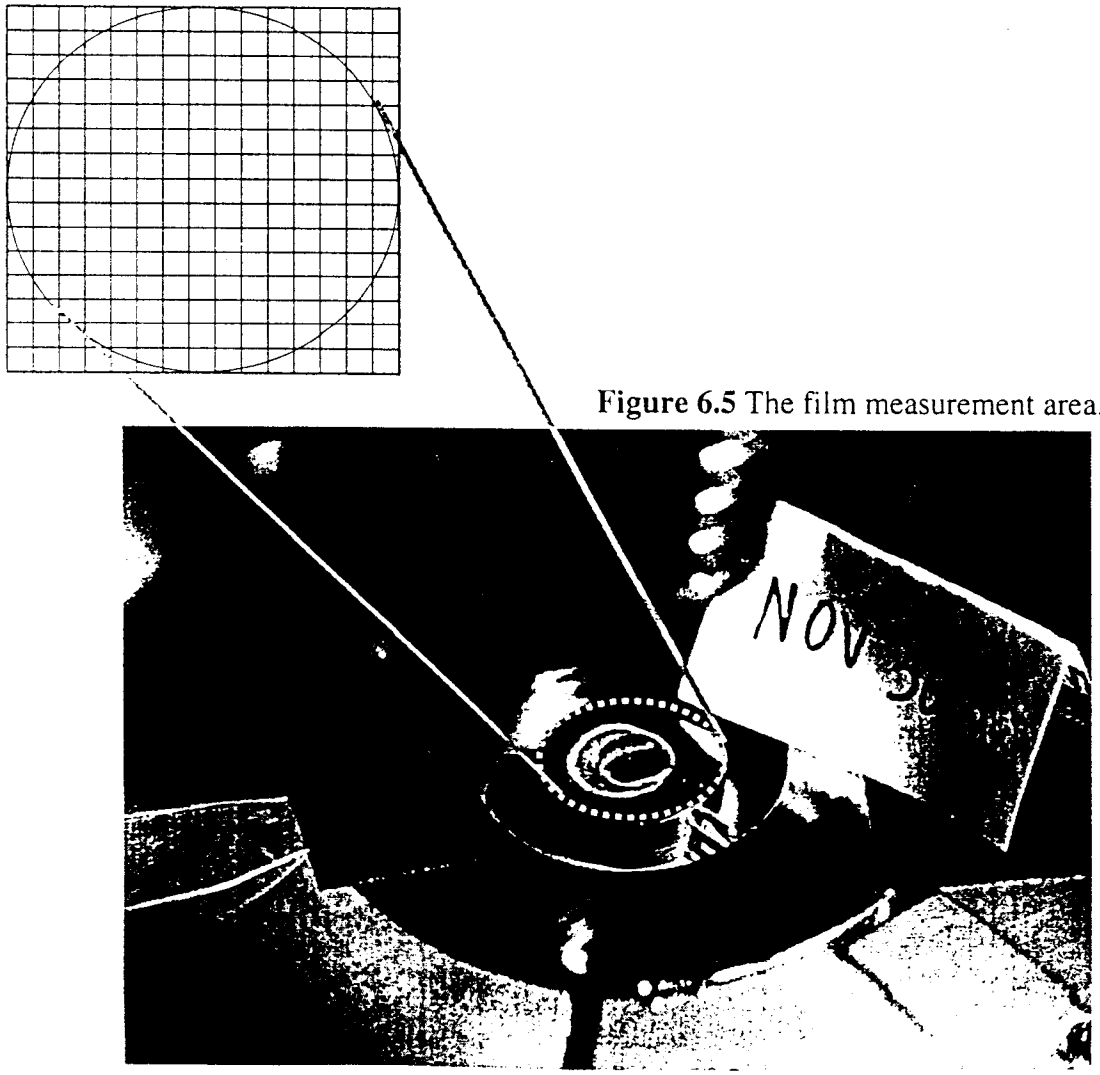

Figure 6.5 The film measurement area.

If we take the average value of the thickness of the film throughout the area near the thermocouples the film is approximately 22.92 μm thick. This is the thickness measured after the experiment when we saw the major change of heat transfer behavior between the molten steel and the copper substrate corresponding to the thermal result shown in Figure 6.1 and 6.2.

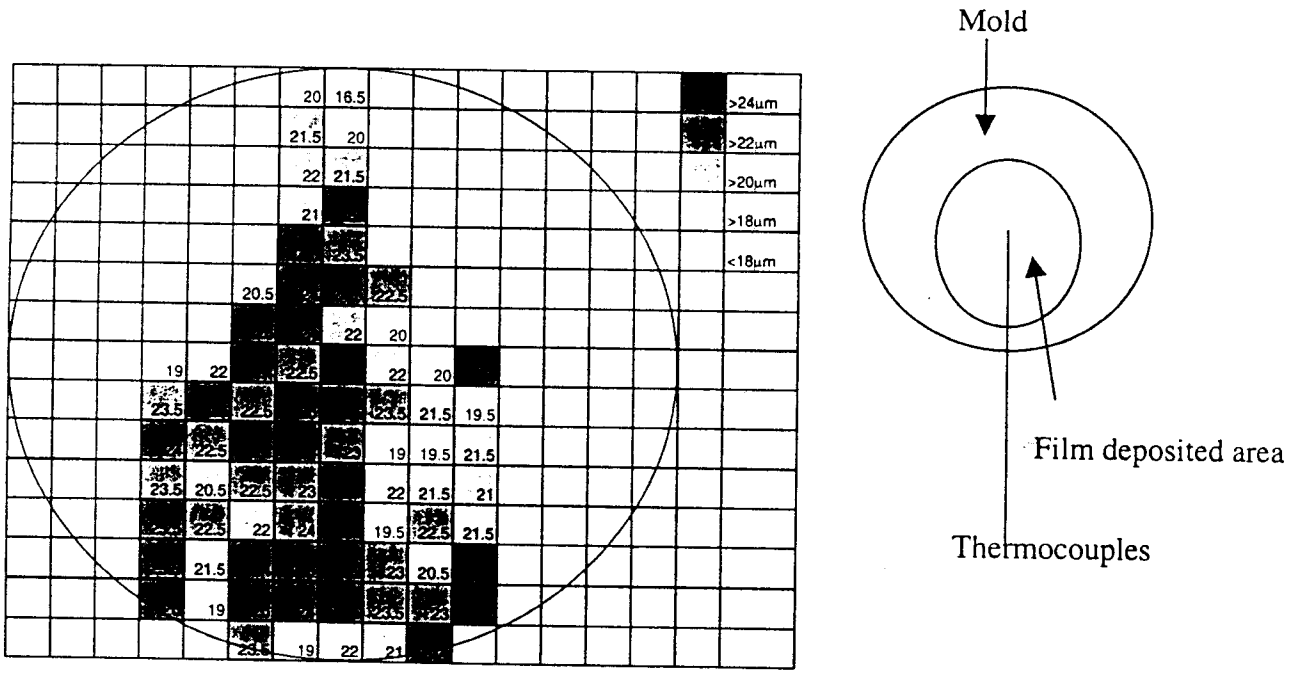

Figure 6.6 The thickness of the deposited film measured near the thermocouple area.

6.4 Deposited Film Analysis

6.4.1 The Study of the Deposited Film Under SEM/EDX

Figure 6.7 and 6.8 show the copper mold before and after the experiment was done, as the molten steel was ejected onto its clean surface. There is a black substance deposited at the contact area between surface of the copper mold and the solidified droplet.

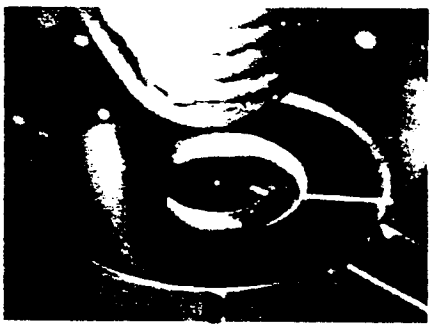

Figure 6.7 The clean copper mold

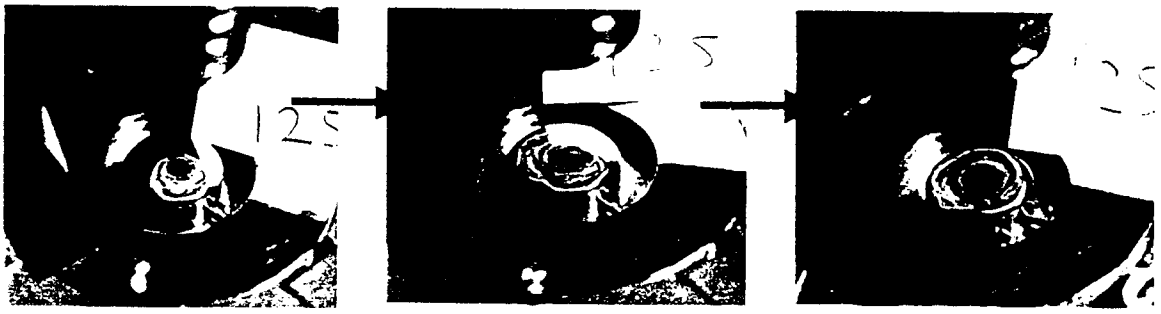

Experiment 1 Experiment 2 Experiment 3

Figure 6.8 shows how the black substance was built up on the surface of the substrate when the experiment was repeatedly done without cleaning the surface of the substrate. As the number of the experiment increased the thickness of the film increased.

SEM-EDX analysis was used to determine the chemistry of the black substance deposited on the surface of the substrate after the first experiment. As seen in the Figure 6.9 at the impingement point, however, the amount of black substance appears to be less concentrated than at any other contact areas.

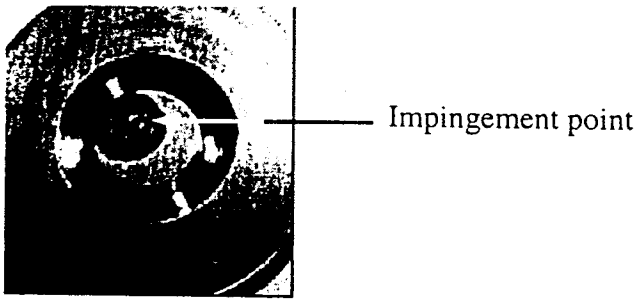

Figure 6.9 A black substance deposited on the surface of the substrate.

The chemical analysis of the black substance, deposited as a droplet solidified on the clean substrate surface, was carried out by using SEM-EDX. Figure 6.10 shows a black substance viewed under Scanning Electron Microscopy, at magnification 38X. Under the SEM, the dark area is the area that is less covered by the film and the clouded gray area is the area covered by the deposited film. By using EDX line scan, Figure 6.11, to analyze the chemical composition of the film it can be seen that the distributions of manganese, silicon and oxygen through scanning line follow the same pattern.

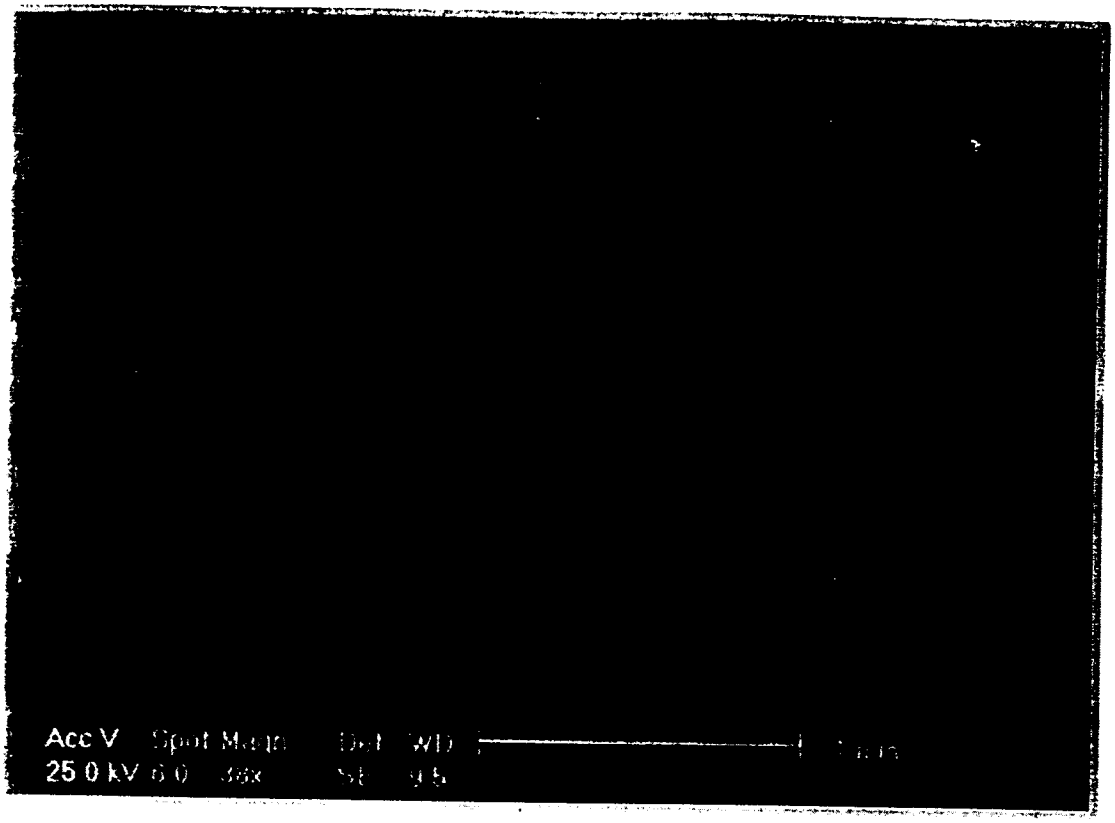

Figure 6.10 An example of a deposited black substance viewed under the Scanning Electron Microscopy.

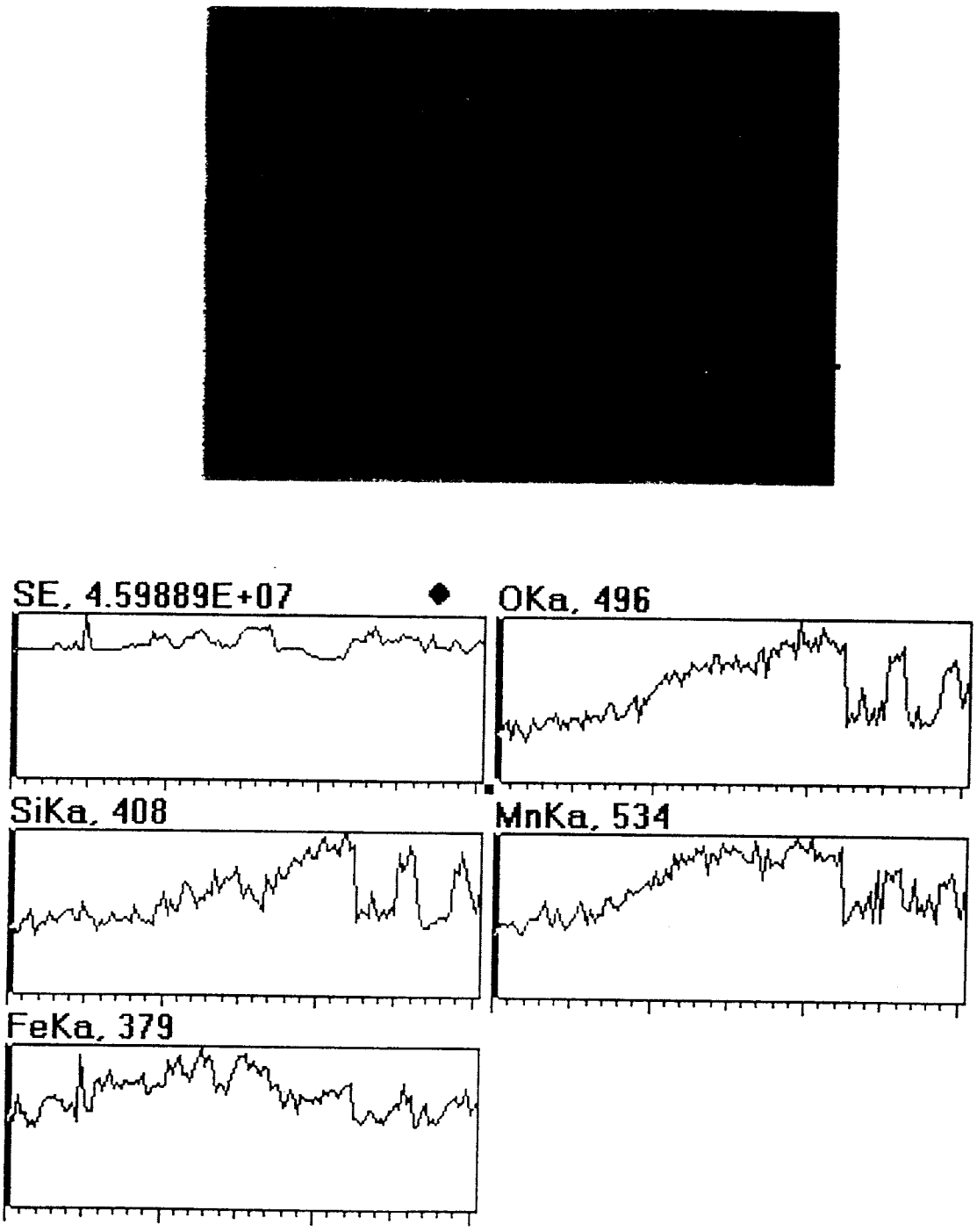

Figure 6.11 Results from EDX line scan.

A close up view of the film was also captured by Scanning Electron Microscope. Figures 6.12 and 6.13 show the picture of the surface of the copper mold with and without the deposited film. It clearly shows that the surface of the copper mold was completely changed after film was deposited.

Figure 6.12 Close up look of clean mold surface.

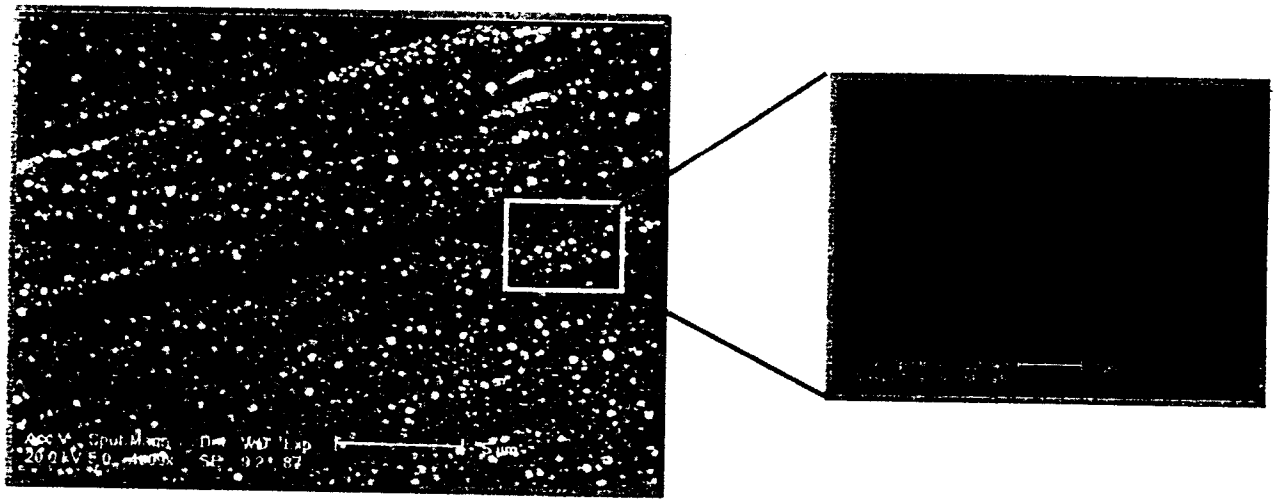

Figure 6.13 Close up look of a mold surface face with oxide film.

Chemical analysis, Figure 6.14 and Table 6.3, was conducted at the surface of the oxide film deposited on the clean substrate surface, produced during first experiment. The result agrees well with the result from EDX line scan. The black substance produced at the substrate surface by Mn-Si killed steel is mainly consisted of Manganese, Silicon and Oxygen.

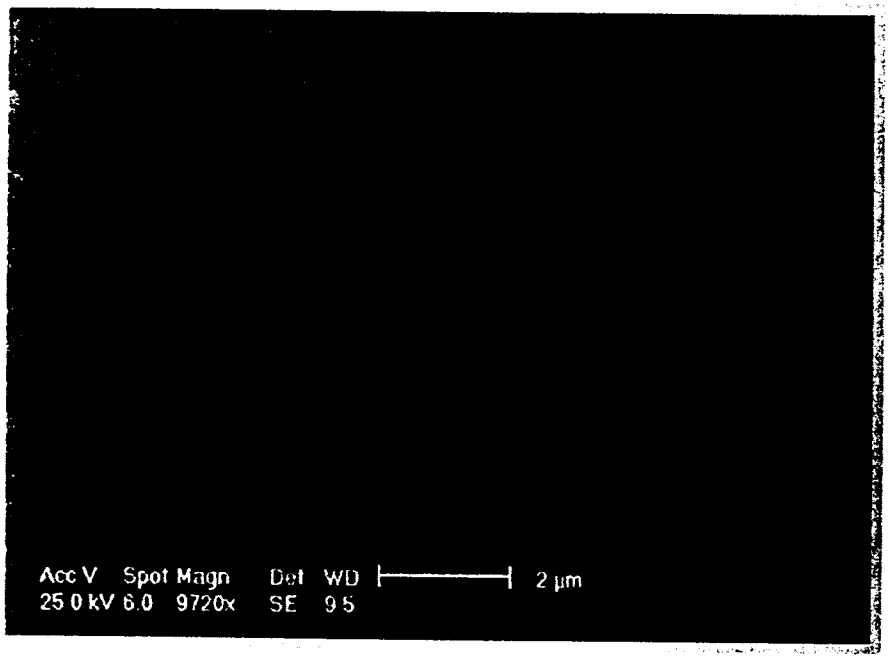

Figure 6.14 Close up look of a mold surface face with oxide film at magnification 9720X.

Element	Spect. Type	%Element	%Atomic
O K	ED	45.59	70.32
Si K	ED	12.33	10.83
Mn K	ED	35.19	15.81
Fe K	ED	6.89	3.05
Total		100.00	100.00

Table 6.3 The chemical analysis of the deposited oxide film.

6.4.2 The Study of the Solidified Specimen Under the SEM/EDX

Since the oxide film found on the surface of the copper mold can change the interface conditions between liquid the steel droplet and the copper substrate, the cast specimen was also collected and investigated along its mold contact area. Figure 6.15 shows the surface of the cast specimen, solidified on the clean surface substrate, viewed under the optical microscopy and Figure 6.16 shows of the cast specimen solidified on the substrate with deposited oxide film on its surface. To be able to see more details of the cast specimen surface, SEM/EDX was employed. Figure 6.17and 6.18 show the result from the SEM. Many spherical particles were found on the surface of the cast specimen. The sizes of the particles vary from less than one micron to larger than 5 micron. By using speed map and area scan in EDX, the results clearly shown that the spherical particles that we found on the surface of the solidified droplet, Figure 6.19 - Figure 6.21, are mainly composed of Mn, O and Si and indicated that they could be the natural liquid inclusion found in a Mn-Si killed steel, $MnSiO_3$, that came from the metal droplet.

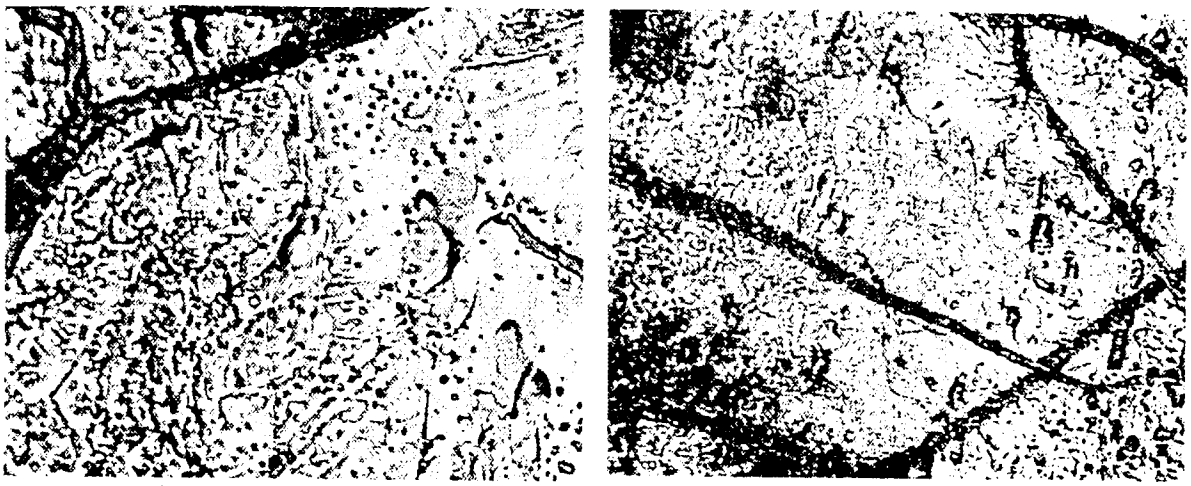

Figure 6.15 The pictures, viewed under optical microscope at magnification (500 X), show the surface of the cast specimen solidified on the a clean copper substrate.

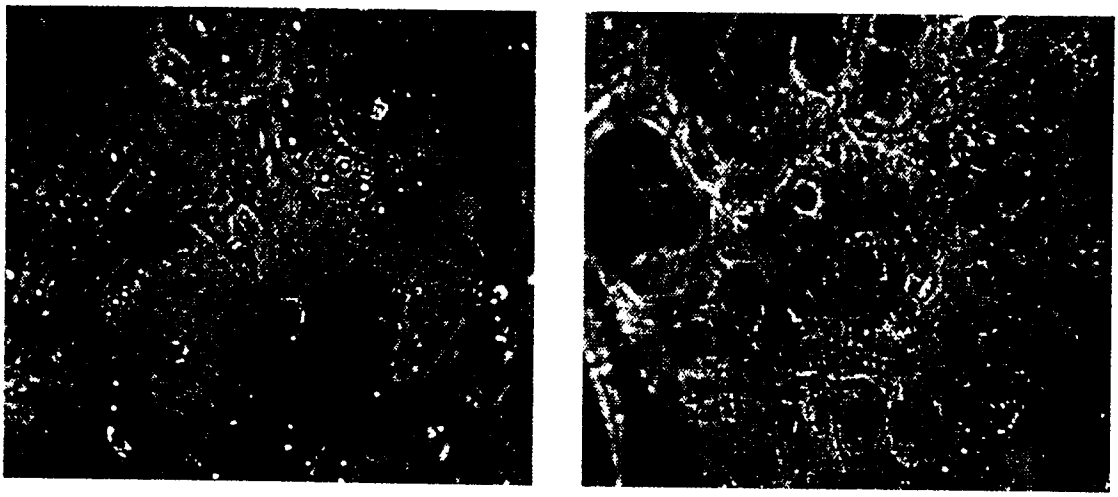

Figure 6.16 The pictures, viewed under optical microscope at magnification (500 X), show the surface of the cast specimen solidified on the substrate with a deposited oxide film on the surface.

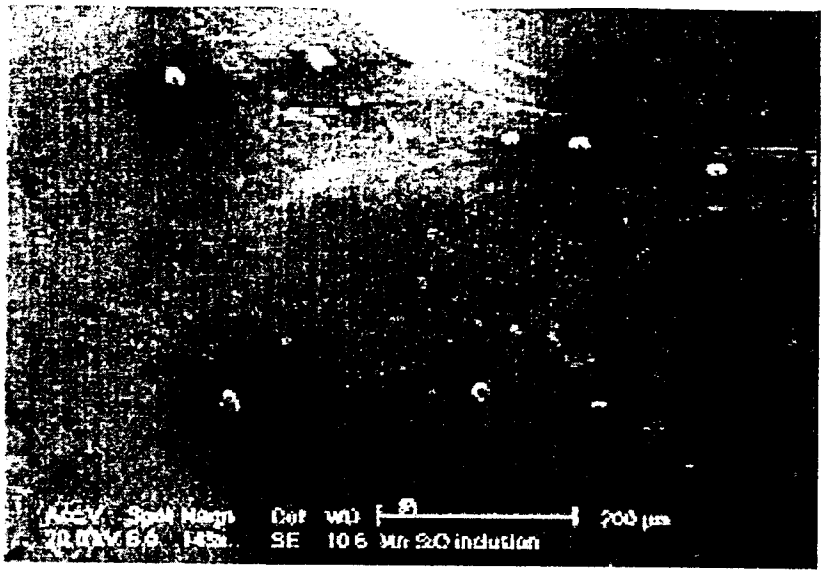

Figure 6.17 The surface of the solidified specimen viewed under SEM 148X.

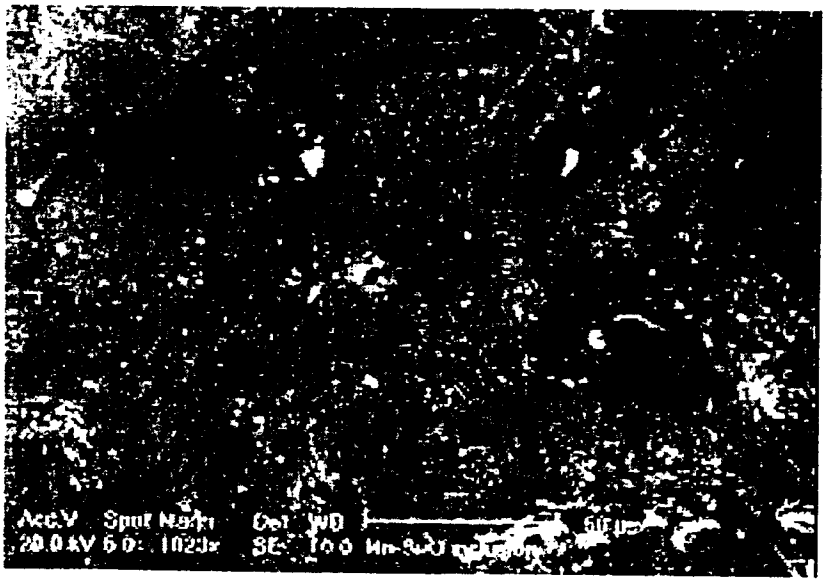

Figure 6.18 A picture viewed under SEM at magnification 1023X shown a closed up look of the surface of a cast specimen solidified on the substrate with a deposited oxide film.

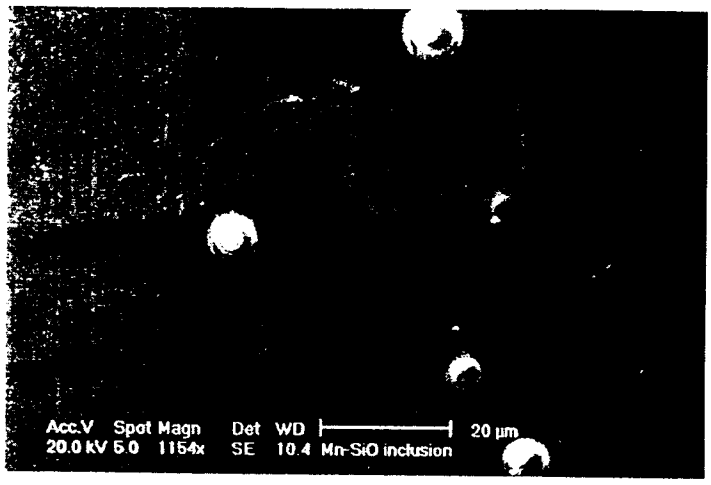

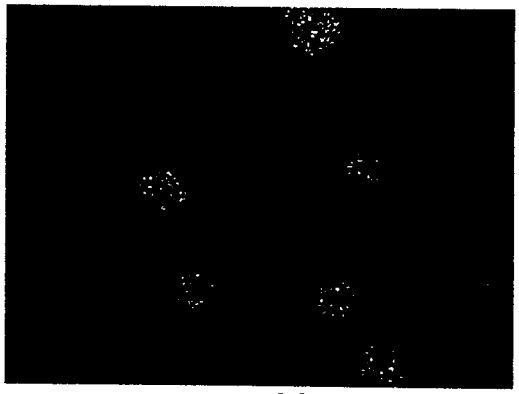

Mn

Si

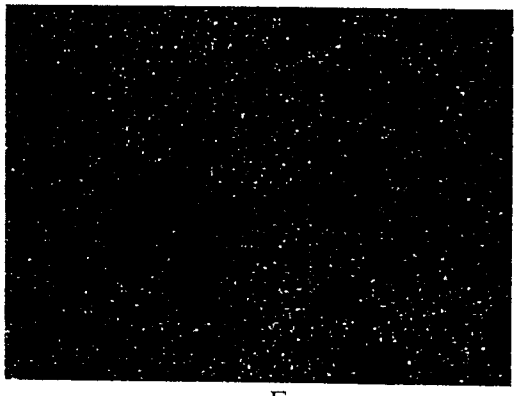

Fe

O

Figure 6.19 The result of the speed map.

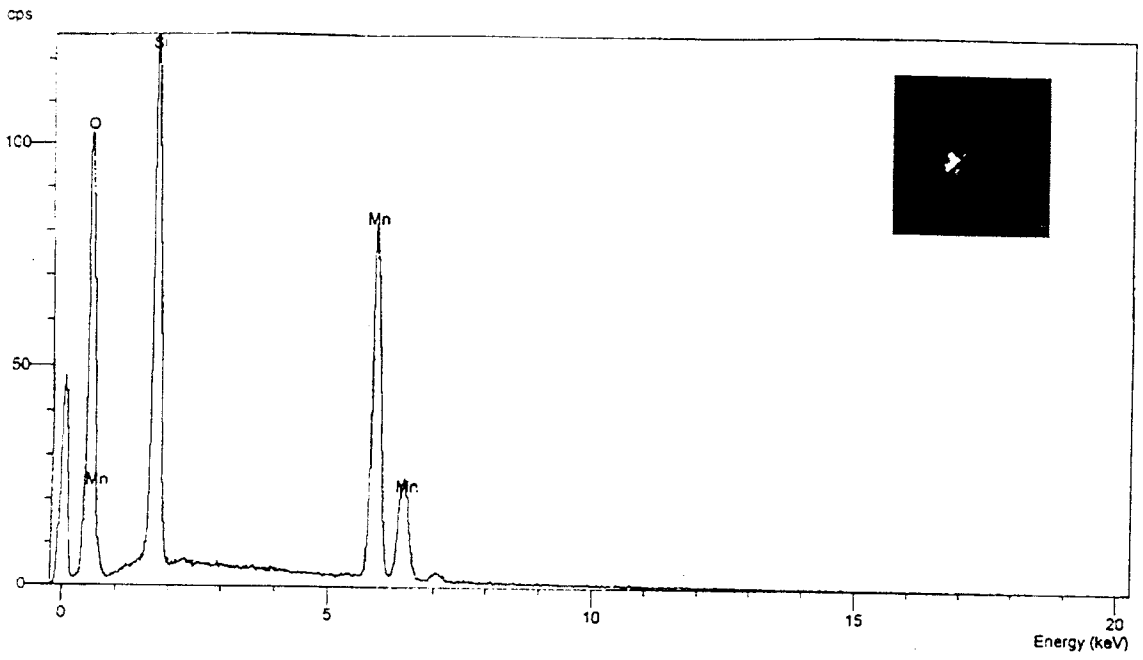

Figure 6.20 The chemical analysis, by EDX, of the rounded shape inclusion found at the surface of the solidified specimen.

Elmt	Spect. Type	Element %	Atomic %
O K	ED	50.98	60.74
Al K	ED	-0.48*	-0.34*
Si K	ED	21.27	14.44
Mn K	ED	39.94	13.86
Fe K	ED	33.13	11.31
Total		144.84	100.00

* = <2 Sigma

Figure 6.21 A chemical analysis of the sphere inclusion found at the surface of the cast specimen.

6.4.3 Inclusion Analysis

With a high percentage of Mn and Si in the steel inclusions can be formed during the melting and solidification process. In order to see an inclusion, a solidified specimen was cut, polished and coated with gold then analyzed by using SEM/EDX.

Round shape inclusions were found inside the droplet suggested that they were liquid inclusions before in the molten steel, Figure 6.22. By using EDX to analyze the chemical composition of the inclusions, Figure 6.23, it was found that the inclusions are mainly consist of manganese, silicon and oxygen and indicated that they are $MnSiO_3$ which is the natural inclusion of the Mn-Si killed steel. This result agrees well with what we found earlier at the cast specimen surface. The results suggested that there might be some interactions between natural inclusions of the steel and the substrate during the initial solidification process.

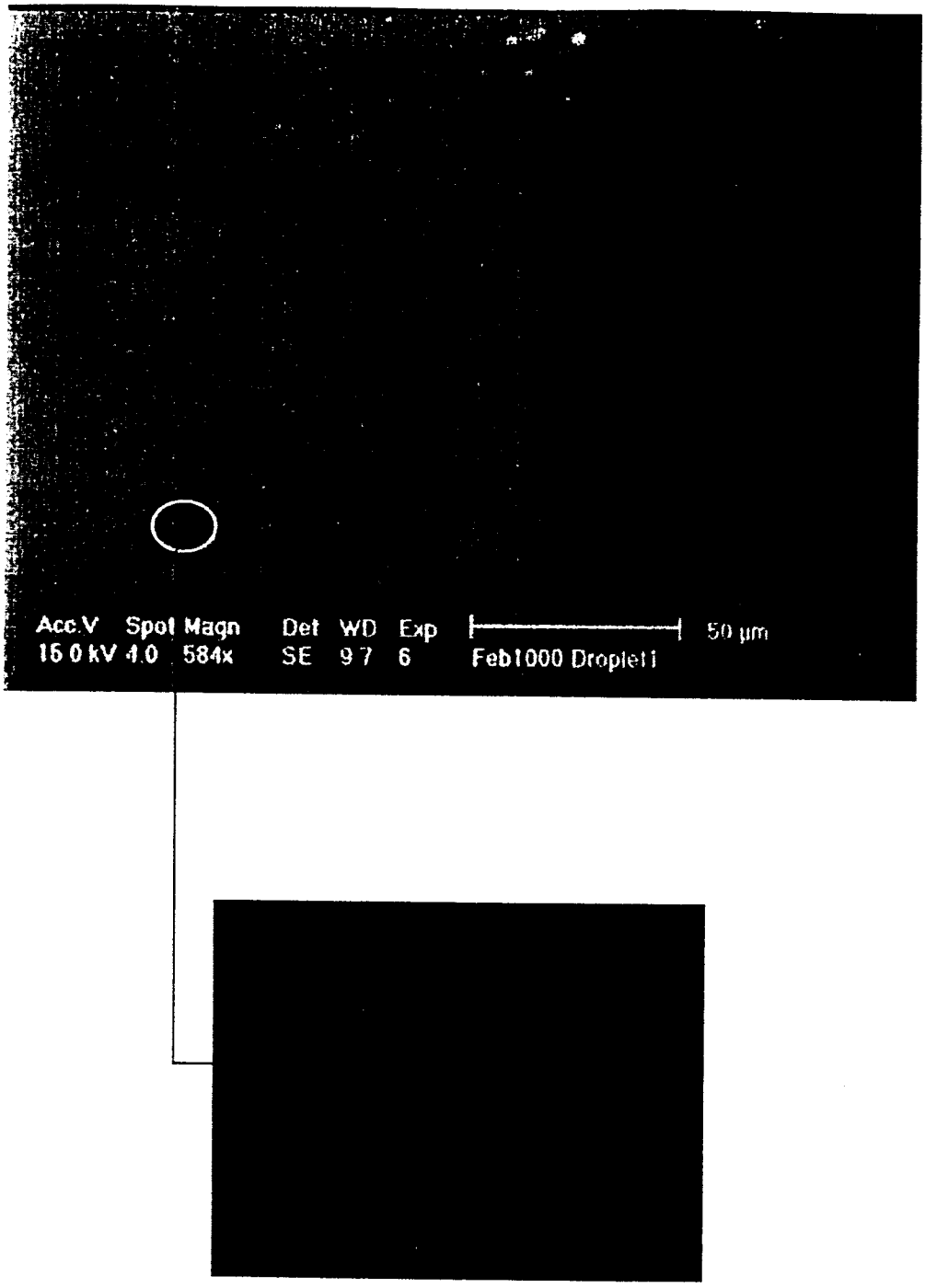

Figure 6.22 A close-up of the inclusion.

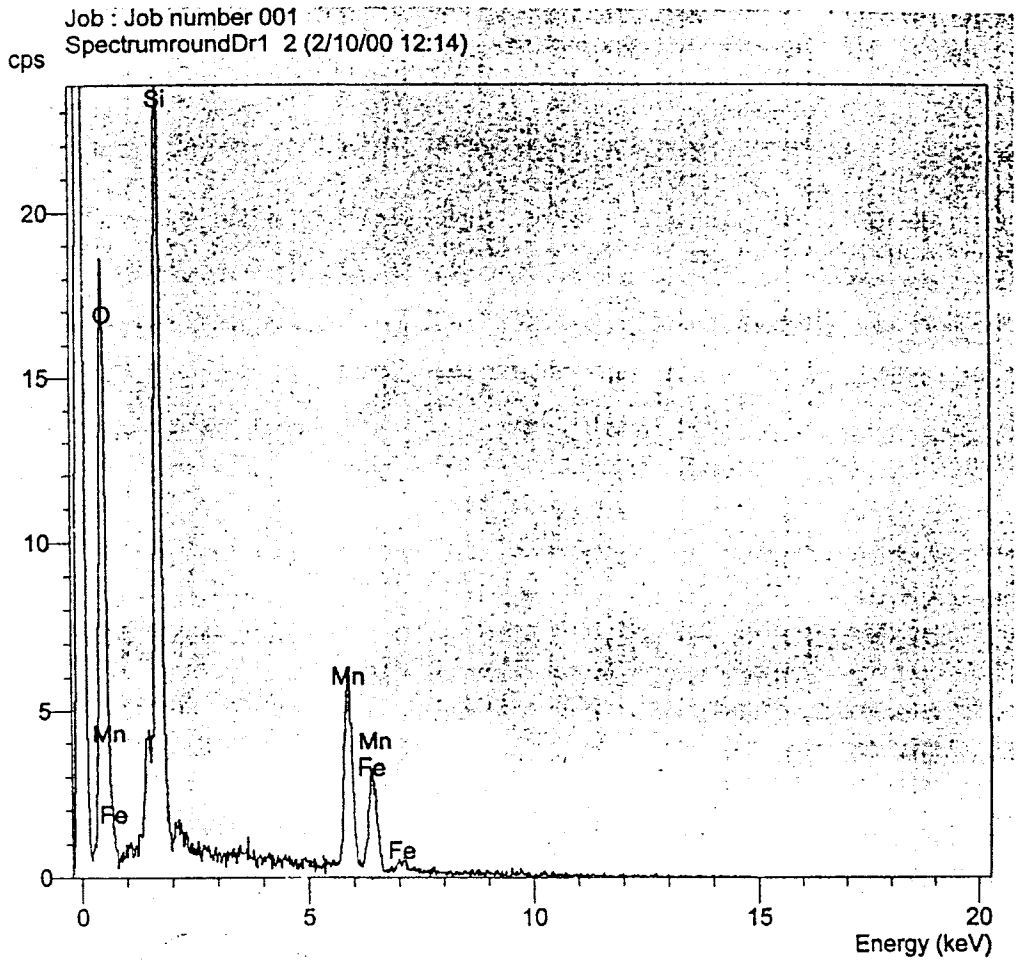

Figure 6.23 The chemical analysis of the rounded shape inclusions found inside the solidified specimen.

6.4.4 The Study of the Deposited Film Under DTA

Differential Thermal Analysis (DTA) is another technique that was employed in this study to analyze the deposited oxide film collected from the surface of the copper substrate. This technique is particularly useful to analyze materials that react or decompose at higher temperatures. The difference in temperature between the sample and an inert reference material, in this case we used pure alumina, is monitored as both are heated in a furnace. Phase transitions and chemical reactions taking place in the sample on heating cause the temperature difference to become larger at temperatures that are characteristic of the sample. In this study the oxide film was collected from the surface of the mold directly after the experiments were completed. Figure 6.24 shows the curve from the experiment using the heating rate of 10°C / min, starting from 800 °C to 1600 °C. The phase transition of the oxide film occurred at temperature between 1270 -1300 °C and another one at 1540 °C which can be the melting point of iron. The phase diagram of MnO – SiO_2 system, Figure 6.25 and 6.26, shows the eutectic point of the MnO-SiO_2 system is at 1251 °C. and the liquidous temperature of both two phase regions ($MnSiO_3$ + Liquid) and (Mn_2SiO_4 + Liquid) vary from 1251 °C -1291 °C, and possibly up 1420 °C if the phase changed to tridymite before it melted, and 1251°C - 1345 °C respectively. By matching both the results from the DTA and the information reading from MnO-SiO_2 phase diagram system it is suggested that the $MnSiO_3$ and Mn_2SiO_4 is the possible component of the deposited oxide film found between the solidified steel droplet and copper substrate.

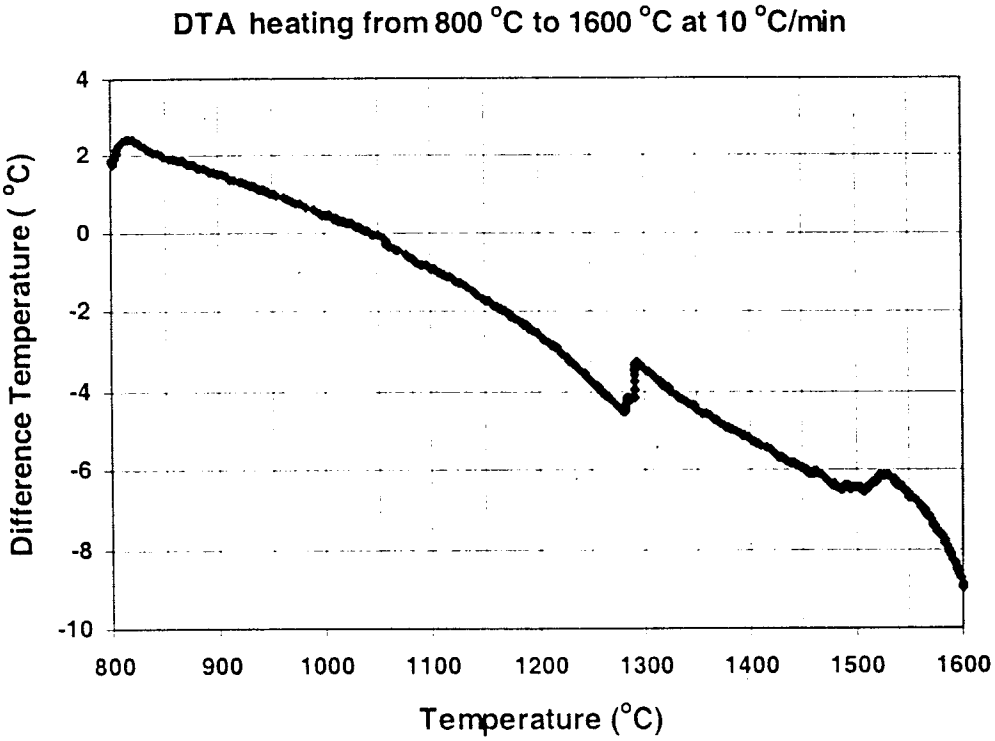

Figure 6.24 A result from DTA.

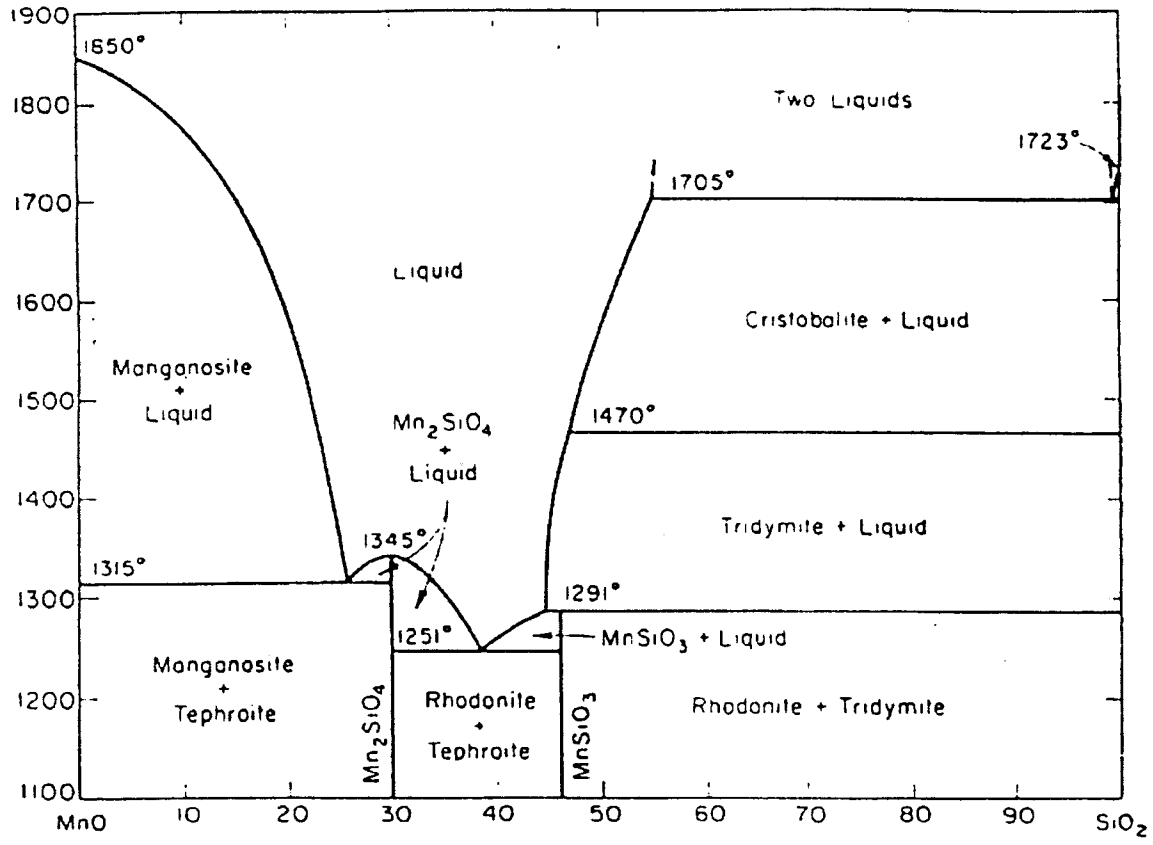

Figure 6.25 The phase diagram of $MnO\text{-}SiO_2$ system.

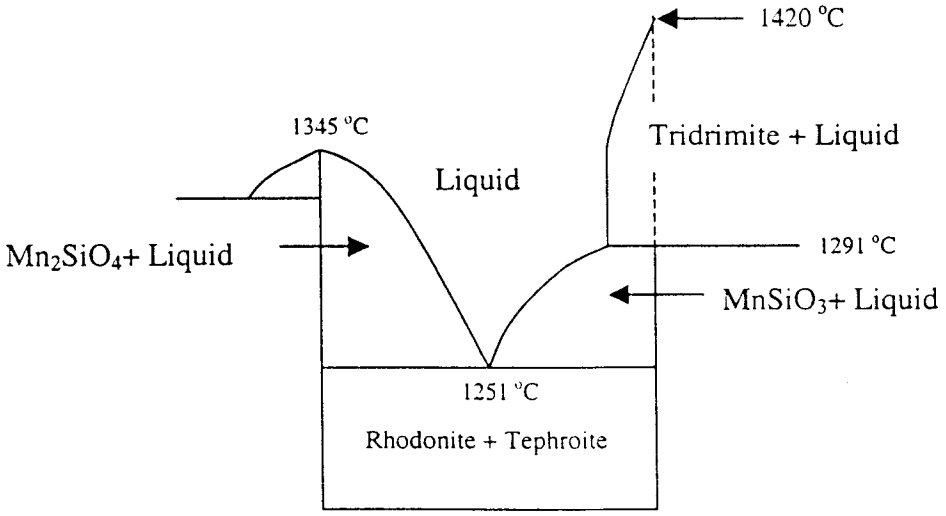

Figure 6.26 A schematic of eutectic region of $MnO\text{-}SiO_2$ system.

6.4.5 Melting Behavior of the Deposited Oxide Film

6.4.5.1 Calculation of the Oxide Surface Temperature

Interfacial thermal resistance plays an important role on the heat flow between the molten steel droplet and the substrate. Due to radiation and convection across the gap, an interfacial air gap can reduce the heat flux at a interface by more than 98% of the total heat flux [1]. The interfacial air gap, however, will be reduced when the substrate surface has oxide film deposition. The experimental results show that the heat flux was significantly improved when the oxide film was built up at the interface. One of the possible reasons is that the effectiveness of the melt/substrate contact was improved due to the presence of the liquid film at the droplet interface. To determine if it is possible to develop a liquid film at the interface, a one dimensional transient heat transfer model was use to calculate the oxide surface temperature profile. By using a numerical approach to solve this transient conduction problem, a fictitious node is placed at the center of each section. An energy balance performed on each node results in algebraic equation for the temperature of each node in terms of neighboring nodal temperatures, geometry, and thermal properties of the material. A verbal expression of the conservation of energy for node 0 surrounded by node 1 and 2 without internal energy generation is

$$\sum_{i=1}^{2} q_{i\to 0} = \text{Time rate of change in internal energy of node 0}$$

$$q_{1\to 0} + q_{2\to 0} = \frac{\partial U_0}{\partial t}$$

Where U_0 is the internal energy of node 0

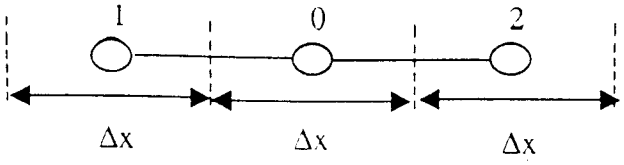

By using finite difference form of the of the Fourier law, the equation above can be approximate as:

$$q_{1\to 0} \cong KA\frac{T_1^t - T_0^t}{\Delta x}$$

$$q_{2\to 0} \cong KA\frac{T_2^t - T_0^t}{\Delta x}$$

The subscripts refer to the location of the nodes and the superscripts specify time or t variation in the temperatures. By assuming constant density and specific heat for material the energy-balance equation for node 0:

$$KA\frac{T_1^t - T_0^t}{\Delta x} + KA\frac{T_2^t - T_0^t}{\Delta x} = \rho A\Delta x c\frac{T_0^{t+\Delta t} - T_0^t}{\Delta t}$$

Solving for $T_0^{t+\Delta t}$ gives

$$T_0^{t+\Delta t} = (F_o)(T_1^t + T_2^t) + [1 - 2(F_0)]T_0^t$$

Where the Fourier number is defined as

$$F_0 = \frac{\alpha(\Delta t)}{(\Delta x)^2}$$

The future temperature at time t+Δt at an arbitrary interior node 0 can be evaluated by knowing the current temperatures at time t at the node 0and its neighboring nodes.

Our system is consisted of three material a copper, film and liquid steel. Each material is separated in tiny section, Δx, and a fictitious node is placed at the center of each section, Figure 6.27.

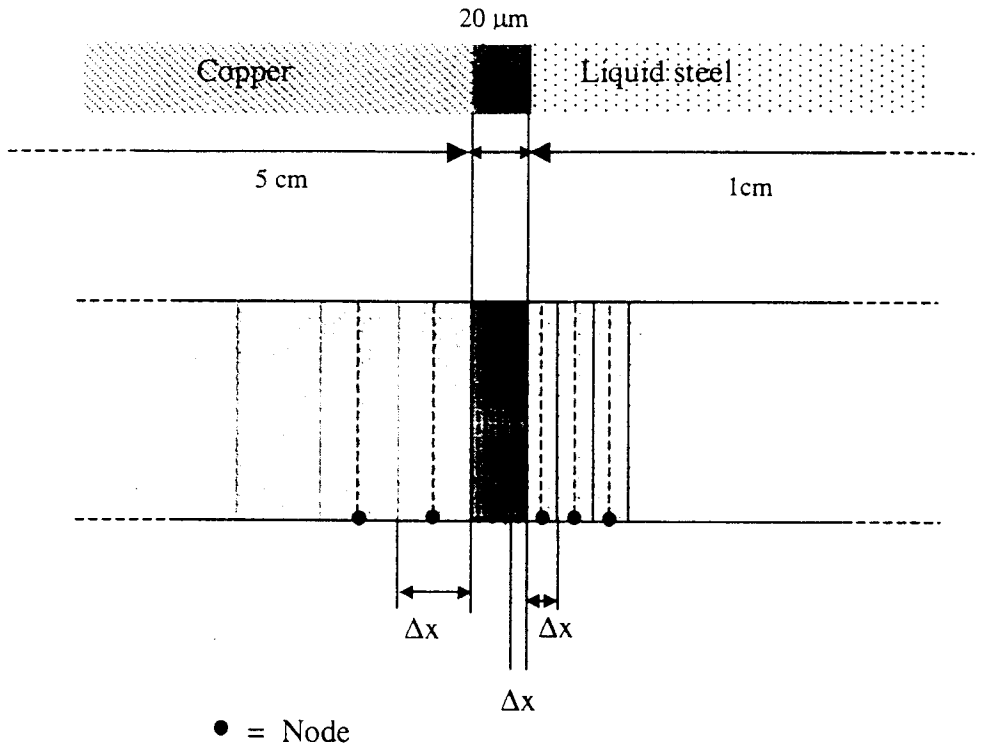

Figure 6.27 The schematic of the fictitious nodes in each area.

The dimension and the boundary condition of the model were set based on the real experimental set up. The temperature at both end of the copper substrate and the liquid steel was used as a boundary condition. At the end of the copper substrate the temperature is constantly set at 25 °C which is the same as the cooling water temperature running inside the copper mold. At the end of the liquid steel the temperature was set at 1600°C constantly. This boundary condition is considered reasonable when the temperature profile is calculated during the first 0.5 to 0.7 seconds which is still in an ejection process of liquid steel, as revealed by the movie captured during the experiment. The element size Δx of copper, oxide film and liquid steel is 1mm, 5μm and 0.5mm respectively. Due to a very small element size was set in the oxide film region the time

interval is set equally, at 0.01 milliseconds, across the entire regions. The temperature of the film and mold at time = 0 equals 25°C and for the liquid steel, at time = 0 the temperature equals = 1600°C. The Fourier number was set differently in each region including when the liquid steel solidified. The computer program written in C++ language was used to calculate the temperature in each nodal position, at 0.01ms time steps. The number of the nodes copper, oxide film and liquid steel is equal 50, 4 and 20 respectively. Figure 6.28 shows the temperature profile in the oxide film, copper and steel region from time equal 0-1 second and Figure 6.29 shows the temperature profile during the time equals 0-20 milliseconds.

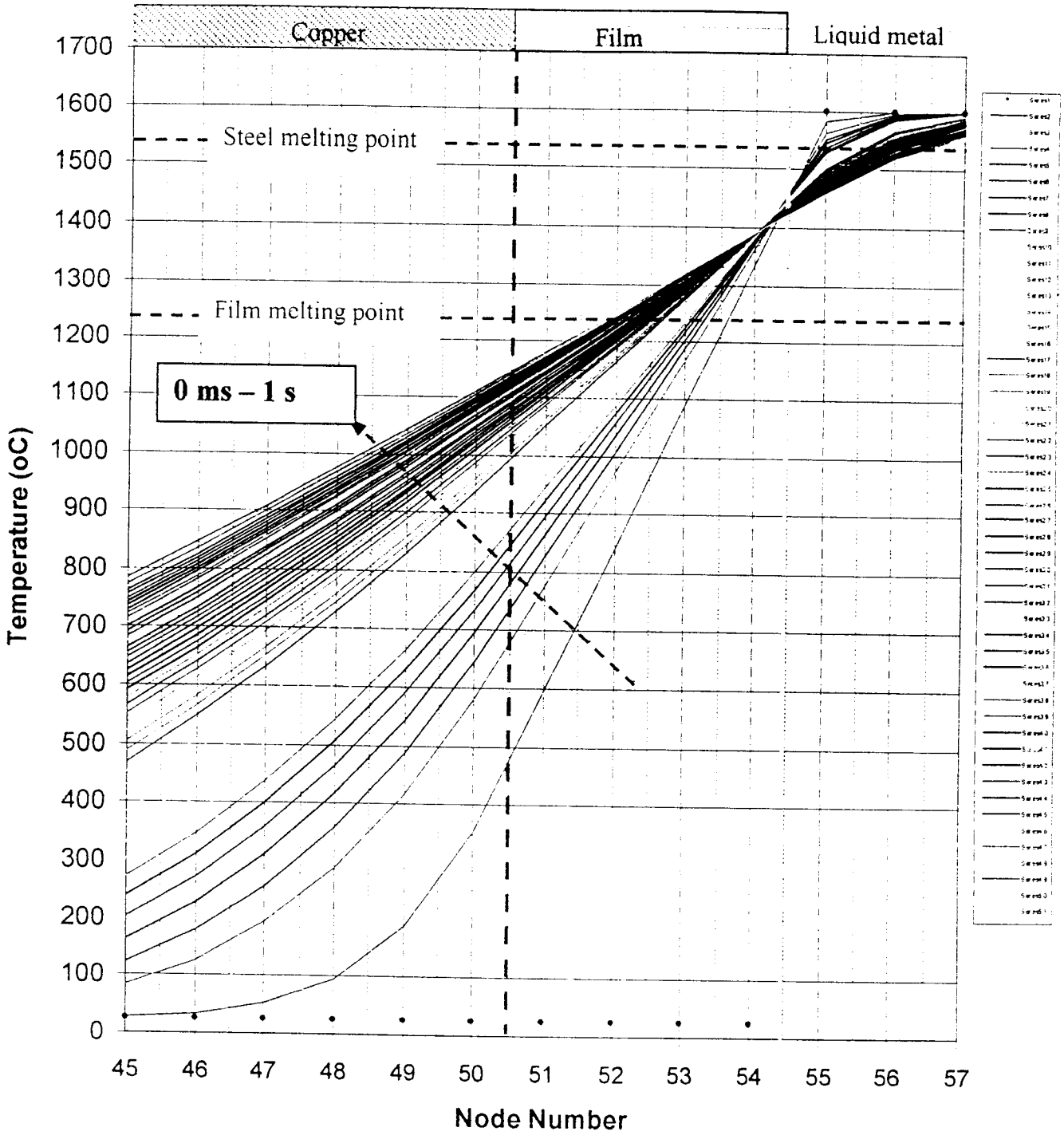

Figure 6.28 The temperature profile at the metal - mold interface during the first second.

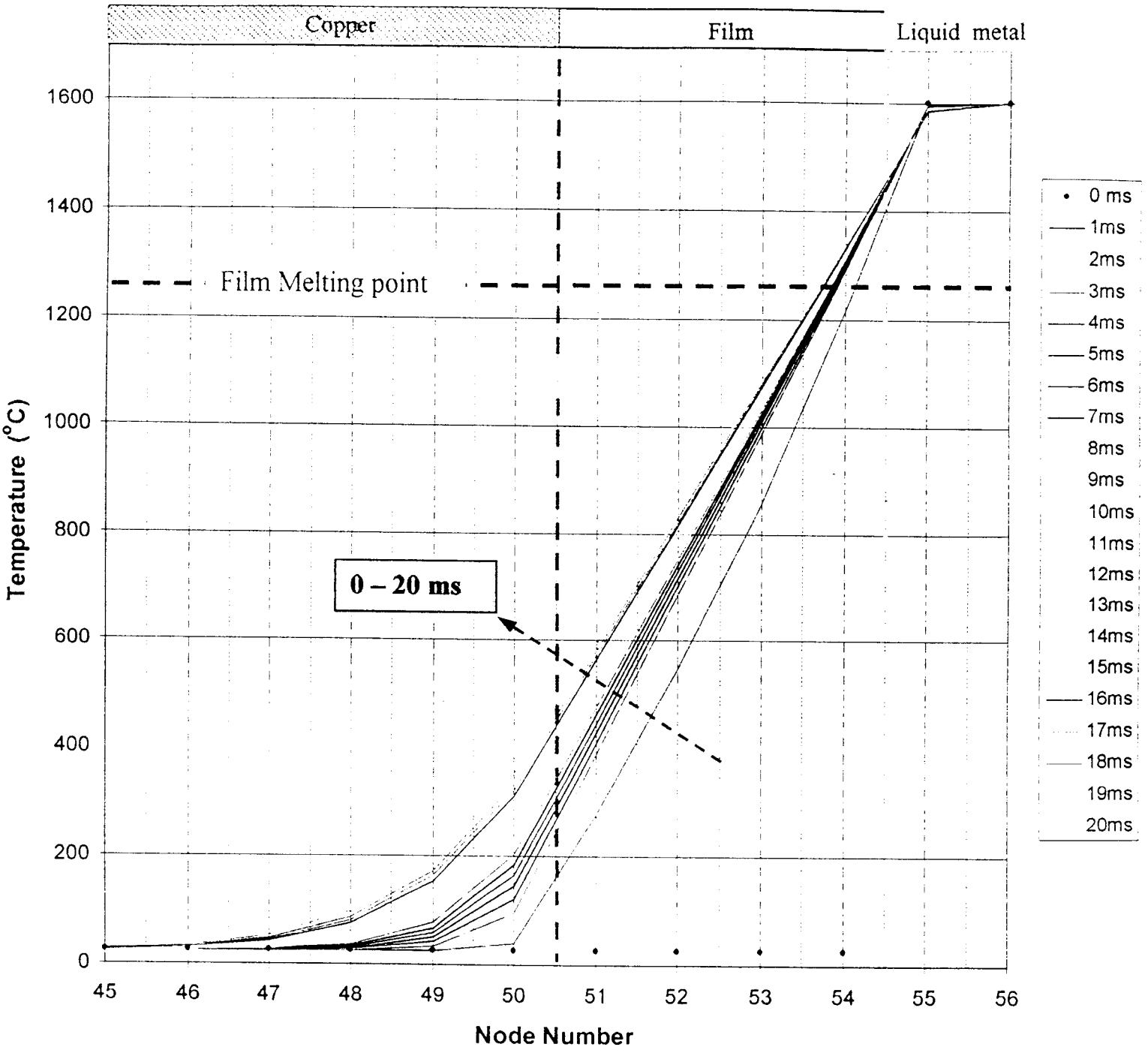

Figure 6.29 The temperature profile at the metal – mold interface during the first 20 ms.

Figure 6.28. shows a temperature profile during the first second, plotted every 20ms. Using the melting point of the film from the DTA experiment and a thermal conductivity of the oxide film equal 0.25 W/mK [2] the temperature profile, Figure 6.28 and 6.29, indicates that, at the interface between the film and the liquid steel, the melting of the oxide film would occur during contact with a steel droplet. The liquid film presence at the interface will improve the interfacial conditions resulting in the significant changes of interfacial heat transfer. These results agree well with the heat flux result shown earlier in Figure 6.2. Therefore the hypothesis of the presence of the liquid film at the interface is proved to be possible.

6.4.5.2 The Study of the Melting Behavior of the Deposited Film Under CSLM

Confocal Scanning Laser Microscopy (CSLM) combines the advantages of confocal optics and a He-Ne laser, thereby making it possible to observe samples at high resolution at elevated temperatures. In this study real-time investigation of the melting behavior of oxide film on Fe surface were carried out under CSLM by observing the melt surface of the Fe covered by the oxide film under argon atmosphere. The oxide film used in this experiment was collected directly from the surface of the copper substrate after the heat flux measurement was done. Figure 6.30 shows the schematic of the specimen before placed inside the CSLM. A small hole was drilled on the surface of the Fe plate and it was filled up by the oxide film. The specimen was heated to temperature until the oxide film melted. The melting behavior of the film was recorded during the experiment. Figure 6.31 shows the specimen before the film melted and after the film was melted. It

can be seen that oxide film has ability to wet on the surface of the Fe plate since it did not form a droplet on the surface of the specimen.

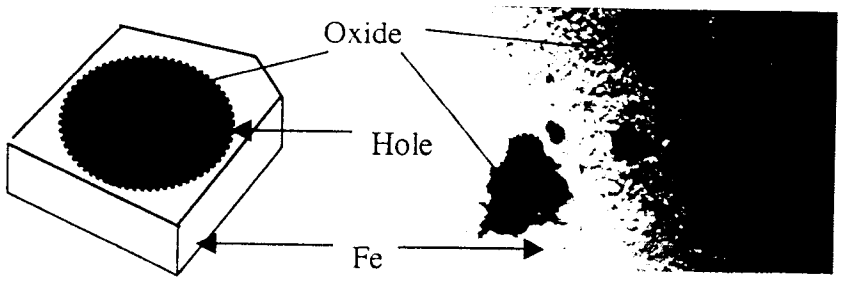

Figure 6.30 Top view of the specimen .

Figure 6.31 The melting behavior of oxide observed under CSLM at temperature 1250 °C – 1350 °C.

To ensure that the film was melted during the initial metal-mold contact time the oxide film deposited on the surface of substrate after the last experiment was completed the deposited oxide was observed under SEM-EDX. Figure 6.32 and Figure 6.33, taken under SEM, show the evidences that the oxide film was liquid during metal-mold contact time. Figure 6.34 shows the oxide film deposited after the first and the last experiment was completed. The chemical analysis was conducted and the results agree well with all the previous results. The film consists of Mn, Si and O, Figure 6.35.

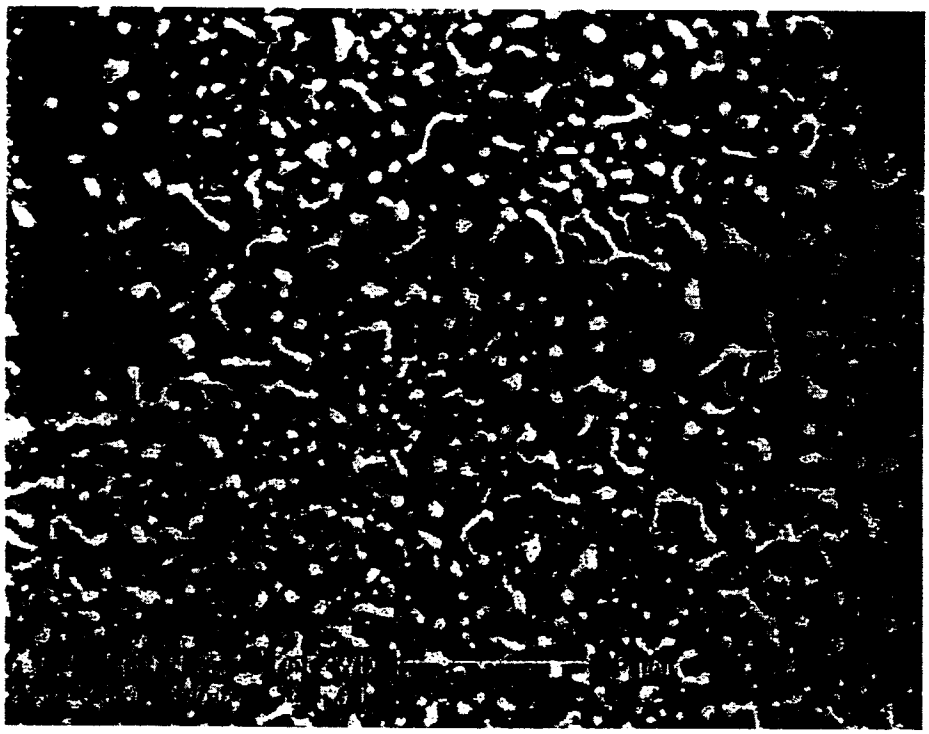

Figure 6.32 The deposited oxide film on the substrate surface taken after the last experiment was completed at magnification 4969X.

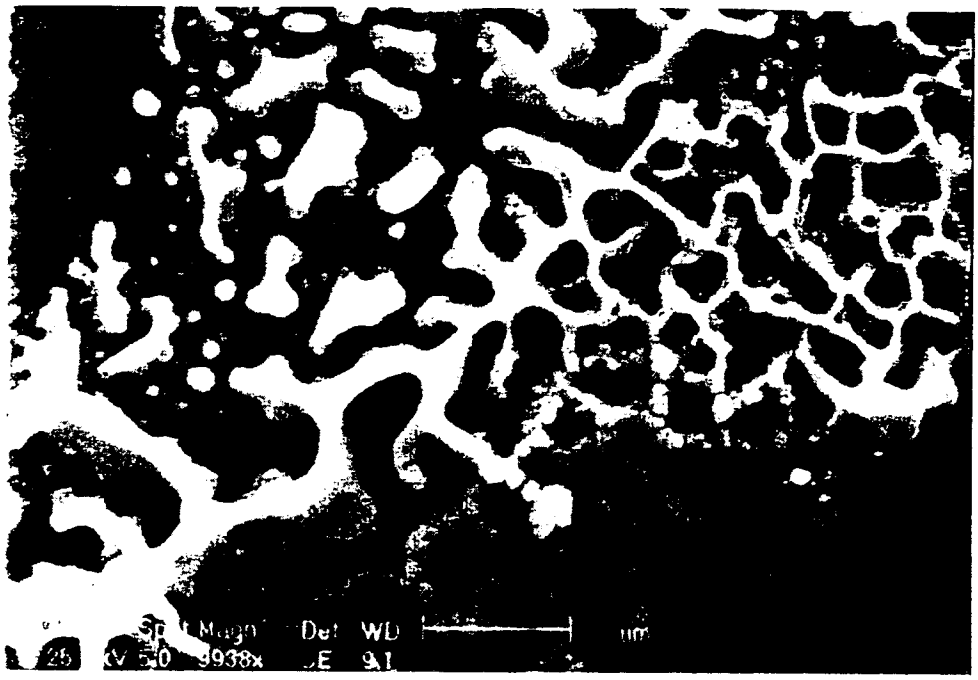

Figure 6.33 The close up look of the deposited oxide film on the substrate surface taken after the last experiment was completed at magnification 9938X.

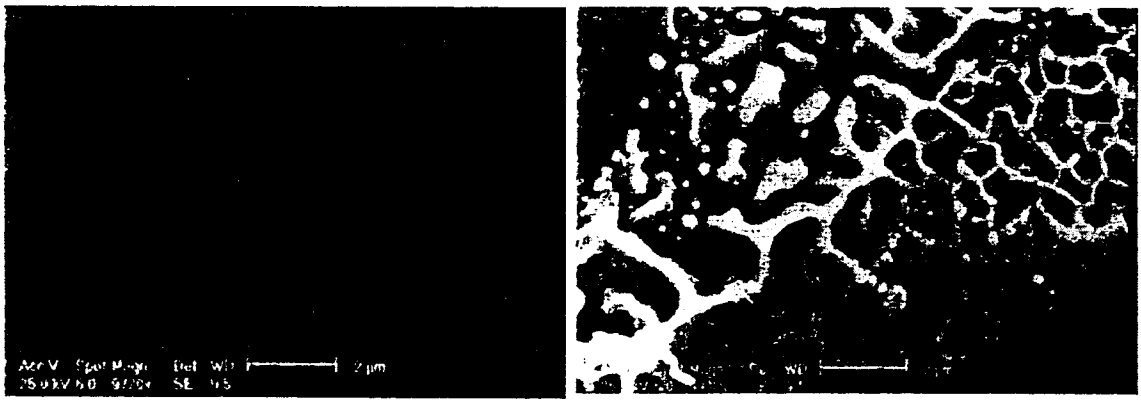

Figure 6.34 Comparison of the oxide film deposited on the substrate surface after the first and the last experiment was completed.

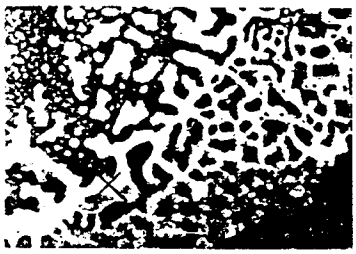

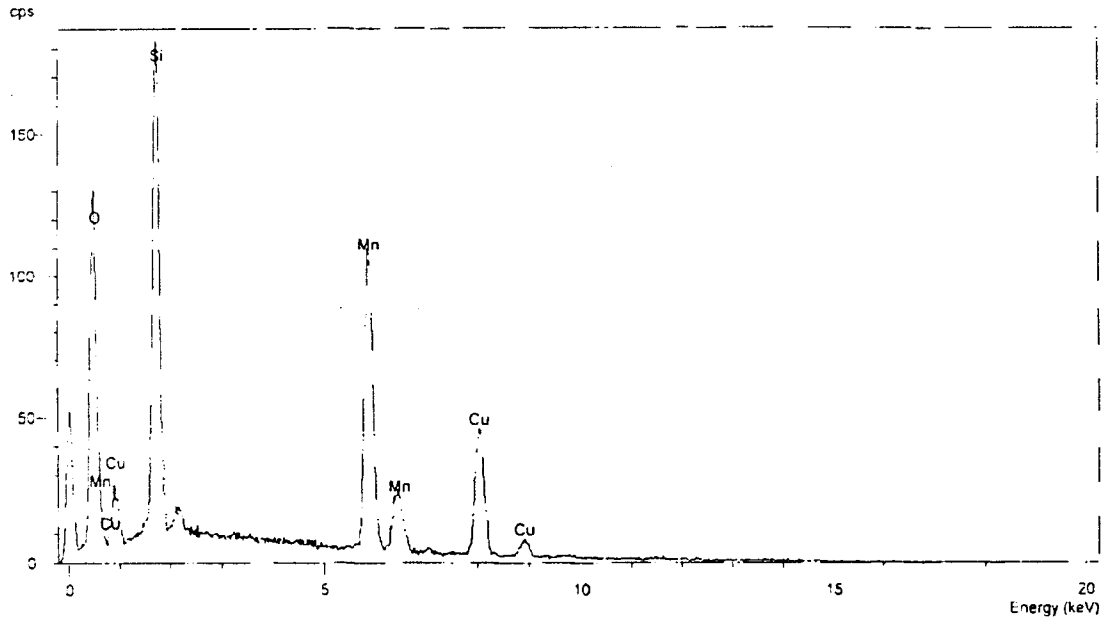

Elmt	Spect. Type	Element %	Atomic %
O K	ED	51.13	71.78
Si K	ED	21.13	16.90
Mn K	ED	24.98	10.21
Fe K	ED	2.75	1.11
Total		100.00	100.00

* = <2 Sigma

Figure 6.35 The chemical analysis of deposited oxide film.

6.5 Surface Roughness Measurement

To understand how the presence of the liquid film at the interface improved the interfacial contact between metal and mold measurement of the cast surface roughness was carried out. The roughness profile was measured through the impingement point area, a small circular area with a diameter 3.2 mm and the measurements were conducted 5 times in different directions.

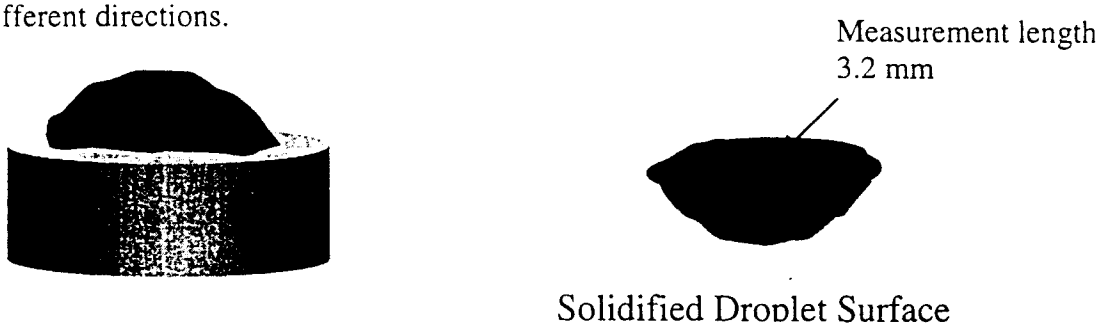

Figure 6.36 shows the schematic of the roughness profile. The maximum negative amplitude of the profile was defined as zero level.

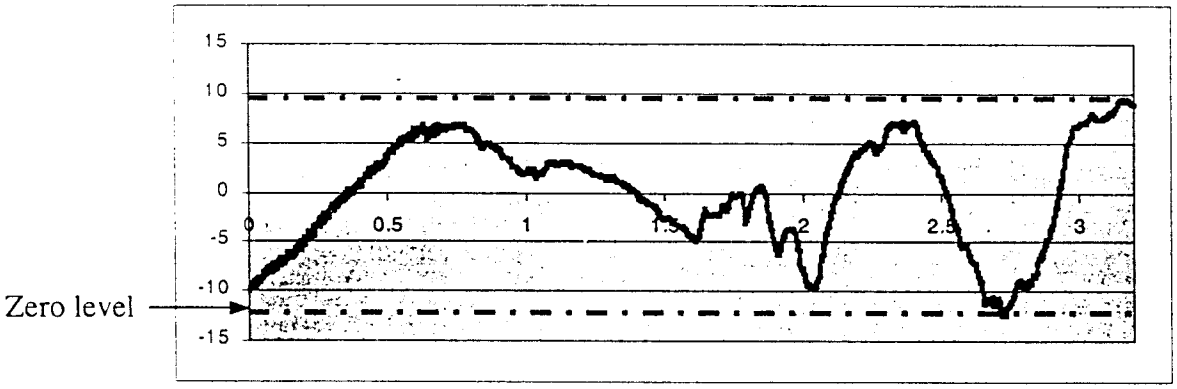

Figure 6.36 The example of the measured roughness profile.

The volume under the roughness profile is calculated by first multiply the small area under the roughness profile by the perimeter to obtain a small volume element with respect to each radius and then integrate each volume element along the radios direction to obtain the volume under the roughness profiles. The schematic of the calculation is shown below in Figure 6.37.

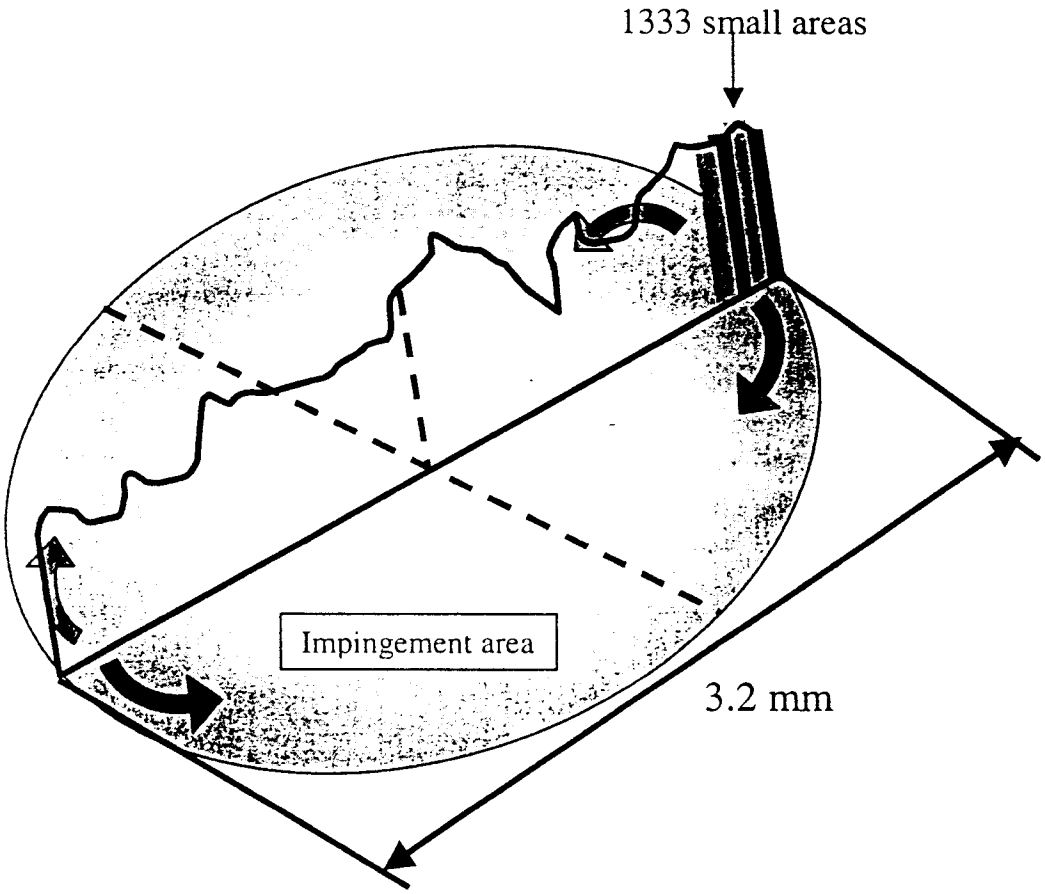

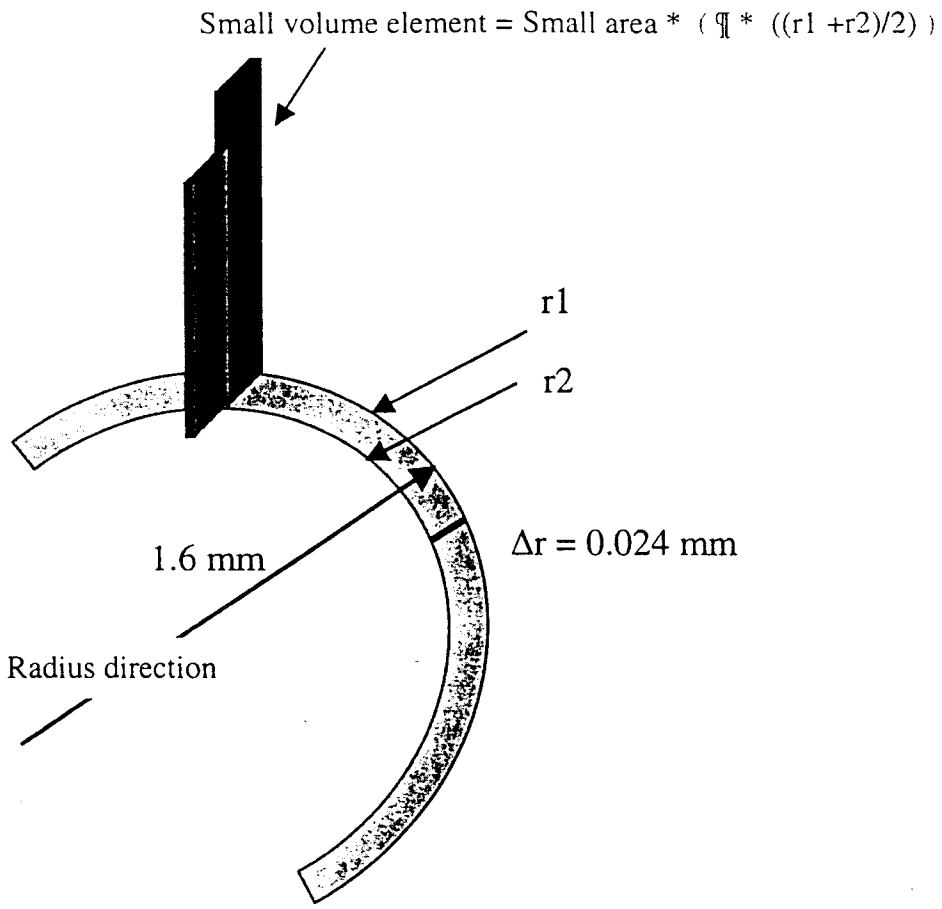

Figure 6.37 The schematic of the calculation of the volume under the roughness profile.

The cavities that need to be filled in order to make the profile perfectly flat was the difference between the volume under the roughness profile and the total volume which can be calculated by using h equal the maximum depth of the profile as shown in Figure 6.38.

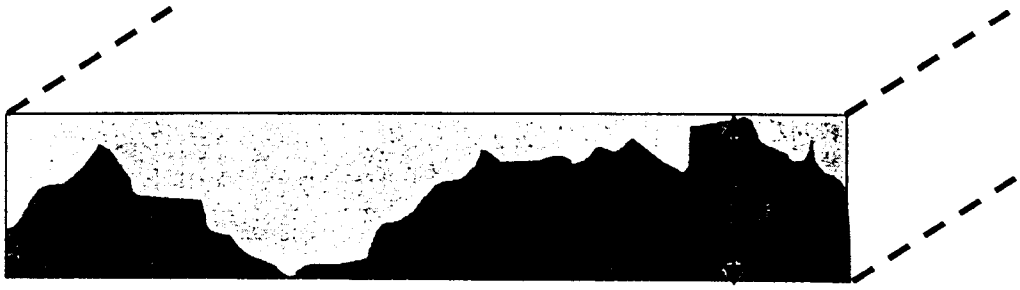

= Volume under the curve

= Cavity volume

+ = ¶ * $(1.6)^2$ * h

Where h = maximum profile depth or the Pt value

Figure 6.38 The schematic of the method to find the volume that needed to be filled.

By using the method mentioned above to calculate the volume of the cavities that must be filled, the average volume, measured and calculated 5 times, is equal 0.13 mm^2. With this volume the film deposited on the surface have to be thick at least 16 microns in order to fill all the cavities and flatten the surface roughness of the solidified specimen. The thickness of the film measured after the last experiment was complete is around 20 microns which is ideally enough to fill all the cavities up to 0.16 mm^2. The surface roughness of the cast surface specimen solidified on the substrate surface covered by film was also measured and the volume of the cavities that need to be filled was also calculated. It was found that the volumes of the solidification roughness are reduced from

0.13 mm^2 to 0.08 mm^2 when we saw the significant changes of the interfacial heat flux between the metal and substrate. This is indicated that the deposited oxide film can improve the contact between metal and mold during the solidification process by reducing the cavity or air pocket at the metal–mold interface. Figure 6.39 and 6.40 show the surface roughness profile of the cast specimen solidified on the clean substrate surface and the substrate that cover by oxide film.

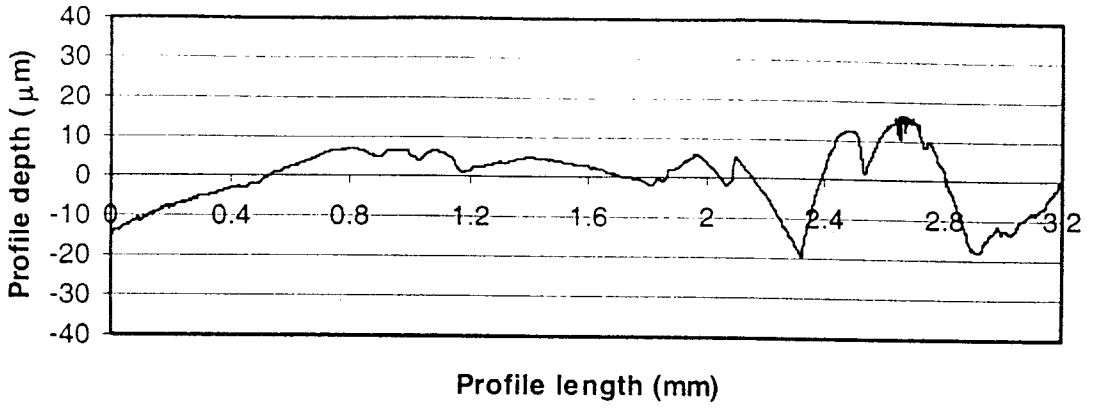
Profile depth (μm)
40
30
20
10
0
-10
-20
-30
-40
0
0.4
0.8
1.2
1.6
2
2.4
2.8
3.2
Profile length (mm)

(a)

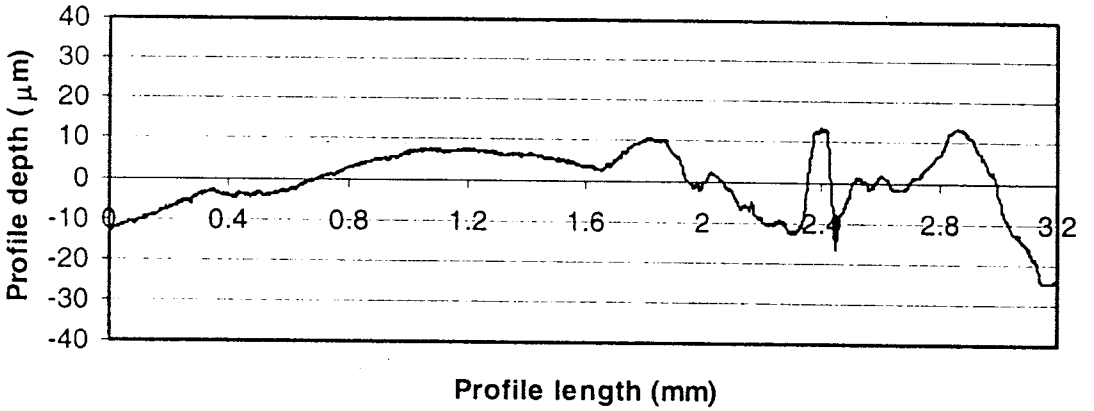
Profile depth (μm)
40
30
20
10
0
-10
-20
-30
-40
0
0.4
0.8
1.2
1.6
2
2.4
2.8
3.2
Profile length (mm)

(b)

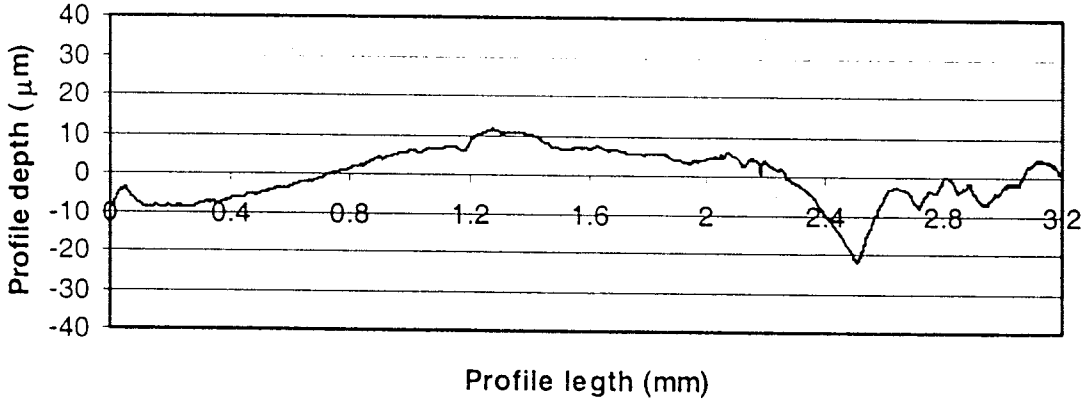
Profile depth (μm)
40
30
20
10
0
-10
-20
-30
-40
0
0.4
0.8
1.2
1.6
2
2.4
2.8
3.2
Profile legth (mm)

(c)

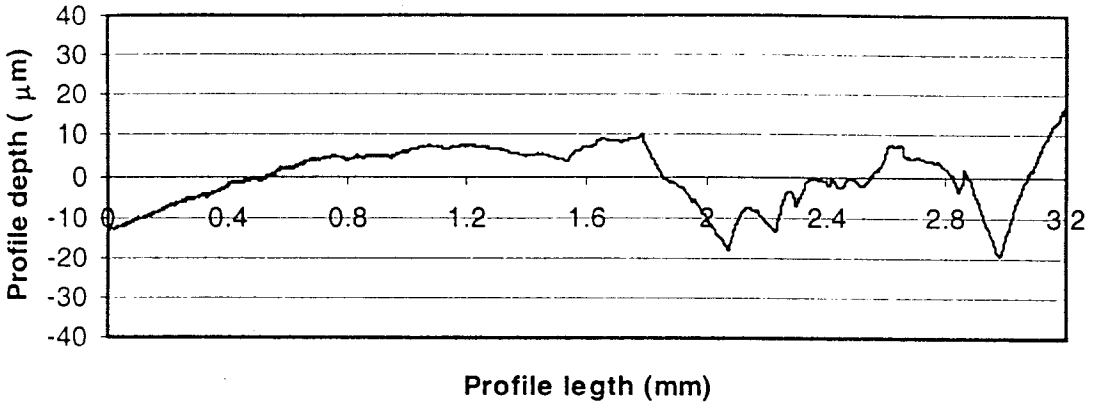

(d)

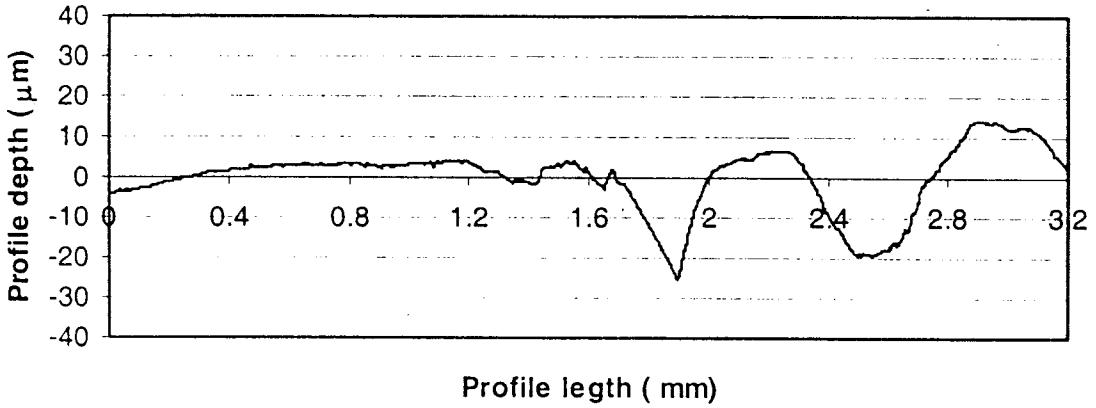

(e)

Figure 6.39(a)-(e) The surface roughness profile of the cast specimen solidified on the clean substrate surface.

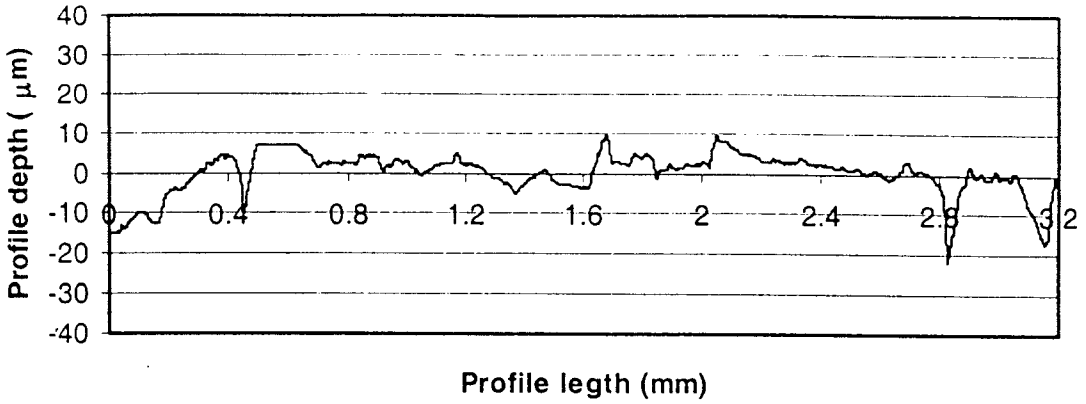
Profile depth (μm)
40
30
20
10
0
-10
-20
-30
-40
0
0.4
0.8
1.2
1.6
2
2.4
2.8
3.2
Profile legth (mm)

(a)

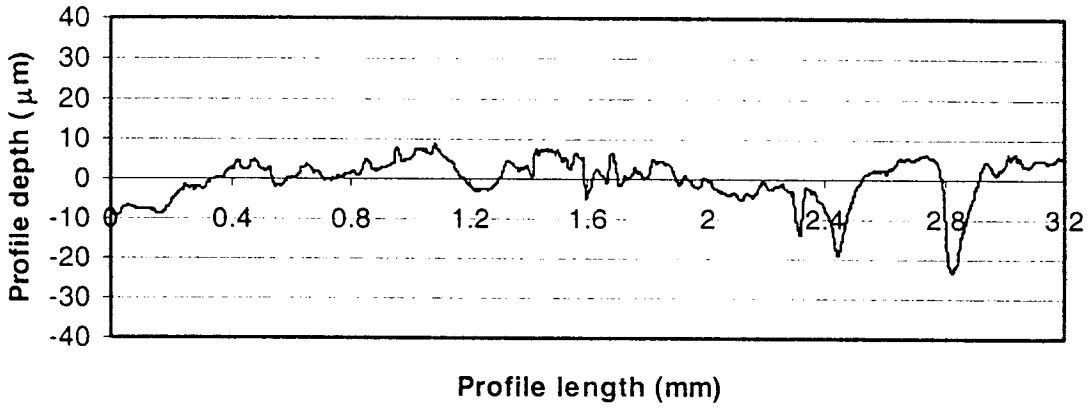
Profile depth (μm)
40
30
20
10
0
-10
-20
-30
-40
0
0.4
0.8
1.2
1.6
2
2.4
2.8
3.2
Profile length (mm)

(b)

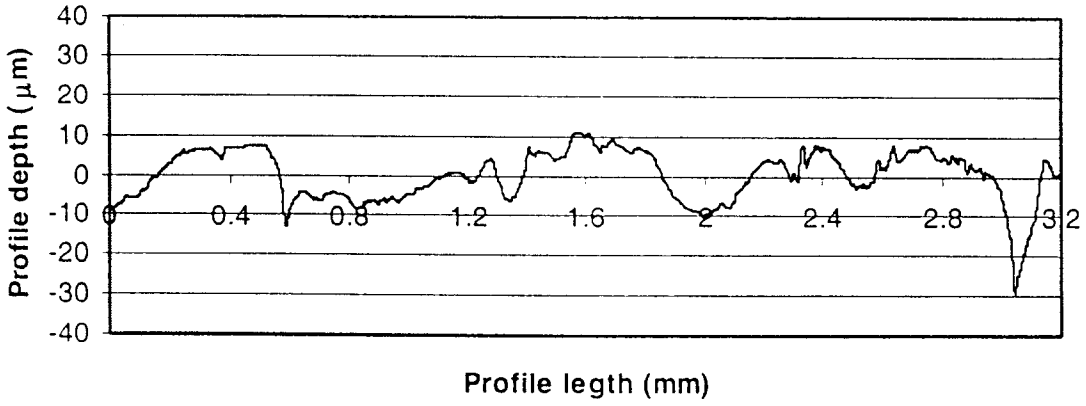
Profile depth (μm)
40
30
20
10
0
-10
-20
-30
-40
0
0.4
0.8
1.2
1.6
2
2.4
2.8
3.2
Profile legth (mm)

(c)

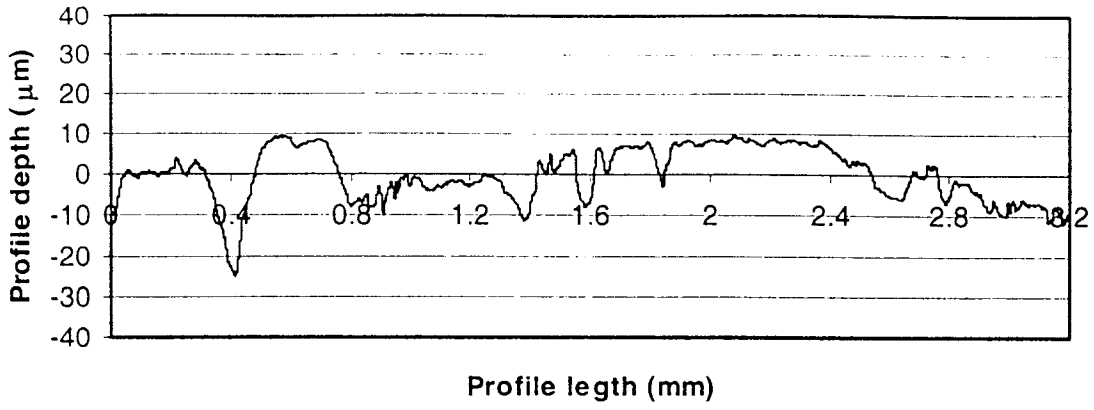

(d)

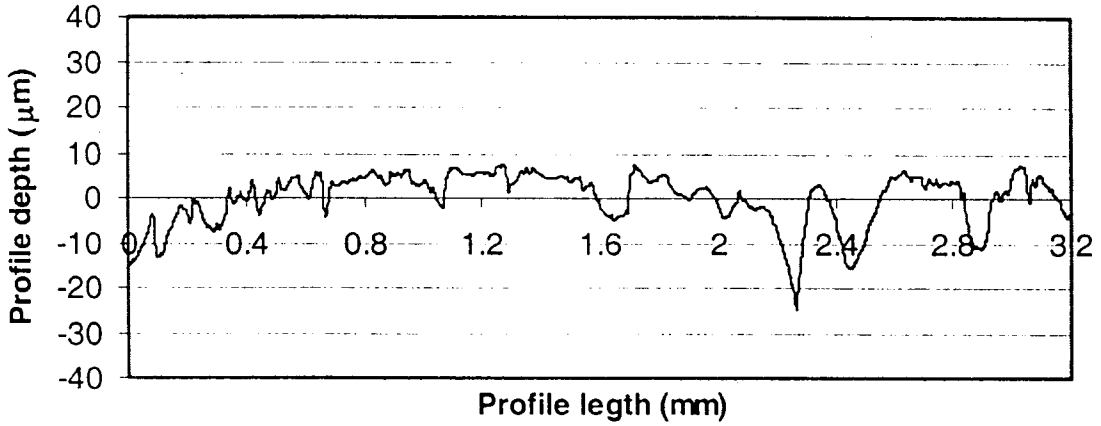

(e)

Figure 6.40(a)-(e) The surface roughness profile of the cast specimen solidified on the substrate surface covered by the oxide film.

To see how the presence of the oxide film improves the interfacial heat transfer between the droplet and the substrate, the interfacial heat flux calculated from the experimental data were compared with the heat flux calculated theoretically assuming perfect contact Figure 6.44 shows the comparison between all heat flux curves.

The theoretically calculated heat flux assumed perfect contact between metal and substrate, Figure 6.41, was calculated as discuss below.

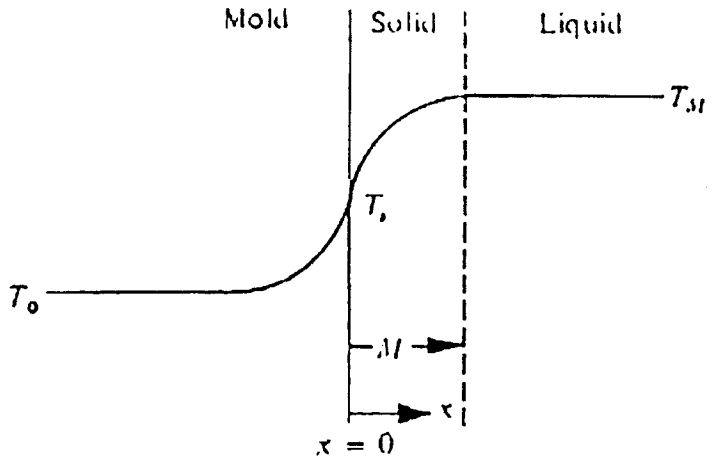

Figure 6.41 The schematic of the temperature profiles at the shell and mold assuming perfect contact at the interface. [80)]

The mold is initially at temperature, To = 25°C. The heat flux into the casting-mold interface from the solidifying metal must equal the flux away from the interface into the mold.

$$\lim_{\xi \to 0}\left[k\left[\frac{\partial T}{\partial x}\right]_{x=0\to\xi} - k'\left[\frac{\partial T}{\partial x}\right]_{x=0\to\xi}\right] = 0 \qquad \textbf{6-1}$$

Apply the boundary conditions

$$T(M,t) = T_M \qquad \textbf{6-2}$$

$$k'\frac{\partial T}{\partial x}(M,t) = \rho' H_f \frac{dM}{dt} \qquad \textbf{6-3}$$

Where T = temperature, t = time, M = shell thickness, ρ' = density of the solidified metal and H_f = heat of fusion.

The mold is semi infinite in the negative x-domain with some unknown surface temperature, Ts, thus

$$\frac{T - T_s}{T_0 - T_s} = erf\frac{-x}{2\sqrt{\alpha t}} \qquad \textbf{6-4}$$

The unknown mold-casting interface temperature Ts can be calculated from the known thermal properties, as shown in Figure 6.42.

$$(T_M - T_0)\left[\frac{C_p'}{H_f}\right] \text{ and } \sqrt{\frac{k'\rho' C_p'}{k\rho C_p}} \qquad \textbf{6-5}$$

where Cp', k' and ρ' = heat capacity, thermal conductivity and the density of a solidified metal. Cp, k and ρ = the heat capacity, thermal conductivity and the density of a substrate.

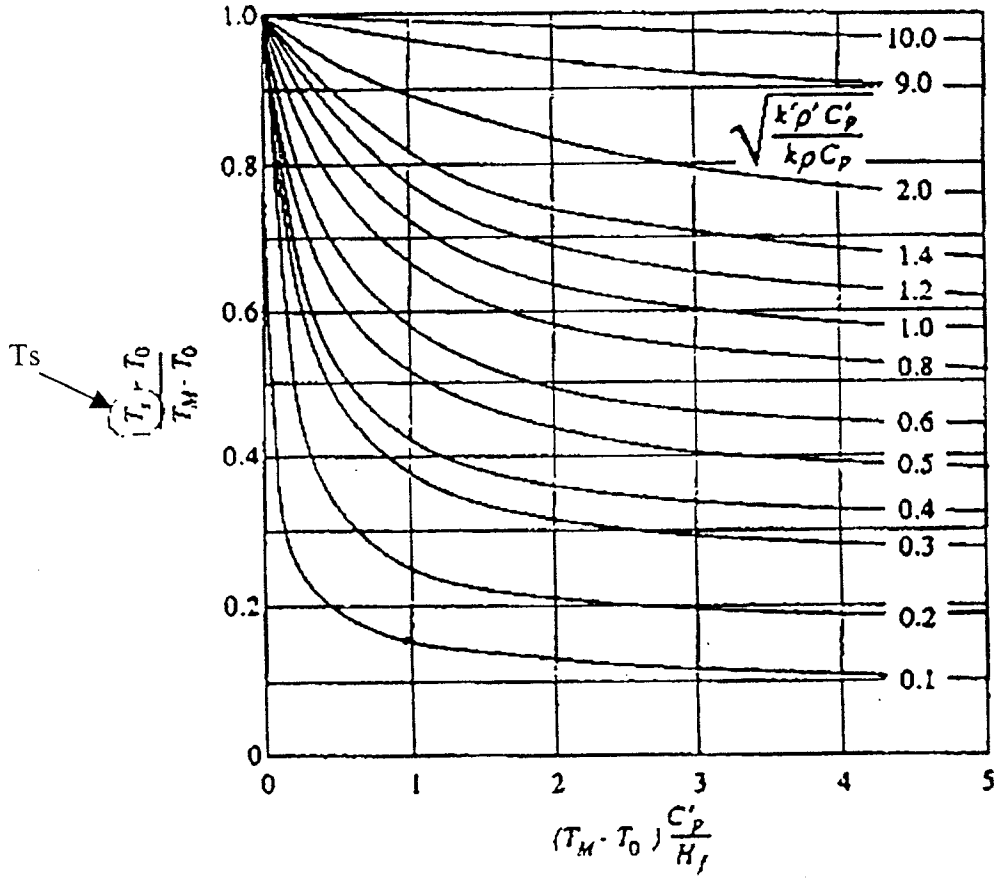

Figure 6.42 Relative mold-casting interface temperatures for unidirectional freezing with no interface resistant.

The heat flux at the interface can be calculated from the differentiation, at x = 0, of the equation 6-4.

$$\left.\frac{\partial T}{\partial x}\right|_{x=0} = -\frac{(To - Ts)}{\sqrt{\pi \alpha . t}} \qquad \textbf{6-6}$$

Thus

$$q = -k\left.\frac{\partial T}{\partial x}\right|_{x=0} = k\frac{(To - Ts)}{\sqrt{\pi . \alpha . t}} \qquad \textbf{6-7}$$

The interfacial heat flux at the film-mold interface, assuming perfect contact, were calculated from the slope at the interface between oxide film and substrate of the temperature profiles gotten from the numerical model assumed a perfect contact one-dimension heat conduction, Figure 6.43. The boundary conditions of the model were based on the real experimental set up. The mold temperature and the melt superheat were set equal the same value used in the real experiment.

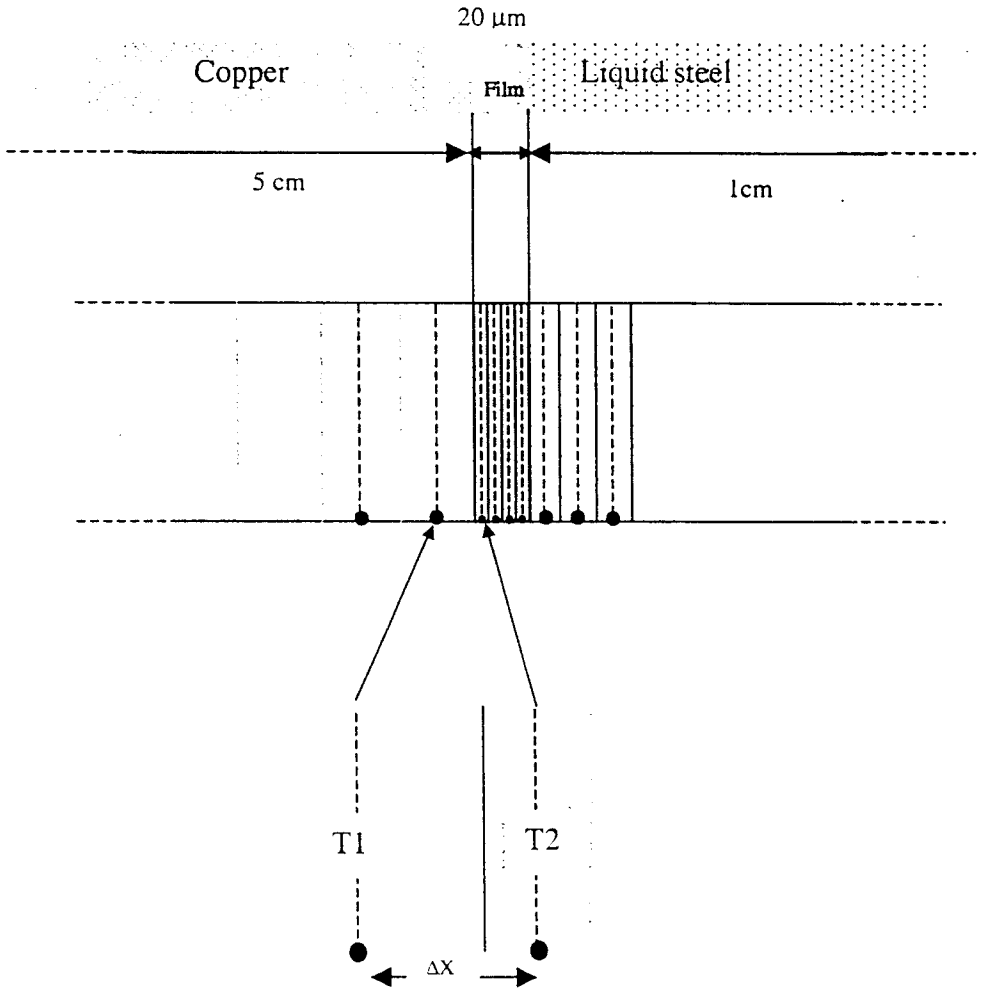

Figure 6.43 The interfacial heat flux at the interface is calculated from the slope of the temperature profiles at the interface, $\frac{\Delta T}{\Delta x}$, between the mold and film.

The orange and green heat flux curves were calculated theoretically which the conditions where there is film thick 20 micron and no film at the metal/mold interface, assumed perfect contact at the interface between metal and mold, metal and film and mold and film.

The calculated heat flux curves were from the experimental data of the droplet solidified on the clean copper mold surface (experiment 1) and the surface substrate covered by oxide film (experiment 8). The difference between the heat flux curves calculated from the experimental data of the droplet solidified on the clean copper substrate and the one calculated assumed perfect contact is large. However the difference between the heat flux calculated from the experiment data of the droplet solidified on the substrate surface covered by film and the one calculated where perfect contact is assumed with a film thick 20 micron at the interface is smaller. It can be seen that both heat flux curves came close together especially during the first milliseconds of the contact time. The presence of the liquid oxide film during the first milliseconds the metal-mold contact resulted in the improvement of the contact between the droplet and the substrate. The results from the roughness measurement and the comparison heat flux are in a good agreement and suggested that when the oxide film, $MnSiO_3$, is present at the substrate surface the improvement of the contact between metal-mold interfaces can be achieved.

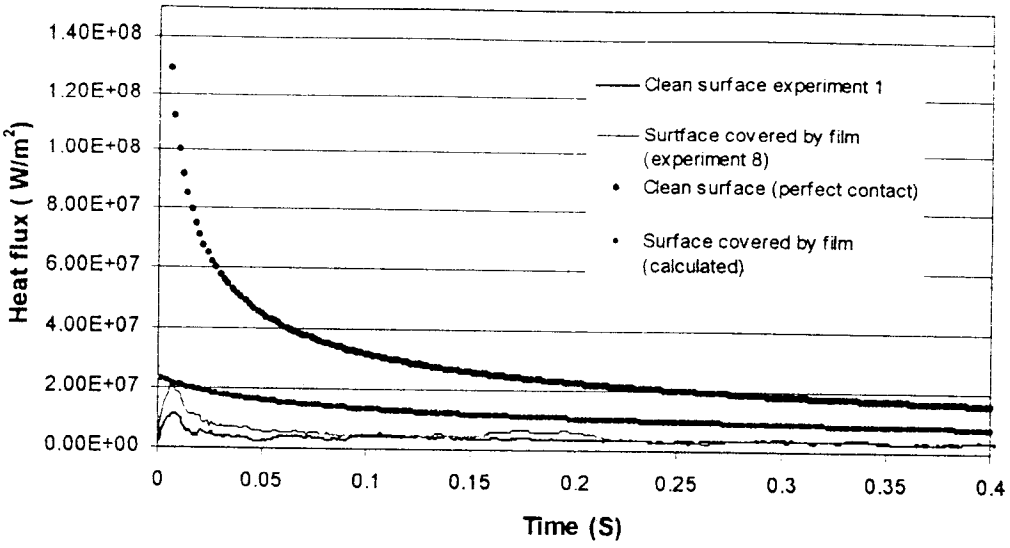

(a)

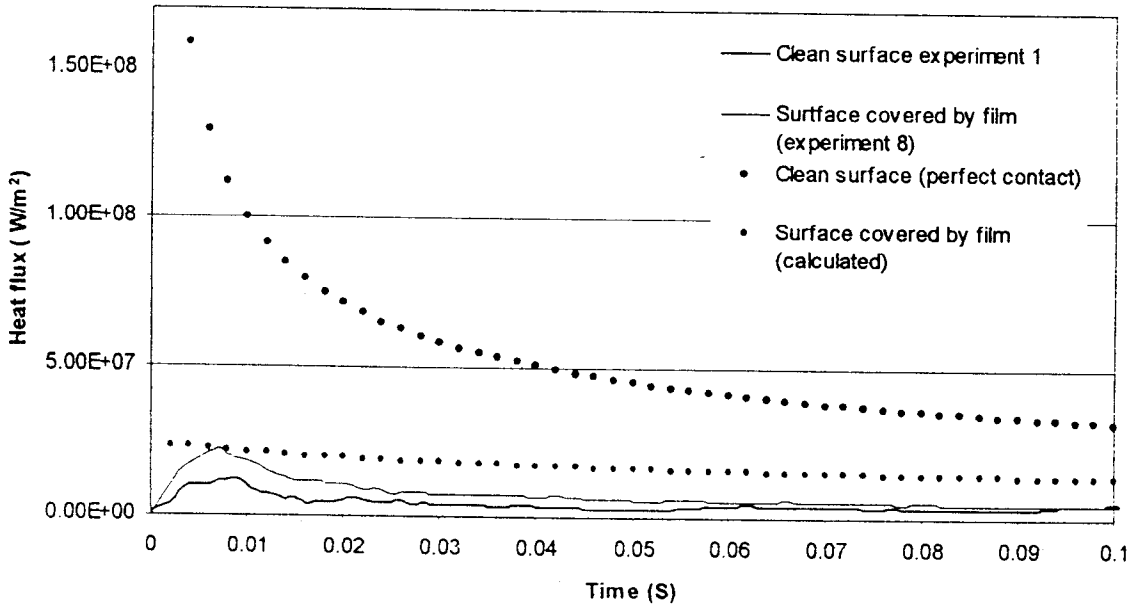

(b)

Figure 6.44 The comparison between heat flux curves during (a) 400 ms (b) 100 ms.

6.6 Summary and Discussion

A film deposited on the surface of the copper substrate affected on the heat transfer behavior of a Mn-Si killed steel droplet and the characteristic of its mold contact surface. The effect of the oxide film on heat flux can be seen when the thickness of the film is reached a critical average thickness of 23 microns. Only the heat flux during the first 50 milliseconds of the droplet solidification process was affected by the oxide film at substrate surface. By using the SEM-EDX system to analyze the composition of the oxide film, it is clear that the film consisted of Manganese, Silicon and Oxygen. The results from DTA were indicated a temperature response that is characteristic of a manganese silicate oxide film. By comparing with the $MnO\text{-}SiO_2$ phase diagram, the result indicated that the possibility that the oxide film can be both $MnSiO_3$ and Mn_2SiO_4 after solidification. The melting behavior of the oxide film was observed under CSLM and the result showed that the oxide film is completely liquid at a temperature around 1350 ^{o}C and has ability to wet the surface of iron. The surface roughness measurement indicated that the presence of oxide film can reduce the surface roughness of the casting which can help increase the initial heat transfer behavior between the metal droplet and the copper substrate.

The shape and the chemical composition of inclusions found at the surface and inside of the solidified specimen indicated that they were natural liquid inclusion of the Mn-Si killed steel. This is indicated that there is a possibility that most of the oxide film found at the surface of the mold could be related to or came from the liquid inclusions naturally existing in the molten steel.

Chapter 7

Conclusions and Application of Results

7.1 Conclusions

An experimental apparatus was developed to study the initial heat transfer behavior and solidification of the molten steel on the chill substrate. The experimental technique imitated the strip casting process by allowing the liquid steel to directly contact the copper substrate and allowed information on the initial heat transfer of the droplet that occurs during the first milliseconds of contact time to be gained, as it was designed for millisecond resolution of heat transfer behavior.

The novel approach of simultaneous in-situ observation and measurement of rapid heat transfer enables a coupling between the interfacial heat transfer rate and droplet solidification to be developed. The technique allowed the solidification rate and the movement of the droplet to be determined resulting in a better interpretation of the measured thermal data. As the phenomena that occurred during the droplet ejection and solidification process was revealed it was found that the spread of the liquid droplet occurred during the ejection process. This result suggested that the fluctuations of the heat flux curves were caused by the movements of the liquid steel during the initial metal/mold contact. Therefore the major parameters that controlled the initial heat transfer rate during the first 50 milliseconds were the ejection pressure, the superheat, the wettability of the liquid steel and the substrate surface condition.

The effects of process parameters such as superheat, melt sulfur content and oxide accumulation at the interface were also studied. Since the initial wetting of the liquid steel ejected on the copper substrate could be influenced by the surface tension of the melt a study of the effect of sulfur content in Fe-S on initial heat transfer behavior was carried out in this work. From this study, it was found that the heat flux increased when the percent of sulfur content increased and the superheat increased. The difference between the heat that was given off from the Fe-S droplet to the substrate during the first milliseconds between the lower and higher superheat is small in the case of low sulfur content and large in the case of higher sulfur content.

Modifications of the metal-mold interface conditions will result in significant changes in interfacial heat transfer. By ejecting the molten Mn-Si killed steel onto the substrate, the black substance was found accumulated at the interface. The deposited black substance was found to be manganese and silicon based oxide. The result from the inclusion analysis indicated the relationship between the natural liquid inclusion, $MnSiO_3$, of Mn-Si killed steel and the deposited oxide film. When liquid steel droplets were ejected onto the copper substrate repeatedly, without cleaning the substrate surface between the ejections, large increase in the interfacial heat flux curves was observed. The deposited oxide composition and melting behavior were studied and the results indicated the liquid oxide film existed at the interface and enhanced the contact between the droplet and the substrate. The surface roughness measurement of the solidified specimen indicated the improvement of the contact between the droplet and the substrate when the liquid oxide film was present at the interface.

7.2 Suggested application of results

The simultaneous in-situ observation and measurement of rapid heat transfer is open for many applications. One of the applications of this novel technique is for study of the solidification behavior of steel. The information that results from this technique can be directly applied to the metal spray deposition and strip casting work. Since the growth of the solidification front can be captured, the solidification rate can be estimated and the substrate temperature profiles can be recorded, this technique can be use to validate the numerical model of the droplet heat transfer deposition along with the study of the solidified specimen microstructure.

The result of the studies of the effects of the oxide accumulation at the interface suggest we must pay attention on the interaction between the steel natural inclusion and the substrate since the results from the study show the relationship between the deposited oxide film and the natural inclusion in the steel. Unlike the conventional continuous casting, there is no mold slag or lubricant in strip casting and roll texturing and surface modification becomes important to moderate and allow uniform heat transfer. The results from the study of the presence of the oxide film at the interface suggest a new way to improve the surface condition of the caster in strip casting. This knowledge can also be used as a factor to decide the proper time to clean the surface of the twin roll caster in order to have a uniform heat transfer.

7.3 Suggested future work

It is very interesting that the solidification behavior of the droplet revealed by video recording can explain the results of the previous work studying the undercooling process of a droplet solidified on the copper substrate[13], where the undercooled curves could be seen in the cast surface temperature profile measured from light sensor. If we can apply this new technique, an in-situ observation and measurement of rapid heat transfer, to estimate the shell growth rate along with using the light sensor to measure the cast surface temperature profile, the effect of casting parameters on undercooling process and solidification time of the droplet can be revealed. Moreover the study of the secondary dendrite arm spacing of the solidified droplet at various positions would be interesting to study since, from the experimental results, we saw two different growth rates of solidified shell.

When the results from a study shell growth by video recording, the cast surface temperature profile by a light sensor and the solidification time by droplet microstructure are combined together the initial solidification and heat transfer behavior of the droplet solidified on the copper substrate will be fully documented and clearly understand.

The results from the study of effect of the deposition film built up at the interface on the interfacial heat transfer rate suggested that there is a relationship between the natural inclusion of steel and the deposited oxide film found at the surface of the copper substrate. It is very interesting to determine if the interaction of various other kinds of inclusion systems that can be found in steel will have a similar effect as the $MnSiO_3$ is shown of the study.

Reference

1. M. Cygler and M.Wolf, "Continuous Strip and Thin Slab Casting of Steel – An Overview," Iron & Steelmaker 13, no.8 (Aug 1986): 27-33.

2. K. Emoto, T. Nozaki and T.Yanazawa, "Hot Connection Between Steelmaking Shop and Hot Rolling Mill," The Inst. of Met. London (1986): 134-139.

3. H. Yasunaka, K. Taniguchi, M. Kokita and T. Inoue, "Surface Quality of Atainless Steel Type 304 Cast by Twin-Roll type Strip Caster," ISIJ International 35, no.6 (1995): 784-789.

4. M. Bamberger, B.Z. Weiss and M.M. Stupel, "Heat Flow and Dendritic Arm Spacing in Chill-Cast Al-Si Alloys," Materials Science and Technology 3 (Jan1987): 49-56.

5. K. Ho and R.D. Pehlke "Transient Methods for Determination of Metal-Mold Interfacial Heat Transfer," AFS Trans. 92 (1983): 689-698.

6. Y. Nishida, W. Droste and S. Engler, "The Air-Gap Formation Process at the Casting-Mold Interface and the Heat Transfer Mechanism through the Gap," Metall. Trans. B 17B (1986): 833-844.

7. N.A. El-Mahallawy and A. M. Asssar, "Coefficient for Aluminum Solidifying Against Copper Chill," Journal of Materials Science 26 (Apr.1991): 1729-1733.

8. R.C. Sun, "Simulation and Study of Surface Conductance for Heat Flow in the Early Stage of Casting," AFS Cast Metal Research Journal 6 (Sept.1970): 1005-1010.

9. T.S.P. Kumar and K.N. Prabhu, "Heat Flux Transients at the Casting/Chill Interface during Solidification of Aluminum Base Alloys," Metall. Trans. B 22B (Oct.1991): 717-727.

10. M. Prates, J. Fissolo and H. Billoni, "Heat Flow Parameters Affecting the Unidirectional Solidification of Pure Metals," Metall. Trans. A 3A (June 1972): 1419-1425.

11. C.A. Muojekwu, I.V. Smarasekera and J.K. Brimacombe, "Heat Transfer and Microstructure during the Early Stage of Metal Solidification," Metall. Trans. B 26B (Apr.1995): 361-382.

12. H. Todoroki, R. Lertarom, A.W. Cramb, I. Jimbo and T. Suzuki, "Evaluation of the Initial of Solidification of Iron against Water Cooled Copper Mold," Proceedings of 54th Electric Arc Furnace Conference, Dallas (1996): 585-590.

13. H. Todoroki, R. Lertarom, T. Suzuki and A.W. Cramb, "Initial Solidification of Iron, Nickel and Steel Droplets," Iron & Steelmaker 26 (Apr.1999): 57-71.

14. H. Todoroki, R. Lertarom, T. Suzuki and A.W. Cramb, "Solidification of Steel Droplets against a Water Cooled Copper Mold," Iron and Steel Society/AIME, Alex Mclean Symposium Proceedings (July1998): 155-175.

15. H. Todoroki, R. Lertarom, T. Suzuki and A.W. Cramb, "Initial Solidification of Iron, Nickel and Steel Droplets," Minerals, Metal and Materials Society/AIME (1998): 327-341.

16. H. Todoroki, R. Lertarom, T. Suzuki and A.W. Cramb, "Solidification and Heat Transfer behavior of 304 Stainless Steel," Minerals, Metal and Materials Society/AIME (July 1997): 2227-2236.

17. H. Todoroki, R. Lertarom, T. Suzuki and A.W. Cramb, "Heat Transfer Behavior of Pure Iron and Nickel against Water Cooled Copper Mold during Initial Stage of Solidification," Iron and Steel Society/AIME, Steel Making Conference Proceedings 80 (Apr. 1997): 667-678.

18. L. Strezov and J. Herbertson, "Experimental studies of interfacial heat transfer and initial solidification pertinent to strip casting," ISIJ Inter (Japan) 38, no.9 (1999): 959-966.

19. T. Evans and L. Strezov, "Interfacial heat transfer and nucleation of steel on metallic substrates," Metall. Trans. B 31B, no.5 (Oct. 2000): 1081-1089.

20. L. Strezov, J. Herbertson and G.R. Belton, "Mechanisms of initial melt/substrate heat transfer pertinent to strip casting," Metall. Trans. B 31B, no.5 (Oct. 2000): 1023-1030.

21. T. Mizoguchi, K. Miyazawa and Y. Ueshima, "Relation between Surface Quality of Cast Strips and Meniscus Profile of Molten Pool in the Twin Roll Casting Process," Tetsu-to-Hagane (Journal of the Iron and Steel Institute of Japan) (Japan) 80, no.1 (1994): 36-41.

22. S. Miyake, H. Yamane, M. Yukumoto and M. Ozawa, "Strip Quality of Highly Alloyed Metals by Twin Roll Casting," ISIJ International 31, no.7 (July 1991): 689-695.

23. G. Li and B.G. Thomas, "Transient Thermal Model of the Continuous Single Wheel Thin-Strip Casting Process," Metall. Trans. B 27B (Jun 1996): 509-525.

24. J.C. Grosjean, J.L. Jacquot, J.M. Damasse, H. Littercsheidt, D. Senk and W. Schmitz, "Twin roll casting developments at Thyssen Stahl AG and Irsid," Iron and Steelmaker 21, no.8 (Aug.1993): 27-32.

25. M. Yukumoto and H.Yamane, "Thin Strip Casting of Ni Base Alloys by Twin Roll Process," ISIJ International 35, no.6 (1995): 778-783.

26. M. Prates and H. Biloni, "Variable Affecting the Nature of the Chill Zone," Metall. Trans. A 3A (June 1972): 1501-1510.

27. K. Ho and R.D. Pehlke, "Meatal Mold Interfacial Heat Transfer," Metall. Trans. B 16B (Sept.1985): 585-594.

28. W. Liu, G.X. Wang and E.F. Matthys, "Thermal Analysis and Measurements for a Molten Metal Drop Impacting on a Substrate: Cooling, Solidification and Heat Transfer," Int. J. Heat Mass Transfer 38, no.8 (1995): 1387-1395.

29. G.-X. Wang and E. F. Matthys, "On the heat transfer at the interface between a solidifying metal and a solid substrate," Minerals, Metals and Materials Society/AIME (1996): 205-236.

30. G.-X. Wang and E. F. Matthys, "Modelling of Rapid Solidification by Melt Spinning: Effect of Heat Transfer in the Cooling Substrate," Mater. Sci. Eng. A136 (1991): 85-97.

31. G.-X. Wang and E.F. Matthys, "Interfacial Thermal Contact during Rapid Solidification on the Substrate," Heat Transfer, The Proceedings of the 1994, International Heat Transfer Conference, London England (1994): 169-174.

32. J. A. Spittle and D.M. Lloyd, Proc Int. Conf. On Solidification and Casting, The Metal Society, London (1797): 15-20.

33. H. Todoroki, R. Lertarom, T. Suzuki and A.W. Cramb, THERMEC '97 : International Conference on Thermomechanical Processing of Steels and Other Materials II, Wollongong, Australia, (July 1997).

34. S. Ozbayraktar and A. Koursaris, "Effect of Superheat on Solidification Structures of AISI 310S Austenitic Stainless Steel," Metal. and Mater. Trans B 27B (Apr.1996): 287-296.

35. R.D. Pehlke, J.T. Berry, W. Erickson, and C.H. Jacobs, Proc. Int. Conf. On Solidification and Casting, The Metals Society, London (1979): 371-379.

36. D.J Hurtuk and A.A.Tzavaras, Proc. Int. Conf. On Solidification and Casting, The Metals Society, London (1979): 21-28.

37. T.W. Cadwell, A.J. Campagna, M.C. Flemings and R. Mehrabian, "Refinement of Dendrite Arm Spacings in Al Ingots Through Heat Flow Control," Metall. Trans. B. 8B (Jun 1977): 261-270.

38. J.V.Beck, B.Litkouhi, and C.R.St.Clair, Jr., Numerical Heat Transfer 5 (1982): 275-286.

39. K.A.Woodbury, "Effect of thermocouple sensor dynamics on surface heat flux predictions obtained via inverse heat transfer analysis," Int.J.Heat Mass Transfer 33, no.12 (1990): 2641-2649.

40. G.Blanc, J.V.Beck, and M.Raynaud, Numerical Heat Transfer Part B 32 (1997): 437-451.

41. M.H. Burden and H. Jones, J. Institute Metals 98, (1970): 249-252.

42. H.A Davis, Solidification Mechanism in Amorphous and Crystalline Ribbon Casting (Elsevier Science Publisher B.V., 1985): 101-106.

43. S.C. Huang and H.C. Fiedler, "Effect of Wheel Surface Conditions on the Casting of Amorphous Metal Ribbons," Metall. Trans. A. 12A, (Jun 1981): 1107-1112.

44. R. Lertarom, "Interfacial Heat Transfer Coefficient between a Water Cooled Copper Chill and a 304 Stainless Steel Droplet," Thesis, Material Science & Engineering Dept., Carnegie Mellon University, (1997).

45. T.J. Evans, "Mechanism of Interfacial Heat Transfer and Nuclieation of Liquid Steel on Metallic Substrate," Thesis, University of Newcastle (Dec 1999).

46. C.H. Amon, K.S. Schmaltz, R. Merz and F.B. Prinz, "Numerical and Exprimental Investigation of Interface Bonding Via Substrate Remelting of Impinging Molten Meat Droplet," Transaction of the ASME 118 (1996): 164-172.

47. L.J. Zarzalejo, K.S. Schmaltz and C.H. Amon, "Molten Droplet Solidification and Substrate Remelting in microcasting Part1: Numerical Modeling and Experimental Verification," Heat and Mass transfer 34 (1999): 477- 485.

48. K. Ho and R.D. Pehlke, " Mechanisms of Heat Transfer at a Metal-Mold Interface," AFS Transactions 92 (1984): 587-598.

49. K. Ho and R.D. Pehlke, "Transient Method for Determination of Metal-Mold Interfacial Heat Transfer," AFS Transaction 91 (1983): 689-698.

50. K.A. Woodbury, "Effect of Thermocouple sensor dynamics on Surface Heat Flux Predictions Obtained via Inverse Heat Transfer Analysis," Int. J. Heat Mass Transfer 33, no.12 (1990): 2264.

51. L. Strezov and G.R. Belton, International Patent PCT/AU93/00593 (1993).

52. J.H. repezko and Uttormark M.J, "Undercooling and Nucleation during Solidification," ISIJ 35, no.6 (1995): 580-588.

53. H. Fujino, T. Suzuki and I. Jimbo, "A Nummerical Model for Cooling Rate Dependence of the Degree of Undercooling during Rapid Solidification of 18Cr-8Ni Stainless Steel," ISIJ International 37, no.11 (1997): 1107-1111.

54. L.T. Shiang and P.J. Wray, "The Microstructure of Strip Cast Low Carbon Steel and Their Response to Thermal Processing," Metall. Trans. A 20A (July 1989): 1191-1198.

55. L. Strezov, T. Evan and R. Dippenaar, " Nucleation and Early Growth Pertinent to Near Net Shape Casting," ICARISM, Perth (Sept. 1999): 85-87.

56. H. Jones, "Prediction versus Experimental fact in the Formation of Rapidly Solidification Microstructures," ISIJ International 35, no.6 (1995): 751-755.

57. K. Oikawa, S. Sumi and K.Ishida, "Morphology Control of MnS Inclusions in Steel during Solidification by the Addition of Ti and Al," Z. Metallkd. 90 (1999): 13-18.

58. C.V. Thompson and F. Spaepen, "Homogeneous Crystal Nucleation in Binary Metallic Melts," Acta metal. 31, no.12 (1983): 2021-2027.

59. S. Das and A.J. Paul, "Determination of Interfacial Heat Transfer Coefficients in Casting and Quenching Using a Solution Technique for Inverse Problem Based on the Boundary Element Method," Metall. Trans. B 24B (Dec 1993): 1077-1086.

60. P.G.Q. Netto and R.I.L. Guthrie, "The Importance of Turbulence Modeling in the Design of a Novel Delivery System for a Single-Belt Steel Casting Process," Inter. J. Heat and Mass Transfer 43 (2000): 21-37.

61. D. Marzumdar and R.I.L. Guthrie, "The Physical and Mathematical Modelling of Continuous Casting Tundish Systems," ISIJ International 39, no.6 (1999): 524-547.

62. S. Fukumoto and W. Kurz, "Solidification Phase and Microstructure Selection Maps for Fe-Cr-Ni Alloys," ISIJ International 39, no.12 (1999): 1270-1279.

63. R.I.L. Guthrie and R.P. Tavares, " Mathematical and Physical Modeling of Steel Flow and Solidification in Twin-Roll/Horizontal Belt Thin-Strip Casting Machines," Applied Mathematical Model 22 (1998): 851-872.

64. L. Strezov United States Patent, Patent Number 5,701,948 (Dec. 1997).

65. J.D. Hwang, H.J. Lin, J.S.C Jang, W.S. Hwang and C.T. Hu, "Relationship between Flow Characteristics and Surface Quality Inclined Twin Roll Strip Casting," ISIJ International 36, no.6 (1996): 660-699.

66. G. Mcmanus and B. Berry, "Nippon, Mitsubishi, Armco Take the Lead in Strip Casting," New Steel (Nov 1993):18-20.

67. A. Mortensen, "On the Rate of Dendrite Arm Coarsening," Metall. Trans. A 22A (Feb 1991): 569-574.

68. P.W. Voorhees, "Coarsening in Binary Solid-Liquid Mixtures," Metall. Trans. A 21A (Jan 1990): 27-30.

69. Y.S. Touloukian, R.W. Powel, C.Y. Ho and P.G. Klemens, "Thermal Conductivity of Non-Metallic Solids," Thermophysical Properties of Matter 2, NewYork, Plenum (1970).

70. W. Kurz and D.J. Fisher, "Fundamental of Solidification," 3rd ed. (Trans Tech Publications Switzerland, 1992).

71. D.R. Poirier and G.H. Geiger, "Transport Phenomena in Materials Processing," (Minerals, Metals & Materials Society 1994).

72. F. Kreith and W.Z. Black, "Basic Heat Transfer," (Harper & Row, NewYork, 1980).

73. J.Crank, "The Mathematics of Diffusion," 2nd ed. (Clarendon Press, Oxford, 1975).

74. E.M. Sparrow, A. Haji-Sheihk and T.S. Lundgren, "The Inverse Problem in Transient Heat Conduction," Trans. ASME, Series E 86 (1964): 389.

75. W.J. Winkowycz, E.M Sparrow, G.E. Schneider and R.H. Pletcher, "Handbook of Numerical Heat Transfer," John Wiley & Son, Inc., 1998.

76. Phase diagram book (will add)

77. H. Todoroki, R. Lertarom and A. W. Cramb, " Effect of Ejection Pressure on Heat Transfer Behavior of Molten Nickel against a Water Cooled Copper Mold," CISR report, 1997.

78. N. Sano, W. Lu, P.V. Riboud and M. Maeda, " Advanced physical Chemistry for Process Metallurgy", Academic Press, 1997.

79. E. Kreyszig, "Advanced Engineering Mathematics", John Wiley & Son, Inc.,1993.

80. D. R. Poirier and G. H. Geiger, " Transport Phenomena in Materials Processing," TMS, 1994.

81 H. Misukami, T. Suzuki and T. Umeda, "Control of Initial Solidification Structure of Rapidly Solidified 18Cr-8Ni Stainless Steel," ISIJ (1992): 95-102.

81. H. Misukami, T. Suzuki and T. Umeda, "Numerical Analysis for Initial Stage of Rapid Solidification of 18Cr-8Ni Stainless Steel," ISIJ (1992): 79-85.

Appendix A

```
////////////////////////////////////////////////////////////////////////////////
//////// Program for finding a median value
//
// Author  :  Natthapong Phinichka
// Date    :  11/24/98
//
// This program is used for finding a median value of a series
// of 10 data points. It will take a column of unlimited size data
//  ,save as notepad format, as an input data. The out put will be
// given out as a notepad file as well. The Metrowork code warrior
// was used as a compiler for this code. The standard library that
// was used in this program was written by Richard Pattis, a lecturer
// in Computer science department at Carnegie Mellon University
//
//
////////////////////////////////////////////////////////////////////////////////
////////////////////////////////////////////////////////////////////////////////

#include <stdexcept>  //Standard C++ Exceptions
#include <iostream>   //Standard C++ I/O: cin/cout >>/<<
#include <iomanip>    //I/O Manipulators: e.g., setw(10)
#include <math.h>     //Standard Math Functions: e.g., pow
#include "syntax.h"   //Standard 15-127 Syntax extensions
#include "prompt.h"   //Prompting functions (see Finish)
#include "fmtutil.h"  //Fmt functions for primitive types
#include <fstream>    //ifstream and operator>>
#include "fileutil.h" //Safe_Open
#include "openfile.h" //OpenFileForReading
#include <string>     //Standard string class: .length() and []
#include <string.h>   //C string library: strlen, strcpy, etc.
#include "vector.h"   //Templated Vector class
#include "matrix.h"   //Templated Matrix class
typedef Vector<double> Dou_Vec;

////////////////////////////////////////////////////////////////////////
////// Function swap ///////////////////////////////////////////////
void swap ( double& a1 , double& a2 )
{
  double original_a1 = a1;
   a1= a2;
   a2 = original_a1 ;
}
////////////////////////////////////////////////////////////////////////
////////////Function Sort ////////////////////////////////////////////

 void Sort ( Vector<double>& temp)
 {
   for( int min= 0 ; min< temp.Used() ; min ++ )
    for ( int test = 0 ; test < temp.Used() ; test++ )
     if ( temp[min] > temp[test] )
      swap( temp[min], temp[test] ) ;
 }
////////////////////////////////////////////////////////////////////////
```

```
//////////////////////////////////////////////////////////////////////////
//////////Function Mid_pos ////////////////////////////////////

 void  mid_pos  ( Vector<double> temp , ofstream& Output )

 {
  for( int a= 0 ; a < temp.Used() ; a ++ )
    if ( a == 5 )
     Output << temp[a] << endl;
  }

//////////////////////////////////////////////////////////////////////////
//////////////////////////////////////////////////////////////////////////
////////////////// Main Program ////////////////////////////////
//////////////////////////////////////////////////////////////////////////

int main ()
{try {
          ofstream Output;
          ifstream Input;
          Safe_Open ( Input , "Enter the file name" ) ;
          Safe_Open ( Output , "Enter the output file to write the data " ) ;

         double x;
          Dou_Vec temp;
          temp.Set_Used(0);
 I        nt count = 0;
         cout << "writting data on file" << endl;
          loop {
                    break_when ( !Input);

                    while ( Input >> x) {
                        break_when ( !Input);
                        count ++;
                        temp.Append(x) ;
                        Sort(temp) ;
                        break_when ( count == 10 );
                        }
                    cout << "*" ;
                    mid_pos(temp , Output);
                    count = 0;
                    temp.Set_Used(0);
                    break_when ( !Input);
                    }
          Input.close();
          Output.close();

          }
catch (const exception& E)        //Catch any thrown exception and print
  {cout << E.what() << endl;}     // its explanation before terminating
return 0;                          //0 means "report no error
}

          ////////////////////// end //////////////////////
```

Appendix 7

Microstructure, Mechanical Properties, and Texture of Strip Cast Low C Steel Sheets

Microstructure, Mechanical Properties, and Texture of Strip Cast Low C Steel Sheets

K. Kumari, P. Misra, A. W. Cramb and A.D. Rollett
Carnegie Mellon University, Pittsburgh, PA

Thin strip casting using the twin roll configuration, has emerged as a revolutionary route to cast commercial quality low carbon sheet steel. The strip cast sheet can be directly cold rolled and annealed, thus eliminating the intermediate hot rolling step. A 1006 grade low C sheet steel was strip cast on a commercial scale system to 2mm thickness. Strip cast samples were cold rolled and batch annealed in laboratory scale experiments. In-line hot rolling was also applied to the strip cast steel in the commercial caster. The as-cast and processed samples were characterized for microstructure, texture development, and mechanical properties. The as-cast structure shows acicular and Widmanstätten ferrite in addition to an irregular polygonal ferrite structure because of the higher cooling rate associated with the strip casting process. Since the initial microstructure of the strip cast steel is different from conventionally processed steel, its behavior in thermo-mechanical processing is also different. Detailed texture analysis has been performed on the deformed and annealed samples with the result that moderate development of the γ-fiber, <111> || ND is observed. The results from cold rolled batch annealed material are very promising in terms of ductility and r-value, and open a door for future applications in new directions.

* This work was supported by the USDOE, AISI, US Steel, National Steel, LTV, Dofasco, AK Steel, SMS Concast and Voest-Alpine

(For publication in the Canadian Metallurgical Quarterly and presentation at the conference of the Canadian Institute of Metallurgy, Ottawa, August'00)

Introduction

Strip casting of steel sheet directly from the liquid metal has been the dream of steel industry technologists for almost a century. However, the recent focus and research in the last decade on the development of strip casting process for mass steel production has made it a viable technology, and it has the potential to be a

replacement for the conventional slab casting process. The major contribution of strip casting is the elimination of hot rolling and intermediate annealing before cold rolling. There is also the possibility of developing newer microstructures and better mechanical properties, all of which are highly promising for the modern steel industry. Our work shows that the strip cast steel can be directly cold rolled into finished products with highly desirable properties.

Commercial strip cast stainless steel has been successfully produced by many companies so far [1,2] and studied by various investigators [3,4]. This is, however, the first successful effort of strip casting low C steel on a commercial scale. The much faster solidification rates observed in strip casting, of the order of 1000 to 10000°C/s, compared to conventional slab casting leads to the development of a blend of acicular, Widmanstätten and irregular polygonal ferrite structure [5-7]. This is different from the polygonal ferrite structure observed for the conventional hot rolled (hot band) low C sheet steel.

Because of the different initial microstructure of the strip cast steel, it is of great interest to develop the post-processing methods for the as-cast strip so as to obtain the desired mechanical and deep drawing properties. In this regard, as-cast, in-line hot rolled, and cold-rolled batch annealed, sheets have been characterized using optical microscopy, X-ray texture measurement, mechanical properties and plastic strain ratio (r-value). The results obtained from this commercial 1006 grade low C steel extend the developments carried out by numerous investigators [8-14] in the areas of strip casting, texture, and mechanical property development. Orientation Imaging Microscopy (OIM) [15] has been carried out to investigate the microstructure of the as-cast strip using lattice orientation contrast. OIM has emerged as a powerful research tool for studying the morphology of grain structure, the orientation of grains, grain size statistics, and the grain boundaries. Few studies on strip cast low C steel are available in the literature, and so this work should contribute to improved understanding of the strip cast structure and properties.

Experimental Methods

The strip cast steel under investigation was obtained from BHP, Australia, in the form of a 2 mm thickness sheet. The composition of this Si-killed steel was (wt%): C: 0.047, Mn: 0.64, Si: 0.27, S: 0.005, P: 0.007, Al: 0.006, O: 0.009, N:

0.006. As-cast samples were cold rolled to different reductions and one batch of 70% cold reduced samples was batch annealed at 721°C for 30 hours. In-line hot rolling (28% reduction) at 1050°C was also carried out at BHP, and this material was also characterized. Samples for metallographic observation were prepared in the usual manner by mechanical polishing, final polishing with diamond suspension, and etched with 4% Nital. To resolve the solidification (dendritic) structure, hot picric acid etch was used on the as-cast samples.

Samples of dimension 520-mm-square were taken for X-ray pole figure measurement, noting the rolling direction and incomplete pole figures were measured for (110), (200) and (112) poles. The pole figure measurements were performed with a conventional texture goniometer by the Schulz reflection method, using Mo K_α radiation at 35kV, 25mA, to study texture in the various samples. Samples of the as-cast material were prepared for examination under Orientation Imaging Microscopy (OIM). OIM utilizes a standard scanning electron microscope in conjunction with high-gain digital imaging to record the backscattered electrons diffracted from crystalline regions of ~0.2 μm in size [15-17]. After mechanical polishing, these samples were electropolished at room temperature by using an electrolyte, consisting of 70 ml distilled water, 730 ml ethanol, 100 ml ethylene glycol monobutyl ether and 78 ml perchloric acid.

ASTM sub-size (25 mm in gauge length) samples for tensile testing and plastic strain ratio were machined from the as-cast strip, in-line hot rolled strip and cold rolled annealed strip, in the rolling, transverse and diagonal directions and were tested according to ASTM E 8-93 and E 517-96a respectively. Hardnesses on the Rockwell B scale were also measured for the various samples.

Results & Discussion

Microstructure:

The as-cast strip shows an inhomogeneous structure, with a blend of acicular ferrite, irregular polygonal ferrite and Widmanstätten ferrite morphologies, as shown in Fig. 1(a) and (b). This is related to the high cooling rate associated with the strip casting process. Moreover, the coarse austenite grains that would have been present at the beginning of the ferrite transformation, also favor the

formation of Widmanstätten ferrite because of the consequent low density of nucleation sites for transformation [6,7].

The solidification structure of the as-cast strip shows well-defined columnar grains, inclined to the sheet normal as seen in Fig. 2. It has not been possible to observe secondary dendrites in the sheet because of the low levels of phosphorus in this steel. The primary dendrite arm spacing was obtained directly from the optical micrograph. In addition, primary and secondary dendrite arm spacings were also calculated with the Procast^{TM} model. The initial and boundary conditions used in the model were:

At $t = 0$, $T = 1600°C$ $\quad 0 \leq x \leq 1$ mm
At $x = 0$, $q = 0$ (center line of the strip)
At $x = 1.0$ mm, $q = 12.5$ MW/m^2 (surface of the strip),

where x is the distance from the center line of the strip and q is the heat flux.

The thermophysical properties of the strip were reasonably approximated with those of pure iron. In strip casting conditions, the shell thickness (x_s) is related to time (t) as [18]:

$x_s = 2.33\ t^{0.575}$

From the above relationship, a surface heat flux value close to 12.5 MW/m^2 can be obtained using the analysis of Sha and Schwerdtfeger [19] and was used as the surface boundary condition. The results from the model together with those from microscopic observations are shown in Fig. 3. Both the experiment and the simulation suggest a primary dendrite arm spacing of 20-30 μm, which is 5-6 times smaller than that observed for conventional slab casting. The secondary dendrite arm spacing is predicted to be between 10 and 15 μm, and is related to the cooling rate during solidification of the sheet. The heat transfer model suggests a cooling rate in the range of 1500-2000°C/sec, which is in agreement with the cooling rates reported for strip casting of low C steel [6].

The in-line hot rolled strip shows a microstructure that is very similar to the as-cast strip. Irregular polygonal ferrite is present, as is some acicular and Widmanstätten ferrite plates (Fig. 4). Some ferrite veining has also been observed at the prior austenite grain boundaries in the hot rolled sheet. This microstructure resembles the structures obtained in welding of low C steel sheets, because of the higher cooling rates of the welding processes [20,21]. The hot rolling microstructure suggests that the temperature for rolling was high enough to result in a large austenite grain size, and the cooling rate was probably also high; both

these factors promote acicular and Widmanstätten ferrite morphologies. However, changing the rolling and coiling parameters may lead to fully polygonal ferrite grain structure, with enhanced ductility, and thus needs further investigation in this direction.

By contrast, the cold rolled and batch annealed samples show a fully recrystallized polygonal ferrite structure as shown in Fig. 5. The initial microstructure has been completely destroyed during cold rolling and batch annealing. The grains are elongated in the rolling direction, i.e. they are pancaked (with an average aspect ratio of 2.3), which is in agreement with the results obtained by various investigators [9,10].

Mechanical Properties:

The engineering and true stress strain curves for the as-cast strip are shown in Fig. 6. It is interesting to note that no yield point phenomenon is observed in the as-cast sheet. The tensile properties and the hardness on the Rockwell B scale are summarized in Table 1. The tensile properties were measured in samples machined parallel to the rolling, transverse and diagonal directions, and the average value has been reported here. The properties are nearly isotropic for the various sheets and the variation is less than 5%. The strip cast steel has slightly higher yield strength due to the high dislocation density that has been observed with Widmanstätten ferrite structure [3,6]. The tensile strength is 80-100MPa higher than the conventional hot band, with almost the same ductility level. This is not surprising because the lower the transformation temperature of austenite to ferrite, the higher the strength and the lower the ductility. The same trend is valid for bainitic and martensitic transformations of austenite, which are obtained at much higher cooling rates than obtained in the cast strip, which is of the order of $10^4 - 10^5$ °C/s.

The in-line hot rolled strip has similar elongations to the as-cast strip, though with slightly higher strength values. This is in agreement with the microstructures observed. The variation in strength values is related to the different volume fractions of the various morphologies of ferrite present in the material. Basically, hot rolling has not been successful in increasing the ductility of the as-cast strip under the current processing conditions. However, the directly cold rolled and batch annealed sheet shows elongations very close to 50%, with useful strength.

The plastic strain ratio (i.e., r-value), obtained by simultaneously measuring the strain in the length and width directions, has been obtained for the various samples as shown in Table 2. The high r-values indicate resistance to thinning during a forming operation. The planar anisotropy factor (Δr), which measures the in-plane variation of the r-value, is predictive of the earing tendency of the sheet and should be minimized for deep drawing applications [22, 23]. A positive value of Δr denotes the tendency of earing in the rolling and transverse directions (typical of annealed material), and a negative value of Δr, a tendency in the diagonal direction (typical of rolled sheet). The plastic strain ratio is related to the amount of gamma fiber present in the sheet, i.e. <111>|| ND, and tends to be high for the Al-killed steel, because of the beneficial effects of AlN precipitation during recrystallization [11,12]. In-line hot rolling decreases the r-value, but cold rolling and batch annealing increases the r-value, though at the expense of high Δr. However, it is of interest to investigate how high an r-value can be obtained with the Si-killed strip cast sheet under different processing conditions.

Texture:

Fig. 7 shows pole figures for both the as-cast and in-line hot-rolled sheet; these are complete pole figures that were calculated from the orientation distribution derived from the experimental data. All six pole figures show weak maxima at the center. In either case, however, the texture is weak. This is the expected result for the as-cast condition because two phase transformations occur during cooling which tend to randomize the texture. The in-line hot-rolled texture is similar to the as-cast condition, which suggests that only a small reduction was applied (here, 30%). The balance between {100} and {111} components is in agreement with r-values close to unity and Δr near zero. The cold rolled batch annealed sample shows a significant increase in r-value and there is a mild development of gamma fiber (Fig. 8).

Fig. 9 shows {111} pole figures for a series of cold rolling reductions applied to the as-cast sheet. They show a progressive development of the gamma fiber as expected. Fig. 10 shows the orientation distribution (OD) for the highest reduction of 80%: most of the intensity lies in the alpha and gamma fibers as expected for this material. As described above, the as-cast material was also subjected to 70% cold rolling followed by annealing using a schedule that corresponds to batch annealing. The OD for this condition (Fig. 11) shows that the alpha fiber is weakened, leaving the gamma fiber as the dominant feature of the texture. Both OD's have been smoothed with a five degree wide Gaussian

filter for legibility. Figs. 12 and 13 show the intensities on the alpha and gamma fibers for all the conditions based on the highest intensity within ten degrees of the ideal position of each fiber. The results show a progressive strengthening of both fibers during plane strain deformation. Again, the texture evolution parallels that in conventional steels as expected. The weak-to-moderate gamma fiber is in agreement with the r-value being greater than unity. The large Δr value suggests, however, that there is room for improvement in the choice of rolling and annealing schedules.

Orientation Imaging Microscopy:

The orientation imaging microscopy (OIM) obtained for the as-cast strip confirms the optical characterization of a very inhomogeneous structure, with large irregular polygonal ferrite, and bands of Widmanstätten ferrite (Fig. 14). The different grain shades correspond to the normal direction of the grains. Thus, we can simultaneously study the grain morphology (size and shape) and orientation. The average grain size obtained from OIM grain mapping is 22μm, compared to 55μm observed by optical microscopy. This significantly finer grain structure obtained from the OIM explains the enhancement of the strength properties for the as-cast strip. OIM shows the presence of low angle grain boundaries, and sub-grain structure explicitly, which are not fully revealed by chemical etching. Fig. 15 shows the mapping of grains in a region dominated by Widmanstätten ferrite side plates, with a particular orientation selected within a tolerance angle of 10°. The image illustrates the presence of parallel laths of ferrite with similar orientation.

Summary

The various observations in this study can be summarized as follows:

- Strip cast steel has an acicular, Widmanstätten ferrite grain structure compared to polygonal ferrite observed in the conventionally cast and hot rolled steel.
- In-line hot rolling with the current processing parameters does not increase the ductility or r-value of the as-cast sheet.
- Cold rolled, batch annealed sheet has promising ductility (close to 50%), and reasonably high strength.

• Cold rolled, batch annealed sheet shows mild development of the γ-fiber, i.e. <111> || ND, and thus, enhanced r-value compared to conventionally cast Si-killed steel.

Acknowledgments

The authors wish to thank Rama Mahapatra and Walter Blejde from BHP, Australia, for providing the strip cast steels and process information. Special thanks are due to Jayanta Jay and Michael Sun of National Steel, and Todd Osman of US Steel for their support in carrying out the rolling and annealing experiments. The support is acknowledged of the US Department of Energy, the AISI (American Iron & Steel Institute), US Steel, National Steel, LTV Steel, Dofasco, AK Steel, SMS Concast and Voest-Alpine. The authors are also grateful to the sponsors for permission to publish this paper.

References

1. A.W. Cramb: *Acero NASJ/North American Steel Journal (Mexico)*, 1998, vol. 4, No. 20, s9.
2. A.W.Cramb: *Canadian Institute of Mining, Metallurgy & Petroleum (Canada)*, 1995, p. 355.
3. D. Raabe: *Metall. Trans A*, 1995, vol. 26A, p. 991
4. S. Teraoka: *Ph.D. Thesis, McGill University, Montreal, Quebec*, 1999.
5. J.F. Bingert: *M.S. Thesis, Colorado School of Mines, Golden, Colorado*, 1990.
6. L.T. Shiang, and P.J. Wray: *Metall. Trans. A*, 1989, vol. 20A, p. 1191.
7. W. Blejde, R. Mahapatra, and H. Fukase: *Iron and Steelmaker (USA)*, 2000, vol. 27, No. 4, p. 29.
8. W. Blejde, R. Mahapatra, and H. Fukase: *Belton Symposium Proceedings*, 2000, p. 253.
9. A. Guillet, E. Es-Sadiqi, G.L'esperance, and F.G. Hamel: *ISIJ International*, 1996, vol. 36, No. 9, p. 1190.
10. A. Okamoto: *Proc. 8th Int. Conf. on Texture of Materials (ICOTON-8)*, 1988, p. 891.
11. R.K. Ray, J.J. Jonas, and R.E. Hook: *Int. Mater. Rev.*, 1994, vol. 39, No. 4, p. 129.

12. L.T. Shiang, and P.J. Wray: *Scr. Metall. Mater.*, 1991, vol. 25, No. 1, p. 143.
13. D. Raabe, and K. Lücke: *Mater. Sci. Forum*, 1994, vol. 157-162, p. 597.
14. K. Ushida, W.B. Hutchinson, J. Argen, and U. von Schlippenbach: *Mater. Sci. Technol.*, 1986, vol. 2, p. 807.
15. B.L. Adams, S.I. Wright, and K. Kunze: *Metall. Trans A*, 1993, vo. 24A, p. 819.
16. V. Randle: *Microtexture Determination and its Applications,* The Institute of Materials, 1992.
17. D.J. Dingley and K.Z. Baba-Kishi: *Scanning Electron Microscopy,* 1986.
18. K. Schwerdtfeger: *Advanced Physical Chemistry for Process Metallurgy, Academic Press*, 1997, p. 381.
19. H. Sha, and K. Schwerdtfeger: *International Journal of Heat and Mass Transfer*, 1998, vol. 41, p. 3265.
20. E. Räsänen, and J. Tenkula: *Scand. J. of Metall.*, 1972, vol. 1, p. 75.
21. A.O. Kluken, _. Grong, and J. Hjelen: *Met. Trans. A*, 1991, vol. 22A, p. 657.
22. W.C. Leslie: *The Physical Metallurgy of Steels*, 1981, TechBooks, Hemisphere Publishing Corporation.
23. D.T. Llewellyn and R.C. Hudd: *Steels: Metallurgy & Applications*, 1998, Butterworth Heinemann publications.

Table 1: Mechanical properties of as-cast, in-line hot rolled, and cold rolled batch annealed sheet

Mechanical Properties	As-cast	In-line hot rolled	Cold rolled, batch annealed
YS (MPa)	40	48	35
UTS (MPa)	62	67	52
El. (%)	32	33	48
HRB	71	77	55

Table 2: Plastic Strain Ratio of as-cast, in-line hot rolled, and cold rolled batch annealed sheet

Processing Type	r-value (r_m)	Plastic Anisotropy factor (Δr)
As-Cast	0.93	0.07
In-line Hot Rolled	0.79	-0.11
Cold Rolled, Batch Annealed	1.1	0.45

Figure 1: Microstructure of as-cast strip, 4% nital etch. (a) region showing acicular ferrite. (b) region showing irregular polygonal and Widmanstätten ferrite

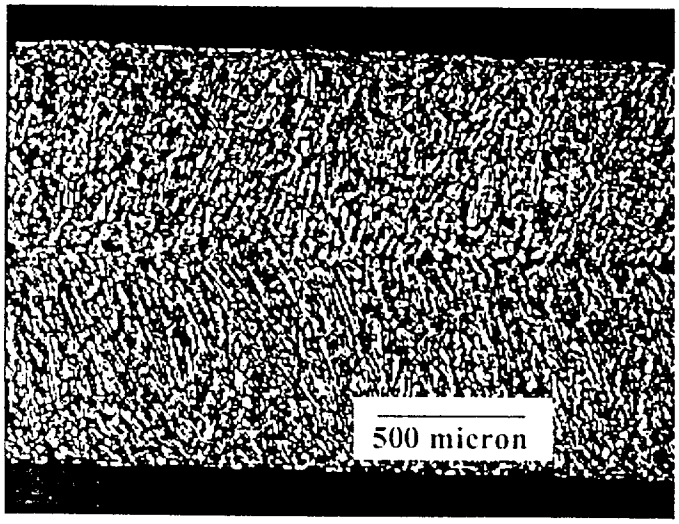

Figure 2: Solidification structure of as-cast strip, hot picric etch, showing primary dendrites

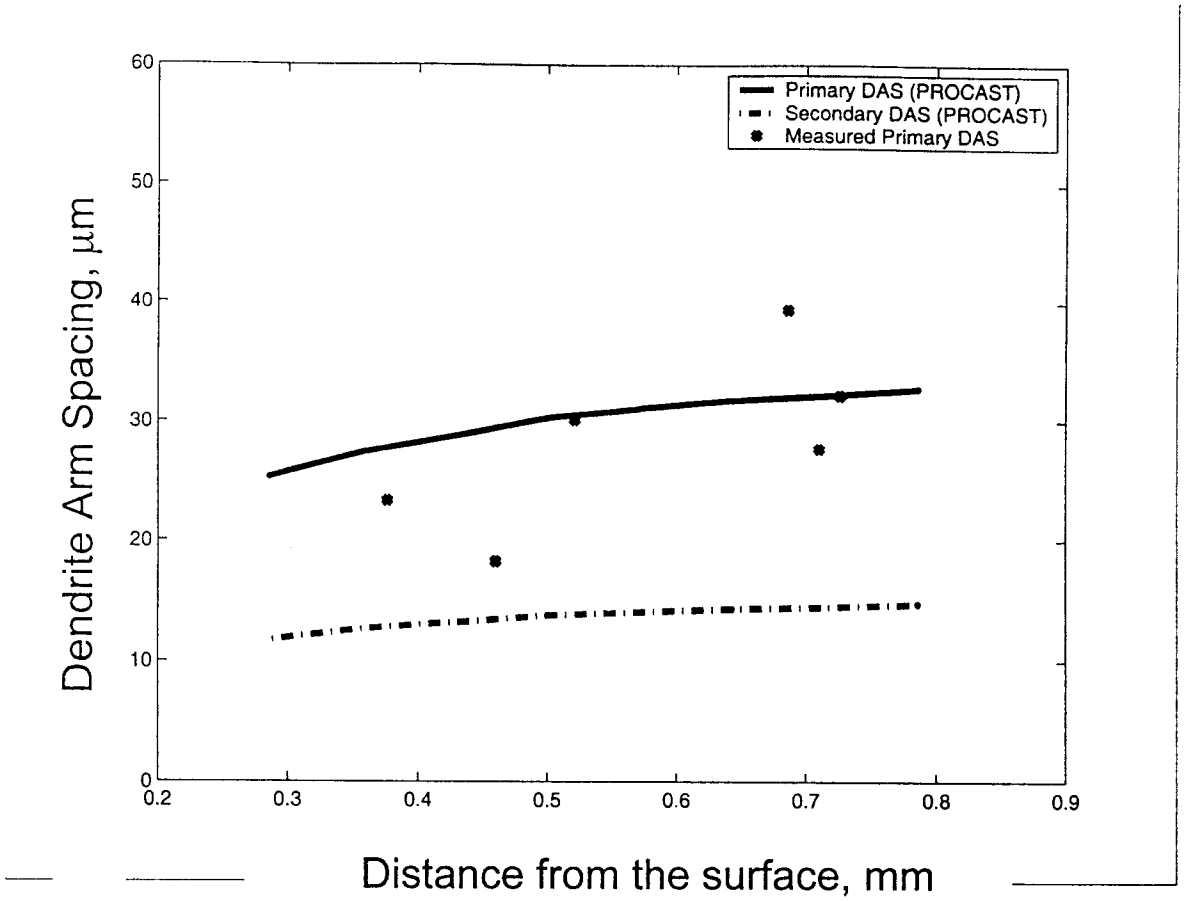

Figure 3: Primary and secondary dendrite arm spacing calculated with Procast and the experimentally measured primary dendrite arm spacing

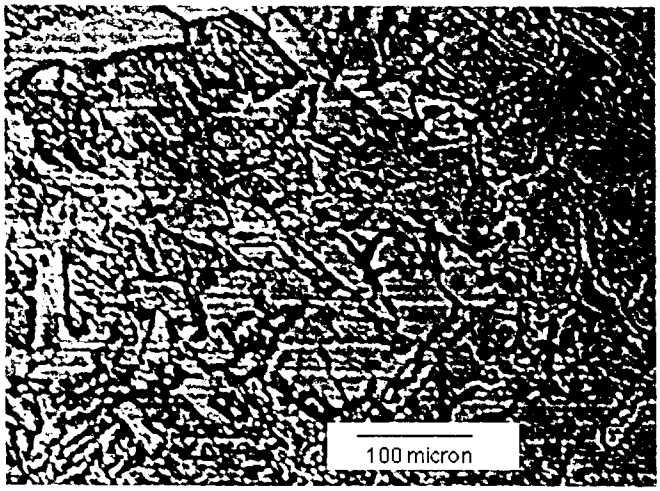

Figure 4: In-line hot rolled strip, 4% nital etch

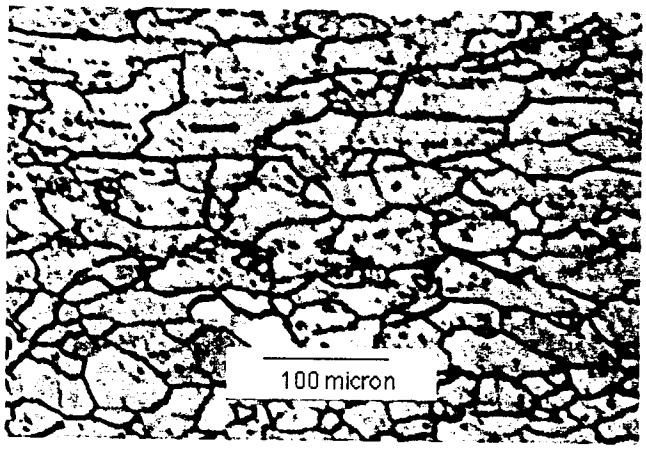

Figure 5: 70% cold rolled, batch annealed sample, nital etch

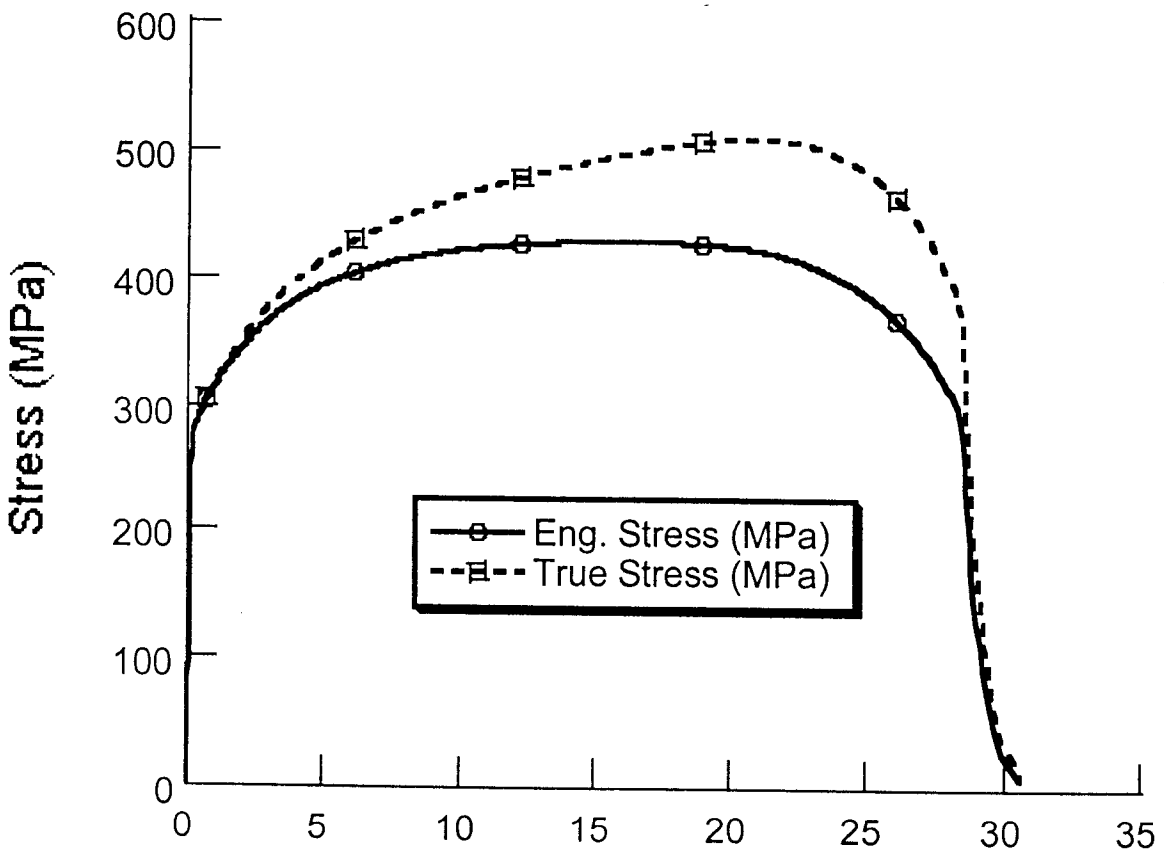

Figure 6: Engineering and true stress strain curves for as-cast sheet

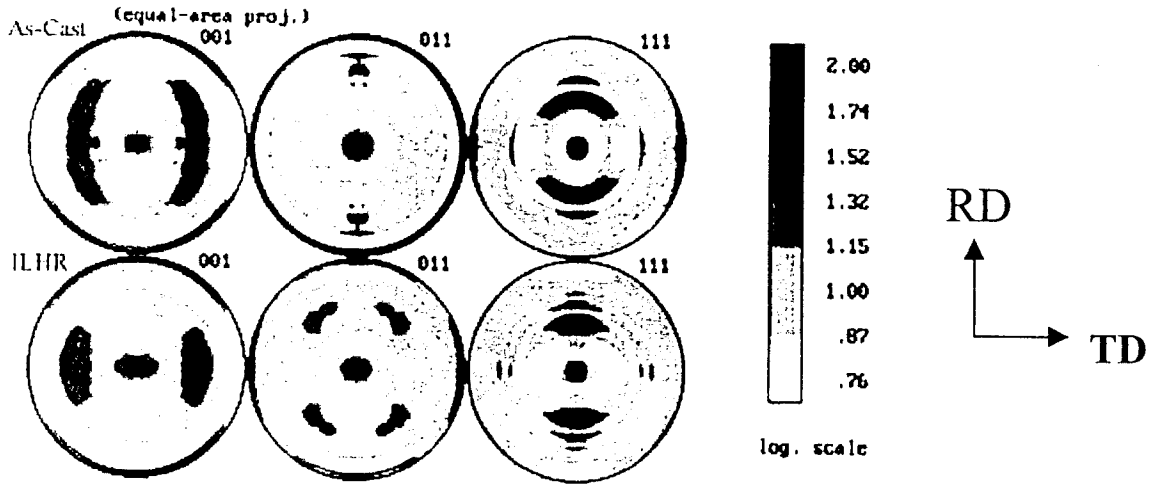

Figure 7: Pole figures for as-cast and in-line hot rolled samples

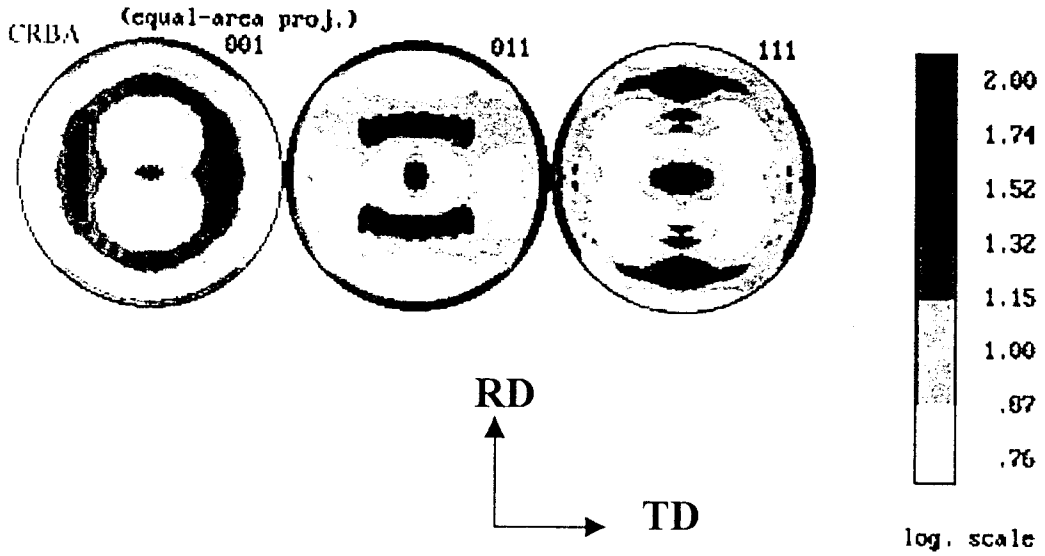

Figure 8: Pole figures for 70% cold rolled, batch annealed sample

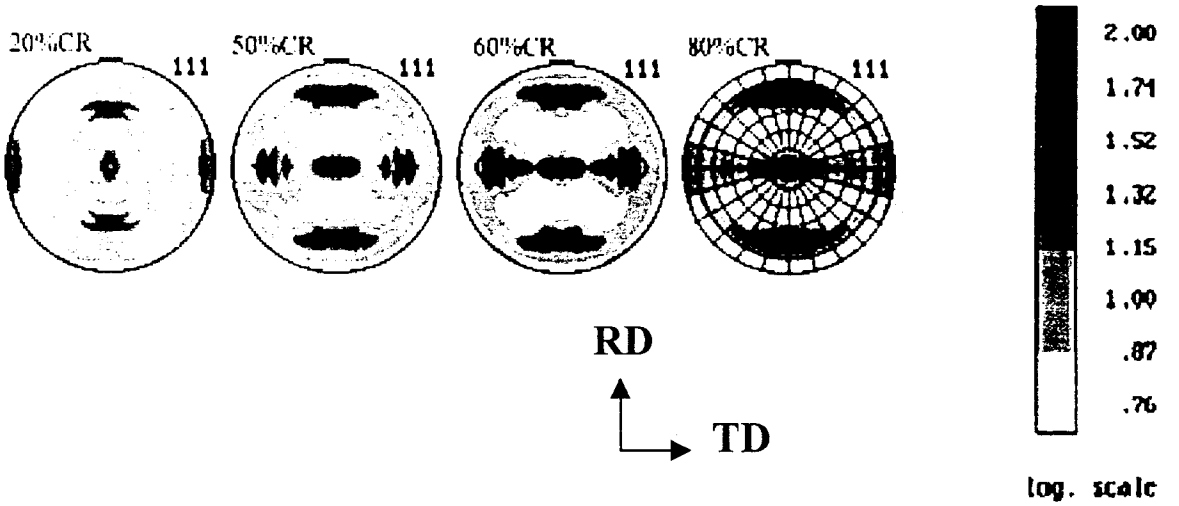

Figure 9: (111) pole figures for 20%, 50%, 60% and 80% cold rolled strip cast samples to show the evolution of gamma fiber

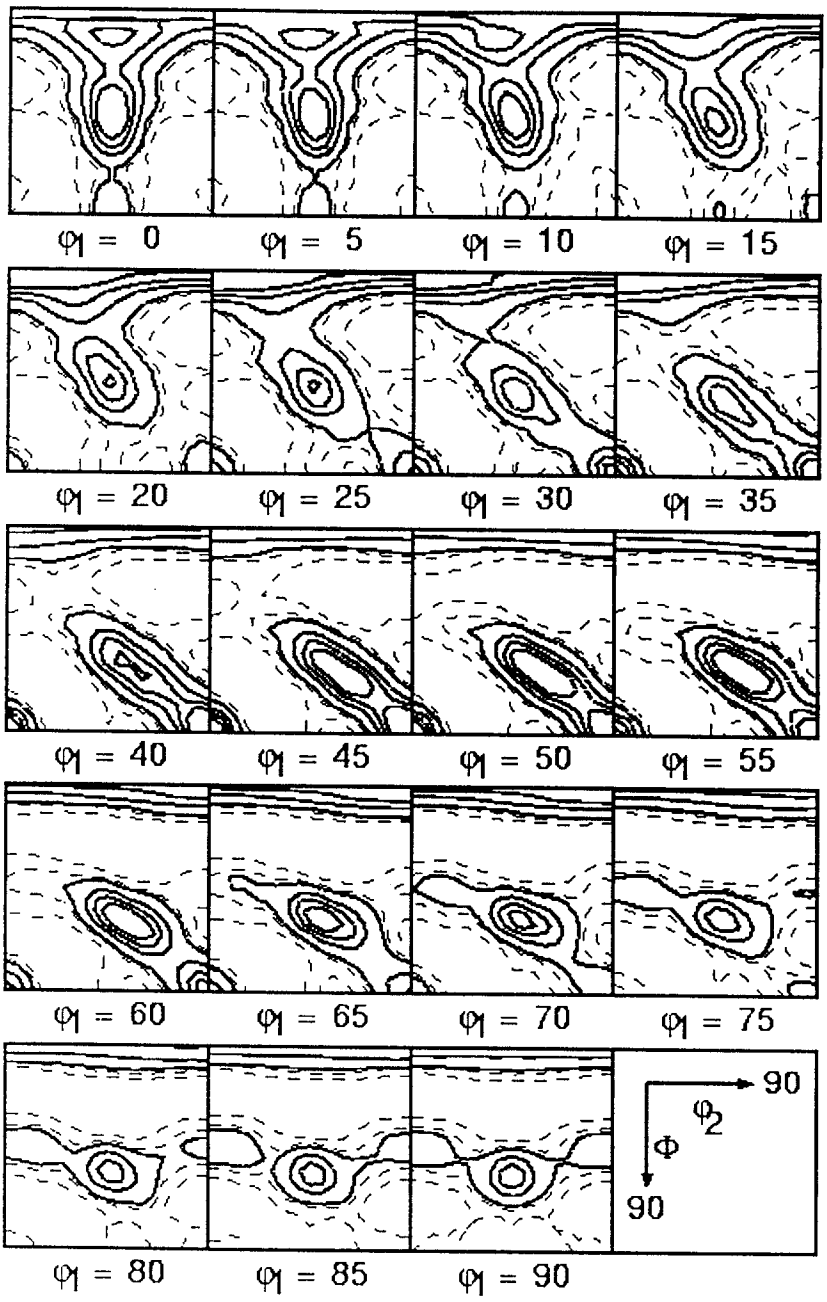

Figure 10: Orientation distribution for strip cast and 80% cold rolled steel sheet

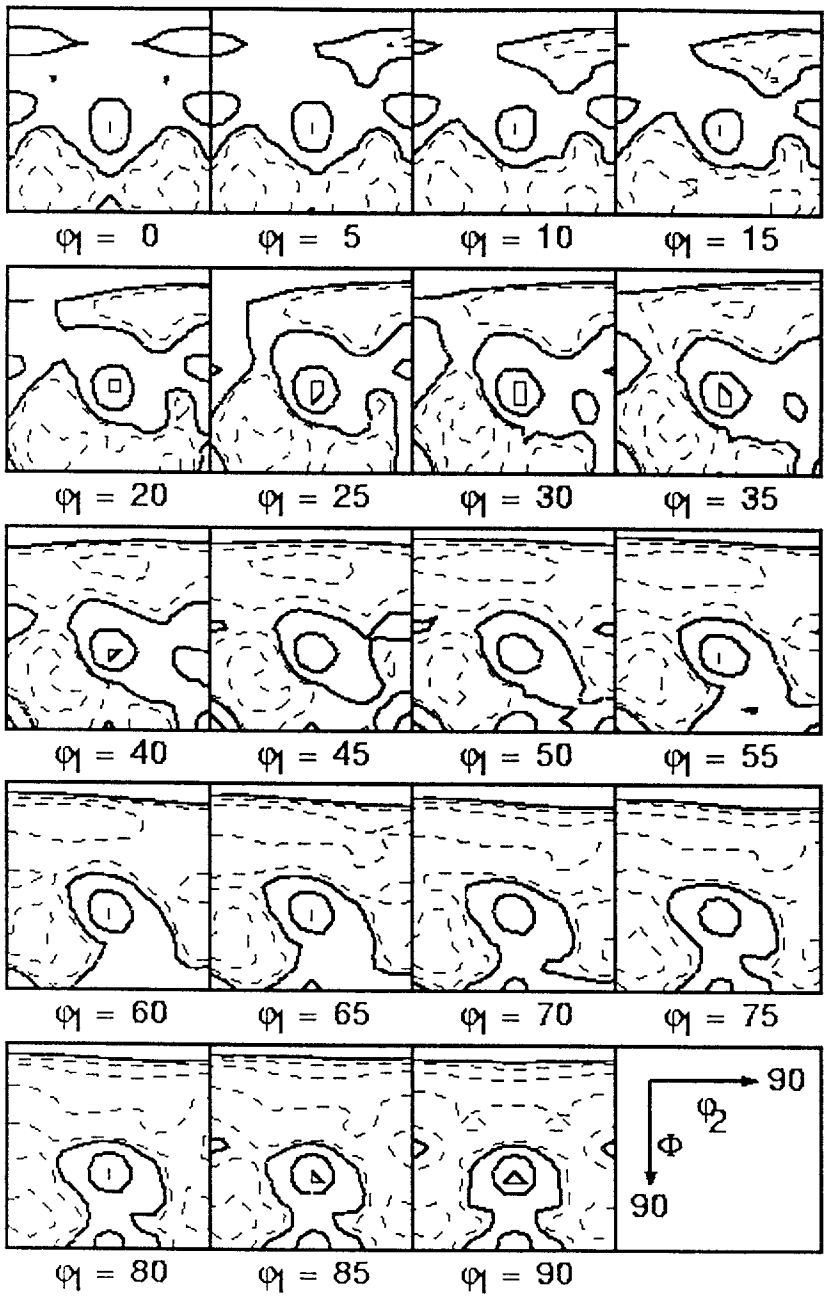

Figure 11: Orientation distribution for strip cast, 70% cold rolled batch annealed steel sheet.

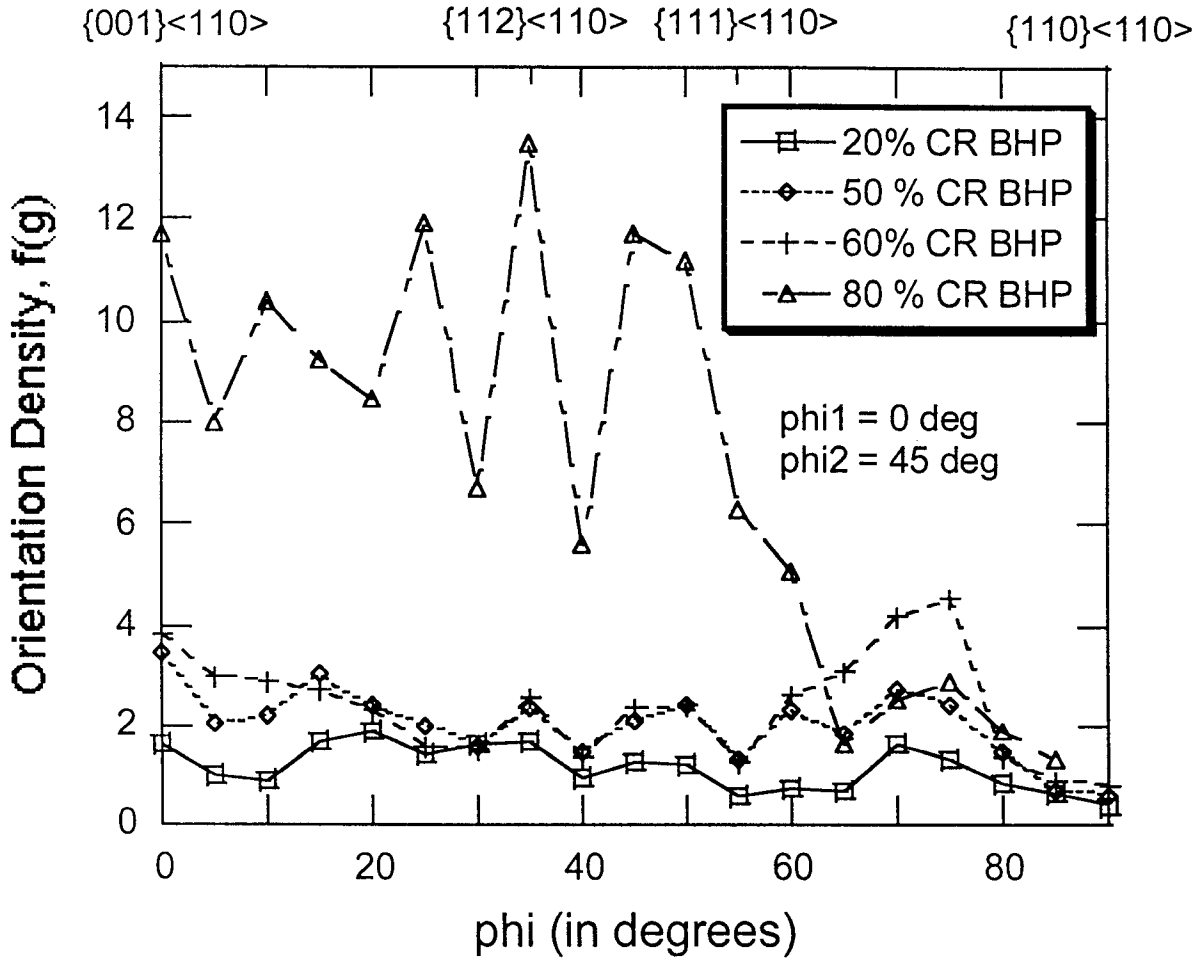

Figure 12: Plot of the variation in the alpha fiber with rolling reduction for the cold rolled strip cast sheet.

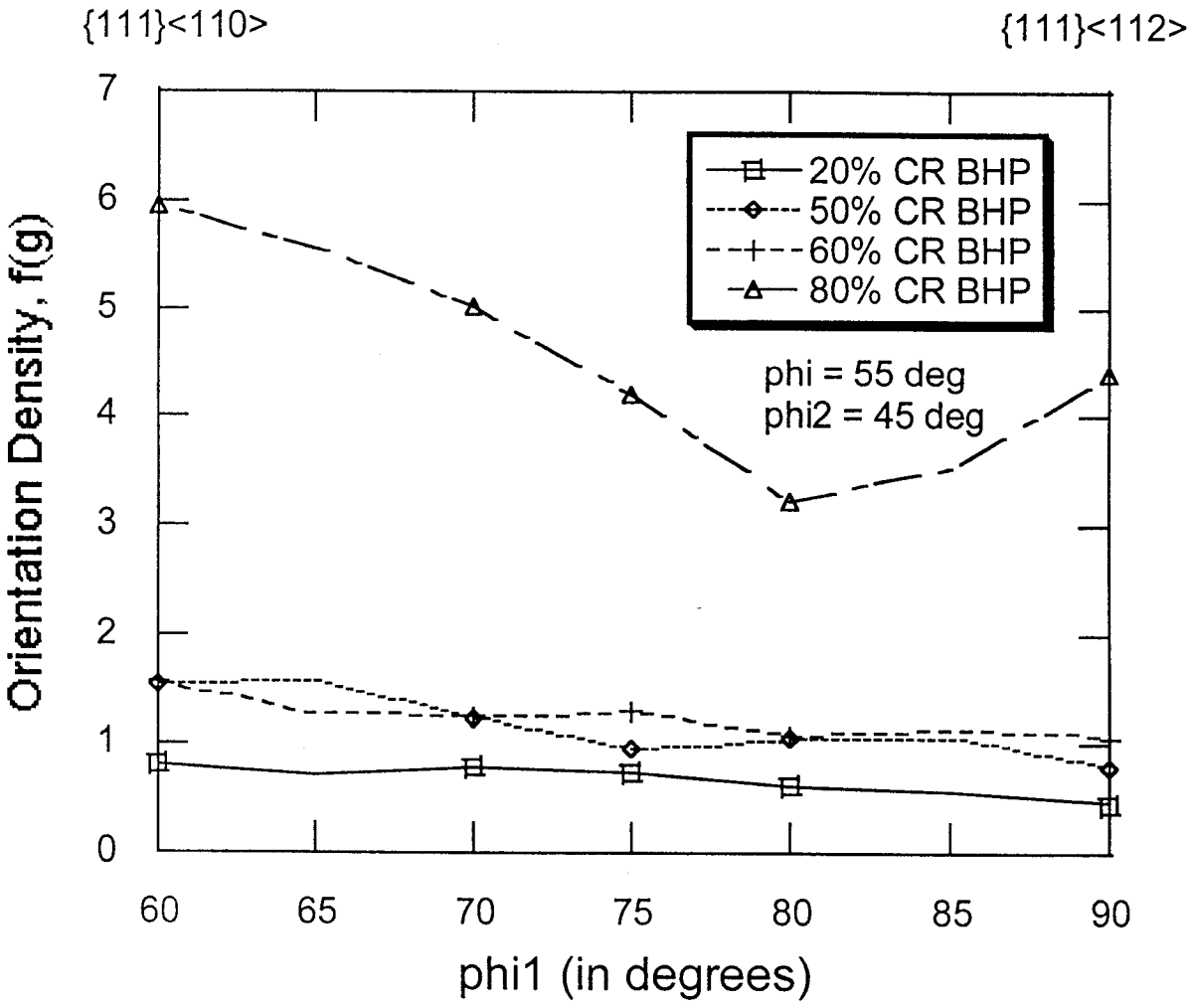

Figure 13: Plot of the variation in the gamma fiber with rolling reduction for the cold rolled sheet.

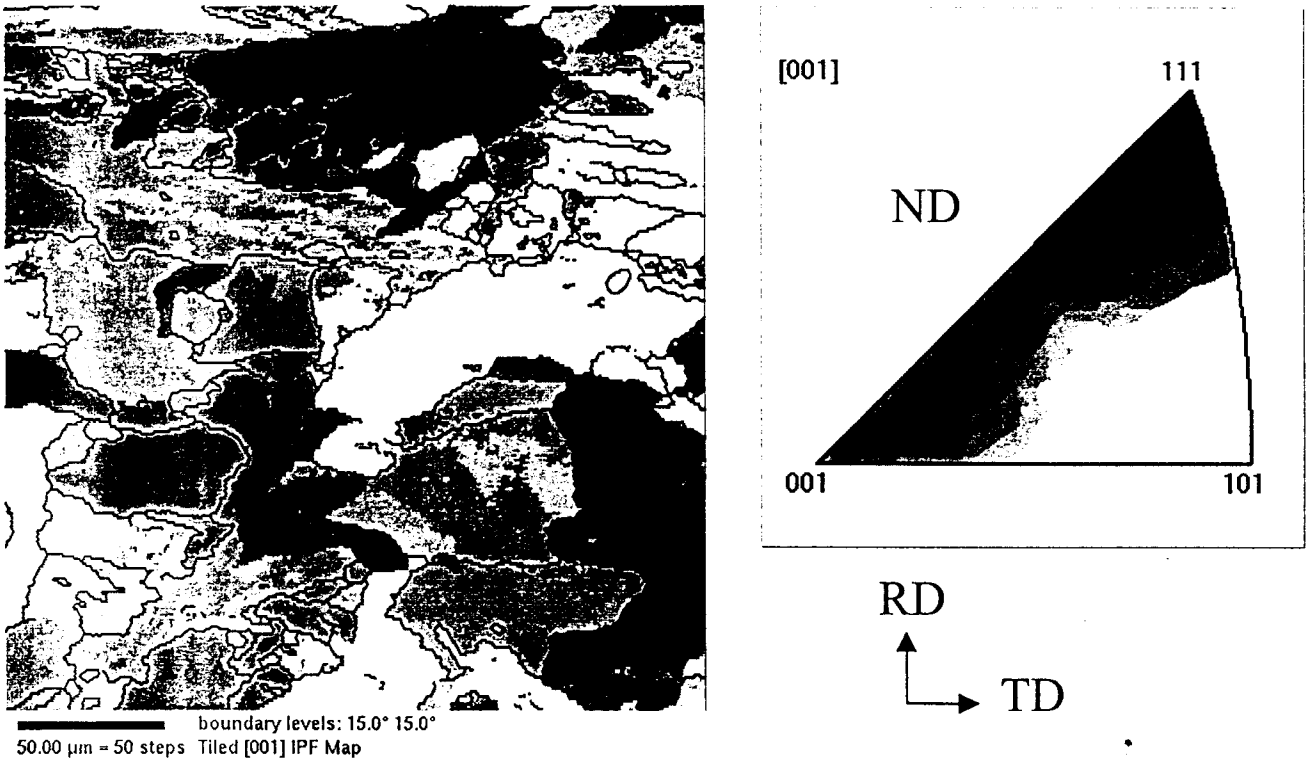

Figure 14: OIM mapping of grains with respect to their orientations parallel to the normal direction; different colors of grains indicate the different orientations present in the sample

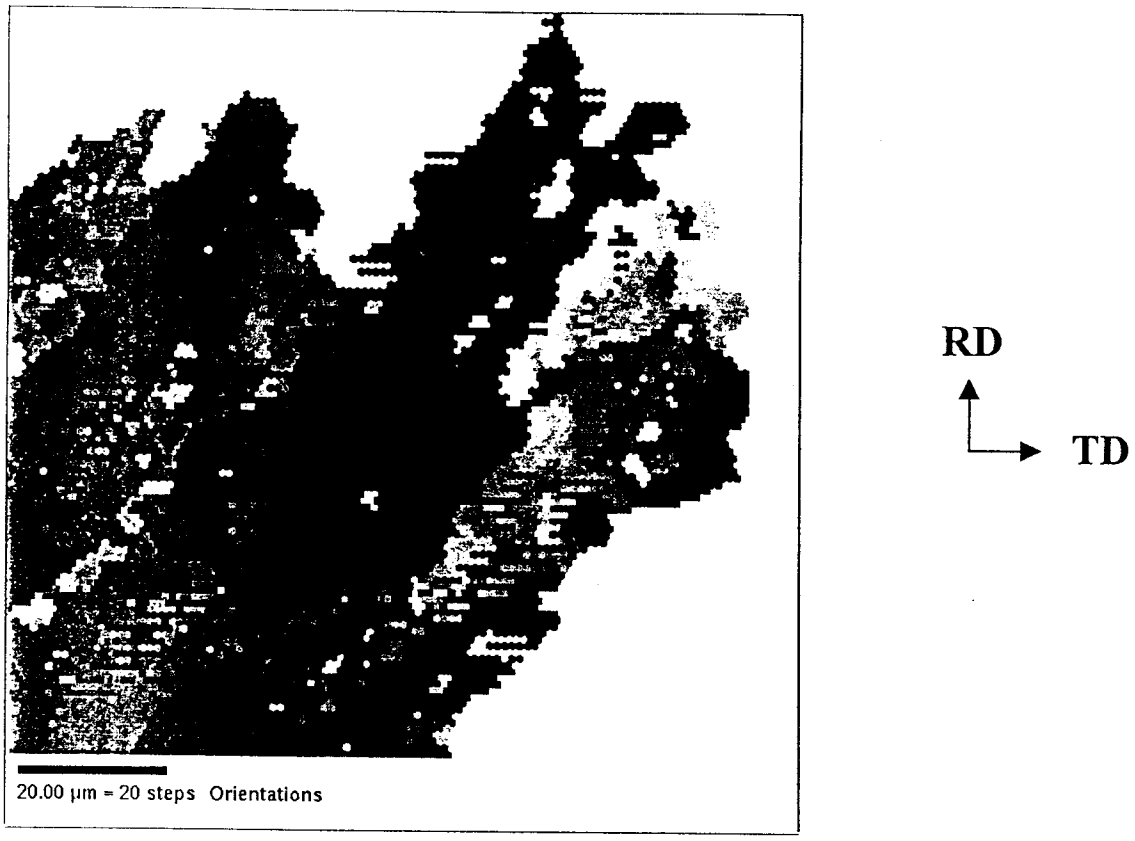

Figure 15: OIM mapping in a region dominated by Widmanstätten ferrite, shaded within a tolerance of 10° of a selected orientation inside the Widmanstätten ferrite structure